

MONTANUNIVERSITÄT LEOBEN

Department Mineral Resources and Petroleum Engineering
Chair of Petroleum and Geothermal Energy Recovery



Dissertation

Sucker Rod Anti - Buckling System Analysis

Dipl.-Ing. Dipl.-Ing. Clemens Langbauer

Supervisor: Univ.-Prof. Dipl.-Ing. Dr.mont. Herbert Hofstätter
Univ.-Prof. Dipl.-Ing. Dr.mont. Thomas Antretter

August 2015

AFFIDAVIT

I declare in Lieu of oath, that I wrote this thesis and performed the associated research myself, using only literature cited in this dissertation.

Clemens Langbauer, August 2015

1 ACKNOWLEDGEMENT

It is a pleasure for me to thank those persons who continuously supported me during the research this thesis is based on. First of all I would like to express my gratitude to Prof. Herbert Hofstätter and Prof. Thomas Antretter for their encouragement, invaluable supervision and interesting discussions on this topic. Thank you for enabling me to extend the understanding for the subject and to accomplish this thesis.

I would like to thank my colleagues at the chair for numerous indispensable discussions of special issues and assistance, especially DI Petr Vita and Sepp Steinlecher, MBA. I am very grateful for the support of Dr. Rudolf Fruhwirth for his continuous help in postprocessing and visualization issues.

It is an honor for me that OMV sponsored this thesis and supplied the required information for the research, as well as the allowance for the usage of a well for the field test. Beside the OMV team in Gänserndorf I would like to express special thanks for their continuous support to DI Reinard Pongratz, DI Christoph Marschall and DI Patrick Bürßner.

2 ABSTRACT

This thesis presents a finite element analysis for investigating the dynamic behavior of the sucker rod pumping system and the implementation of the Sucker Rod Anti Buckling System (SRABS). At the beginning the components and the working principle of a standard sucker rod pump are presented as well as the limitations of a standard pump and the design of SRABS, which effectively prevents the rod string completely from buckling.

Then the western history of sucker rod pumping and the impact of sucker rod pumps on today's oil production are summarized.

The literature review summarizes the mathematical background and the research performed so far for analyzing the dynamic behavior of sucker rod pumping. Models for describing the rod string, developed from the sixties until now, are presented with strengths and weaknesses. The theory of buckling is presented, including an extensive review of the influence of liquid, surrounding the rod string, on the buckling behavior of rods.

Thereafter models are investigated and selected for representing the motion of the polished rod and the load profile at the pump plunger. The results are compared on one hand with commercial software result and on the other hand with field dynamometer measurements. The basics of the employed finite element analysis are presented. A fluid – solid interaction simulation is performed to quantify the viscous friction between the tubing, sucker rod string and the lifted fluid, including a sensitivity analysis to find the major impact parameter. Rod guide friction coefficient experiments are performed to find the influence of different fluid compositions on the frictional behavior.

Measurements with self-developed Downhole Dynamometer Sensors are performed to get data of motion and load of an operating pumping system, along the complete sucker rod string. In addition to the very interesting information about the temperature profile of an operating oil well, the results are compared with the pump plunger load profile.

A dynamic finite element method analysis simulates the complete behavior of the sucker rod string and allows by post processing of the simulation results, the derivation of energy consumption, system efficiencies, rod string motion and load behavior. Predictive and diagnostic simulations can be performed with the model. An extensive case study investigates the performance of different tapered sucker rod strings under various pumping speeds with and without SRABS.

The economic evaluation summarizes the huge saving potential, which can be achieved by using SRABS. Along with the electricity savings and a reduction of required workover operations, Health, Safety and Environmental issues can be improved as well.

During the research for this thesis the ability for preventing buckling when applying the patented tensioning element is proved. In addition a patent, using the liquid pressures in tubing and casing in a favourable way for reducing the buckling tendency drastically, is generated during the research. A simulation routine is developed, which is able to analyze the dynamics of the sucker rod string and in addition the impact of the patented developments. The evaluation procedure allows an accurate prediction of the actual production costs, which enables a proper economic evaluation of the sucker rod pumping system.

At the end of this thesis recommendations for further research issues are presented. Beside others one of the most important influencing parameter is the interference of gas on the overall frictional behavior of the sucker rod string. New technology, like a continuous sucker rod string or an asymmetric stroke profile should be investigated in addition.

3 KURZFASSUNG

Diese Arbeit präsentiert eine Finite-Elemente-Analyse zur Untersuchung des dynamischen Verhaltens von Gestängetiefpumpen und der Anwendung des Sucker Rod Anti-Buckling System (SRABS). Zu Beginn sind die Bauteile und die Funktionsweise einer Standard-Gestängetiefpumpe, sowie die Grenzen einer Standardpumpe und die Gestaltung der SRABS Pumpe, die das Ausbeulen des Pumpgestänges effektiv verhindert, dargestellt.

Im Anschluss werden die westliche Geschichte der Gestängetiefpumpen und der Einfluss von Gestängetiefpumpen auf die heutige Ölproduktion diskutiert.

Die Literaturrecherche befasst sich mit den mathematischen Hintergründen und der bis jetzt unternommenen Forschungsaktivität auf diesem Gebiet. Modelle zur Beschreibung des dynamischen Verhaltens des Gestänges, beginnend in den sechziger Jahren bis heute, mit einer Zusammenfassung der Stärken und Schwächen, werden vorgestellt. Auf die Knicktheorie wird unter einer umfassenden Darstellung der Flüssigkeitseinflüsse auf das Knickverhalten von Stäben eingegangen.

Danach werden Modelle zur Beschreibung der der Bewegung an der Polierstange und das Lastverhalten am Pumpenkolben ausgewählt. Die Ergebnisse sind auf der einen Seite mit jenen von kommerziellen Softwarepaketen und andererseits mit Feldprüfmessungen verglichen. Die Grundlagen der angewandten Finite-Elemente-Analyse werden vorgestellt. Eine Flüssigkeits - Festkörper Interaktionssimulation wird durchgeführt, um die viskose Reibung zwischen der Verrohrung, dem Pumpgestänge und der gepumpten Flüssigkeit, einschließlich einer Sensitivitätsanalyse, zu quantifizieren. Experimente zur Bestimmung der Reibbeiwerte zwischen Verrohrung und Pumpgestänge unter dem Einfluss verschiedener Flüssigkeitszusammensetzungen werden vorgestellt.

Die Auswertung von Feldmessungen mit selbst entwickelten Downhole-Dynamometer-Sensoren wird präsentiert. Aufgabenstellung ist die Erfassung von Bewegung und Belastung des Gestänges entlang der gesamten Stranglänge. Neben sehr interessante Informationen über das Temperaturprofil einer Ölsonde, werden die Ergebnisse mit dem Lastprofilmodell verglichen.

Eine dynamische Finite-Elemente-Methode-Analyse simuliert das vollständige Verhalten des Pumpgestänges und ermöglicht durch Aufbereitung der Simulationsergebnisse, die Ableitung des Energieverbrauches, die Systemeffizienz und das Gestänge Bewegungs- und Belastungsverhaltens. Vorhersagen für neue Pumpenanwendungen, sowie die Diagnose von bereits bestehenden Pumpanlagen können mit dem entwickelten Modell durchgeführt werden. Eine umfangreiche Fallstudie untersucht die Leistung unterschiedlicher Pumpgestängemodifikationen, sowie SRABS.

Die wirtschaftliche Bewertung der Simulationsergebnisse fasst die beachtlichen Einsparpotenziale, die durch die Nutzung von SRABS erreicht werden können zusammen. Neben Einsparungen an Energieverbrauch und einer Verringerung der erforderlichen Behandlungsarbeiten, können auch in den Bereichen Gesundheit, Sicherheit und Umwelt Verbesserungen erzielt werden.

Während den Forschungsarbeiten wurde die Fähigkeit des patentierten Spannelement zur Verhinderung von Knicken bewiesen. Zusätzlich dazu ergab sich aus den Arbeiten zu diesem Thema ein weiteres Patent. Dieses zeigt den vorteilhaften Einfluss der Flüssigkeitsdrücke in Verrohrung und Produktionsrohr auf die Knickneigung des Pumpgestänges in Form einer drastischen Reduktion. Eine Simulationsroutine wird vorgestellt, die in der Lage ist, die dynamischen Vorgänge des Pumpgestänges und zusätzlich die Einflüsse der patentierten Entwicklungen zu analysieren. Das Auswertungsverfahren ermöglicht eine genaue Vorhersage der tatsächlichen Produktionskosten, die die wirtschaftliche Bewertung von Gestängetiefpumpen wesentlich verbessert.

Am Ende dieser Arbeit werden Empfehlungen für weitere Forschungsteilbereiche auf diesem Gebiet vorgestellt. Einer der wichtigsten Einflußgrößen auf das Gesamtsystem ist die Interaktion von Gas auf das Reibungsverhalten des Pumpgestänges. Daher wird vor allem eine genauere Betrachtung für Systeme, die an Sonden mit einem hohen Gas - Öl Verhältnis eingesetzt werden, empfohlen. Der Einfluss neuer Technologien, wie die Verwendung eines kontinuierlichen Pumpgestänges oder eines asymmetrischen Hubprofils sollten zusätzlich untersucht werden.

TABLE OF CONTENTS

Affidavit	iii
1 Acknowledgement.....	v
2 Abstract	vii
3 Kurzfassung.....	ix
Table of Contents	xi
1 Introduction and Problem Description	1
1.1 Introduction	1
1.2 Pump and Problem Description	4
1.3 Operating Principle and Dependent Problems	7
1.4 Problem Description.....	8
2 Western History of Sucker Rod Pumping.....	13
3 Impact of SRP's on Oil Production	15
4 Mathematical Background.....	17
4.1 Models for Vertical Wells	17
4.2 Models Implementating the Dynamics of the Liquid Column.....	23
4.3 Models for Inclined Wells.....	24
4.4 Buckling Models.....	29
4.5 Summary.....	34
5 The Sucker Rod Pumping System.....	37
5.1 Surface Boundary Condition - Behaviour at the Polished Rod.....	38
5.1.1 Displacement at the Polished Rod	38
5.1.2 Load at the Polished Rod.....	50
5.1.3 Pump Jack Dynamics.....	51
5.2 Behaviour of the Sucker Rod String	55
5.2.1 Finite Element Method - Basics.....	57
5.2.2 Finite Element Method - Application.....	61
5.3 Fluid Flow Behavior in the Tubing	61
5.3.1 Modelling the Pressure Behavior in the Tubing	62
5.3.2 Modelling the Viscous Drag on the Sucker Rod String.....	64
5.4 Rod Guide Friction Coefficients	70

5.5	Behaviour of the Pump Plunger.....	73
5.5.1	Load Behaviour of the Pump Plunger	73
5.5.2	Downhole Boundary Condition Comparison with Rodstar	90
6	Downhole Dynamometer Sensor Measurements.....	93
6.1	Sensors So Far.....	93
6.2	Downhole Dynamometer Sensor (DDS):	94
6.2.1	Temperature Sensor Calibration	96
6.2.2	Accelerometer Calibration	97
6.2.3	Strain Gauge Calibration	98
6.3	Well OMV 1	105
6.4	Measurement Procedure	107
6.5	Data Processing and Interpretation	109
6.5.1	Temperature Sensor	109
6.5.2	Accelerometer Sensor	110
6.5.3	Strain Gauge Sensor	112
6.6	Surface Dynamometer Card Comparison	122
6.7	Downhole Dynamometer Card Comparison	123
7	Dynamic Finite Elements Method Analysis	125
7.1	Input File Structure / Definition.....	126
7.1.1	Mesh Definition	126
7.1.2	Contact Definition	131
7.1.3	Material Property Definition	133
7.1.4	Boundary Condition and Amplitude Definition	133
7.1.5	Step Definition	134
7.1.6	Load Definition	134
7.1.7	SRABS Implementation.....	135
7.2	Simulation Cases.....	136
7.2.1	Sucker Rod String Friction Analysis.....	137
7.2.2	Diagnostic Analysis.....	138
7.2.3	Predictive Analysis	140
8	Case Study.....	149
9	Economic Evaluation of SRABS.....	159
10	Conclusion	163
11	Recommendations	165
	Bibliography.....	167
	Nomenclature.....	175
	List of Abbreviations.....	181
	List of Figures	183

List of Tables..... 191

Appendix A..... 193

Appendix B..... 197

Appendix C..... 203

Appendix D..... 209

Appendix E..... 213

Appendix F..... 223

Appendix G..... 235

Appendix H..... 247

1 INTRODUCTION AND PROBLEM DESCRIPTION

1.1 INTRODUCTION

According to the U.S. Energy Information Administration, the total global crude oil consumption is about 92 million barrels per day and is steadily increasing by 1,6 percent per year. This corresponds to a consumption of 2 liters of oil for each single person on the planet per day. This fact makes crude oil irreplaceable today, still. Nothing can substitute its convenience in supply and energy density, yet.

Figure 1 presents the “World Liquid Fuels Production and Consumption Balance over time”. This chart shows that consumption of crude oil is almost equal to the production or even bigger. This means the implied stock change or spare capacity is rather small, which may have three reasons: (1)

- 1) To obtain higher prices on the market the supply of crude oil is controlled to closely meet the consumption. Large amounts of spare capacities could lead to falling prices but long periods with a relative high oil price would stimulate the installation of alternative energy sources, which may also be undesired by the oil industry.
- 2) The second possibility may be the fact that it is difficult to develop new reservoirs to meet the demand. In this case it is even more important to improve the technology and equipment to get as much hydrocarbon as possible out of existing and developed oilfields under economic conditions.
- 3) Speculations at the stock market.

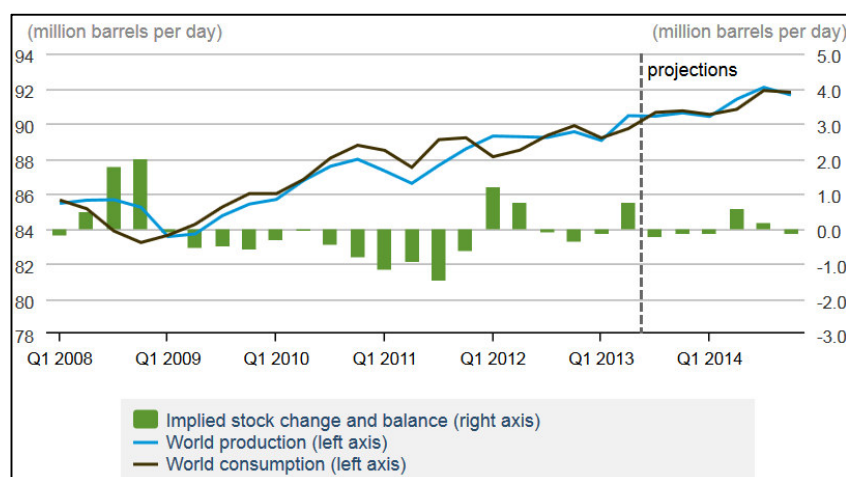


FIGURE 1: WORLD LIQUID FUELS PRODUCTION AND CONSUMPTION BALANCE (1)

The production of liquid hydrocarbons from their reservoirs requires a certain amount of energy. This energy must be provided as pressure of a magnitude basically depending on the depth of the reservoir, on the friction pressure losses in the production tubing, and on the composition of the lifted fluid.

As a result reservoirs can be differentiated into naturally flowing reservoirs, where the initial reservoir pressure is above the required pressure for lifting, and non-naturally flowing reservoirs, where the initial pressure of the hydrocarbon reservoir is too low and artificial lift methods need to be applied. During the depletion of hydrocarbon reservoirs, pressure declines if no pressure stabilizing measures, like water flooding, are applied and at a certain point in the life of these reservoirs the pressure drops below the required flowing pressure. Figure 2 presents the Inflow Performance Relationship (IPR), which shows the inflow performance of the reservoir and the Vertical Lift Performance (VLP), which represents the required pressure for lifting.

To enable production from non-naturally flowing reservoirs and increase the recovery factor under economic conditions, energy in form of pressure Δp has to be added to the reservoir by using pumps. There are several pump types available, which differ in their working principle, to meet the requirements of the pumped fluid. Selecting a suitable pump type depends on the production rate, the required lifting pressure and the properties of the pumped fluid.

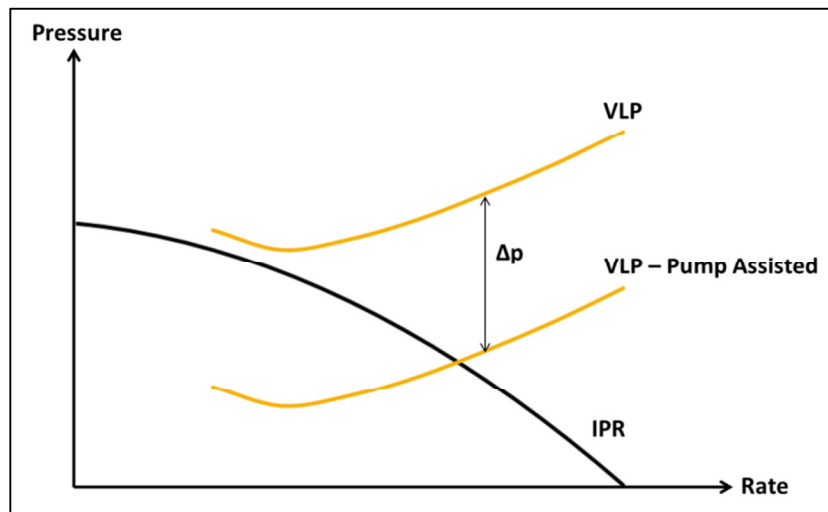


FIGURE 2: INFLOW PERFORMANCE RELATION SHIP

The most common artificial lift types are:

- Sucker rod pumps (ROD)
- Electric submersible pumps (ESP)
- Hydraulic pumps (HP)
- Progressive cavity pumps (PCP)
- Continuous gas lift (C-GL)
- Plunger lift (PLNG)

Figure 3 shows the application of the different artificial lift methods in the United States in percent on the base of about 500 000 U.S. oil wells. (2)

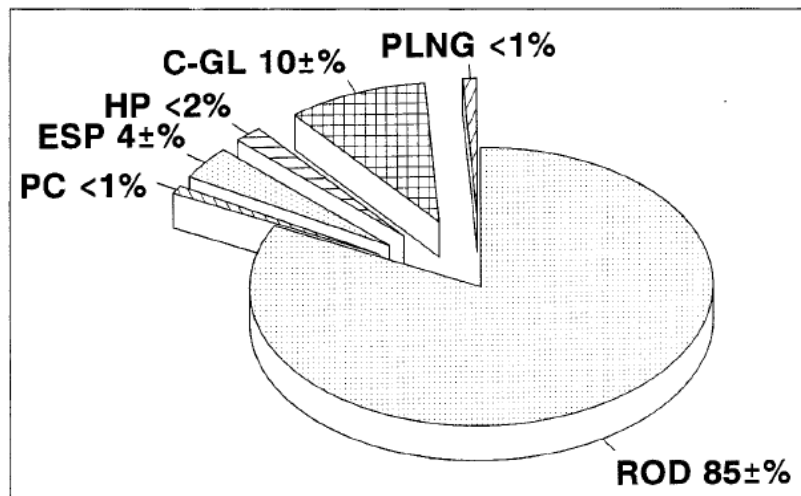


FIGURE 3: USAGE OF DIFFERENT ARTIFICIAL LIFT METHODS IN THE U.S. (2)

Figure 3 also displays the percentage of gas lift systems. A gas lift system is not a real pumping system but it counts as an artificial lift method because it lowers the density of the lifted fluid by injecting gas and allows the oil flow under the reservoir’s own pressure again.

Newer data (3) for all artificially lifted wells present 82% sucker rod pumps, 10% gas lift, 4% electric submersible pumps and 2% hydraulic pumps. So there is almost no change in the distribution of artificial lift systems over more then three decades. Another publication (4) estimates the worldwird usage of artificial lift systems for GL, ESP, SRP, PCP and HP equal to 50, 30, 17, >2 and <2%, which seems doubtful.

A major percentage of all artificially lifted wells employ sucker rod pumps. As a result the economic impact of this pump type is enormous. The understanding of the pumping operation and its influencing parameters are of essential importance for designing the pump in order to operate under best economic conditions.

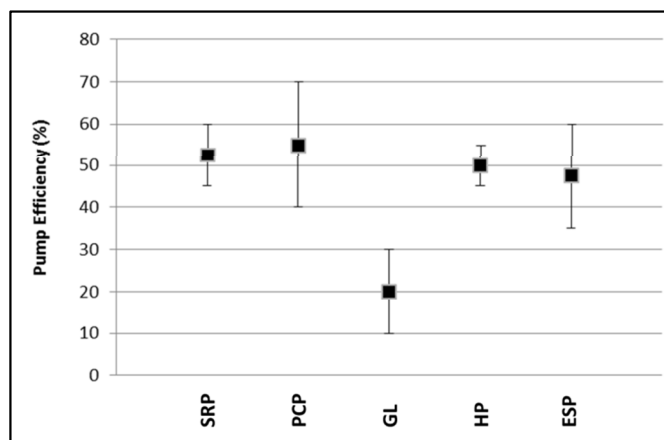


FIGURE 4: HYDRAULIC HORSEPOWER EFFICIENCY COMPARISONS FOR THE MAJOR ARTIFICIAL LIFT – METHODS (5)

Figure 4 compares the efficiencies of different artificial lift techniques, whereas the efficiency is defined as the ratio of benefit to expense. The benefit is the energy consumed by purely for liquid lifting and expense is the energy, required for driving the whole pumping system.

The efficiency does not only depend on the pump itself, but also on the operation conditions and its application. The efficiency of sucker rod pumps is between 45 and 60 percent, which is in the upper range compared to others. Only progressive cavity pumps can reach better efficiencies under certain conditions.

1.2 PUMP AND PROBLEM DESCRIPTION

For sucker rod pumps there is still room for improvement. The reasons why sucker rod pumps are preferred over other lift methods are: Ref (6), page 9

- Independent surface equipment
- Available in many different sizes and material combinations
- Simple technical installation
- Relatively good overall efficiency
- Simple adaption of the operation parameters, thus pumping rate

The usage of sucker rod pumps also implicates some concerns: Ref (6), page 9

- Limited operation depth and pumping rate by exposure to stress of the sucker rods
- Change and maintenance of subsurface pumps is time consuming and costly
- Heavy equipment for pulling of the equipment is required
- Wear problems due to buckling of the sucker rods and the tubing

The following schematic gives an overview on the most important components of a sucker rod pumping system, consisting of a conventional pump jack and an insert pump:

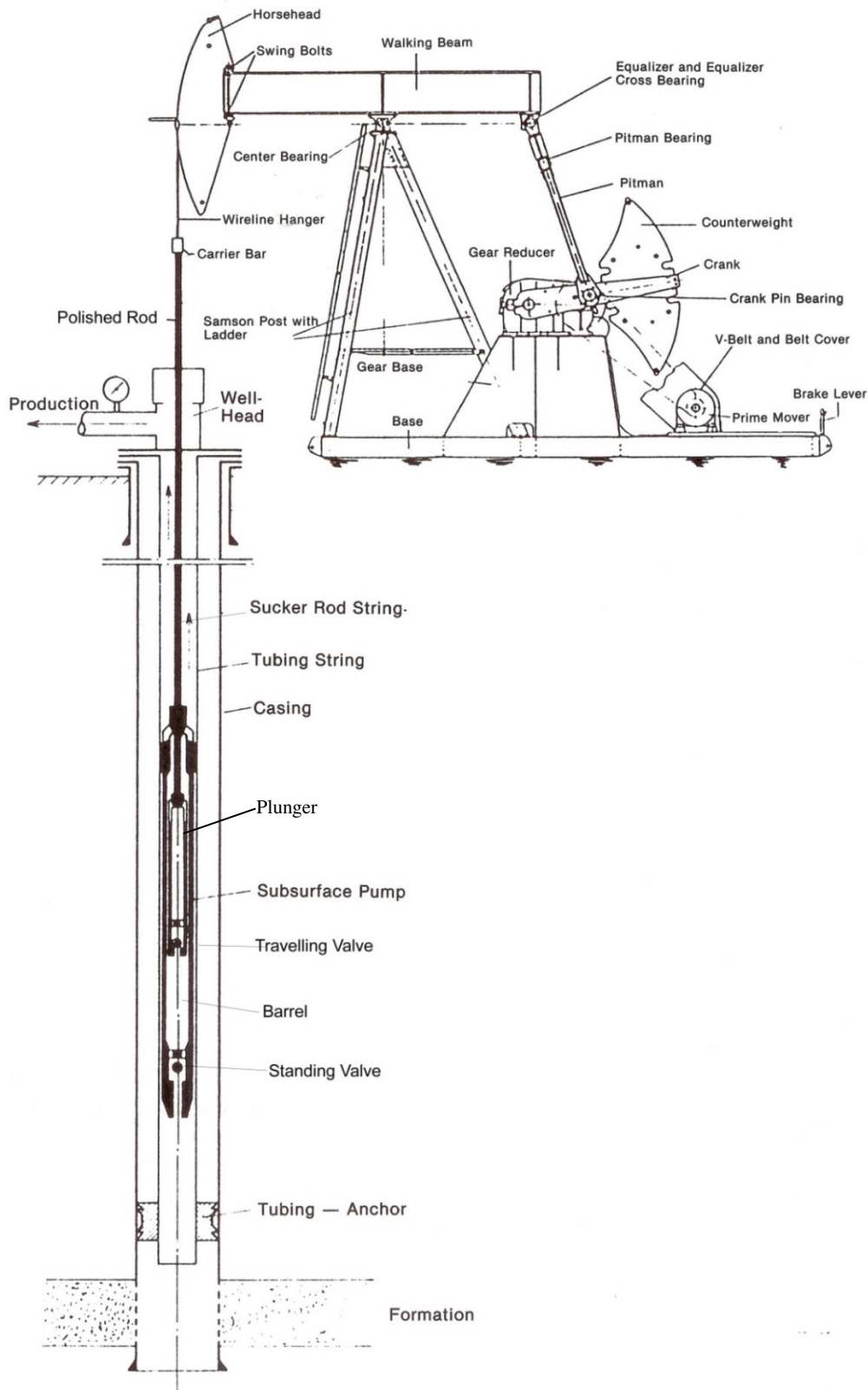


FIGURE 5: SUCKER ROD PUMP REF (6) PAGE 10

Important terms for sucker rod pumps: Ref (7), page 8-2

- Pumping Unit:* A pumping unit (also called pump jack, nodding donkey, pumping unit, horsehead pump, beam pump, sucker rod pump) is a mechanism that generates the reciprocating up- and down-motion of the polished rod, which in turn is attached to the upper end of the sucker rod string.
- Sucker Rod:* A sucker rod itself is a thin rod. When numerous sucker rods are mounted to each other, they form the sucker rod string, which is the connecting link between the surface pumping unit and the subsurface pump, located at or near the bottom of the oil well. The longitudinal motion of the surface pumping unit is transferred to the subsurface pump by the sucker rod string. The sucker rod string can also be composed of tapered rod sections with different diameters.
- Sinker Bar:* A sinker bar is a heavy weight sucker rod, in most cases installed directly above the subsurface pump, to reduce the buckling tendency.
- Polished Rod:* The polished rod is the uppermost part of the sucker rod string.
- Plunger:* The pump plunger is a closely fitted tubular piston equipped with a check valve for displacing the pumped fluid from the pump barrel into the tubing - sucker rod annulus.
- Barrel:* The barrel is the cylinder into which the pumped fluid is displaced by a closely fitted pump plunger.
- Traveling Valve:* The traveling valve is the discharge valve, which moves with the plunger.
- Standing Valve:* The standing valve is the intake valve of the pump and generally consists of a ball type check valve. The valve assembly remains stationary during the pumping cycle.

There are three broad classifications of pumps operated by sucker rods:

- 1) The first type is known as **tubing pump**. Within this pump the barrel is directly attached to the tubing and lowered to its final position in the well as the tubing is run. The plunger with the traveling valve is run into the well on the lower end of the sucker rod string. A second possibility is that the plunger is in run into the wellbore with the tubing string and in place connected with the sucker rod string. Tubing pumps are the most common used pumps for higher production rates.
- 2) The second type is the **insert pump**. To install the insert pump the complete assembly of barrel, traveling valve, plunger and standing valve is attached at the lower end of the sucker rod string and seated in a special seating nipple in the tubing. The insert pump has the obvious advantage that the entire pump assembly can be removed for repair or replacement from the well with only one pulling job. A tubing pump requires separate

pulling of both, the rods and the tubing to remove the pump barrel. The disadvantage of insert pumps is their smaller maximum capacity for a given tubing size.

- 3) The third type is known as *casing pumps*, which are seldomly used, because on one hand the produced fluid gets over a long distance in contact with the casing and can corrode it. On the other hand the rod rubs on the casing inner surface and causes erosion - a damaged casing is very difficult to maintain or replace.

1.3 OPERATING PRINCIPLE AND DEPENDENT PROBLEMS

The schematic in Figure 6 illustrates the subsurface pump and its pumping cycle:

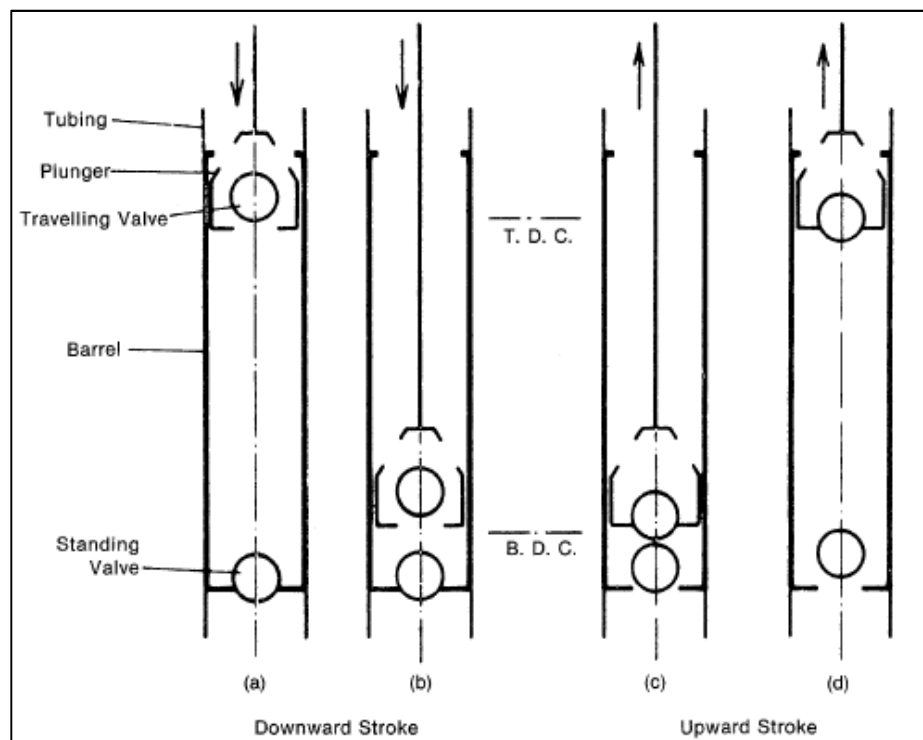


FIGURE 6: SCHEMATIC REPRESENTATION OF THE PUMPING CYCLE REF (6), PAGE 11

The overall working principle of the pump is that the two check valves are alternately opened by fluid flow and closed by pressure. At the beginning of the pumping operation the pump plunger is at the lowest position (c), which is called bottom dead center (B.D.C.). As the plunger starts moving upwards the travelling valve, installed at the bottom of the pump plunger is closed by the pressure of the fluid in the production tubing and the standing valve is opened by the inflow of the reservoir fluid. The barrel is filled with reservoir fluids until the top dead center (T.D.C.) is reached (d). As the plunger starts moving in the opposite direction, the standing valve closes, the fluid in the barrel is trapped and the travelling valve is opened and allows inflow into the production tubing (a). At the end of the downstroke the plunger is back at its initial position and the cycle starts again (b).

The pumping operation causes cyclic production, which means that the main production is achieved during the upstroke. There is also a smaller fluid production during the

downstroke. A part of the downstroke production is achieved at the pump plunger, as a direct result of the displacement of the plunger rod at the pump, which connects the pump plunger with the rod string that is pushed into the wellbore, hence into the barrel, during the downstroke. But the total downstroke production is a result of the polished rod, which is pushed through the stuffing box into the wellbore.

A problem caused by this cyclic production is the permanent load change in the rod string as well as for the pump jack. During the upstroke the total dynamic load composes of the buoyant weight of the rod string, the fluid load, inertia effects, the flowline backpressure and the friction forces, caused by the fluid and the rod – tubing contact. During the downstroke the fluid load is supported by the standing valve, thus the total dynamic load only composes of the buoyant weight of the rod string, inertia effects and the friction forces.

Especially during the downstroke the sections of the rod string directly above the plunger, where the supported string weight is very low, require closer observation. The friction forces are acting upwards against the direction of motion and cause compression of the sucker rod string. The weight of the pump plunger itself in most cases is too low to keep the string in tension. Due to the fact that a slim rod string only can support a certain amount of compressive load before bending, buckling occurs if the compressive force surpasses a critical value, defined by the rod diameter and the material.

1.4 PROBLEM DESCRIPTION

Compression of the rod string, directly above the pump plunger during the downstroke cannot be prevented with the equipment available at the market today. The only possibility to reduce the buckling effect in these sections is to use rods with a high critical collapse value, so called sinker bars. Buckling in general causes a reduction of the stroke length thus a reduction of the volumetric efficiency and as a result higher specific lifting costs. An additional problem occurs at the contact points between the tubing and the rod string. At these points material abrasion and wear occurs, which supports corrosion of the rod string, as well as corrosion of the tubing string.

Figure 7 shows the typical problem, which occurs if there are high compressive loads in the rod string during the downstroke. The neutral point is defined as the position where there is neither compression nor tension. Above the neutral point buckling is not possible because there is only tension in the rod string.

Over time the rod string breaks and an expensive workover is required to replace the worn out rod and tubing string.

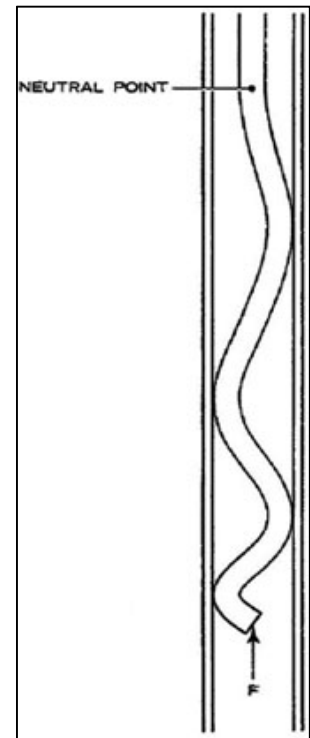


FIGURE 7: SCHEMATIC OF A BUCKLED ROD STRING (8)

The **Meantime Between Failure (MTBF)** is an indicator for the error rate of a system and represents the operation duration between two subsequent system failures. Table 1 shows the development of the MTBF for sucker rod pumps, obtained from an Austrian Oil Company the last 15 years. Whereas in the years 2006 to 2010 the MTBF was relatively high with a peak of 1308 day in 2008, it decreased in the last years to 913 days in 2014. The average over all 15 years is 1130 days.

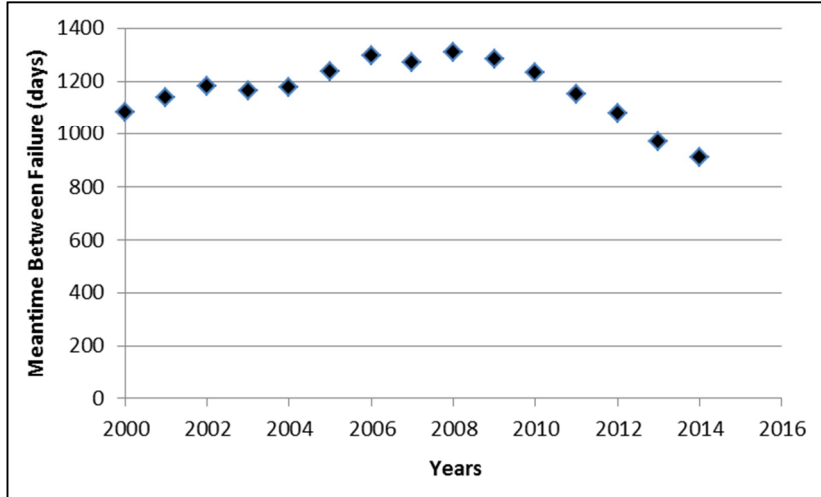


TABLE 1: MTBF FOR SRPS OF AN AUSTRIAN OIL COMPANY REF (9), PAGE 52

A statistical review of the failure rates of 532 beam pumped wells, performed by J.F.Lea (10), in the United States over a period of years is presented in Figure 8. The costs of the workover for replacing and servicing the wells are shown on top of the bars. The basis for the presented data is a mix of deep (3000m, 926 BOPD - barrel of oil per day - and 8562 BWPD - barrel of water per day) and shallow wells (1400m, 2,885 BOPD and 37577 BWPD).

Figure 8 shows that the required number of pulls, especially at the beginning of the nineties, was reduced by measures to improve the mean time between failures, but through the years 1995, 1996 and 1997 it remained more or less constant, with about 900 days.

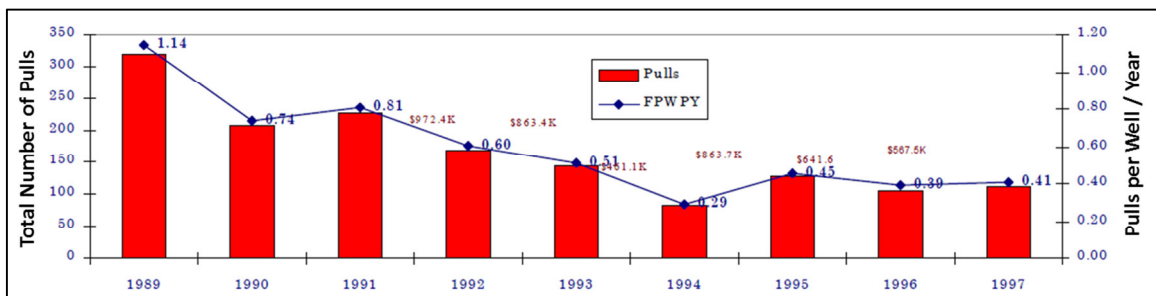


FIGURE 8: HISTORY OF TYPICAL BEAM PUMP OPERATION: FAILURES PER YEAR WITH APPROXIMATE ASSOCIATED COSTS (10)

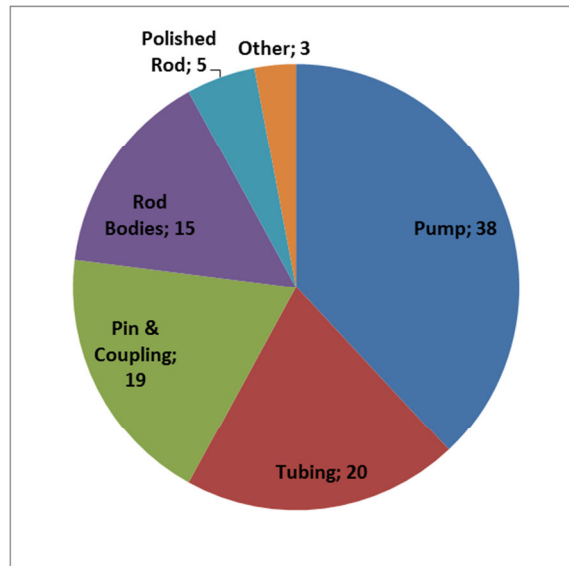


FIGURE 9: TYPICAL DISTRIBUTION OF FAILURES AMONG THE BEAM PUMP SYSTEM COMPONENTS (10)

The pie chart in Figure 9 presents a breakdown of the major causes for failure of the beam pump systems. More than 50 percent of all failures occur at the rod string and might be a result of buckling. In addition pump failure, which are more than one third of all failures, can also be caused by buckling of the adjacent sucker rod string. In conclusion if the problem of buckling can be solved, the number of well interventions will be reduced essentially.

To maintain oil production and increase the oil recovery factor under profitable conditions for almost depleted reservoirs, the objective is to keep the production costs low, consequently to decrease the required number of maintenances and interventions.

This thesis will analyze, design, test and incorporate a system called SRABS (11) (**Sucker Rod Anti-Buckling System**) in combination with the invention “A puming device for pumping fluid” (12). The application of these systems, completely prevent compressive loads within the total sucker rod string, causing essential benefits:

- No buckling of the sucker rod string
- No wear as a result of tubing / sucker rod contact
- Increase in downstroke velocity without buckling is possible
- Rod string diameters can be reduced, thus own-weight of the system is saved
- Higher material strength of the rods because there are no cyclic load oscillations between tension and compression
- Usage of wires or cables as rod string instead of steel bars is now possible as well

The working principle of any sucker rod pump doesn't allow compressive loads during the upstroke, but within a standard sucker rod pump, as described above, the occurring compressive loads during the downstroke can cause buckling of the rod string. To overcome

buckling and the associated problems, a new sucker rod pump design (SRABS pump) is introduced, which applies the principles of the two inventions.

The invention “A pumping device for pumping fluid” concentrates on the liquid loads, acting on the pump plunger and claims that the previously unfavourable liquid pressure in the tubing string can be used for stabilizing the rod string and reduces the risk of buckling.

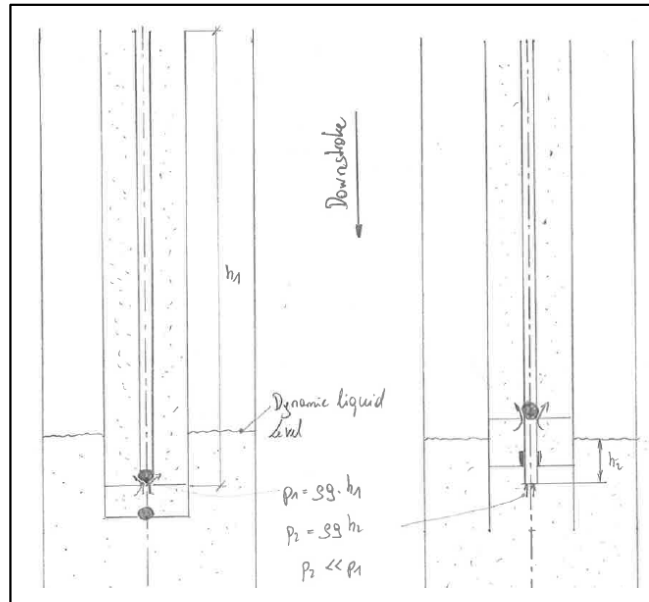


FIGURE 10: LIQUID LOADS ON PLUNGER ROD (12)

Figure 10 shows the liquid loads on the plunger rod for the standard and SRABS design, where ρ is the density of the fluid at the pump conditions, g is the acceleration due to gravity, h_1 is the liquid level in the tubing, which normally extends up to the christmas tree and h_2 is the dynamic liquid level in the casing – tubing annulus.

To achieve the benefit the standing valve is redesigned. The ball valve is substituted by a hollow cylinder valve, which allows the plunger rod to pass through it. As a result this plunger rod is no longer loaded by the tubing pressure during the downstroke, but loaded by the dynamic liquid level load from the casing-tubing annulus, which is essentially lower. As a result the upward acting forces are reduced drastically. Nevertheless the plunger rod passes through the high pressure tubing, which stabilizes the adjacent sucker rod string and still reduces the danger of buckling.

A limitation of the SRABS pump is a slight reduction of the production rate. Whereas the standard pump produces during up- and downstroke, the SRABS pump produces exclusively during the upstroke. To obtain the same production for the SRABS pump, compared to the standard pump, the only way is to slightly increase the number of strokes. The main influencing parameter is the diameter of the plunger rod, which defines the displacement volumes. Therefore a major objective is the reduction of the plunger rod diameter to get a SRABS pump with almost the same production rate as a standard pump.

The minimum plunger rod diameter is a result of the lifted liquid rate and the danger of buckling within the barrel, as well as the shape stability of the plunger rod itself, because its

surface is the seal against the hollow cylinder valve. To reduce the necessity of guidance of the plunger rod, the pump is designed reverse, which means that the plunger is installed below the standing valve.

The stabilization effect, caused by liquids, drastically reduces the buckling tendency especially for low stroke numbers. Higher stroke numbers, starting with 8 to 9 SPM increase the system dyanamics essentially and the SRABS patent must be considered to still prevent buckling of the sucker rod string. The additional measure is the usage of a so called tensioning element. The tensioning element is basically a mass below the pump plunger which tensions the rod string and thereby completely prevents compression of the rod string. The actual weight of this mass is highly dependent on the pumping speed and a design parameter, which must be investigated.

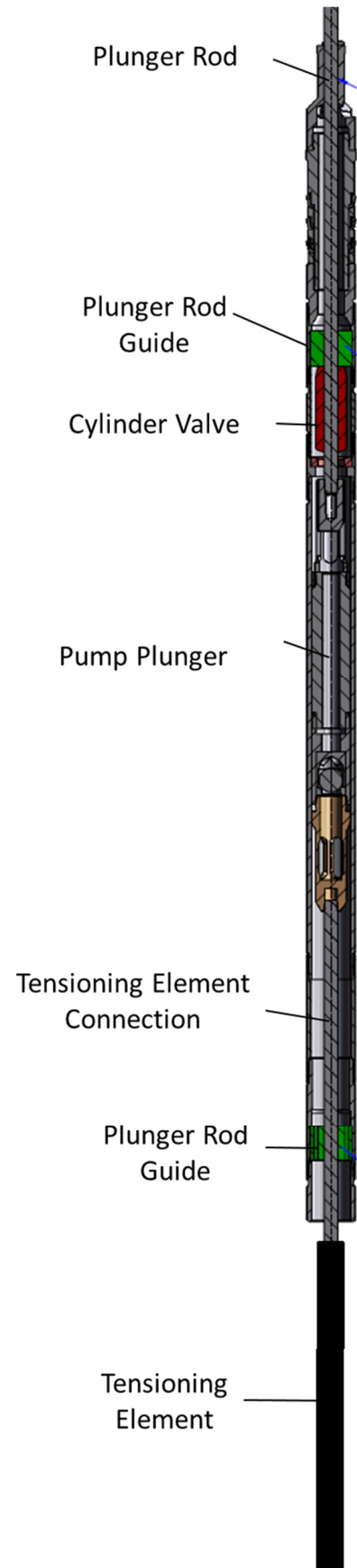


FIGURE 11: REVERSE SRABS PUMP DESIGN (13)

2 WESTERN HISTORY OF SUCKER ROD PUMPING

In history the Chinese were the first ones that used the sucker rod lift method to get water out of the ground as early as 400 B.C. (14). The literature does not provide any further information about the eastern history of sucker rod pumping. As a result only the western history of sucker rod pumping is presented here. The American Oil & Gas Historical Society found out that the first person, who applied this principle in the context of oil production, was Edwin L. Drake in August 1859. He used a common water well hand pump to get the oil from the first commercial oil well, with a reservoir depth of 69,5 feet. Due to the increased need for pumping oil out of the ground, the oil industry started to adapt the water-well technology to this problem and used steam-driven walking beam pumping systems. There were even designs available, where one steam engine was used to drive four wooden walking beams. Figure 12 illustrates a patent drawing from 1875 that shows how oil is pumped from four wells using multiple “walking beams” from a single power source.

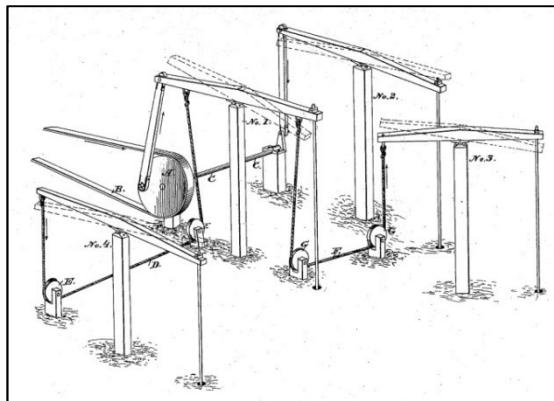


FIGURE 12: PATENT DRAWING OF A HISTORIC SRP SYSTEM (15)

By and by a more efficient and compact mechanism replaced the multiple driven wooden pumping system. The Simplex Pumping Jack was manufactured from 1913 on in Pennsylvania and got very famous. The pump jack was operated by steel rod lines. Thus one central power source was able to drive more pumping units.

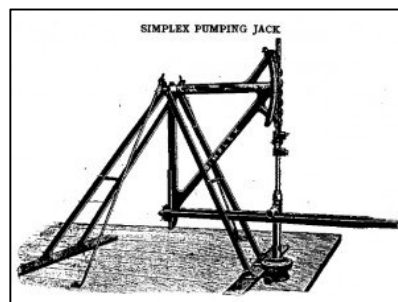


FIGURE 13: SIMPLEX PUMPING JACK (15)

The increase in technology for driving units lead to a jump in the design of pumping units. Walter Trout, a worker at Lufkin Foundry & Machine Texas in 1925 had the idea of a counterbalanced oil field pump jack. The prototype was installed within a year's period in a Humble Oil Company (16) oilfield. The Lufkin Foundry & Machine Company discovered new opportunities in the oil field and prospered. Figure 14 shows a sketch by Walter Trout in 1925. It is a prototype of his counterbalanced pump jack.



FIGURE 14: WALTER TROUT'S REVOLUTIONARY PROTOTYPE (15)

Today modern stripper wells still look much like Walter Trout's original. The underlying concept has not changed since the Chinese, 2400 years ago, but the materials and details in technology have improved essentially. Extensive research was performed to find methods to reduce erosion, to prevent gas locking and to make the system more efficient.

The use of "smart" technology did not stop by pumping units. Today the computer-based technology allows the monitoring and analyzing of the pump systems in real-time from thousands of miles away with minimal human interference and in minimum time. This constant supervising of the pumping units leads to optimum energy usage, while maximizing the amount of oil recovered from the reservoir.

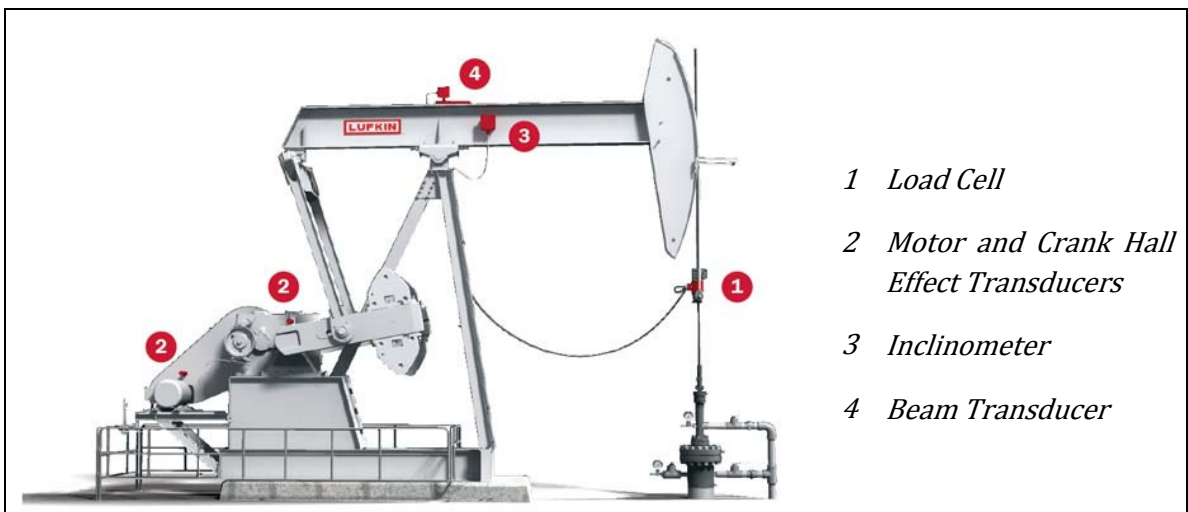


FIGURE 15: AUTOMATED PUMP JACK (17)

3 IMPACT OF SRP'S ON OIL PRODUCTION

Sucker rod pumps were the first artificial lift method that was used to lift crude oil to the surface. Its long history, decades of development and enhancement still make sucker rod pumping systems very popular in today's oil well pumping all over the world. Currently, about 80 percent of all artificially produced wells employ sucker rod pumping systems for lifting of the oil (1). A majority of these wells are so called stripper wells, making less than 10 barrels of oil per day. (10)

It is very complicated to hold of published data that show the number of sucker rod pumps in use and the corresponding production rate. In 1993 G. Takacs presented in his book 'Sucker-Rod Pumping Manual' Ref (18), page 6 a comparison of rod pumped wells in the USA and USSR, which is referred to data from Rothrock, Moore and Grigorashsenko.

Country	U.S.A.		U.S.S.R.	
Year	1978	1985	1963	1973
Number of Oil Wells (thousands) = Artificially Lifted	528	679	38	57
(thousands) =	490	638	31	49
% of Total =	93%	94%	81%	85%
Rod Pumped				
(thousands) =	419		27	40
% of Total =	79.3%		72%	69%
% of Artificially Lifted =	85.4%		89%	81%

TABLE 2: COMPARISON OF ROD PUMPED WELLS USA/USSR REF (18), PAGE 7

Table 2 clearly indicates that the total number of oil wells as well as the number of artificially lifted wells was increased over time. The percentage of sucker rod lifted wells to total wells is between 70 and 80 percent. If only the artificially lifted wells are considered, the fraction of sucker rod pumped wells is even higher and lies between 80 and 90 percent. The restriction of the above presented table is that the contribution to the total crude oil gross production is not shown. The production rate of sucker rod pump can vary between a few barrels up to a few hundred barrels of liquid per day. (18) states that in the USA 441 500 wells are stripper wells. Despite the relatively small production rate the enormous number of sucker rod pumped wells make them an essential contributor to the total oil production.

Paul Nelson from Weatherford International Ltd. in Houston gave a very interesting interview to the American Oil & Gas Historical Society. He said *"Oil wells will run dry, but advances in "artificial lift systems" technology can put off the inevitable. But even with today's best technologies, more than half of the oil can remain trapped underground. Low-volume marginal or "stripper" wells produce no more than 15 barrels a day. The average*

stripper well produces only about 2.2 barrels per day. These wells comprise 84 percent of U.S. oil wells and produce more than 20 percent of all domestic oil. Marginal oil and natural gas wells number about 650,000 of the nation's 876,000 wells. Once shutdown, they are lost forever. Keeping them in production has long been a challenge for a special breed of oilman Smart well technology is of particular importance to the United States, where a very large portion oil is produced from thousands of stripper wells producing less than 10 barrels a day. Many of these wells have reached such a depleted pressure state that once they are shut in they can never be economically restarted. The majority of them are being kept alive by pump jacks. "(15)

P. Nelson concluded *"By improving pump efficiencies without adding significantly to operating costs, smart well technology stands to extend by years the economic life of many of these wells and, by extension, add millions of barrels of oil to U.S. reserves."*

The economic life time of a field can be extended by improving the pump efficiency and / or reducing the pump costs.

For sucker rod pumps there is a maximum production rate that can be achieved. The limitation is a result of the rod weight and liquid load on the sucker rods. J.D. Clegg analysed the influences and developed a diagram that shows the maximum production rate against lift depth for the largest conventional pumping unit available. The higher the lifting depth, the lower the production rate. The reason is the higher own weight of the rods. By using new materials, like fibre glass, steel wires, or cables even the pumping rate eventually can be increased in the future.

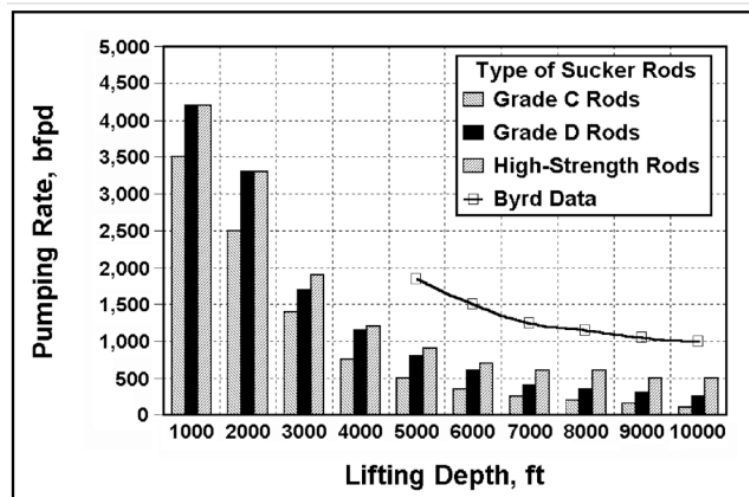


FIGURE 16: PRODUCTION VERSUS LIFTING DEPTH (18)

Figure 16 shows the acomplished pumping rate versus lifting depth for different rod materials, which is basically the limitation for reaching larger lifting depths.

The following chapter presents a summary of the technical background on sucker rod pumping, starting with relatively simple models from the 1960's up to advanced models, which are state of the art today.

4 MATHEMATICAL BACKGROUND

Already in the early history of sucker rod pumping research institutions, oil companies, as well as service providers investigated the sucker rod pumping system and tried to mathematically describe the sucker rod string. Starting with the wave equation, which is a simple second order partial differential equation with strong limitations in its applicability, over the decades more and more complex models were developed to get a reliable analysis of the behavior of the sucker rod string. Nowadays these models are powerful and assist in the design of sucker rod pumping systems.

The following subchapters now summarize the most important steps in the development of complex models, used for analyzing the dynamic behavior of the sucker rod string today. The presented models are described by increasing complexity.

4.1 MODELS FOR VERTICAL WELLS

The first professional attempt for describing the sucker rod pump performance was done by S.G.Gibbs in 1963. In his publication “Predicting the Behavior of Sucker-Rod Pumping Systems” the viscously damped wave equation ^{Ref (19), EQ. 1} is used to describe the longitudinal vibrations within the sucker rod string:

$$\frac{\partial^2 z(x,t)}{\partial t^2} = a^2 \frac{\partial^2 z(x,t)}{\partial x^2} - \frac{\pi a v}{2L} \frac{\partial z(x,t)}{\partial t} \quad \text{Eq. 1}$$

Where z is the displacement in z – direction, t is the time, a is the velocity of sound in the sucker rods, x is the observed position, v is a dimensionless damping coefficient and L is the total length of the sucker rod string.

Together with boundary conditions that describe the initial stress and the velocity of waves in the rod string, the motion of the polished rod, and the forces at the downhole pump a simple description of the rod string behavior was found. Due to the fact that a lot of papers are based on the model of Gibbs, it is worth to show the essential derivations, used for the model derivation. A detailed derivation of the viscous damped wave equation can be found in the ‘Sucker Rod Pumping Manual’ from G.Takacs (18), starting on page 184.

The starting point is the behavior of the rod itself. Therefore Figure 17 shows the forces, acting on a downward accelerated, cylindrical rod segment with length dx , immersed in fluid at any position x along the rod string. The considered forces are the viscous force F_D , caused by fluid friction, the acceleration force F_A , and the forces in the rod cross-section, caused by stresses, F_x and F_{x+dx} . The sum of all forces, acting on the rod segment, must be zero. It is not necessary to consider the selfweight of the sucker rod, for evaluating the

dynamic behavior, because it causes a constant elongation, which is always present and not influenced by the dynamics.

$$\sum_{i=1}^n F_i = 0 \quad \longrightarrow \quad F_x + F_D + F_A - F_{x+dx} = 0$$

F_x is the force in the rod cross-section at position x , F_{x+dx} is the force in the rod cross-section at position $x + dx$, F_D is the damping force, acting on the rod's surface and F_A is the inertia force.

The equations for the individual forces are:

$$F_x = AE\varepsilon = AE \frac{\partial z}{\partial x}$$

$$F_{x+dx} = F_x + \frac{\partial}{\partial x} (F_x)dx + \dots = AE \frac{\partial z}{\partial x} + AE \frac{\partial^2 z}{\partial x^2} dx$$

$$F_A = m \cdot \ddot{z} = A\rho \frac{\partial^2 z}{\partial t^2} dx$$

$$F_D = 2r\pi\mu \frac{1}{r_T - r} \frac{\partial z}{\partial t} dx$$

Where ε is the strain in the sucker rod, A is the cross-section of the sucker rod, r_T is the inside diameter of the tubing and r is the radius of the sucker rod.

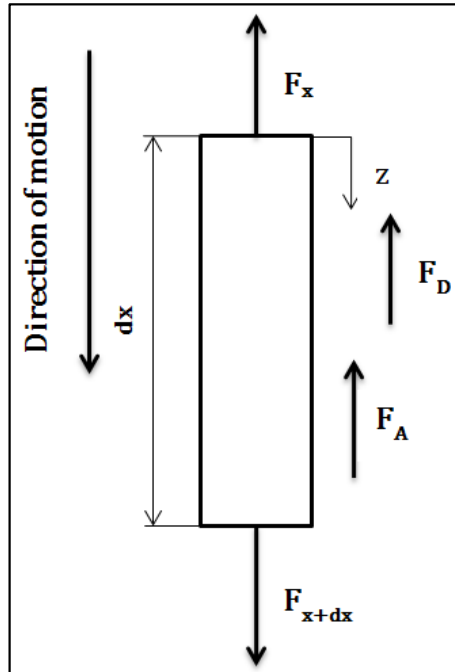


FIGURE 17: FORCES ACTING ON A VERTICAL ROD SEGMENT (20)

Hence,

$$AE \frac{\partial z}{\partial x} + 2r\pi\mu \frac{1}{r_T - r} \frac{\partial z}{\partial t} dx + A\rho \frac{\partial^2 z}{\partial t^2} dx - AE \frac{\partial z}{\partial x} - AE \frac{\partial^2 z}{\partial x^2} dx = 0$$

Using the following relationships, where E is the modulus of elasticity:

$$a = \sqrt{\frac{E}{\rho}} \qquad c = \frac{2\mu}{\rho r(r_T - r)}$$

Cancelling the term $AE \frac{\partial z}{\partial x}$ and dividing by $A \rho dx$ yield:

$$\frac{\partial^2 z(x, t)}{\partial t^2} = a^2 \frac{\partial^2 z(x, t)}{\partial x^2} - c \frac{\partial z(x, t)}{\partial t}$$

This partial differential equation describes the longitudinal vibrations in a long vertical rod string, neglecting rod couplings and protectors and it considers the phenomenon of force wave reflection at the end of the rod string. The equation includes a damping term, which considers viscous damping effects but no wax. ^{Ref (21)}

$$c = \frac{\pi a v}{2L} \qquad \text{Eq. 2}$$

Gibbs stated in his publication that the friction term is even able to consider non-viscous effects, like Coulomb friction. Field measurements were used to evaluate the dimensionless damping factor v , hence no models are available to adapt the friction to other pump and well conditions. L in his model is the total length of the sucker rod string. Gibbs also concluded that the non-viscous effects are relatively small in sucker rod pumping systems, thus the viscous damping approximation is adequate. This assumption is only valid for vertical wells. As a result the described damping model cannot be used for systems that are installed in deviated wellbores. (19)

$$\frac{\partial^2 z(x, t)}{\partial t^2} = a^2 \frac{\partial^2 z(x, t)}{\partial x^2} - \frac{\pi a v}{2L} \frac{\partial z(x, t)}{\partial t} \qquad \text{Eq. 1}$$

represents a boundary value problem, which requires the definition of the motion at the polished rod and the load at the pump plunger at any time, during one pumping cycle. The motion of the polished rod is defined by the geometry of the pump jack (Conventional, Mark II, etc.) and the operation conditions (Stroke length, SPM, etc.). The position of the polished rod versus the crank angle is presented in Gibbs publication ^{Ref (19)}. EQ. 2 and can be derived from trigonometrical considerations:

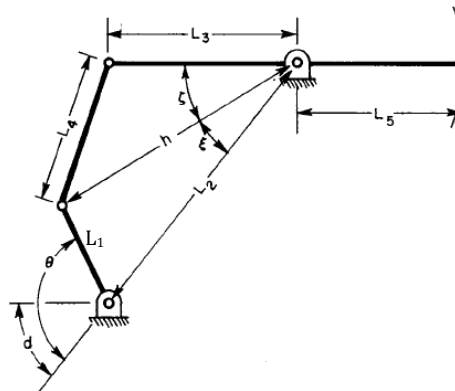


FIGURE 18: BEAM PUMPING UNIT SHOWN AS A FOUR-BAR LINKAGE (19)

Position of the polished rod in dependency of the crank angle θ : (19)

$$u(0, \theta) = L_5 \cdot \left[\sin^{-1} \left(\frac{L_1 \sin \theta}{h} \right) + \cos^{-1} \left(\frac{h^2 + L_3^2 - L_4^2}{2L_3 h} \right) \right] \quad \text{Eq. 3}$$

$$h = \sqrt{L_1^2 + L_2^2 + 2L_1 L_2 \cos \theta} \quad \text{Eq. 4}$$

L1 to L5 represent dimensions from the pump jack geometry.

The more important, but also much more difficult boundary condition is the load behavior at the pump plunger. Due to the load change during up- and downstroke the formulation of one explicit expression does not work properly. As a result the following equation was developed to describe one pumping cycle.

$$\alpha \cdot z(t) + \beta \cdot \frac{\partial z(t)}{\partial x} = P(t) \quad \text{Eq. 5}$$

The parameters α, β and $P(t)$ are adjusted according to the corresponding pump condition. By selecting these parameters correctly, the flexibility needed to describe various pump conditions can be achieved. The intervals are defined by a load change at the pump plunger (19) and correspond to Figure 19:

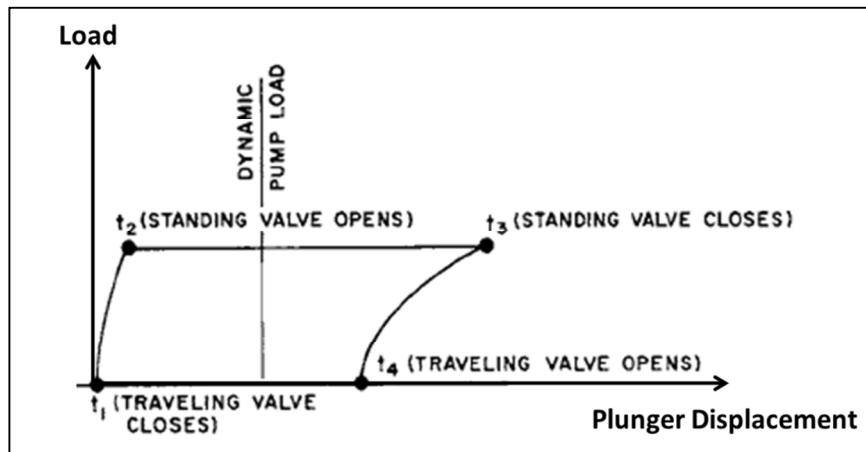


FIGURE 19: TYPICAL PUMP DYNAGRAPH SHOWING VALVE OPERATION (19)

$$\begin{aligned} \alpha &= 0 \\ \beta &= 1 \\ P(t) &= G_1 [z(L, t_1) - z(L, t)] \end{aligned} \quad t_1 \leq t \leq t_2$$

$$\begin{aligned} \alpha &= 0 \\ \beta &= 1 \\ P(t) &= W_r / EA \end{aligned} \quad t_2 \leq t \leq t_3$$

$$\begin{aligned} \alpha &= 0 \\ \beta &= 1 \\ P(t) &= W_r / EA - G_2 [z(L, t) - z(L, t_3)] \end{aligned} \quad t_3 \leq t \leq t_4$$

$$\begin{aligned} \alpha &= 0 \\ \beta &= 1 \\ P(t) &= 0 \end{aligned} \quad t_4 \leq t \leq t_1'$$

The shape functions G_1 and G_2 consider the downhole behavior, eg. gas interference or fluid pound and define the shape of the pump card. W_f is the total buoyant weight of the sucker rod string.

Finally the partial differential equation is solved using the finite differences method. A big advantage of the problem description after Gibbs is that in addition an analytical solution is also available.

Gibbs method offers some advantages as well as limitations: (21)

- Valid only for vertical wells
- Neither Coulomb friction nor viscous effects or wax can be considered
- No acceleration or deceleration of the crank shaft can be modelled
- Bottom boundary condition definition is complicated and limited to simple cases
- Damping coefficients have to be selected artificially, but have a big influence on the result
- Solution is only one-dimensional – radial movements to beam axis cannot be determined, thus buckling cannot be seen directly

Another publication of S.G.Gibbs “Method of Determining Sucker Rod Pump Performance” (21) discusses the diagnostic process for sucker rod pumping, which is slightly different to the previous application. The analysis basically uses the same second order partial differential equation but with another load boundary condition. For the diagnosis of sucker rod pumping the load is not defined at the pump plunger, but at the polished rod. The analysis process evaluates the load at the pump plunger and allows a diagnosis of the working conditions.

Mathematically this small change in the boundary condition causes a big effect on the solution procedure. The equation cannot be treated as a boundary value problem anymore, which causes on one hand very awkward numerical solutions or requires on the other hand an analytical solution. Such an analytical solution is presented in Gibb’s publication (21). Measured position / load pairs as a basis for the Fast Fourier Transformation replace the previously used modeled boundary conditions.

$$D(\omega t) = L(\omega t) - W_r = \frac{\sigma_0}{2} + \sum_{n=1}^{\infty} (\sigma_n \cos(n\omega t) + \tau_n \sin(n\omega t)) \quad \text{Eq. 6}$$

$$U(\omega t) = \frac{v_0}{2} + \sum_{n=1}^{\infty} (v_n \cos(n\omega t) + \delta_n \sin(n\omega t)) \quad \text{Eq. 7}$$

Where $U(\omega t)$ is polished rod displacement function, $L(\omega t)$ the total polished rod load function, $D(\omega t)$ the dynamic polished rod load function, $\sigma_0, \sigma_n, \tau_n, v_0, v_n, \delta_n$ are Fourier Coefficients, O_n, P_n, O'_n, P'_n are factors, ω is the angular velocity of the pump jack and n is the index for the number of Fourier Coefficients.

An analytical procedure using the separation of variables results in the following solution, which allows the evaluation of the load and displacement at any position within the vertical sucker rod string.

$$z(x, t) = \frac{\sigma_0}{2EA}x + \frac{v_0}{2} + \sum_{n=1}^{\bar{n}}(O_n(x)\cos(n\omega t) + P_n(x)\sin(n\omega t)) \tag{Eq. 8}$$

$$F(x, t) = EA \left[\frac{\sigma_0}{2EA} + \sum_{n=1}^{\bar{n}}(O'_n(x)\cos(n\omega t) + P'_n(x)\sin(n\omega t)) \right] \tag{Eq. 9}$$

The limitations of this procedure are again the weaknesses of the used mathematical equation as already discussed for the previous model.

Another possibility to solve the equations, used for the diagnosis of sucker rod pumps, is the method of characteristics (22). The method of characteristics reduces second order partial differential equations to a system of ordinary differential equations. J.E.Chacin presented a solution, based in this approach (23). In addition a comparison with measured downhole data was performed. The method of characteristics is said to be more accurate than an analytical solution, because other dissipation models than the viscous friction can be used.

The supplementary publication “Computer Diagnosis of Down-Hole Conditions In Sucker Rod Pumping Wells” (24), also from S.G.Gibbs discusses the interpretation of the diagnostic analysis results in terms of tubing leaks, an unanchored tubing string and the effectiveness of tubing anchors. Despite the strong limitations of the used mathematical model, useful results could be obtained.

Over the decades the level of technology increased and already solved problems were recalculated by more advanced methods. In this specific case the analytical solution of the viscously damped wave equation for downhole diagnosis was substituted by a finite differences method. T.A.Everitt claims in the publication “An Improved Finite-Difference Calculation of Downhole Dynamometer Cards for Sucker-Rod Pumps” (25) that the analytical model tends to round the corners of the downhole pump card, which is a result of the Fourier series approximation of the boundary conditions. Within this context the numerical solution seems to deliver more accurate results.

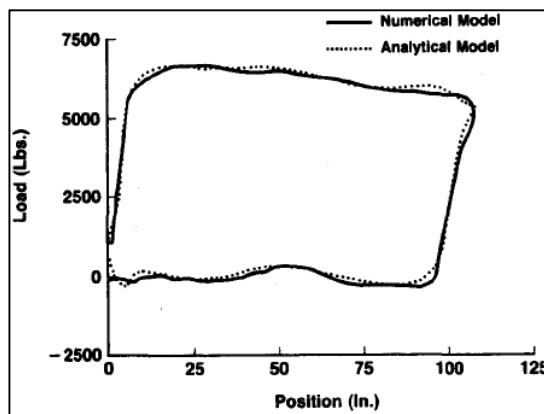


FIGURE 20: COMPARISON OF NUMERICAL AND ANALYTICAL DIAGNOSTIC MODELS (25)

As accuracy is of essential importance, D.J.Schafer and J.W.Jennings concentrated in their work (26) on a sensitivity analysis. Analytical models, used for the diagnostic analysis, and numerical models, used for the predictive analysis are discussed. In addition tapered rod strings, which allow a more efficient design of the sucker rod sting, are implemented in the analysis.

The major outcomes of the research were:

- Ten to fifteen Fourier coefficients are enough for most applications
- The damping factor c should be in a range of 0,5 to 1,2 s-1 to give realistic results
- The maximum element length for the numerical solution, used in the predictive model should be between 152 and 229 meters.
- Three pumping cycles are sufficient to overcome the initial start-up effects. Higher SPM could cause four cycles

4.2 MODELS IMPLEMENTATING THE DYNAMICS OF THE LIQUID COLUMN

The next step in the development of accurate sucker rod pumping models was the implementation of the dynamics of the liquid column. In 1983 D.R.Doty and Z.Schmidt presented a model (27) that combines the liquid dynamics and the rod string dynamics by a system of partial differential equations, which is solved by the method of characteristics. The equations are based on a standard momentum equation on the rod string, yielding a first - order partial differential equation: Ref (21), EQ. 1

$$\rho \cdot A \cdot \frac{\partial v_r}{\partial t} = \frac{\partial f_r}{\partial x} + F_{rf} + F_{cf} + F_{rt} - \rho \cdot g \cdot A \tag{Eq. 10}$$

Where v_r is the rod velocity and f_r is the rod tension. The functions F_{rf} , F_{rt} and F_{cf} represent various friction forces per unit length Ref (27), EQ. 2, EQ. 3, EQ. 4, like friction between rod and tubing F_{rf} , coupling and tubing F_{rt} and viscous friction F_{cf} .

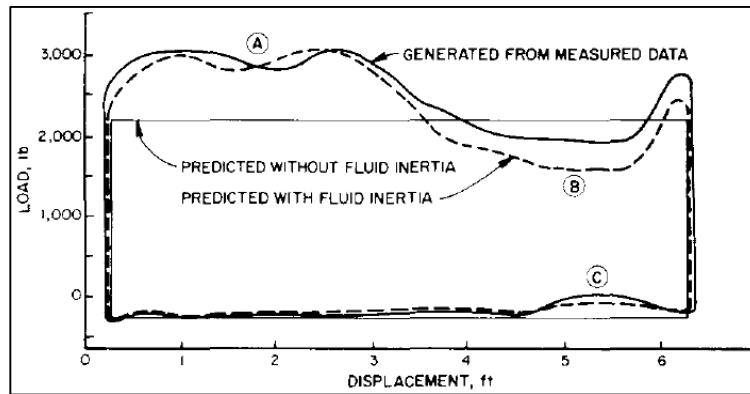


FIGURE 21: COMPARISON OF BOTTOMHOLE PUMP DYNAGRAPH (27)

As a conclusion the authors of the publication claim that it is inevitable to consider fluid inertia effects if the analysis has to be accurate. In addition the research considered effects of motor slip, different types of pumping units, and various inertia effects in the surface equipment, tapered rod strings, fiberglass rods, sinker bars, unanchored tubing, gas interference and fluid pound.

Tripp and Kligor (28) also proved that the consideration of dynamic fluid effects produces more accurate results for predictive models.

Another publication “A New Approach for Modeling Fluid Inertia Effects on Sucker-Rod Pump Performance and Design” dealing with the same problem was published by A.Kodabandeh and S.Miska in 1992 (29). The major difference is the solution approach. The authors used instead of the wave equation a system of linear algebraic equations and the Bergeron method (30). The viscous damping was modeled for laminar flow, but turbulent flow modelling is also possible, when choosing the adequate model.

The publication of D.R.Doty and Z.Schmidt (27) was also the starting point for “A Comparison Between Predicted and Measured Walking Beam Pump Parameters” from H.A.Tripp and J.J.Kilgore. They extended the Doty and Schmidt pump model to simulate the downhole pump. A comparison of the predicted parameters and the corresponding field measurement results of 92 wells show the necessity to consider the fluid dynamics in the analysis of the sucker rod string behavior, especially in the predictive analysis.

4.3 MODELS FOR INCLINED WELLS

A further step in the development of advanced models was set in the nineties starting with S.A.Lukasiewicz’s publication “Dynamic Behavior of the Sucker Rod String in the Inclined Well” from 1991 (31). He presented a model for predicting and analyzing the behavior of the sucker rod string in inclined wells. The used model incorporates the dynamics of the curved sucker rod string, fluid inertia and viscosity and the friction, resulting from the contact of the rods with the tubing string. The system of two partial differential equations was solved by the finite differences method.

The dynamic behavior of sucker rod strings in inclined wellbores is essentially different to that in vertical ones. One reason therefore is that in inclined wellbore the rod string is not only hanging in the wellbore at the polished rod, like in pure vertical wells, but also resting on the tubing walls at the inclined section. As a result there is significant Coulomb friction between the sucker rod string and the tubing string. Another reason is the curvature itself, which causes the lateral displacement of the rods and couples the longitudinal vibrations with transverse vibrations.

The motion of such a sucker rod string can be described by a system of two differential equations. These equations are derived by employing a force balance on a short section of the rod’s string, with the length ds (Figure 22).

The equation of the motion in the direction tangential to the rod can be derived by employing a force balance $\sum_i^n F_{i,t,r} = 0$ in the corresponding direction. It is assumed that the rod segment is sliding downward.

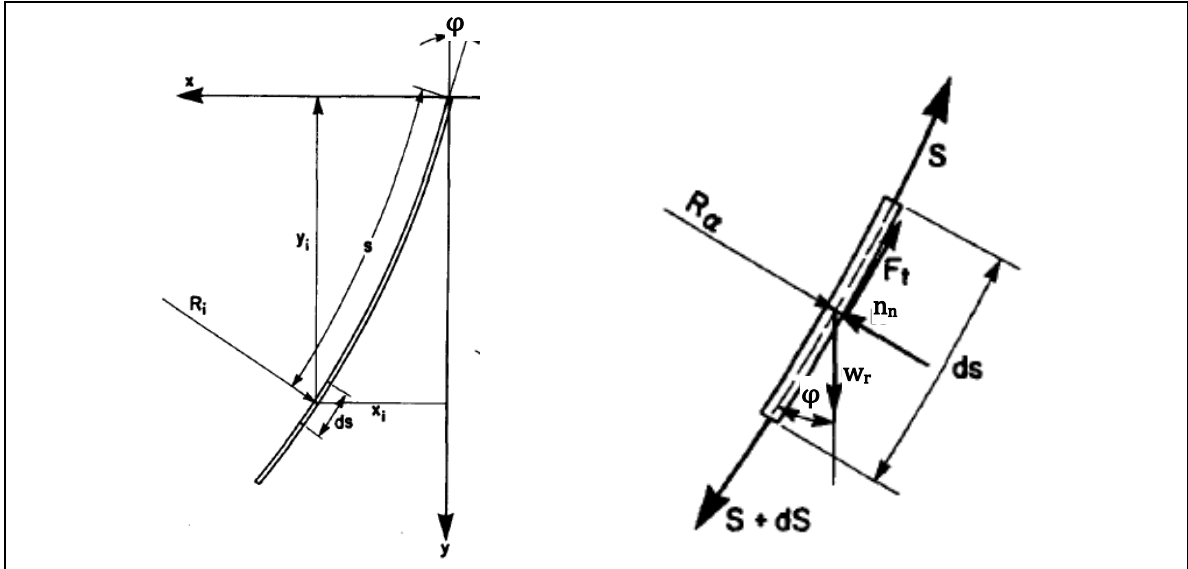


FIGURE 22: FORCE BALANCE IN DIRECTION OF MOTION (31)

$$\begin{aligned}
 & \text{Acceleration force} \quad \text{Coulomb friction} \\
 & -S + S + dS + \underset{\substack{\uparrow \\ \text{Gravity force} \\ \text{tangential to rod} \\ \text{direction}}}{\rho g A \cos \varphi ds} - A \rho \frac{\partial^2 z}{\partial t^2} ds - \underset{\substack{\uparrow \\ \text{Viscous friction}}}{v \frac{\partial z}{\partial t} ds} - \mu ds = 0
 \end{aligned}$$

The friction itself consists of a viscous term and a Coulomb term, where the normal force per unit length is used. s represents the measured length along the curved rod, μ is the Coulomb friction coefficient, S is the force in cross-section of the curved rod and φ is the inclination of the rod string.

Simplification leads to:

$$\frac{\partial S}{\partial s} - A \rho \frac{\partial^2 z}{\partial t^2} + \rho g A \cos \varphi - \eta \frac{\partial z}{\partial t} - \mu = 0 \tag{Eq. 11}$$

The second equation of motion $\sum_i^n F_{i_n,r} = 0$ is in the direction normal to the rod. Again a force balance is used:

$$\begin{aligned}
 & \text{Acceleration force} \quad \text{Gravity force normal to rod direction} \\
 & \frac{dM}{ds} + A \gamma \frac{\partial^2 w}{\partial t^2} ds + F_n - \gamma g A \sin \varphi ds + S \sin \varphi = 0
 \end{aligned}$$

\uparrow Bending force \uparrow Friction \uparrow Normal

Where M is the bending torque in the rod and w is the traverse displacement of the rod. Using the following relationships, the equation can be simplified:

$$\frac{dM}{ds} = \frac{dEI}{ds} \frac{1}{R} = EI \frac{d}{ds} \left[\frac{1}{R_\alpha} + \frac{\partial^2 w}{\partial s^2} \right]$$

$$\frac{1}{R} = \frac{1}{R_\alpha} + \frac{\partial^2 w}{\partial s^2} \quad \text{and} \quad d\varphi = \frac{ds}{R}$$

$$F_n = n_n ds + n_p ds + n_t \frac{\partial w}{\partial t} ds$$

$$F_R = S \sin d\varphi \sim S d\varphi = S \frac{ds}{R}$$

I is the moment of inertia, R_α is the radius of the curvature of the unloaded rod in the wellbore, R is the actual radius of the curvature of the bended rod, n_t is the viscous damping coefficient in the lateral direction, n_p is the traverse normal force due to the fact the the curved rod is surrounded by the liquid under the surrounding pressure p , n_n is the traverse normal force resulting from the reaction of the tubing during contact and r is the rod's radius.

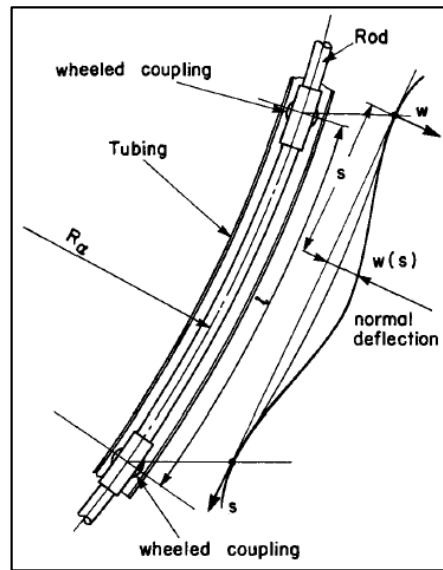


FIGURE 23: DEFLECTED SUCKER ROD STRING (31)

When applying these terms in the equation, it results in:

$$EI \frac{d^2}{ds^2} \left[\frac{1}{R_\alpha} + \frac{\partial^2 w}{\partial s^2} \right] ds + A\rho \frac{\partial^2 w}{\partial t^2} ds + n_n ds + n_p ds + n_t \frac{\partial w}{\partial t} ds - \rho g A \sin \varphi ds + S \frac{ds}{R} = 0$$

$$EI \frac{\partial^2}{\partial s^2} \left[\frac{1}{R_\alpha} + \frac{\partial^2 w}{\partial s^2} \right] + A\rho \frac{\partial^2 w}{\partial t^2} + n_n + n_p + n_t \frac{\partial w}{\partial t} - \rho g A \sin \varphi + \frac{S}{R} = 0$$

There are some additional relationships that can be applied:

$$n_p = \pi \frac{pr^2}{R\alpha} \quad n_p \text{ is caused by the surrounding fluid pressure:}$$

$$S = A\sigma = AE \left[\frac{\partial z}{\partial s} + \frac{1}{2} \left(\frac{\partial w}{\partial s} \right)^2 \right]$$

$$n_n = \rho g A \sin \phi - \frac{S}{R}$$

Hence, the basic equation changes to (squares of the derivation of $\frac{\partial w}{\partial s}$ are small and therefore neglected)

$$\frac{\partial^2 z}{\partial s^2} - \frac{1}{a^2} \frac{\partial^2 z}{\partial t^2} + \frac{\rho g \cos \phi}{E} - \frac{v}{AE} \frac{\partial z}{\partial t} - \frac{v}{R} \frac{\partial z}{\partial s} - \frac{\mu \rho g \sin \phi}{E} = 0 \quad \text{Eq. 12}$$

These equations create a system of two coupled nonlinear differential equations of fourth order, which can be solved by using numerical methods.

The advantages and limitations of this model are the following:

- + Finite difference method is suggested for solving
- + Applicable for deviated systems
- + Solution is two-dimensional – radial movements to beam axis can be determined
- Higher complexity compared to Gibbs model – solution process is more complicated
- Impossible to distinguish rod guides from rod couplings
- Inflexible, concerning friction forces and different friction coefficients
- The real well bore geometry, like dog legs etc. cannot be represented

A comparison with data from an oil field in Alberta, Canada, showed that the model is able to predict surface rod loadings and production with an accuracy less than 10%.

Another publication, dealing with inclined wellbores, was published by G.W.Wang, S.S.Rahman and G.Y.Yang in 1992 under the title “An Improved Model For The Sucker Rod Pumping System” (32). They studied the three dimensional vibrations of the sucker rod string, the motion of the tubing string and dynamics of the liquid column, without considering gas and keeping the fluid properties constant, in the sucker rod pumping system. The resulting equations were solved by the finite differences method. Conclusively the authors claim that their model is an improvement over the existing one-dimensional and two-dimensional models.

In addition in reality not all tubing strings combined with sucker rod pump installations are anchored. A free moving tubing string causes a loss of energy by its contraction and expansion and therefore the pump efficiency declines under full pump conditions. P.A.Lollback, G.Y.Wang and S.S.Rahman (33) derived six partial differential equations that

are governing the vibrations of the rod sting, tubing and fluid column. Despite these improvements in the development of a realistic model, describing the motion of the sucker rod string there are still some limitations and room for improvement:

- Constant slip of the prime mover is assumed
- The pumped fluid is considered without gas
- A smooth well with no sudden deviations, that can occur during drilling, is assumed
- Tubing-rod contact only at couplings

According to the authors the major areas of improvement are the fluid dynamics and the fluid/tubing and fluid/sucker rod interaction.

Beside the conventional derivation of partial differential equations, other methods for describing the vibrations of the sucker rod string are used in addition. The effect of transverse displacement can be calculated with the Galerkin energy principles (34), presented by J.Xu (35), the principle of virtual displacement and the method of geometry can be used (36) or the D'Alembert's solution (37) of a simplified system description using a transfer matrix method (38), which allows an easier analysis of telescopic multi-segment rod strings. According to the author such models allow the usage of an approximate formula of rod-tubing drag force. The results show that the Coulomb friction forces are largely dependent on the trajectory of the borehole and the axial loads in the sucker rod string. In addition a least squares fitting method is introduced to better describe the borehole geometry, required due to the poor deviation surveys provided from boreholes. Semi-infinite domain solutions also show that the key element in the rod pumping analysis is the exact rod friction law. (39)

The advancement in the computer technology allows the fast solution of large equation systems generated for instance by the finite elements method. The finite elements method allows an analysis of the reciprocating motion of the sucker rod string and the occurring longitudinal vibrations, lateral vibrations and torsional vibrations under various loads (40). A representation of the rod string by beam elements and a definition of the contact friction state of the rod and tubing provide the theoretical support for the design of sucker rod strings (41).

The development of smart oil fields requires automated real time diagnosis of the controlled system. Y.Yang, J.Watson and S.Dubljevic (42) introduced a method, which is in contrast to the former Fourier series truncation or finite differences based model an infinite-differential state space representation of the viscous damped wave equation. The viscous damped wave equation is cast into a system of coupled ordinary differential equations, which can be solved according to the authors in real time and applied for period and non-period stroke motion. The limitation of this method is that the model is based on the one dimensional wave equation, which drastically reduces the accuracy for deviated wellbores. Beside fast analytical solutions, also numerical methods were developed for the

diagnosis of sucker rod pumping units. A.P. Araujo Junior (43) derived a model considering the three-dimensional trajectory of the borehole. The evaluation of the downhole card is in addition based on the model developed by Costa (44), which allows an accurate estimation of the intake pressure. The recommendations for further research are the investigation of the friction factors between rod / tubing for liquids with impurities like sand and different kinds of rod guides.

4.4 BUCKLING MODELS

Buckling is in reality not always a problem of the strength of the used material, but a stability problem, which happens to long slim structures as e.g. a sucker rod string. Steel rod can for example support a certain amount compression before buckling, whereas fiberglass is unable to support compression.

The classical buckling theory distinguishes four cases with different boundary conditions immersed in a gas with negligible density. As a result the shape of the bent structure changes, which results in different critical buckling loads (45).

	Case 1	Case 2	Case 3	Case 4
<i>Buckling length</i>	$s = 2.L$	$s = L$	$s = 0,7.L$	$s = 0,5.L$
<i>Buckling load</i>	$F_{crit} = \frac{EI\pi^2}{4.L^2}$	$F_{crit} = \frac{EI\pi^2}{L^2}$	$F_{crit} = \frac{2EI\pi^2}{L^2}$	$F_{crit} = \frac{4EI\pi^2}{L^2}$

FIGURE 24: EULER BUCKLING CASES (46)

If the material is assumed to behave linear-elastic, buckling is defined as Euler-buckling. Larger cross-sections can exceed the elastic limit and buckling is referred to Tetmajer-buckling. The actual model to be used is dependent on the slenderness of the construction.

$$\lambda = \frac{\text{Buckling Length } s}{\text{Gyrationradius } i} \quad (41) \tag{Eq. 13}$$

$$i = \sqrt{\frac{I_{min}}{A}} \quad (41) \tag{Eq. 14}$$

Where I_{\min} is the minimum moment of inertia of the cross-section A of the construction supposed to buckle. If the actual slenderness λ is below the cross-slimming, which is a constant value depending on the material, inelastic buckling occurs – above elastic buckling occurs.

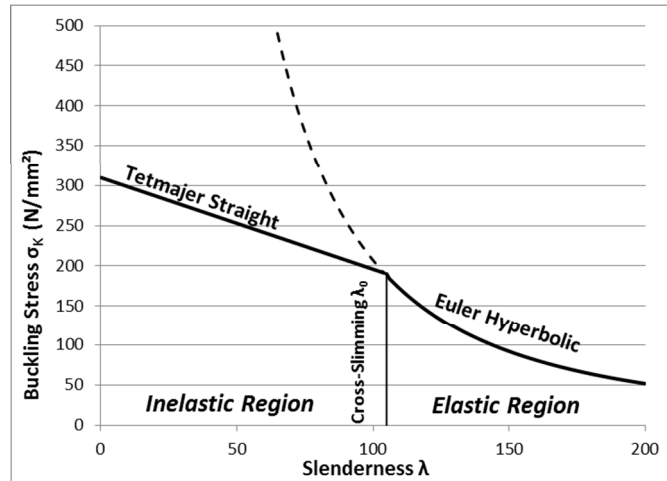


FIGURE 25: BUCKLING STRESS IN DEPENDENCE OF THE SLENDERNESS λ FOR THE STEEL S235JR (47)

The shape and the displacement w of a buckled structure can be described by an ordinary partial differential equation of second order. The two boundary conditions, required for a proper solution, are defined by the buckling case, hence the support at the structure's ends.

$$w'' + \frac{F}{EI} w = 0 \quad (48)$$

Eq. 15

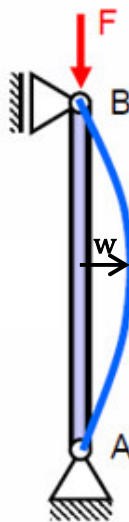


FIGURE 26: SHAPE OF A BUCKLED STRUCTURE (48)

The part stated above represents the general description of buckling in mechanics. The application of this concept for the sucker rod string requires additional considerations. Sucker rod strings are installed in tubing strings, which cause a limitation of the maximum displacement w of the buckled rod, the rod string is normally immersed in liquid and the trajectory of the wellbore is not necessarily only vertical. These effects have already been shown in publications. The most important conclusions thereof are presented in the following section.

A lot of research for describing the buckling behavior of drill strings and tubing strings was done in the past, especially by A. Lubinski (49). The results cannot be taken directly for describing the buckling behavior of sucker rod strings, because the motion is entirely different. A drill string is subject to rotation with relatively large compressive force, called weight on bit, whereas the sucker rod string is moving up and down under relatively low compressive load.

In reality one can distinguish two essential different buckling types of a slim structure – lateral and helical buckling. If the critical buckling load is exceeded the slim structure will start to buckle laterally, which results in a sinusoidal shape of the buckled structure (Figure 27).

$$(r_T - r) \cdot \sin\left(\frac{\pi x}{L}\right) \tag{Eq. 16}$$

Where $(r_T - r)$ is the amplitude of the wave (tubing radius minus rod radius), x is the observed position and L is the length of one wave of the deformation. The critical compressive force can be calculated according to the Euler-hyperbol.

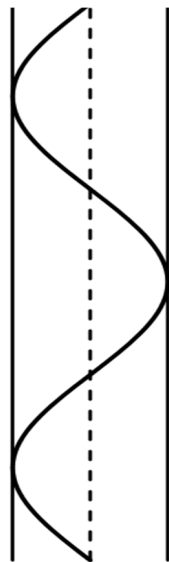


FIGURE 27: SHAPE OF LATERAL BUCKLING

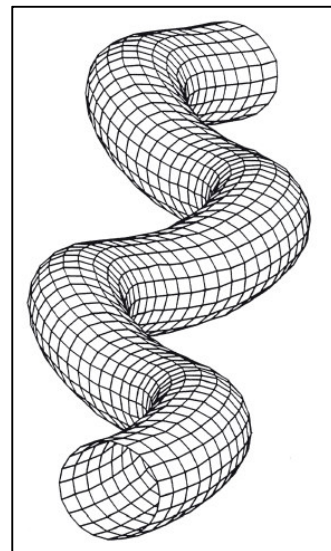


FIGURE 28: LATERAL BUCKLING DEFORMATION (50)

If the compressive force is further increased, helical buckling occurs. The slim structure, e.g. a sucker rod string, coils like a helix in the tubing string.

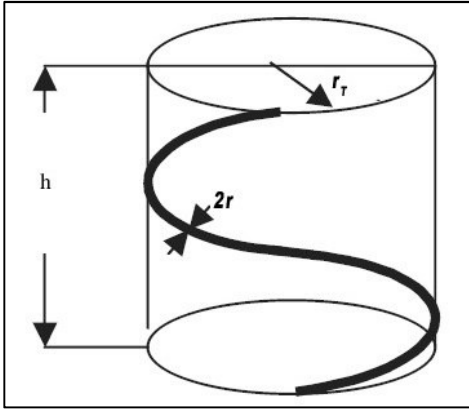


FIGURE 29: SHAPE OF HELICAL BUCKLING (51)

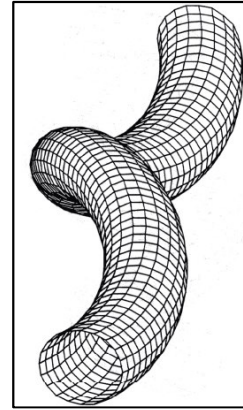


FIGURE 30: HELICAL BUCKLING DEFORMATION (50)

h describes the height of the helix, r the radius of the rod string and r_t the inner radius of the tubing string. The critical helical buckling force is higher than the lateral buckling force, but the actual magnitude is still under discussion and several models have been developed in the past.

One model, derived by S.A.Lukasiewicz (51) and confirmed by J.B.Cheatham and P.D.Patillo (52), is based on the differentiation of the total potential energy with respect to r .

$$F_{crh} = \frac{4\pi^2 EI}{L_h^2} \quad (51) \quad \text{Eq. 17}$$

A second model, introduced by S.A.Lubinski (49), based on the force equilibrium on a buckled beam with constant radial clearance, which is also confirmed by the publications of Y.W.Kwon (53) and R.F.Mitchell (54), results in a critical helical buckling load twice as high as the critical buckling force obtained by the first model.

$$F_{crh} = \frac{8\pi^2 EI}{L_h^2} \quad (51) \quad \text{Eq. 18}$$

J.B.Cheatham and P.D.Patillo (52) suggested that

Eq. 17 should be used for the load of the string, whereas

Eq. 18 should be used for unloading.

The true value for helical buckling lies in between those two critical forces (51). During the operation of a sucker rod pump the tubing is completely filled with the pumped fluid. As a result fluid pressure is acting on the sucker rod string. During the development of buckling a differential area, shown in Figure 31, is created, that causes in combination with the liquid pressure a force, which acts against the buckling process. As a result higher compressive forces can be supported by the sucker rod sting. The critical forces can be adjusted to (51):

$$F_{crl} = \frac{\pi^2 EI}{L_w^2} + p\pi r^2 \quad \text{for lateral buckling} \quad \text{Eq. 19}$$

$$F_{crh} = \frac{4\pi^2 EI}{L_h^2} + p\pi r^2 \quad \text{for helical buckling} \quad \text{Eq. 20}$$

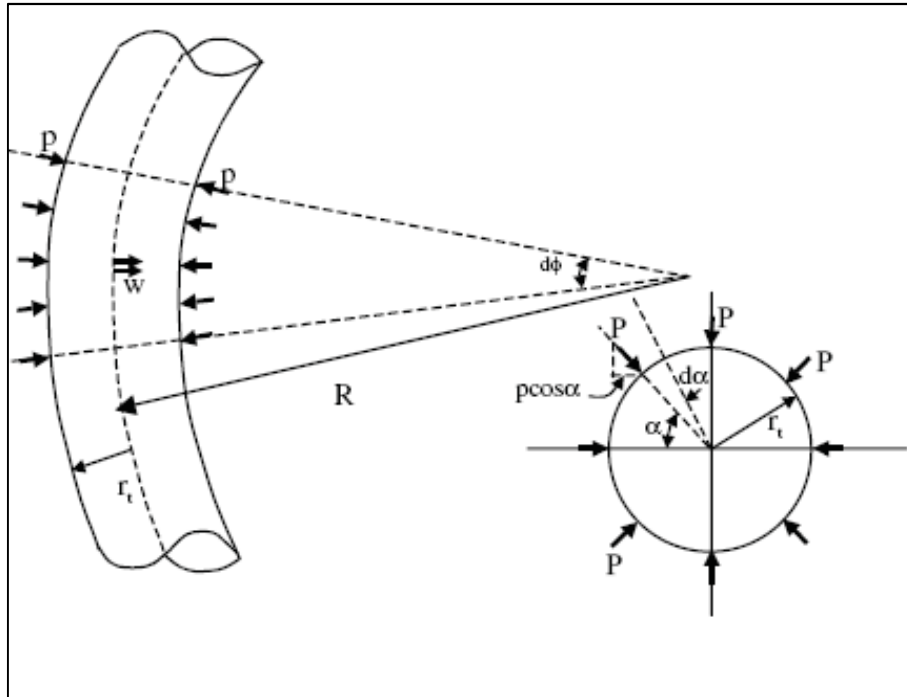


FIGURE 31: FORCE ON ROD DUE TO FLUID PRESSURE (51)

The above presented model is confirmed by J.F.Lea and P.D.Pattillo (55). They claim that only the effective tensile force (or compressive force) T_{eff} , is responsible for buckling, rather than the true tensile force T_{true} .

$$T_{eff} = T_{true} + p_0 \cdot A \quad (55) \quad \text{Eq. 21}$$

If the effective tensile force is negative, buckling will occur if in addition the structural resistance is overcome.

New technology allows drilling almost any trajectory of wells. As a result sucker rod pumps are also installed in non-vertical sections and buckling may also occur in these horizontal sections. In deviated or even horizontal sections the buckling behavior is entirely different. The selfweight of the pipe stabilizes the pipe at the bottom of the inclined section (56). The compressive force $F_{cr,h}$, required to laterally buckle the rod string, was investigated by R.Dawson and P.R.Paslay (57):

$$F_{cr,h} = \sqrt{\frac{4w_r EI}{(r_T - r)}} \quad \text{Eq. 22}$$

w_r is the unit-weight of the rod string. Helical buckling in horizontal sections was investigated by Y.C.Chen and Y.H.Lin (58) and occurs if the compressive force exceeds

$$F_{cr,h} = \sqrt{\frac{8w_r EI}{(r_T - r)}} \quad \text{Eq. 23}$$

Another important information is that a rod string can be considered as a long pipe if the dimensionless length is greater than 5π . The boundary effects can be ignored for practical design application. The effects of friction on lateral buckling are significant as friction increases the critical loads for buckling (59). The critical loads for sinusoidal buckling will increase by 30 to 70% for friction coefficients between 0.1 and 0.3, concerning rod string and tubing (59).

“Paslay and Bogy (1964) studied the stability of a circular, laterally constrained rod with two pinned ends in an inclined well by using the energy method. For a short rod, their critical load approaches that of Euler’s prediction when the rod is subjected to an axial compressive load without any lateral constraint except at both pin ends. For a long rod, their formula can be simplified (Dawson and Paslay 1984) as follows:”(59)

$$F_{cr1} = 2 \sqrt{\frac{EIw_r}{r_T - r}} \quad \text{Eq. 24}$$

In addition rod couplings have an essential influence on the buckling behavior in horizontal wells, because their weight causes the rod to sag (60).

In the last years Finite-Element-Analysis (FEA) was used to analyze the critical buckling load of drillstrings. M.Hajianmaleki and J.S.Daily (61) used an explicit ABAQUS (62) model. The results show that no tuning of the simulation was required to obtain results close to theoretical and experimental results.

4.5 SUMMARY

This section summarizes the major findings from the literature review, which should be considered for an accurate analysis of the sucker rod string:

- Models for vertical wells do not accurately predict the behaviour of sucker rod stings in inclined wells. The proper analysis of deviated wells requires three-dimensional models and the accurate trajectory of the well.
- It is an absolute necessity to consider the fluid dynamics in the analysis of the sucker rod string behavior, especially in the predictive analysis.
- The major focus for improvement lies in the fluid dynamics and the fluid/tubing and fluid/sucker rod interaction.
- Coulomb friction forces are largely dependent on the trajectory of the borehole and the axial loads in the sucker rod string.
- Investigations of the friction factors between rod/ tubing for liquids with impurities like sand and different kinds of rod guides should be performed. Solutions show that the key element in the rod pumping analysis is the exact rod friction law.
- Fluid effects on buckled sucker rods must be considered.

- The boundary effects for buckling can be ignored for a rod string assumed to be long.
- Friction significantly increases the critical loads for buckling.
- Rod couplings have an essential influence on the buckling behavior in horizontal wells.
- A certain amount of compression at the bottom of the rod does not necessarily cause buckling.
- The effect of waxes and precipitations have not been investigated closer.
- The real critical lateral buckling force is lower than the critical helical buckling force.
- Finite-Element-Analysis (FEA) can be used to analyze the critical buckling loads.
- The rod string can be represented by beam elements.
- There is currently no effective system available to prevent buckling, without the usage of sinker bars.
- SRABS has to be evaluated, to show the benefits in comparison to existing designs.

5 THE SUCKER ROD PUMPING SYSTEM

This chapter covers the theoretical input, required for the simulation of the sucker rod pumping process and the verification of the Sucker Rod Anti-Buckling System under the aspects gained during the literature review from the previous chapter.

The term “Sucker Rod Pumping System” comprises all components that are necessary to obtain a working pumping system. The major parts are the pump jack, which defines the motion of the polished rod, the downhole pump that defines the downhole load on the rod string and the sucker rod string, which is submersed in the pumped fluid and during buckling in contact with the tubing string. Thus the major issues of this chapter are:

- Behavior at the polished rod
- Behavior of the tapered sucker rod string with liquid and tubing interaction
- Behavior at the pump plunger

A Sucker rod pumping system is a very flexible (63) and adjustable artificial lift method. Therefore Table 3 presents numerous alternatives and combinations for their installation. The highlighted components are considered in the analysis presented within this thesis. They represent a base case to start the evaluation, while all the other components can principally be included after some adaptations.

Types of Pumping Units	Driving Unit
<ul style="list-style-type: none"> • Conventional Unit • Mark II Unit • Air Balanced Unit • Beam Balanced Unit • Reverse Mark Unit • Long Stroke Unit • Low Profile Unit 	<ul style="list-style-type: none"> • Diesel Engine • Electrical Engine (with and without variable speed drive) <ul style="list-style-type: none"> • Synchronous Engines • Asynchronous Engines (slip)
Working Condition	Wellbore Trajectory
<ul style="list-style-type: none"> • Stationary • Start / Stop 	<ul style="list-style-type: none"> • Vertical Wells • Deviated Wells (Coulomb Friction)
Sucker Rods	Equipment
<ul style="list-style-type: none"> • Rod Material <ul style="list-style-type: none"> • Steel Rods • Fibre Glass Rods • Ropes, Wires • Rod String <ul style="list-style-type: none"> • Polished Rod • Tapered Rod String 	<ul style="list-style-type: none"> • Tubing (RWAC) and Insert Pumps (TP) • Beam Gas Compressor • Gas Anchor • Rotators <ul style="list-style-type: none"> • Tubing Rotator • Rod Rotators <ul style="list-style-type: none"> • Mechanical

<ul style="list-style-type: none"> • Sinker Bars • Rod Guides • Fixed Rod Guides • Wheeled Rod Guides 	<ul style="list-style-type: none"> • Electrical
Tubing	Fluid
<ul style="list-style-type: none"> • Anchored • Non - Anchored 	<ul style="list-style-type: none"> • Medium viscous oil with low GOR • Paraffin • Solids • High GOR • High Viscosity Oils

TABLE 3: SRP DESIGN OPTIONS

5.1 SURFACE BOUNDARY CONDITION - BEHAVIOUR AT THE POLISHED ROD

The polished rod is atop of the sucker rod string and directly connected - by the so called wireline hangers - to the horsehead of the pump jack. As a result the motion of the polished rod is defined by the geometry of the pump jack and the operating conditions, like strokes per minute (SPM), etc. This results in the displacement boundary condition at the polished rod.

Due to observation reasons, load measurements are often performed at the polished rod, called dynamometer measurements (64). A load cell (Figure 88) is attached to the polished rod and loaded with the weight of rods and the pumped liquid. The measured data are commonly used for failure interpretation and pump optimization. The problem with these data is that the measurement tool is calibrated very rarely, because the companies are not really interested in the exact magnitude of the load, but only in the tendency for problem analysis. Inaccuracies occur in the magnitude of about 5 kN. Nevertheless these data can be corrected and used as load boundary condition at the polished rod for later simulations.

Supplementary measurement systems like Ecometers as MURAG (65), allow the automated fluid level measurement from surface, hence a production optimization, reservoir pressure evaluation and an increase of the pumping system runtime.

5.1.1 DISPLACEMENT AT THE POLISHED ROD

The displacement over time behaviour of the polished rod is not a simple sine or cosine function, but a more complex relationship, resulting from the geometry of the pump jack.

The rod string is driven by the prime mover via gearbox, crank shaft, pitman, walking beam and finally the wirelines with the wireline hanger and polished rod. This means that the polished rod motion is, apart from motor speed variation, which is a result of the load, only dependent on the prime movers rotations per minute (RPM), as a result of the current frequency powering the electrical engine, the transmission ratio of the sheaves and gearbox as well as the geometry of the pump jack. As a result the polished rod motion can be

evaluated relatively exact, with the limitation of the slip of the belt, connecting the prime mover with the gear box. This is very important because almost everything else is in some kind dependent on the motion of the polished rod e.g. production rates, dynamic loads, fluid friction, etc.

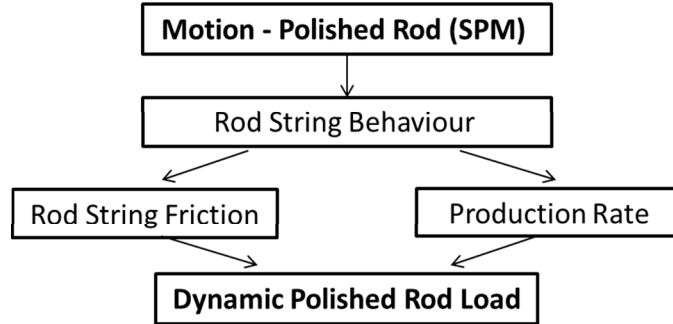


FIGURE 32: BLOCK DIAGRAMM – POLISHED ROD

This chapter presents different models that describe the motion of the polished rod in dependency of pump jack geometry and crank shaft speed. These models are compared with a measurement, performed on a real sucker rod pumping system. The polished rod motion is highly dependent of the pump jack type. A Conventional Pumping Unit behaves completely different than a Mark II Unit (66) or other pump jack designs. In Austria an essential majority of SRP use Conventional Units. As result only this pump jack type is considered within this thesis. An adjustment for other pump jacks can be performed easily.

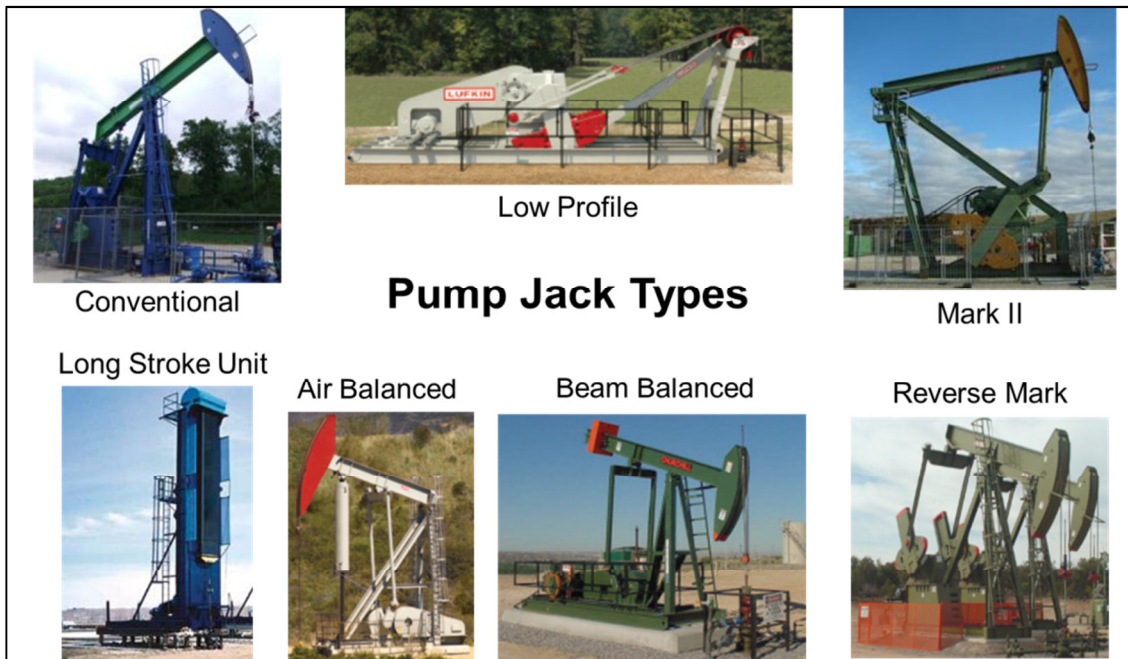


FIGURE 33: PUMP JACK TYPES (66)

5.1.1.1 H.E. GRAY MODEL (67)

H.E. Gray in 1963 was the first who tried to describe the polished rod position in dependency of the crank angle at the crank shaft. The pump jack itself can be displayed as a four-bar linkage system, where five geometrical dimensions are required to convert the RPM from the crankshaft to the displacement at the polished rod. Figure 34 shows a schematic of the four-bar linkage system, used by Gray.

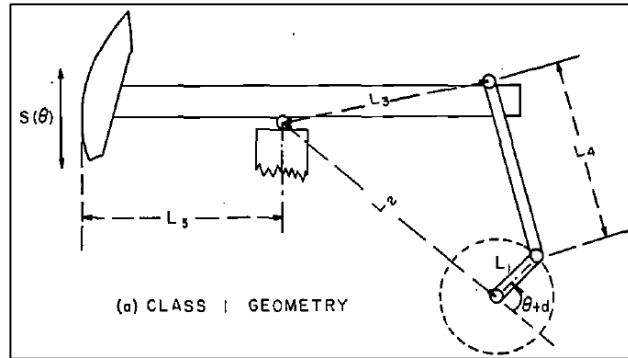


FIGURE 34: FOUR – BAR LINKAGE SYSTEM / GRAY (60)

The information about the lengths of L_1 to L_5 can be obtained from pump jack manufacturers. For instance Lufkin provides full information about dimensions, torque factors and structural unbalance. (68)

API Geometry Dimensions (inches)

Unit Size	A	C	I	P	H	G	R1, R2, R3, R4	S.U.*	T.F. @ 90°/Stroke Length
C-1824D-305-240	228	120.03	120	226.75	340.00	111.00	60, 53, 46, 39	-2740	111.78/240
C-1280D-305-240	228	120.03	120	226.80	340.00	111.00	60, 53, 46, 39	-2855	111.78/240
C-912D-305-240	228	120.03	120	226.75	340.00	111.00	60, 53, 46, 39	-2740	111.78/240
C-1824D-365-216	235	120.03	120	172.50	286.00	111.00	53, 46, 39, 32	-2030	101.31/216
C-1280D-427-192	210	120.03	120	172.50	286.50	111.00	53, 46, 39, 32	-995	90.43/192
C-1824D-365-192	210	120.03	120	172.50	286.00	111.00	53, 46, 39, 32	-1985	90.51/192
C-1280D-365-192	210	120.03	120	172.50	286.00	111.00	53, 46, 39, 32	-1800	90.51/192
C-912D-365-192	210	120.03	120	172.50	286.00	111.00	53, 46, 39, 32	-1800	90.51/192
C-912D-305-192	210	120.03	120	172.50	286.00	111.00	53, 46, 39, 32	-1800	90.51/192

TABLE 4: LUFKIN - PUMP JACK DIMENSIONS (68)

Table 4 is a short section of the geometrical data for pumping units, provided by Lufkin. The dimension L_1 corresponds to the values R_1 to R_4 , which stands for different crank shaft hole positions. The bigger the value of R , the higher is the stroke length of the pump jack. The pitman can be fixed at different crank shaft positions to adjust the stroke length of the pump jack, without changing the overall structure.

L_2 can be calculated with the dimensions G, H and I ($L_2 = \sqrt{(H - G)^2 + I^2}$), L_3 is equal to C and L_4 is the pitman length P. L_5 is the distance between central bearing and wireline hangers at the horse head, which is labelled with A in Table 4.

The terms structural unbalance “S.U.” and torque factor “T.F.” within Table 4 are well explained in the API standards. (69) The following is the definition of the two terms from the API standards:

Structural Unbalance S.U.:

Force required at the polished rod to balance the beam in horizontal position with the Pitmans disconnected from the crank pin and no well load applied.

NOTE: The structural unbalance is considered positive when the force required at the polished rod is directed downward, and negative when upward.

Torque Factor T.F.:

Factor for any given crank angle that, when multiplied by the load at the polished rod, gives the torque at the crankshaft of the beam pumping units speed reducer.

NOTE: The torque factor has the unit of length.

H.E. Gray calculated the position of the polished rod $s(\theta)$, using this geometrical information, in dependency of the crank angle θ , by the following equation:

$$s(\theta) = \pm L_5 \left[\cos^{-1} \left\{ \frac{\frac{L_1^2 + L_2^2 + L_3^2 - L_4^2}{2L_2L_3} + \frac{L_1}{L_3} \cos(\theta R + d)}{\left[1 + \left(\frac{L_1}{L_2} \right)^2 + 2 \frac{L_1}{L_2} \cos(\theta R + d) \right]^{\frac{1}{2}}} \right\} + \sin^{-1} \left\{ \frac{\frac{L_1}{L_2} \sin(\theta R + d)}{\left[1 + \left(\frac{L_1}{L_2} \right)^2 + 2 \frac{L_1}{L_2} \cos(\theta R + d) \right]^{\frac{1}{2}}} \right\} \right] \quad \text{Eq. 25}$$

where

$$d = \frac{\pi}{2} (1 \pm 1) - \cos^{-1} \left[\frac{L_2^2 - L_3^2 + (L_4 \pm L_1)^2}{2L_2(L_4 \pm L_1)} \right] \quad \text{Eq. 26}$$

According to Gray, some conventions must be considered, when applying this equation:

1. *“The sign convention for polished-rod position $s(\theta)$ is positive upwards.*
2. *θ is the crank angle in radians measured from the point at which the polished rod is at its lowermost position.*
3. *In making a calculation for a complete cycle, θ always goes from 0 to 2π ; i.e. the positive direction of θ is taken in the direction of crank sweep.*

4. The direction of rotation is provided for by the factor R . $R = +1$ indicates that the crank falls toward the Sampson post (Conventional Units) and $R = -1$ indicates the reverse rotation (Mark II Unit).
5. Where the \pm or \mp sign option is indicated, the first sign applies for Class 1 units and the second for Class 2.
6. The phase angle d (in radians) is the crank angle shift required by the condition that $\theta = 0$ corresponds to the bottom of the polished-rod stroke." (67)

Figure 35 presents the polished rod position versus crank shaft angle behaviour for a conventional pumping unit with a maximum stroke length of 3,66 m (144") by using the model after Gray. The boundary condition for the curve is a constant rotation speed of the crank shaft, thus no motor speed variations.

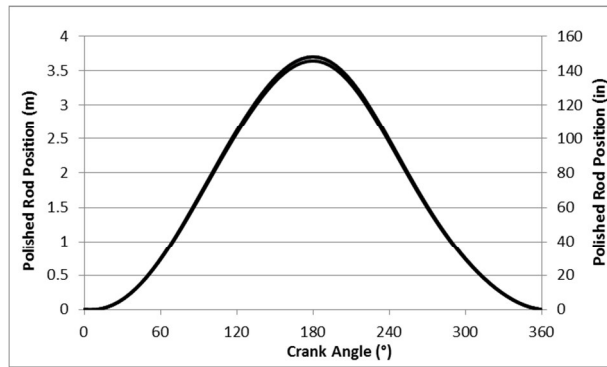


FIGURE 35: DISPLACEMENT - POLISHED ROD / GRAY – LUFKIN C 228 D 200 144 - 144" STROKE LENGTH

To provide a better comparability with other units and models, Gray suggested an adjustment to a mean value of zero and normalization to unity amplitude:

$$s^*(\theta) = \frac{s(\theta) - \frac{1}{2}\{[s(\theta)]_{\max} + [s(\theta)]_{\min}\}}{\frac{1}{2}\{[s(\theta)]_{\max} - [s(\theta)]_{\min}\}} \quad \text{Eq. 27}$$

$s^*(\theta)$ can be regarded as a non-dimensional form of the polished-rod position function.

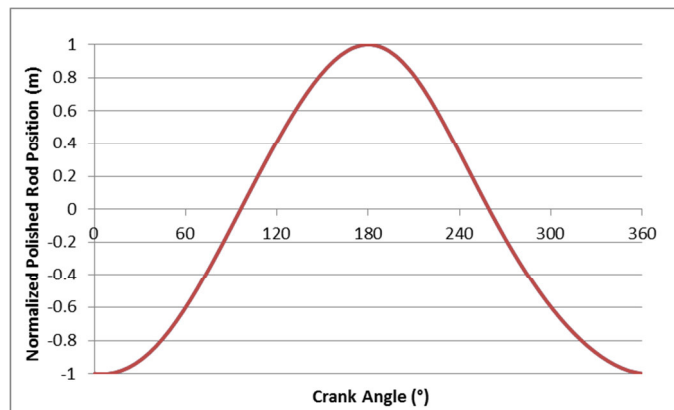


FIGURE 36: NORMALIZED DISPLACEMENT OF THE POLISHED ROD / GRAY

Further criteria and important parameters are the velocity and the acceleration at the polished rod. Even when the displacement curve might look the same, the velocity and acceleration profile can be essentially different.

Normally simple differentiation of the polished rod displacement would result in the polished rod velocity and acceleration. Due to the complexity of the displacement equation, numerical differentiation is preferred.

Hence, the velocity in dependency of the crank angle is: $v^*(\theta) = \frac{s^*(\theta+\Delta)-s^*(\theta-\Delta)}{2\Delta}$ Eq. 28

and the acceleration is $a^*(\theta) = \frac{s^*(\theta+\Delta)-2s^*(\theta)+s^*(\theta-\Delta)}{\Delta^2}$ Eq. 29

Figure 37 shows the displacement, velocity and acceleration of the polished rod for a conventional pump jack.

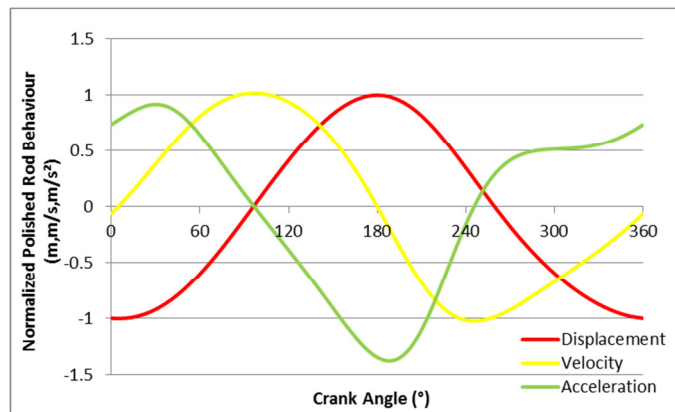


FIGURE 37: NORMALIZED POLISHED ROD BEHAVIOR AFTER GRAY

To highlight the significance of the differences in the pump jack behaviour, Gray distinguishes between four different pump jack designs: (see Figure 33)

- Class 1 units designed for rotary counterbalance (C/1R)
- Class 1 units designed for beam counterbalance (C/1B)
- Class 2 units designed for air counterbalance (C/2A)
- Class 2 units designed for rotary counterbalance (C/2R)

For simplicity and better comparison, he normalized the variables L_2 , L_3 , and L_4 for $L_1 = 1$, too. Figure 38 shows the polished rod displacement, velocity and acceleration for four different units from Gray’s publication:

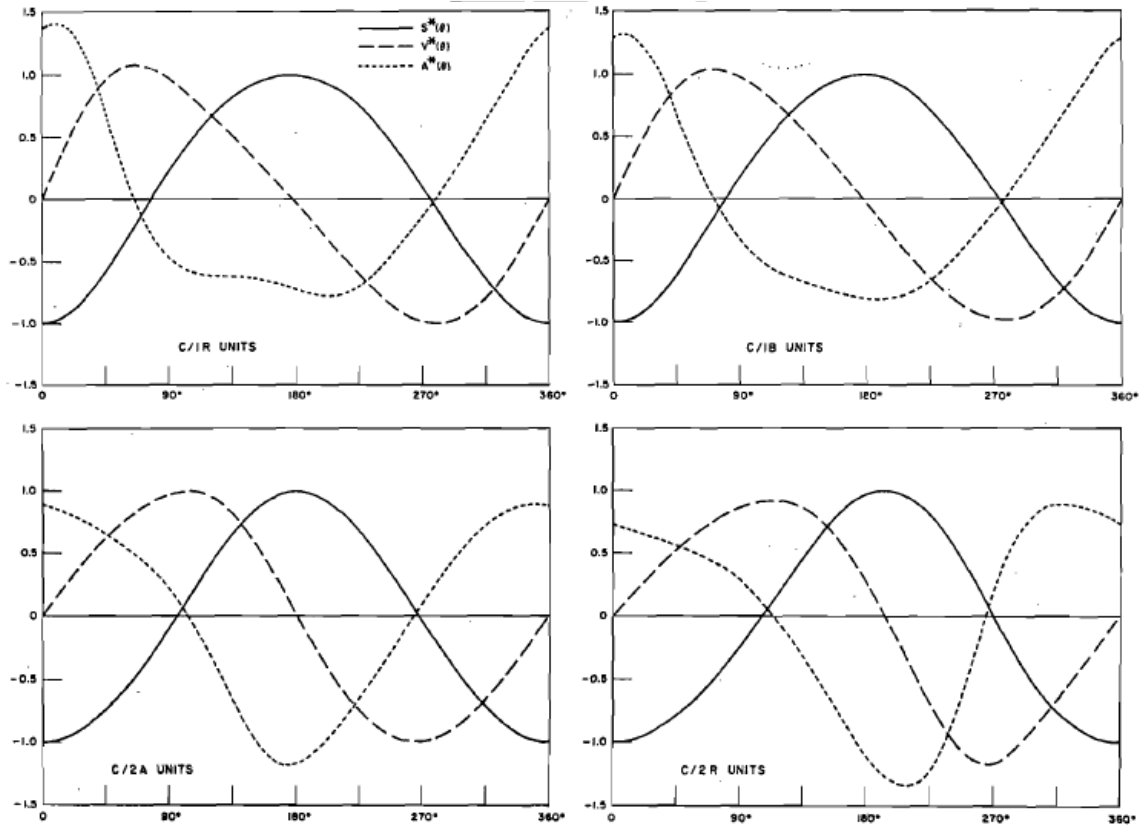


Fig. 4 – Non-Dimensional Polished-rod Position Velocity, and Acceleration vs. Crank Angle for Typical Conventional Pumping Units

FIGURE 38: NORMALIZED POLISHED ROD BEHAVIOR / DIFFERENT PUMP JACK TYPES (67)

Although the displacement over time function has for all cases almost the same shape, the acceleration profile is significantly different. Hence, it is essential to use the correct pump jack type and geometry to obtain accurate results.

Limitation of Gray's model:

Grays model only allows the calculation of the motion at the polished rod, but not at any other point within the pump jack, which is a strong limitation when inertia effects of the pump jack must be considered in the calculations.

There is a second model for describing the motion of the polished rod available, which allows a much higher flexibility. This model was published by John G. Svinos in 1983 with the title "Exact Kinematic Analysis of Pumping Units" (70). The following section presents the essential findings from this publication.

5.1.1.2 JOHN G. SVINOS MODEL: (70)

John G. Svinos introduced a set of equations that allow the kinematic analysis of any component within the four-bar linkage problem, for Conventional-, Mark II and Air Balanced Units. It's even possible to consider speed variations of the crank shaft, caused by the load dependent behaviour of the prime mover or designed changes of the excitation frequency in the motor's stator.

According to John Svinos, some conventions must be adapted: (see Figure 39)

- Angles θ_2 , θ_3 , θ_4 and θ_5 are measured from the reference line 0 - 0 and are positive in the counter clockwise direction for conventional units.
- For conventional pumping units, the crank angle θ is zero at the 12 o'clock position and progresses positively in the clockwise direction.

Figure 39 shows the full denomination of the conventional pumping unit:

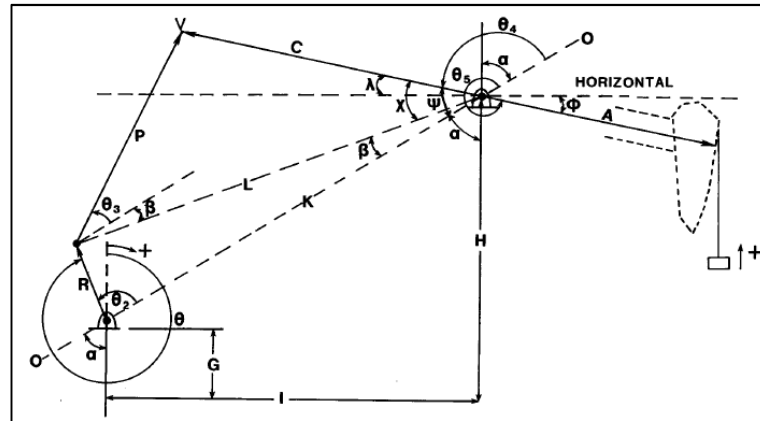


FIGURE 39: NOMENCLATURE OF THE CONVENTIONAL PUMPING UNIT (70)

The following section is taken from J.G.Svinos' publication (70) and summarizes the equations that are required to calculate the displacement at the polished rod for a conventional pumping unit:

$$\theta_2 = 2\pi - \theta + \alpha \quad , \text{ where } \quad \alpha = \sin^{-1}\left(\frac{I}{K}\right)$$

$$L = \sqrt{K^2 + R^2 - 2KR \cos(\theta_2)}$$

$$\beta = \cos^{-1}\left(\frac{L^2 + K^2 - R^2}{2KL}\right) * j \quad , \text{ for } \quad j = \begin{cases} 1 & \text{for } 0 < \theta_2 < \pi \\ -1 & \text{for } \pi < \theta_2 < 2\pi \end{cases}$$

$$\theta_3 = \cos^{-1}\left(\frac{P^2 + L^2 - C^2}{2PL}\right) - \beta$$

$$\theta_4 = \cos^{-1}\left(\frac{P^2 - L^2 - C^2}{2CL}\right) - \beta$$

Using the calculated θ_4 , the polished rod displacement PR can be expressed as:

$$PR = A \left(\theta_4 - \frac{\pi}{2} - \alpha \right) \quad \text{Eq. 30}$$

$\theta_4 - \pi/2 - \alpha$ Eq. 30 clearly indicates that the displacement of the polished rod itself is only dependent on the crank angle position, but independent from the angular velocity of the prime mover.

For evaluating the velocity and the acceleration of the polished rod, the angular velocity and angular acceleration must be derived. Therefore the angular velocity $\dot{\theta}_2$ and the angular acceleration $\ddot{\theta}_2$ of the prime mover are required. At this point several acceleration profiles can be used, to adjust the model to pumping units with changing prime mover speed, caused e.g. by variable speed drives.

$$\dot{\theta}_3 = \frac{R\dot{\theta}_2 \sin(\theta_4 - \theta_2)}{P \sin(\theta_3 - \theta_4)} \quad \text{Eq. 31}$$

$$\dot{\theta}_4 = \frac{R\dot{\theta}_2 \sin(\theta_3 - \theta_2)}{C \sin(\theta_3 - \theta_4)} \quad \text{Eq. 32}$$

$$\ddot{\theta}_4 = \dot{\theta}_4 \left[\frac{\ddot{\theta}_2}{\dot{\theta}_2} - (\dot{\theta}_3 - \dot{\theta}_4) \cot(\theta_3 - \theta_4) + (\dot{\theta}_2 - \dot{\theta}_3) \cot(\theta_2 - \theta_3) \right] \quad \text{Eq. 33}$$

The resulting velocity and acceleration of the polished rod are:

$$VR = A * \dot{\theta}_4 \quad \text{EQ. 34}$$

$$AR = A * \ddot{\theta}_4 \quad \text{EQ. 35}$$

A, C, G, J, K, P, R are pumping unit geometric dimensions (specified in API 11E), $\beta, \theta_2, \theta_3, \theta_4$ are geometric angles, PR is the polished rod position, VR is the polished rod velocity, AR is the polished rod acceleration, $\dot{\theta}_2, \dot{\theta}_3, \dot{\theta}_4$ are angular velocities and $\ddot{\theta}_2, \ddot{\theta}_3, \ddot{\theta}_4$ are angular accelerations.

It can be seen from the equations that the angle, the angular velocity and the angular acceleration for any angle in the system can be calculated, which allows a dynamic analysis of all components in the four-bar linkage system.

For a conventional pumping unit with constant prime mover speed, the polished rod motion results in the following curves:

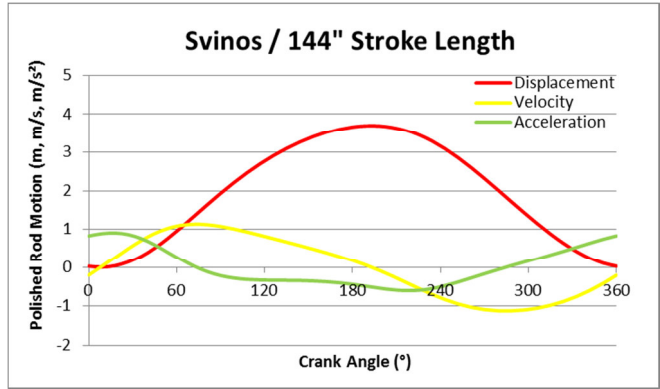


FIGURE 40: POLISHED ROD MOTION

To allow a better comparison of different models, the normalized displacement, velocity and acceleration are plotted in Figure 41:

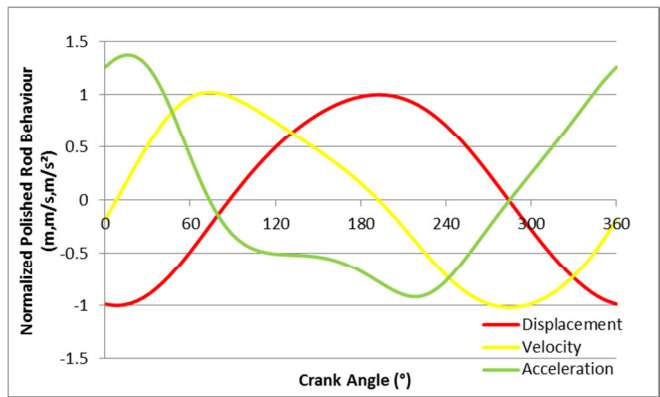


FIGURE 41: NORMALIZED POLISHED ROD BEHAVIOR / SVINOS

Figure 42 represents a comparison of the model after Gray and the model after Svinos. The solid lines represent the output from the Svinos model and the dashed lines the output from the Gray model. Although the displacement looks quite similar, the acceleration resulting from these two models is quiet different. Due to the essential influence of this motion for any further simulation, it is important to find the model fitting reality best. Therefore field measurements of the motion of the polished rod for numerous pump jacks were performed.

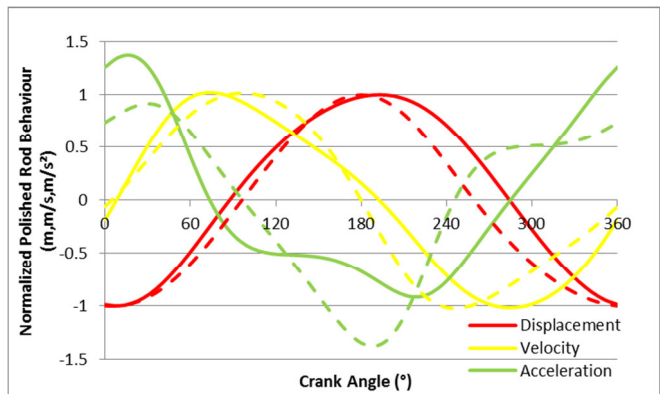


FIGURE 42: COMPARISON GRAY / SVINOS

5.1.1.3 MODEL REVIEW BASED ON POLISHED ROD MOTION FIELD MEASUREMENTS:

Surface dynamometer measurements were carried out at eleven pump jacks, to obtain real motion data from the polished rod. Figure 43 shows a picture of the surface dynamometer measurement. The data were digitally recorded and processed, which resulted in the position over time behaviour.



FIGURE 43: SURFACE DIGITAL MEASUREMENT TOOL (71)

This chapter now presents the comparison of the field measurement results, the Gray model, Svinos model and the simple Sinus function.

All of the units, where the field measurements were performed, had different pumping frequencies and geometric dimensions, as displayed in Table 5. To allow a comparison the time required for one pumping cycle was converted linearly into a crank angle of 360° and the position was normalized.

Well Name	Stroke Length		Cycle Duration
	(m)	(in)	
Well 1	4,30	168	10,40
Well 2	1,91	74	14,85
Well 3	1,91	74	17,00
Well 4	3,71	144	15,46
Well 5	3,11	122	7,80
Well 6	1,98	74	10,10
Well 7	3,69	144	16,13
Well 8	3,15	122	12,77
Well 9	3,72	144	15,79
Well 10	2,20	86	22,06
Well 11	2,20	86	7,06

TABLE 5: GEOMETRIC DIMENSIONS / CONVENTIONAL UNITS

The normalized plot in Figure 44 demonstrates a comparison of Gray’s model, Sivos’ model, a Sinus function and the measured data.

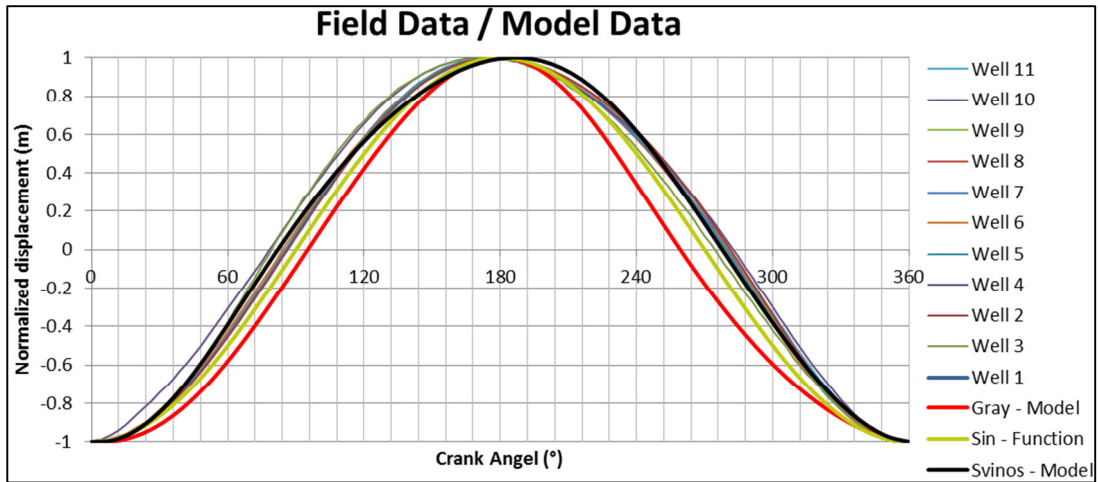


FIGURE 44: NORMALIZED PLOT / SURFACE MEASUREMENT

The red line represents the Gray model. It can be seen that the fit is far from perfect while the black line is representing the displacement calculated with Sivos’ model offering a very good fit to the measured well data. The sine function seems to provide a good fit, too.

For a final selection of the model, the velocity and acceleration should be observed more closely. The corresponding measured field data are averaged to prevent confusion and thus result in a little wavy line. The velocity curves all fall within a narrow band. The acceleration curves indicate that the Sivos model approximates the field data better than the sine function. The inaccuracy is a result of field data averaging, which is necessary not to overload the graph.

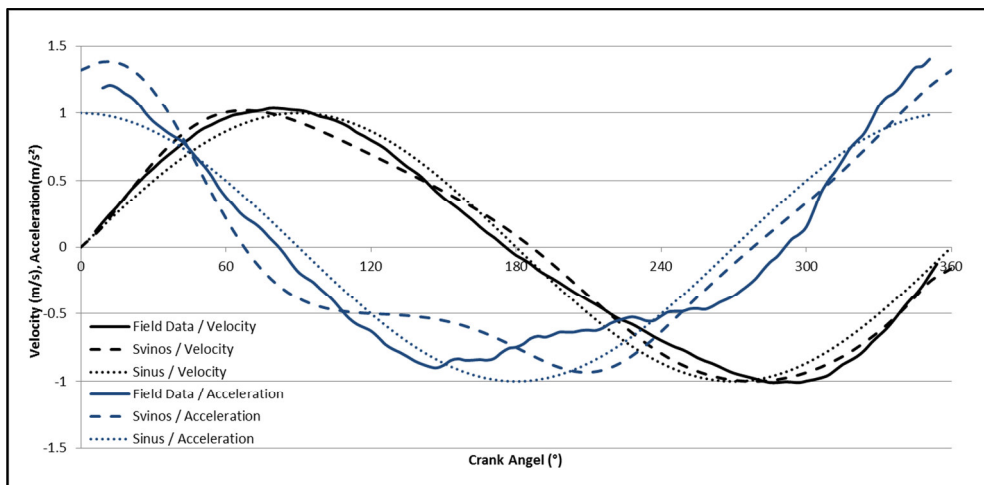


FIGURE 45: VELOCITY / ACCELERATION COMPARISON

Another possibility to display the different models is by using a dynamometer card plot. A measured dynamometer card is compared with those obtained by the models. The load stays the same for all models, but the displacement clearly changes from model to model. No averaging is used to obtain the graph.

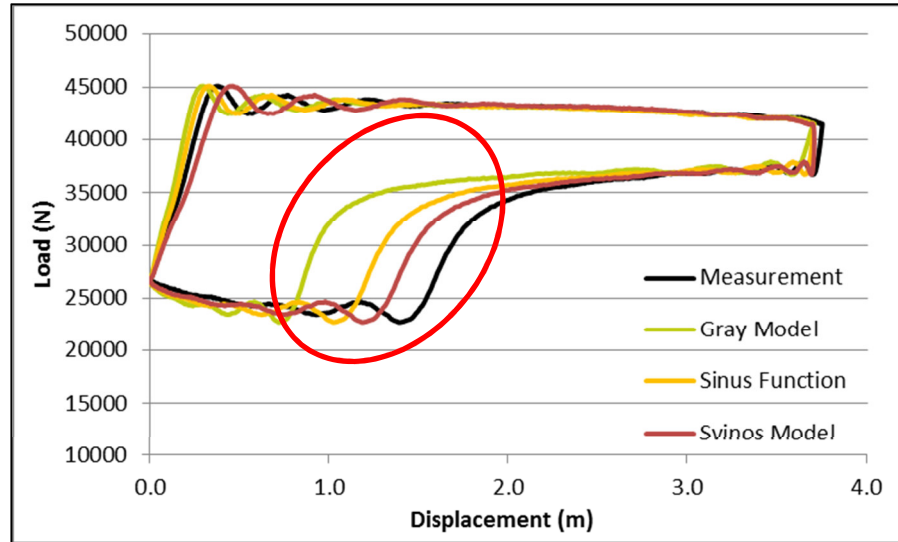


FIGURE 46: DYNAMOMETER CARD REPRESENTATION

Beside the high flexibility of the Svinos model being a huge advantage in the comparison with the other models, Figure 45 and Figure 46 show clearly that the Svinos model provides the best match. This statement is based on the visual impression of the four lines during the downstroke, where the Svinos model is closest to the measurement. Hence, this model seems to represent the surface motion of the polished rod best.

5.1.2 LOAD AT THE POLISHED ROD

The load at the polished rod results from rod and fluid weight, buoyancy, friction forces, inertia and acceleration forces, and oscillation effects. Hence this load is directly dependent on the motion of the polished rod, thus the geometry of the pump jack and the behaviour of the prime mover.

It is definitely impossible to calculate this load without accurate knowledge of the downhole conditions and the behaviour of the sucker rod string. However this load can be measured for a given system within the common Dynamometer Card Measurement procedure. Such measurements are often performed in an analogous way. Hence load over displacement cards are available.

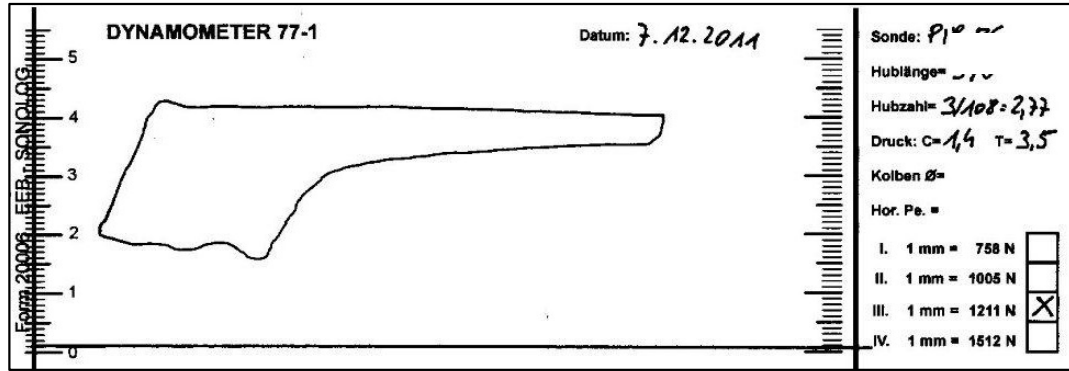


FIGURE 47: ANALOGOUS DYNAMOMETER CARD (72)

For the usage of this information as, for instance simulation boundary condition the data must be converted into time dependent data, e.g. load over time. (Appendix A)

- 1) The first step is digitizing of the analogous dynamometer card.
- 2) For the second step it is very helpful to use the Svinos model for the motion of the polished rod. The position over time function is created for the corresponding pump jack for predefined times.
- 3) Finally the displacement at known times is assigned to the corresponding displacement from the dynamometer card, where the load is known. This results in the load function at the polished rod, derived from the dynamometer measurement.

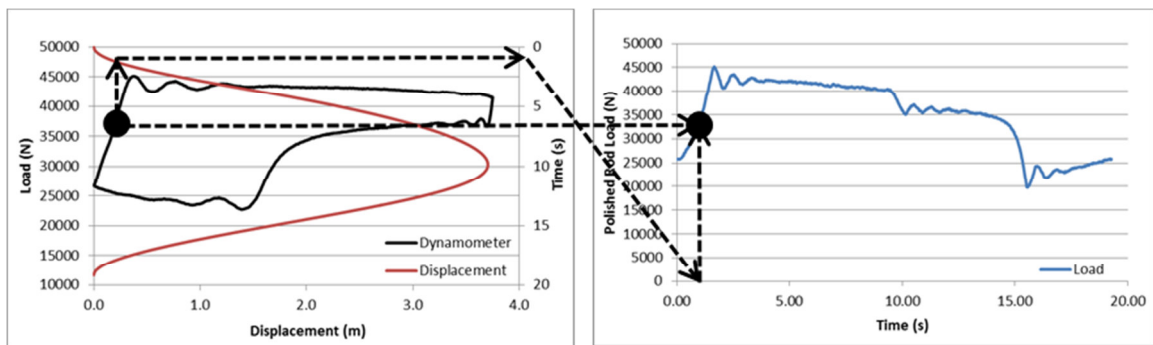


FIGURE 48: LOAD FUNCTION DERIVATION

5.1.3 PUMP JACK DYNAMICS

So far, the previous sections only concentrated on the motion and load at the polished rod. Other very important parameters are the torque at the crank shaft - for dimensioning the counterweights and sizing the gear box - and the required speed of the prime mover. Today, variable speed drive systems are often used, which allow variable prime mover speed. In such cases the transmission ratios of the belts and the gear box are of interest.

Due to the conversion of the rotation into an oscillation at the cranks, some components of the pump jack are accelerated and decelerated several times during one pumping cycle. This causes additional torque at the cranks. Therefore the polished rod load must be converted into torque at the cranks, too.

Hence the total torque at the crank shaft is composed of three components,

- the polished rod load,
- the counterweights,
- the pump jack structure.

5.1.3.1 POLISHED ROD LOAD

The polished rod load (PRL) is a result of the processes in the wellbore. The conversion into torque is relatively simple and shown with reference to Figure 39. Within the first step, the torque factor is calculated by dividing polished rod velocity through the crank angular velocity. Afterwards the PRL is multiplied by this torque factor, which results in the torque at the crank shaft (73). Figure 49 presents the conversion from a measured polished rod load profile of an Austrian SRP to torque at the crank shaft.

$$TF = \frac{VR}{\dot{\theta}_2} \tag{Eq. 36}$$

$$T_{load} = TF \cdot PRL \tag{Eq. 37}$$

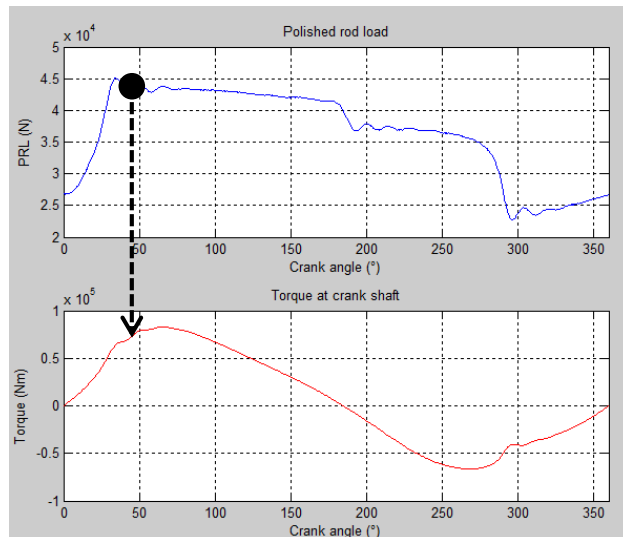


FIGURE 49: CRANK SHAFT TORQUE FROM POLISHED ROD LOAD

5.1.3.2 COUNTERWEIGHTS

The counterweights are installed directly at the cranks; hence they rotate with the crankshaft and cause a sine-shaped torque. The magnitude of the caused torque can be adjusted, within limits, in two ways: by adding or removing weight and by changing the position of the weight at the cranks. The observed exemplary pumping unit is equipped with two 330 kg counterweights, positioned 2,1 meters from the crank shaft. The resulting torque is:

$$T_{\text{counter weight}}(\theta) = M \cdot \sin(\theta - \gamma) \tag{Eq. 38}$$

γ Counterbalance offset angle (0 for conventional units) (66)

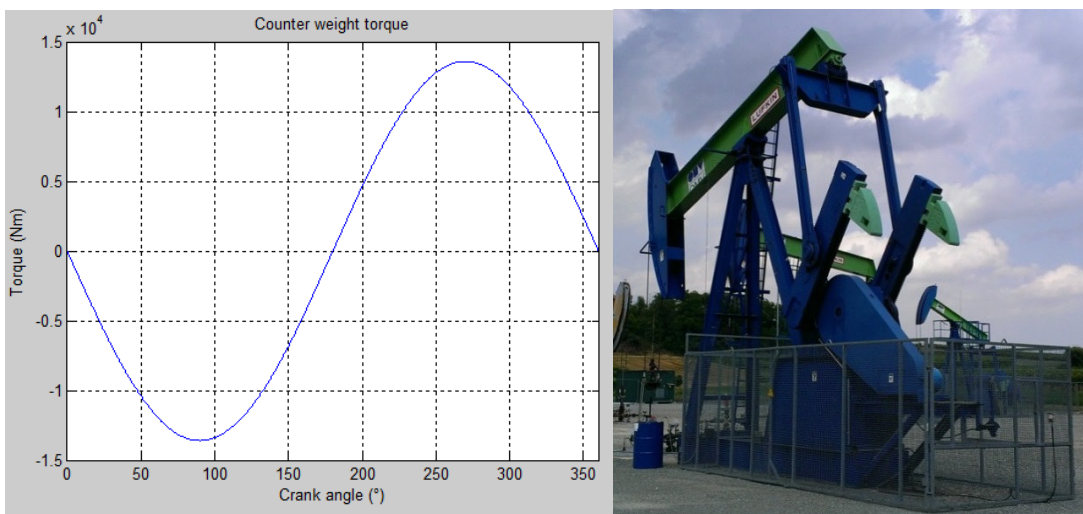


FIGURE 50: CRANKSHAFT TORQUE FROM COUNTERWEIGHTS

5.1.3.3 PUMPING JACK STRUCTURE

The pumping structure itself consists of rotating masses, like cranks, part of the pitmen and oscillating masses, like horse head, walking beam, equalizer beam, etc. The mass moment of inertia of the pumping unit structure is used to analyze its dynamics and required torque to run the pump jack.

Also the structural unbalance of the pump jack must be considered. Its magnitude for the observed exemplary unit C-320D-256-144 (68) is -1788 Newton. The torque caused by the pump jack structure is calculated by the following equation: (70)

$$T_{\text{structure}}(\theta) = TF(\theta) \cdot (S.U.) - I_g \cdot \ddot{\theta} + TF(\theta) \cdot \frac{I_B}{A} \ddot{\theta}_4 \tag{Eq. 39}$$

Where S.U. is the structural, I_g is the moment of inertia of all rotating components and I_B is the moment of inertia of all oscillating components.

Table 6 summarizes the weight, dimensions and the mass moment of inertia, etc. for the individual components of the above selected pump jack:

Component	Motion	Mass (kg)	Dimension (-)	I (kgm ²)
Horsehead	oscillating	350	-	8745
Walking beam	oscillating	1980	W30x173	10730
Equalizer beam	oscillating	82	W24x55	760
Pitman	oscillating	55	W8x10	512
	rotating	55	W8x10	78
Cranks	rotating	3530	94110CA	10600

TABLE 6: PUMP JACK COMPONENTS DIMENSIONS (68) (74)

The results of Figure 51 are based on a slightly deviated, 900 m long sucker rod string, operating with 3,2 SPM. The total torque, instead of the polished rod or structural torque, must be provided by the gearbox and the prime mover.

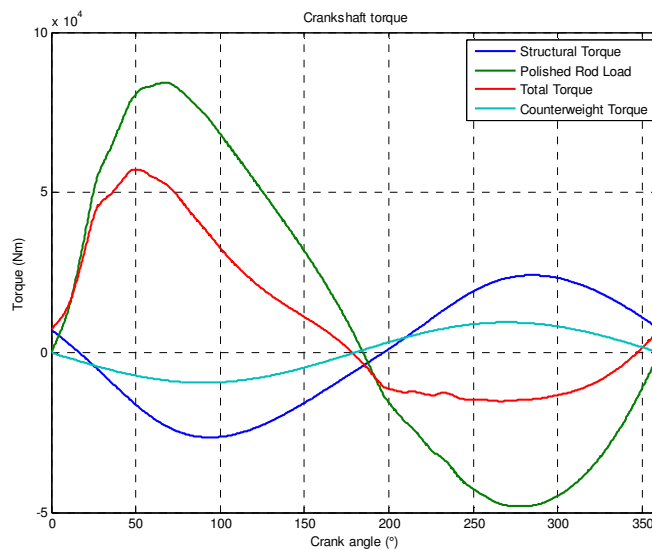


FIGURE 51: TOTAL CRANKSHAFT TORQUE

High transmission ratios e.g. 384 in the above shown case keep the required torque at the prime mover low and allow a high speed reduction, causing relatively small electrical engines. The prime mover in this case is running with 1200 rpm and 20 Hz frequency.

Figure 52 presents the prime mover torque. It can be seen that between 80 and 190 degree crank angle, the torque is negative, which means that the engine works like a generator and energy could theoretically be generated. The problem is that the switch of electrical engines from motor to generator mode is accompanied with a lot of losses. Additionally the driving systems are not designed to recover energy and do not allow this in most cases.

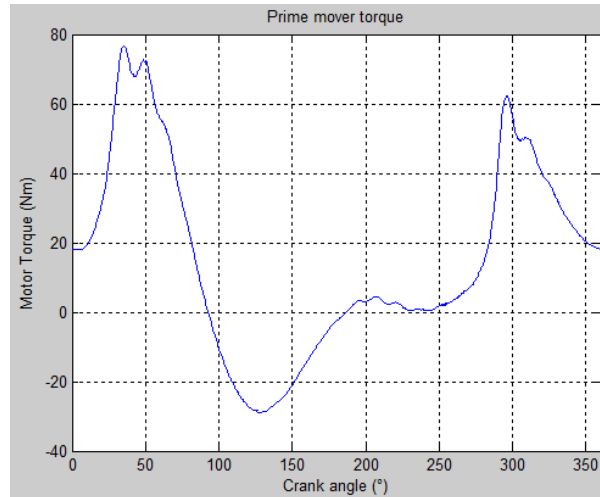


FIGURE 52: PRIME MOVER TORQUE

5.2 BEHAVIOR OF THE SUCKER ROD STRING

The sucker rod string can be compared with an electronic transmission line. At one end, the transmitter sends information into the transmission line (see Figure 53). After the transfer of the information by the transmission line, it can be recorded at the other end by the receiver. Due to the properties of the transmission line, the information at the receiver is disturbed. By selecting a proper model for the behavior of the transmission line, the original data can be re-assembled at the receiver.

When applying this concept for sucker rod pumping units, the transmitter is the pump plunger, the polished rod represents the receiver and the rod string is the transmission line. Information about the down-hole pump condition is continuously transmitted upwards along the sucker rod string in the form of strain waves. The travel speed of these waves represents the velocity of sound in the rod material. The problem is that the information received at the surface does not directly reflect the information from the pump because of the interference of the rod string caused by friction forces, viscous forces and the elastic behavior of the material. To enable a reverse calculation to the original data, the rod string behavior must be understood. In most cases in the literature the rod string's dynamic behavior is described by a partial differential equation. Its complexity depends on the number of incorporated effects. The interpretation of the information received at the polished rod is done by solving the boundary value problem. (24)

For solving this set of partial differential equations, boundary equations are required. Two different problem settings are commonly used: (19) (75)

Predictive approach:

The predictive approach is used for the behavior of a not yet installed pumping system. It is used to design a new pumping system and to perform case studies to get an optimized and efficient system with the available components under the predefined boundary conditions. The limitation of the predictive approach is that no real measured data from the pump are available and the required input data must be represented by mathematical models, which are not as accurate as measurements. The greatest difficulty is to get a representative behavior of the forces at the pump plunger.

Diagnostic approach:

The diagnostic approach is used to diagnose the behavior of operating pumps. Measurements, performed at the polished rod, act as boundary conditions for the evaluation model, which delivers the requested information of the behavior at the pump plunger. In general the accuracy of the diagnostic approach is higher than of the predictive one.

The following block diagram illustrates the general work flow of the diagnostic approach, used in the sucker rod pump analysis.

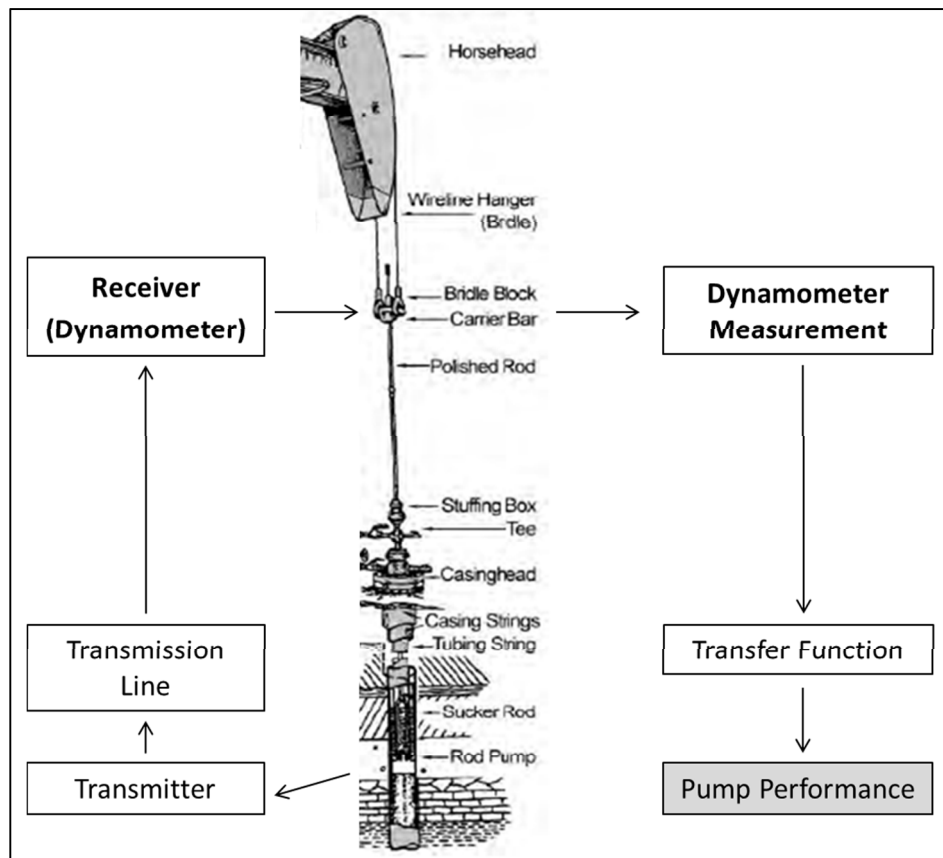


FIGURE 53: BLOCK DIAGRAM / SUCKER ROD STRING EVALUATION (76)

The literature review resulted in the conclusion that only a Finite Element Analysis has the flexibility to consider all effects, occurring during sucker rod pumping. As a result a FEA is used for this thesis. The following section gives a short overview on the FEA basics.

5.2.1 FINITE ELEMENT METHOD - BASICS

The most flexible method for analyzing a sucker rod string is the Finite Element Method (FEM). In the following, a summary of the theory of the Finite Element Method is given. A detailed description can be found in the book of Bernd Klein (77), which is also the reference of the following section:

The finite element method is a very useful tool to analyze the behavior of structures as a result of external influences. The structure of the analyzed body is divided into finite elements. Each element possesses predefined properties. To describe the elastic-mechanical behavior of a body 15 equations are required. These 15 basic equations must be satisfied at each material point of the body. These equations are:

- 6 displacement-strain equations
- 6 strain-stress equations
- 3 equilibrium equations

Figure 54 shows the normal and shear stresses, acting on the surface of an element cube.

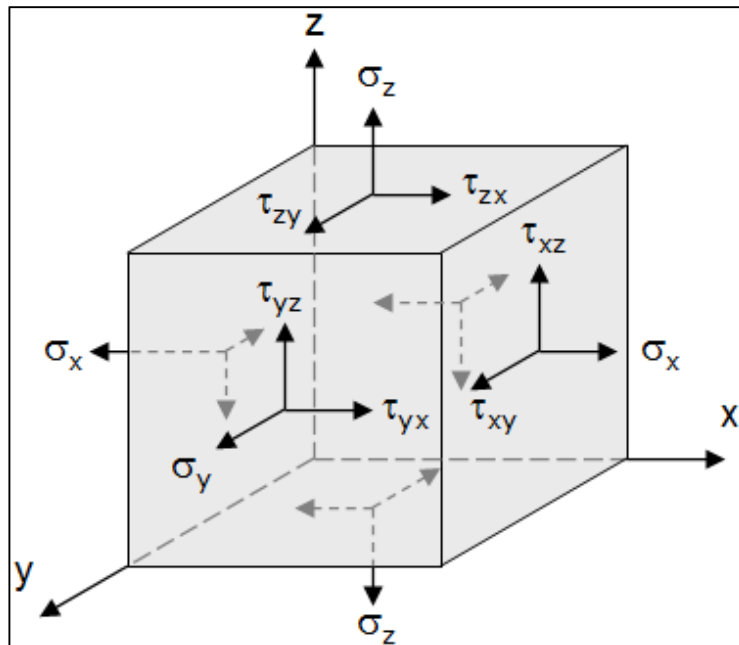


FIGURE 54: STRESSES ON AN ELEMENT CUBE (78)

In the 15 basic equations 15 unknowns characterize the mechanical behavior of the structure. The unknowns are:

- 3 displacements $\underline{u}^t = [u \ v \ w]$
- 6 strains $\underline{\epsilon}^t = [\epsilon_{xx} \ \epsilon_{yy} \ \epsilon_{zz} \ \gamma_{xy} \ \gamma_{yz} \ \gamma_{zx}]$
- 6 stresses $\underline{\sigma}^t = [\sigma_{xx} \ \sigma_{yy} \ \sigma_{zz} \ \tau_{xy} \ \tau_{yz} \ \tau_{zx}]$

Where the vector \underline{u} , with its components u , v and w , is the displacement in the corresponding directions x , y , and z . The vector $\underline{\epsilon}$ includes the strains and the vector $\underline{\sigma}$ the stresses in the element.

In Figure 55 the dependencies of the strains and the derivatives of the displacement can be seen easily.

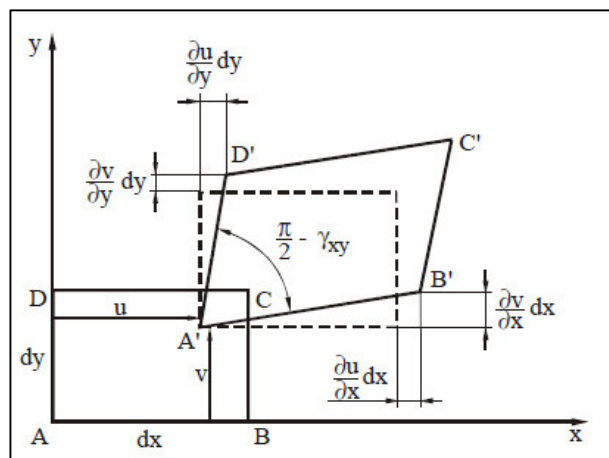


FIGURE 55: SLICE DISTORTIONS / DISPLACEMENTS (77)

By using this relationship the distortion vector can be expressed by the matrix D and the displacement vector \underline{u} :

$$\underline{\epsilon} = \begin{bmatrix} \epsilon_{xx} \\ \epsilon_{yy} \\ \epsilon_{zz} \\ \gamma_{xy} \\ \gamma_{yz} \\ \gamma_{zx} \end{bmatrix} = \begin{bmatrix} \frac{\partial}{\partial x} & 0 & 0 \\ 0 & \frac{\partial}{\partial y} & 0 \\ 0 & 0 & \frac{\partial}{\partial z} \\ \frac{\partial}{\partial y} & \frac{\partial}{\partial x} & 0 \\ 0 & \frac{\partial}{\partial z} & \frac{\partial}{\partial y} \\ \frac{\partial}{\partial z} & 0 & \frac{\partial}{\partial x} \end{bmatrix} \cdot \begin{bmatrix} u \\ v \\ w \end{bmatrix} = \underline{D} \cdot \underline{u} \tag{Eq. 40}$$

Applying Hooke's law (79), which describes a linear elastic material behavior, the strain is coupled with the stresses. For an isotropic material behavior it is sufficient to provide the module of elasticity E and the Poisson ratio ν .

$$\underline{\sigma} = \begin{bmatrix} \sigma_{xx} \\ \sigma_{yy} \\ \sigma_{zz} \\ \tau_{xy} \\ \tau_{yz} \\ \tau_{zx} \end{bmatrix} = \frac{E}{(1+\nu)(1-2\nu)} \begin{bmatrix} (1-\nu) & \nu & \nu & 0 & 0 & 0 \\ & (1-\nu) & \nu & 0 & 0 & 0 \\ & & (1-\nu) & 0 & 0 & 0 \\ & & & \frac{(1-2\nu)}{2} & 0 & 0 \\ & & & & \frac{(1-2\nu)}{2} & 0 \\ & \text{sym.} & & & & \frac{(1-2\nu)}{2} \end{bmatrix} \cdot \begin{bmatrix} \epsilon_{xx} \\ \epsilon_{yy} \\ \epsilon_{zz} \\ \gamma_{xy} \\ \gamma_{yz} \\ \gamma_{zx} \end{bmatrix} = \underline{E} \cdot \underline{\epsilon} \quad \text{Eq. 41}$$

To link the external forces to stresses, the three equilibrium equations are used. Figure 56 shows all stresses in the x-axis. The stresses in y and z - axis follow analogously.

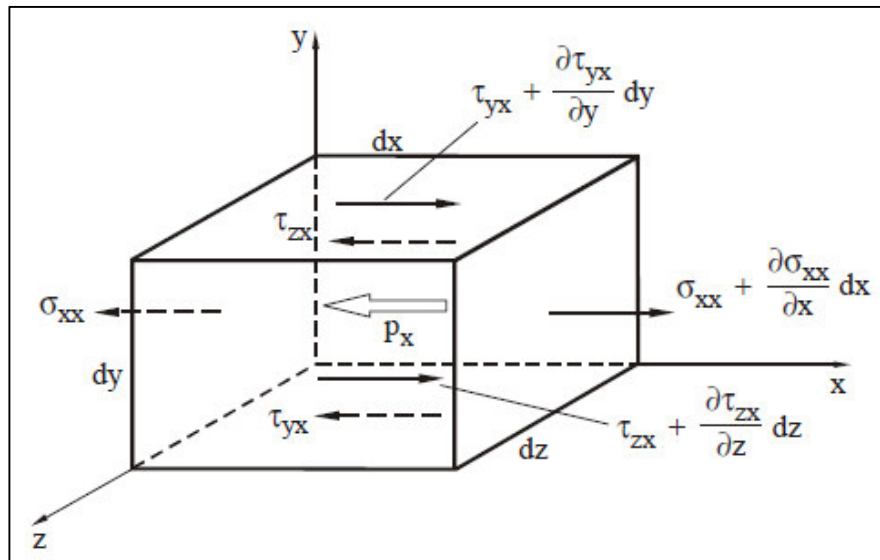


FIGURE 56: EXTERNAL AND BODY FORCES / X-AXIS (77)

For an element in balance, all the forces along the axes must be zero. The following equation demonstrates the force equilibrium in the x-direction, where p_x is the body force in x direction.

$$\sum K_x = 0: -\sigma_{xx} \cdot dy \cdot dz + \left(\sigma_{xx} + \frac{\partial \sigma_{xx}}{\partial x} dx \right) dy \cdot dz - \tau_{yx} \cdot dx \cdot dz + \left(\tau_{yx} + \frac{\partial \tau_{yx}}{\partial y} dy \right) dx \cdot dz - \tau_{zx} \cdot dx \cdot dy + \left(\tau_{zx} + \frac{\partial \tau_{zx}}{\partial z} dz \right) dx \cdot dy - p_x \cdot dx \cdot dy \cdot dz = 0$$

After simplification, the equations in x, y and z - axis become:

$$\frac{\partial \sigma_{xx}}{\partial x} + \frac{\partial \tau_{yx}}{\partial y} + \frac{\partial \tau_{zx}}{\partial z} - p_x = 0$$

$$\frac{\partial \sigma_{yy}}{\partial y} + \frac{\partial \tau_{xy}}{\partial x} + \frac{\partial \tau_{zy}}{\partial z} - p_y = 0$$

$$\frac{\partial \sigma_{zz}}{\partial z} + \frac{\partial \tau_{xz}}{\partial x} + \frac{\partial \tau_{yz}}{\partial y} - p_z = 0$$

Note that momentum equilibrium is satisfied due to the symmetry of the stress tensor. This equation can be expressed as:

$$\underline{\underline{D}}^t \cdot \underline{\underline{\sigma}} - \underline{\underline{p}} = \begin{bmatrix} \frac{\partial}{\partial x} & 0 & 0 & \frac{\partial}{\partial y} & 0 & \frac{\partial}{\partial z} \\ 0 & \frac{\partial}{\partial y} & 0 & \frac{\partial}{\partial x} & \frac{\partial}{\partial z} & 0 \\ 0 & 0 & \frac{\partial}{\partial z} & 0 & \frac{\partial}{\partial y} & \frac{\partial}{\partial x} \end{bmatrix} \cdot \begin{bmatrix} \sigma_{xx} \\ \sigma_{yy} \\ \sigma_{zz} \\ \tau_{xy} \\ \tau_{yz} \\ \tau_{zx} \end{bmatrix} - \begin{bmatrix} p_x \\ p_y \\ p_z \end{bmatrix} = \begin{bmatrix} 0 \\ 0 \\ 0 \end{bmatrix} \quad \text{Eq. 42}$$

In all cases where the forces are time dependent, also stresses, displacements and distortions will become time dependent - $u(x,y,z,t)$, $\epsilon(x,y,z,t)$, $\sigma(x,y,z,t)$. Additionally inertia effects ($-\rho \cdot \ddot{u}$) must be considered for a dynamic problem.

$$\underline{\underline{D}}^t \cdot \underline{\underline{\sigma}} - \underline{\underline{p}} = -\rho \cdot \ddot{\underline{\underline{u}}} \quad \text{Eq. 43}$$

The final equation, which must be solved for each element of the body, is:

$$\rho \cdot \ddot{\underline{\underline{u}}} + \underline{\underline{D}}^t \cdot \underline{\underline{E}} \cdot \underline{\underline{D}} \cdot \underline{\underline{u}} - \underline{\underline{p}} = \mathbf{0} \quad \text{EQ. 44}$$

Eq. 44 can be solved by approximating the displacement field inside an element by shape functions. Inserting these shape functions into the Galerkin (34) framework leads to a residue vector that must be minimized by adjusting the free coefficients of the shape function.

Applying this principle on the above described problem and with the matrix $\underline{\underline{G}}_t$ containing

$$\underline{\underline{u}} + \underline{\underline{D}}^t \cdot \underline{\underline{E}} \cdot \underline{\underline{D}} \cdot \underline{\underline{u}} - \underline{\underline{p}} = \mathbf{0} \quad \text{Eq. 44}$$

becomes:

$$\int_V \underline{\underline{G}}^t (\rho \cdot \ddot{\underline{\underline{u}}} + \underline{\underline{D}}^t \cdot \underline{\underline{E}} \cdot \underline{\underline{D}} \cdot \underline{\underline{u}} - \underline{\underline{p}}) dV = 0$$

Inserting known function approach $\underline{\underline{u}} = \underline{\underline{G}} \cdot \underline{\underline{d}}$ leads to

$$\int_V \underline{\underline{G}}^t \cdot \rho \cdot \underline{\underline{G}} \cdot dV \cdot \ddot{\underline{\underline{d}}} + \int_V (\underline{\underline{D}} \cdot \underline{\underline{G}})^t \cdot \underline{\underline{E}} \cdot (\underline{\underline{D}} \cdot \underline{\underline{G}}) \cdot dV \cdot \underline{\underline{d}} - \int_V \underline{\underline{G}}^t \cdot \underline{\underline{p}} \cdot dV = 0$$

this is equal to the vibration differential equation:

$$\underline{\underline{m}} \cdot \ddot{\underline{\underline{d}}} + \underline{\underline{k}} \cdot \underline{\underline{d}} - \underline{\underline{p}} = \mathbf{0} \quad \text{Eq. 45}$$

Eq. 45 shows the two most important matrices of the Finite Element Method, the mass matrix $\underline{\underline{m}}$ and the stiffness matrix $\underline{\underline{k}}$. The mass matrix $\underline{\underline{m}}$ is dependent on the elements' density and the shape functions.

The stiffness matrix is dependent on the shape functions, the material behavior and the relationship between distortion and displacement. $\underline{\hat{p}}$ is the external load vector.

$$\underline{\underline{m}} = \int_V \underline{\underline{G}}^t \cdot \rho \cdot \underline{\underline{G}} \cdot dV$$

$$\underline{\underline{k}} = \int_V \left(\underline{\underline{D}} \cdot \underline{\underline{G}} \right)^t \cdot \underline{\underline{E}} \cdot \left(\underline{\underline{D}} \cdot \underline{\underline{G}} \right) \cdot dV$$

The complete rod string is in such a case a composition of short beam elements. Additionally the tubing and the rod protectors can be considered as well. Any well trajectory can be simulated. It is possible to assign different parameters and forces to each element, which allows the highest flexibility. One disadvantage is a much higher calculation effort.

5.2.2 FINITE ELEMENT METHOD - APPLICATION

There are powerful software packages available that are working according to the Finite Element Method. Well known representatives are for example: (80)

- ABAQUS (62) from Assault Systems
- ANSYS from ANSYS Inc.
- NASTRAM from MSC Software

Due to the high flexibility of FEM software packages to analyze the sucker rod pumping system, their usage is obvious. In this specific case the ABAQUS software package is selected. Beside others the main reasons are its comfortable input file generation and handling and the perfect interaction with programming software for data analysis, presented later within this thesis.

5.3 FLUID FLOW BEHAVIOR IN THE TUBING

The flow regime of the oil, water and gas mixture in the tubing significantly influences the pumping system's behavior. The multiphase flow in conjunction with the dynamics of the sucker rod string and its components, like couplings and rod guides, must be analyzed in detail for the up- and downstroke.

During the upstroke the pumped fluid moves, dependent on the gas – oil ratio (GOR), more or less with the rod string upwards. During the downstroke some fluid is displaced by the rod string, hence fluid is flowing upwards and the rod string is moving downward. This additional restriction causes a pressure reduction and viscous drag in the fluid on one hand and friction forces on the sucker rod string on the other hand. Therefore the analysis is divided into two parts. In the first part the friction pressure drop, caused by the fluid flow is

evaluated. The second part concentrates on the friction force evaluation on the rod string by a numerical computational finite volume method.

5.3.1 MODELLING THE PRESSURE BEHAVIOR IN THE TUBING

A classical sucker rod pump not only produces fluid during the upstroke but also during the downstroke, caused by the displacement of the polished rod string in the tubing. If a tapered rod string is used, one has to distinguish between production at the pump plunger and production at the surface, because changes in rod diameter along the rod string cause an additional displacement during the downstroke. The actual production is dependent on the relationship plunger - to rod diameter, respectively polished rod diameter. Table 7 summarizes the relationship of up- to downstroke production under the assumption that there is only liquid in the tubing in percent of the total production.

Plunger size	Rod size	Polished rod size	Upstroke Production @ plunger	Downstroke Production @ plunger	Upstroke Production @ wellhead	Downstroke Production @ wellhead
1.5	3/4	1 1/8	75	25	44	56
	7/8	1 1/4	66	34	31	69
	1	1 1/2	56	44	0	100
1.75	3/4	1 1/8	82	18	59	41
	7/8	1 1/4	75	25	49	51
	1	1 1/2	67	33	27	73
2	3/4	1 1/8	86	14	68	32
	7/8	1 1/4	81	19	61	39
	1	1 1/2	75	25	44	56
2.25	3/4	1 1/8	89	11	75	25
	7/8	1 1/4	85	15	69	31
	1	1 1/2	80	20	56	44
2.5	3/4	1 1/8	91	9	80	20
	7/8	1 1/4	88	12	75	25
	1	1 1/2	84	16	64	36

TABLE 7: RELATIONSHIP UPSTROKE TO DOWNSTROKE PRODUCTION

Figure 57 shows the production ratio for up- and downstroke at the plunger. A value of 100 means the complete surface production is produced during the upstroke. It can be seen that for small plunger sizes (1,5" and 1,75") the upstroke production is between 55 and 80 per cent. With an increase in plunger size, the upstroke production ratio also increases toward 80 to 90 per cent, depending on the lowest rod size.

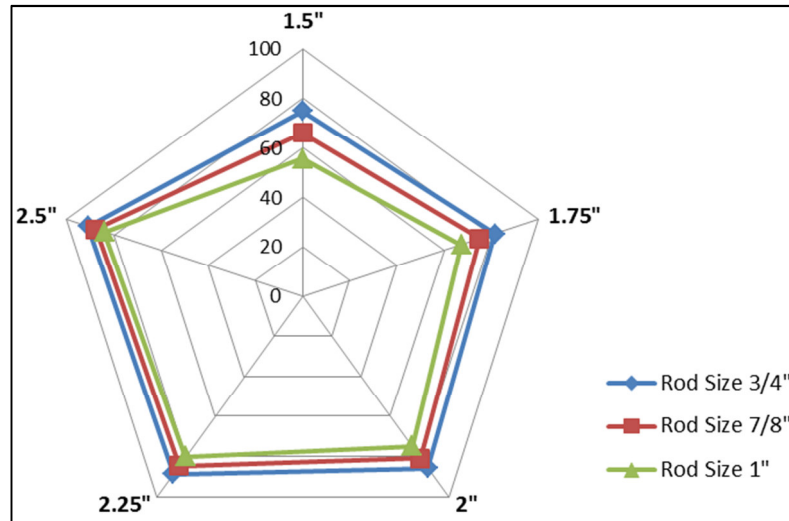


FIGURE 57: UP- AND DOWNSTROKE PRODUCTION AT THE PLUNGER

Normally the polished rod size is bigger than the thinnest rod's size, except sinker bars. As a result the upstroke production ratio decreases for increasing polished rod sizes. An extreme ratio can be seen for the 1,5" plunger and the 1 ½" polished rod. Theoretically there would not be any production during the upstroke, but only during the downstroke.

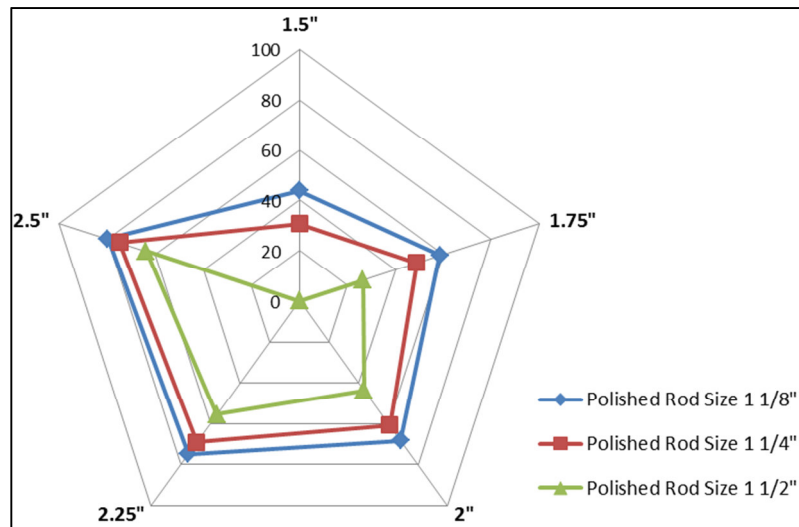


FIGURE 58: UP- AND DOWNSTROKE PRODUCTION AT THE WELLHEAD

In reality there is a certain amount of gas that is dissolved in the produced oil. Due to the fact that the rising gas disturbs the liquid flow by faster flowing and the elasticity of the column, it is assumed that the production is more or less the same for the up- and downstroke. By using this assumption, the commercial software PROSPER (81) can be used to approximate the vertical lift performance of the produced fluid.

Figure 59 presents the pressure traverse curves for Well OMV 1 for different GOR and a liquid rate of 17,8 m³/day. The essential point is that the higher the GOR, the lower the required pressure to lift the column to the surface, caused by a decrease in the overall density of the mixture.

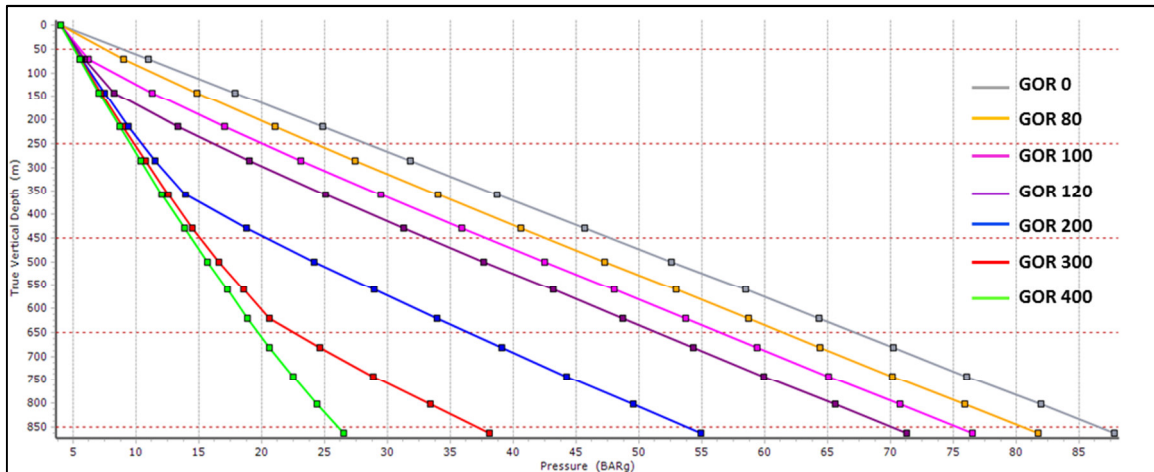


FIGURE 59: PRESSURE TRAVERSE CURVE FOR WELL OMV 1 AND DIFFERENT GOR'S

The second part of this section is about the viscous drag evaluation on the sucker rod string.

5.3.2 MODELLING THE VISCOUS DRAG ON THE SUCKER ROD STRING

The pumping process of a common sucker rod pump causes fluid flow during the upstroke and a small quantity of fluid flow during the downstroke. Due to the operation principle of sucker rod pumps, the production comes along with a relative motion of tubing against fluid and fluid against rods. This relative motion causes a viscous drag on the surfaces in the counter direction of the motion. The magnitude of the viscous drag depends on multiple parameters, like diameters, pumping speeds and fluid properties. Especially important are flow restrictions caused by rod couplings or rod guides. Despite the relatively low flow rate of sucker rod pumps in comparison to other pump types; these restrictions in diameter create a complicated, turbulent velocity profile in the tubing – rod annulus. In combination with the behavior of the oil – water mixture, no analytical method is able to accurately estimate viscous drag on the surfaces, yet. Hence the numerical computational fluid dynamics (CFD) simulation software Open Foam (82) is used.

The simulation consists of three parts:

- Mesh generation
- Property definition
- Problem solving

5.3.2.1 MESH GENERATION

The mesh is composed of finite volumes that represent the volume of the fluid in the tubing – rod annulus. Boundary conditions are defined for the volumes in contact with surfaces, respectively in- and outlet. To obtain accurate results it is not possible to model the complete length of the pumping system, hence only the length of one 24 ft sucker rod string is modelled and analyzed. In addition at the inlet the length is increased by 0,7 meters to overcome the turbulent behavior, caused by the fluid flow and its boundary condition. The model considers two protectors and one rod coupling at the bottom. Furthermore the axisymmetric model consists of a wedge of 5 degrees to reduce the simulation time, followed by a multiplication by 72 to get the full viscous drag values for the complete pipe.

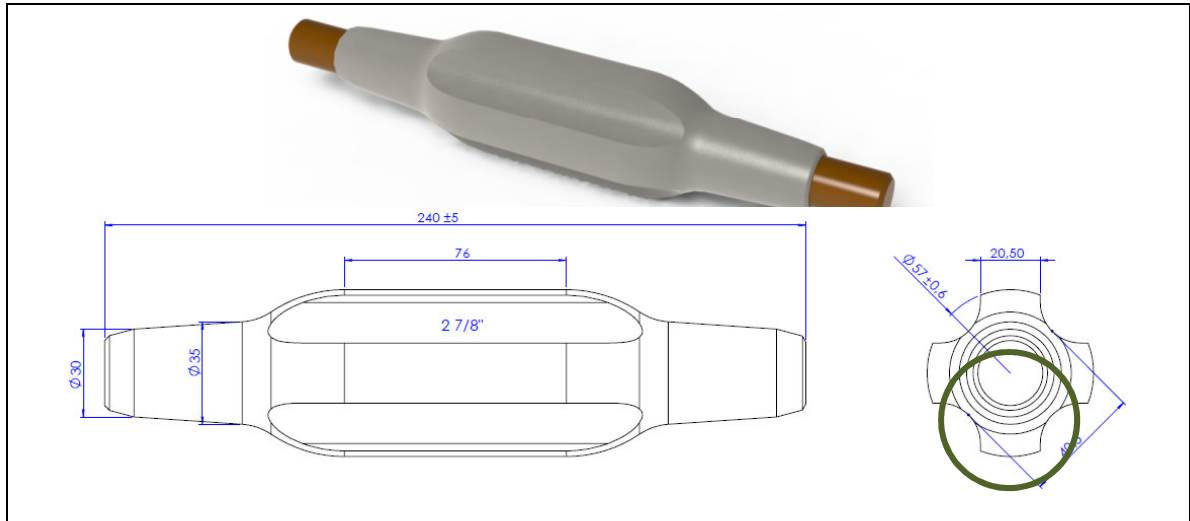


FIGURE 60: ROD GUIDE GEOMETRY (13)

Special attention must be paid to the rod guides. Figure 60 presents a three dimensional rod guide and the dimensions of a typical rod guide for a 2 7/8” tubing. The grooves for the oil flow cannot be modelled within this axisymmetric simulation. For the model the grooves are represented by a cylinder, where the cross-section for the liquid flow is equal to the original design. The green line in Figure 60 represents the equivalent cross-section. The size of rod guides depends on the tubing size. Values for different tubing sizes are represented by Table 8.

Rod Guides Size	Equivalent Diameter (mm)
2 3/8”	42,3 mm
2 7/8”	50,6 mm
3 1/2”	59 mm

TABLE 8: EQUIVALENT ROD GUIDE DIAMETER

Furthermore the rod guides are modelled with their distances presented in Figure 61.

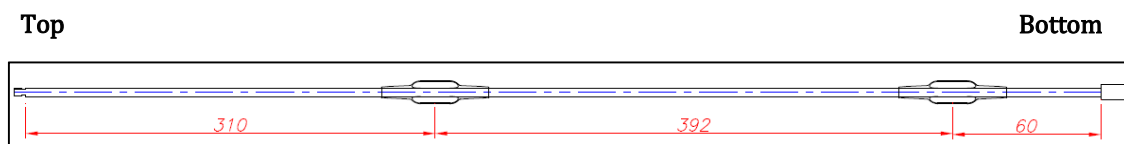


FIGURE 61: ROD GUIDE ASSEMBLY (13)

The information gained above is used to generate the mesh. This mesh has to be very fine where it is in contact with surfaces to obtain accurate shear forces, hence accurate viscous drag. Additionally in the region of the rod guides the mesh should be very fine scaled and smooth. The final mesh is shown in Figure 62 with details from the rod guides.

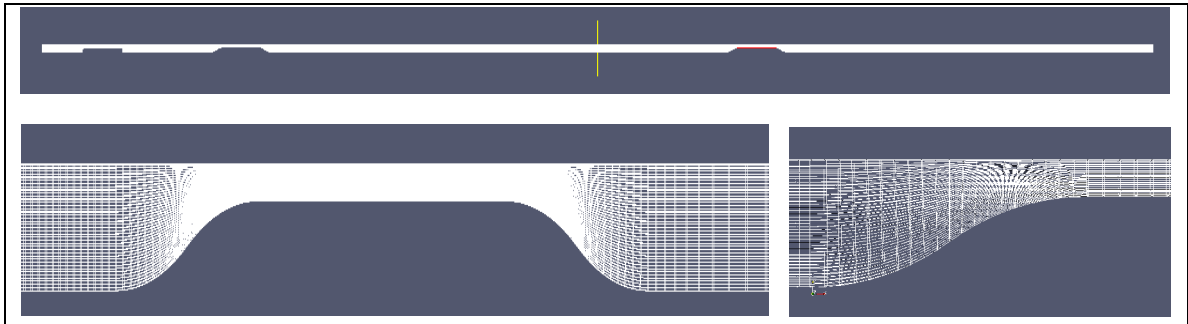


FIGURE 62: OPEN FOAM MESH / ROD GUIDE DETAIL

5.3.2.2 PROPERTY DEFINITION

Fluid flow simulations require the definition of fluid properties. The major influencing parameter is the fluid viscosity. Due to the fact that the pumped fluid in most cases consists of a mixture of oil, water and gas, the viscosity also is a composite variable out of these three single viscosities. Figure 63 shows the viscosity of oil under several temperature conditions (green), the viscosity of water (blue) and gas (red). It can be seen that water and gas viscosity remain more or less constant over a wide pressure and temperature range. Hence the mixture viscosity variation is mainly caused by the oil’s viscosity. The oil viscosity itself varies between 0,002 Pas and 0,07 Pas, but is in general depending on the oil composition, the pressure and temperature. The oil viscosity can be calculated, using the PROSPER software (81), which considers different viscosity models that are also accounting for temperature effects, or analytical approaches (83).

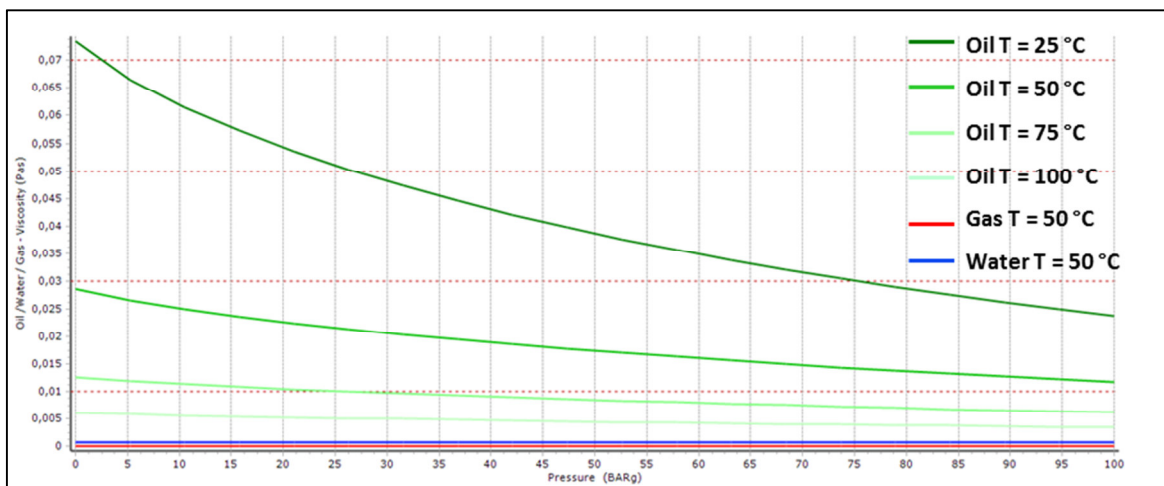


FIGURE 63: VISCOSITY OF OIL, WATER AND GAS

The simulation itself considers the mixture density from oil, gas and water, but the simulation itself only accounts for liquid flow.

5.3.2.3 PROBLEM SOLVING

For the solution of the problem, the so called Piso Foam – Solver (84) is used, which is a transient solver for incompressible flow. Its algorithm can be summed up by the following (85):

- *Solve the discretized momentum equation to compute an intermediate velocity field*
- *Compute the mass fluxes at the cell faces*
- *Solve the pressure equation*

The result is the velocity profile and the viscous drag on the surfaces, caused by the fluid flow. The result for a mixture viscosity of 5 mPas and 3 strokes per minute is shown in Figure 64. Surface roughness of the tubing causes additional turbulence. For the simulation the roughness of a new pipe is considered.

The red line represents the viscous drag at the rod surface, whereas the green line is the viscous drag on the tubing surface. As long as the fluid moves with the rod upwards, the viscous drag on the rods is small, but during the downstroke, the drag increases to 3 N per 24" sucker rod string. The viscous drag on the tubing surface during the upstroke is with a peak value of 5 N higher than the friction on the sucker rods.

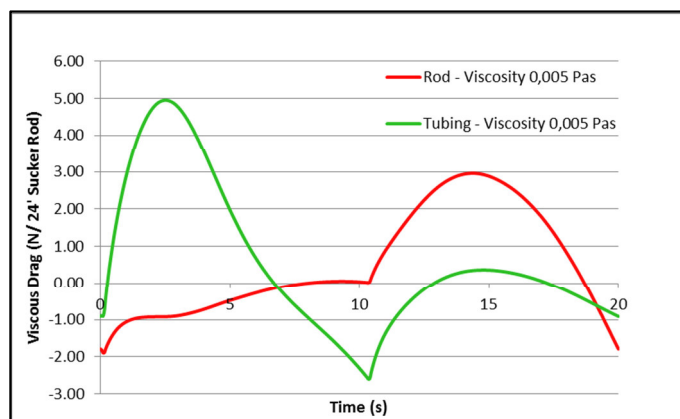


FIGURE 64: VISCIOUS DRAG FOR 0,005 Pas

A fluid drag simulation of the complete wellbore length is not possible due to very high simulation times. During the rise of the fluid column, the gas - oil ratio changes from low to high. The friction, caused by the fluid is much higher, than the friction caused by a single gas phase. Therefore on the one hand gas reduces the overall viscous drag, but on the other hand it disturbs the fluid flow which again increases the viscous drag. It is assumed that these effects balance themselves more or less and are therefore not considered in the viscous drag simulation.

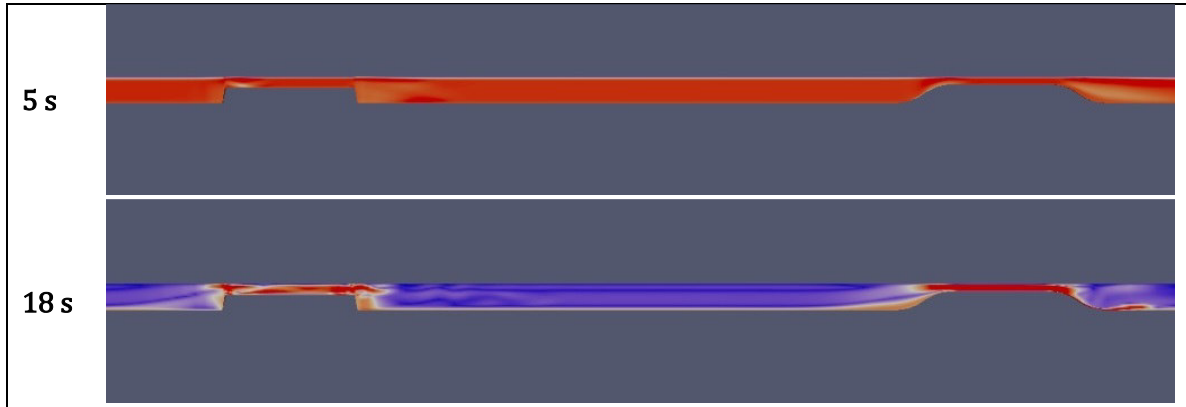


FIGURE 65: VISCOUS DRAG SIMULATION FOR 3 STROKES PER MINUTE

Figure 144 represents the visualized velocity profile after 5 s and 18 s for 3 strokes per minute (SPM). Blue areas represent slow flow velocities, whereas red areas indicate high flow velocities. The results of the simulation in one second intervals can be found in Appendix B. Red zones show the regions of high fluid velocities, hence larger shear rates and shear forces, whereas the blue regions represent areas of low flow rates. It can be identified that the influence of the rod couplings is at least as important as the influence of the rod guides.

The viscous drag simulation results are used for two applications. The rod friction is used in the sucker rod string simulation and increases the required surface load during the downstroke. The tubing friction must be overcome during the upstroke, which means that then an additional load occurs at the plunger.

5.3.2.4 SENSITIVITY ANALYSIS

The results presented above only represent one set of properties. In reality there are numerous influencing parameters. The most important are summarized in a sensitivity analysis:

- Mixture viscosity
- Tubing diameter in combination with the protector diameter
- Rod and coupling diameter
- Stroke length
- Strokes per minute

Each of those parameters is compared with the reference case: 0,005 Pas, 2 7/8" tubing, 7/8" rods, 144" stroke length and 6 SPM. Figure 66 presents the maximum friction force on the rod and the tubing for one complete stroke for the studied parameters. The biggest

influence on the friction force is caused by the viscosity, followed by the SPM, whereas the influences of the rod and tubing sizes appear to be of minor importance.

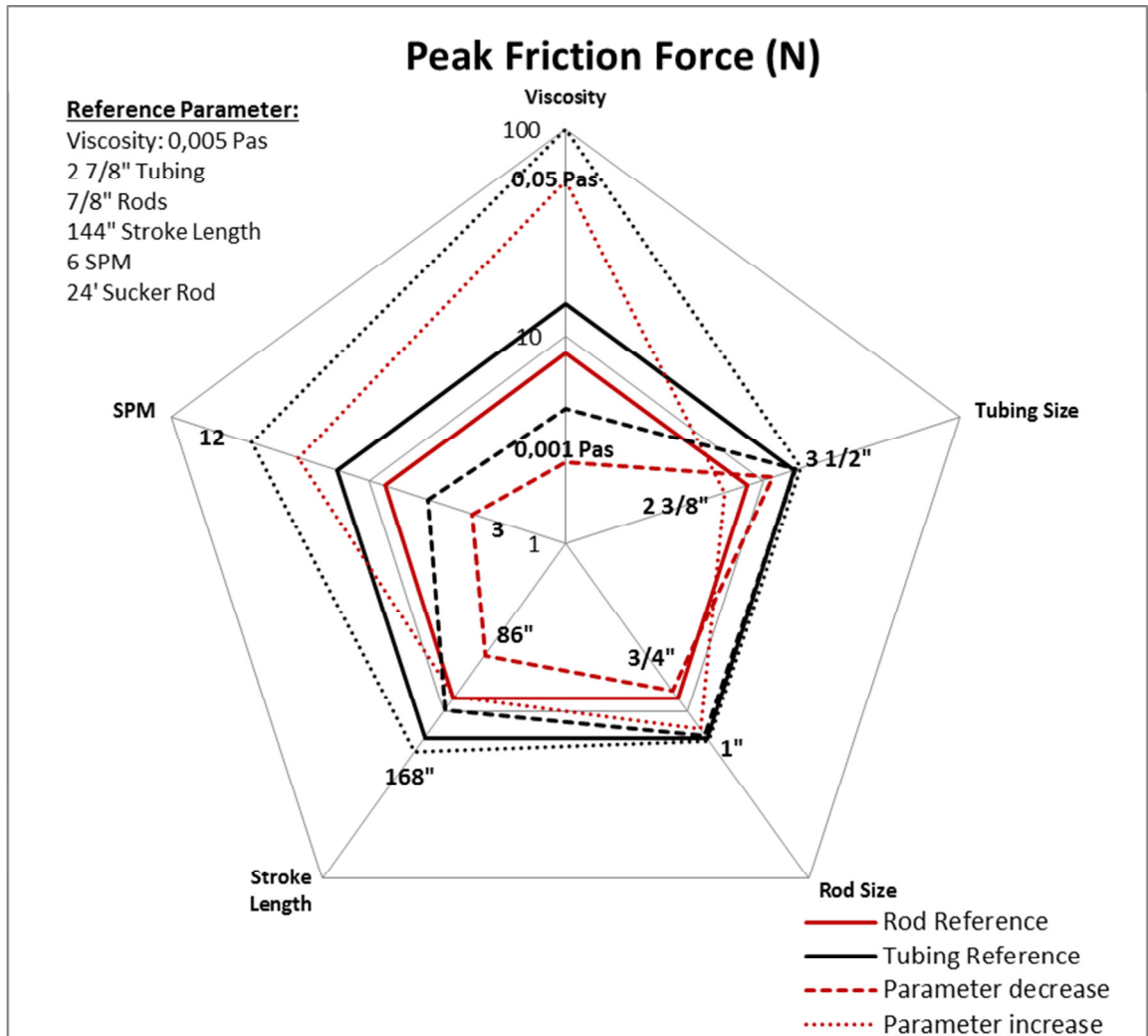


FIGURE 66: MAXIMUM FRICTION FORCE ON RODS AND TUBING / SENSITIVITY ANALYSIS

Appendix B presents the complete sensitivity study of all five parameters. To understand the potential impact of these data, the simulation results are compared with the publication “Total Downhole Friction from Dynamometer Analysis” from Scott W. Long et.al. (86)

This publication refers to pumping units from the Spraberry Field in Midland, Texas. The dynamometer cards of about 400 pumping units were analyzed and grouped by average polished rod velocity and plunger size. The average sucker rod string length for the published pumping units is about 7100 ft, hence about 300 pieces of 24” sucker rods. Finally the maximum total downhole friction for the 1,5” plungers is published with about 844 pounds or 3750N. Divided by 300 pieces of sucker rods gives a viscous drag of 12,5 N per 24” sucker rod. Compared to Figure 147 and depending on the rod size, the simulation is exactly within this range.

5.4 ROD GUIDE FRICTION COEFFICIENTS

Rod guides are made of synthetic substances and are injection molded at specific distances on the sucker rods. Depending on the expected operation conditions the number of rod protectors normally varies between one and four pieces per 24" sucker rod. Due to the relatively high costs of rod guides, some installations even do not use them. Figure 67 shows a typical 2 7/8" rod guide on a 7/8" sucker rod.



FIGURE 67: 2 7/8" - 7/8" ROD GUIDE

Within conventional applications rod guides have two objectives. On the one hand they are used to remove paraffin and waxes from the tubing walls. Therefore the spacing between two successive guides must be smaller than the stroke length to remove the paraffin deposits effectively and gapless. On the other hand rod guides are used to guide the sucker rods through the tubing, especially in deviated sections and protect the rods and the tubing from excessive friction and wear. Without rod guides the sucker rod string would rest, especially in deviated sections completely on the inner tubing surface. Each stroke would cause tubing to rod contact with friction and erosion, always at the same position, creating grooves, which are prone to break and leak. Finally, this would result in tubing leakages and rod fatigue (see Figure 68). Correctly designed rod guides separate the tubing from the sucker rods, except in regions where buckling occurs.



FIGURE 68: TUBING EROSION AND LEAKAGE CAUSED BY ROD GUIDES (87)

One very important parameter of the rod guides are their friction coefficient under different conditions. Detailed information about the friction coefficients, especially of different fluids, can hardly be found in the literature. Due to their absolute necessity in the sucker rod string analysis, friction coefficient experiments for understanding static and kinetic friction were performed. Five different conditions were observed:

- dry tubing
- water in the tubing
- oil in the tubing
- oil and formation sand in the tubing
- hot oil in tubing (only static experiments)

The Coulomb friction coefficient itself is calculated by dividing the required friction force through the applied normal force; hence it is theoretically completely independent on the contact surface size and the sliding velocity for evaluating the kinetic friction. In reality it is important to keep a constant velocity, because otherwise additional forces, like acceleration forces, will influence the results.

$$\mu = \frac{F_R}{F_N} \quad (88) \quad \text{Eq. 46}$$

For the experiments a one meter long, used 2 7/8" tubing was installed horizontally and the rod guides were pulled through the tubing. The friction force was measured during the experiments by a force measurement tool, with a range of 1 to 5000 N and an accuracy of 1 Newton.

In addition some of the rod guides have grooves to allow fluid flow during the downstroke of the pumping system. In theory the Coulomb friction coefficient is independent of the contact surface, but in reality there are significant differences for rod guides. As a result all tests were carried out for two different contact specifications – 0 degrees and 45 degrees.



FIGURE 69: 0° AND 45° ROD GUIDE ORIENTATION

The test results of the friction experiments are plotted in Figure 70 with their average values and standard deviations. The highest friction coefficients occur for pure oil in the tubing. The lowest friction coefficients can be achieved by having pure water in the tubing. In general the static friction coefficients are higher than the kinetic friction coefficients.

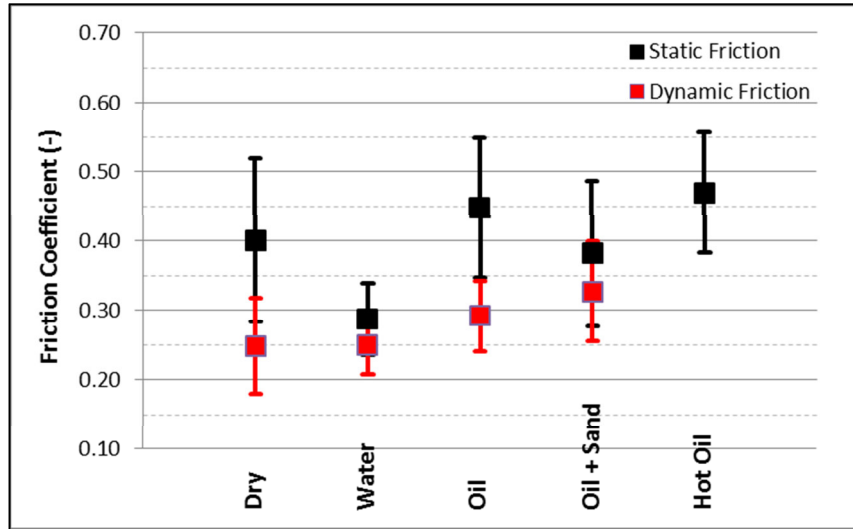


FIGURE 70: SUMMARY FRICTION COEFFICIENT EXPERIMENT

Glide tests were also executed by the company CANAM Pipe & Supply (89) and their results are presented in Table 9. One limitation of these results is that the influence of different fluids was not examined. Therefore only a comparison for the dry case is possible. Table 9 clearly indicates that the above presented results for the dry case show higher friction coefficients. One reason could be a different sliding speed or a different tubing composition. CANAM is specialized on Progressive Cavity Pumps. Those pumps might require other rod guide materials than Sucker Rod Pumps. Most likely the reason lies within the difference in the roughness of the used tubing.

Due to the differences the results define the range of the friction coefficients, but further measures have to be taken to obtain more accurate friction coefficients, which are very important for the rod string’s frictional behavior.

Glide Specifications			
Coefficient of Friction			
		Coefficient of Friction (a)	
Sliding Surface	Sliding Speed	Static	Kinetic
On Itself	2 in./min	0.35	0.25
On chrome-plated steel	2 in./min	0.23	0.17
On stainless steel	2 in./min	0.25	0.14
On cold-rolled steel	2 in./min	0.31	0.18
On brass	2 in./min	0.21	0.15

a) Coefficient of friction tests conducted on Instrumentors Slip-Peel tester, Model SP-101A

TABLE 9: FRICTION COEFFICIENTS / CANAM PIPE & SUPPLY (89)

5.5 BEHAVIOR OF THE PUMP PLUNGER

The pump plunger is installed at the lower end of the rod string. It moves up- and downward within a closely fitted pump barrel. The pump plunger supports the travelling valve and the fluid column in the tubing during the upstroke. During the downstroke, the pump plunger travels through the almost stationary fluid, kept in place by the standing valve (see Figure 73).

In general one can theoretically define the displacement over time and the load over time behavior at the pump plunger. The motion of the pump jack from the surface drives the polished rod, which transmits the motion along the sucker rod string to the plunger. Due to the elasticity of the rod string, the displacement that arrives at the pump plunger is not the same as at surface. It is phase shifted and is depending on the working conditions like SPM, friction and rod diameters, shorter or longer in its magnitude.

The load behavior at the pump plunger is the most important information in the analysis of the sucker rod pumping problem. It is the starting point for all the other loads in the pumping system. According to Gibbs (19) the mathematical description of the pump plunger load behavior is the greatest difficulty in the analytical treatment of the sucker rod pumping system. A strong restriction is that some loads are dependent on the motion of the pump plunger, hence acceleration, velocity and displacement, which are, as discussed above, very difficult to obtain, especially when using an analytical solution.

The theoretical background summarizing the downhole boundary condition within one equation has already been presented on page 19. In addition the following subchapter presents a practical mathematical model to develop the downhole load boundary condition as a function of the pump plunger motion, which is very useful if a numerical solution of the rod pump problem is used. Additionally the so generated load profile is compared with the results of the commercial RODSTAR software (90).

5.5.1 LOAD BEHAVIOR OF THE PUMP PLUNGER

The method presented by Gibbs is, when selecting appropriate shape functions, very flexible for a perfect working pump or gas interference. However in reality there are several additional conditions or parameters that may occur at the pump plunger right after pump installation, depending on design, operation- and fluid conditions. These significantly influence the plunger behavior, hence must be included to get an appropriate approximation. The conditions can be: fluid pound, an unanchored tubing string, excessive friction of the pump plunger and buoyancy.

“The shape of the downhole dynamometer card depends only on how the pressure changes inside the pump barrel.”(91) The most important behavior type is a so called “Full Pump”, which is explained in the following part. Other operating modes, like gas interference, fluid

pound, etc. are described in Appendix D. Another very useful explanation of the pump cards can be found in the publication of W.Gilbert (92) on page 98.

The ideal behavior at the pump plunger is a so called “Full Pump”, which excludes excessive friction and gas in the pump barrel. A full pump barrel and a constant liquid level in the annulus are assumed. The valve action is idealized; hence no valve opening and closing overlap, but immediate opening and closing of the valves occur.

Beginning at point D in the dynamometer card from Figure 71, the plunger is at its lowest position and both valves are closed. Then the plunger starts moving upwards and immediately the fluid load is transferred from the tubing string to the rod string, which results in a vertical line in the dynamometer card. Since the pressure above the plunger is dependent on the fluid in the tubing string and the tubing is assumed to be completely filled, the load on the pump plunger is more or less constant during the upstroke. At the uppermost position (point B) the behavior is vice versa. The load is immediately transferred from the rods to the tubing string and afterwards the load is assumed to be constant during the complete downstroke.

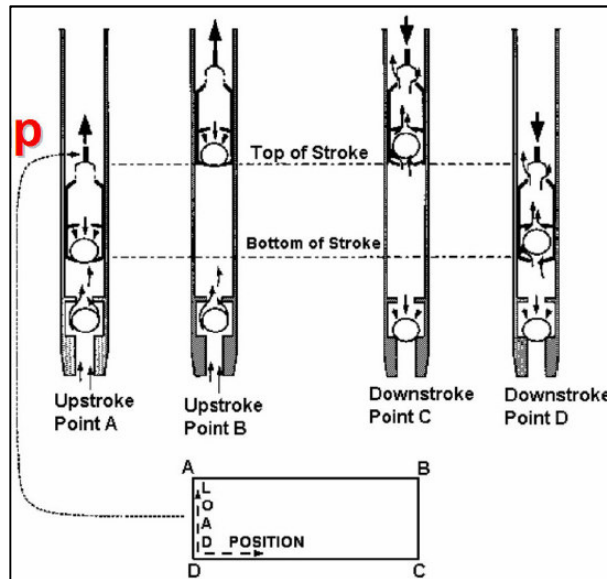


FIGURE 71: FULL PUMP – DYNAMOMETER CARD (91)

In addition to the above discussed operation modes, all rod pumped wells can generally be divided into two groups. The essential difference between these two groups is the effect of fluid inertia. Fluid inertia forces are caused by the acceleration of the pumped fluid during the up- and downstroke. The higher the acceleration and the higher the fluid mass, the higher are the resulting fluid inertia forces. One effect that smooths the magnitude of the actual acceleration, hence reducing the influence of fluid inertia is rod stretch. The higher the rod stretch, which increases with sucker rod string length, the lower is the influence of fluid inertia. As a result the fluid inertia effects are directly dependent on the length of the rod string and the weight of the pumped fluid column, thus the diameter of the plunger.

John G. Svinos distinguished the wells by the following characteristics: Ref (83), Page 223

Group 1	Group 2
Pump depth > 4000' & any plunger size Pump depth < 4000' & plunger size ≤ 2"	Pump depth < 4000' & plunger size > 2"
<u>Pump card depends on:</u> Only on pump conditions	<u>Pump card depends on:</u> Pump condition, pump depth, tubing size, plunger size, fluid compressibility, pumping speed

For group 1 wells the fluid inertia effects are of minor importance and there exists one downhole pump card shape for a full pump and all conditions can be derived from/based on this pump card shape. Group 2 wells are completely different. "... group 2 wells are significantly affected by fluid inertia effects, their downhole dynamometer cards are never the same. Even for a full pump, the downhole dynamometer card will be very different from well to well and depends on several variables ..." Ref (91), Page 249

Figure 72 shows a surface and downhole dynamometer card for a typical group 2 well. Especially important are the two peaks, caused by stress wave reflections. They vary in magnitude and position, depending on operation conditions, which makes predictions of group 2 wells more complicated.

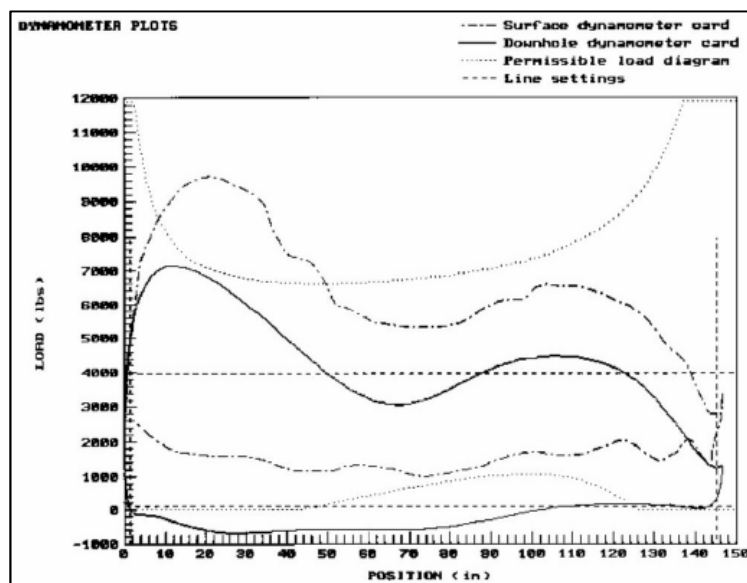


FIGURE 72: GROUP 2 DYNAMOMETER CARD (91)

5.5.1.1 FORCES AT THE PLUNGER

Designing an accurate, artificial downhole dynamometer card for certain pump conditions, requires an investigation of all forces, acting on the pump plunger in more detail than presented in Reference (19). A detailed analysis must be performed, especially for the up- and downstroke, because these sections define the maximum and minimum forces. The transitions between up- and downstroke, which represent the opening and closing of the valves, are considered thereafter.

Before a detailed force analysis at the plunger can be performed, the components of the pump, which include pump plunger, pump barrel, etc., must be discussed. A very detailed description of all pump components can be found in the API Specification 11AX, Specification for Subsurface Sucker Rod Pumps and Fittings (93).

The following part shows the components of a top anchored, heavy wall insert pump (RHA), which means a top anchored, heavy wall, stationary barrel insert pump.

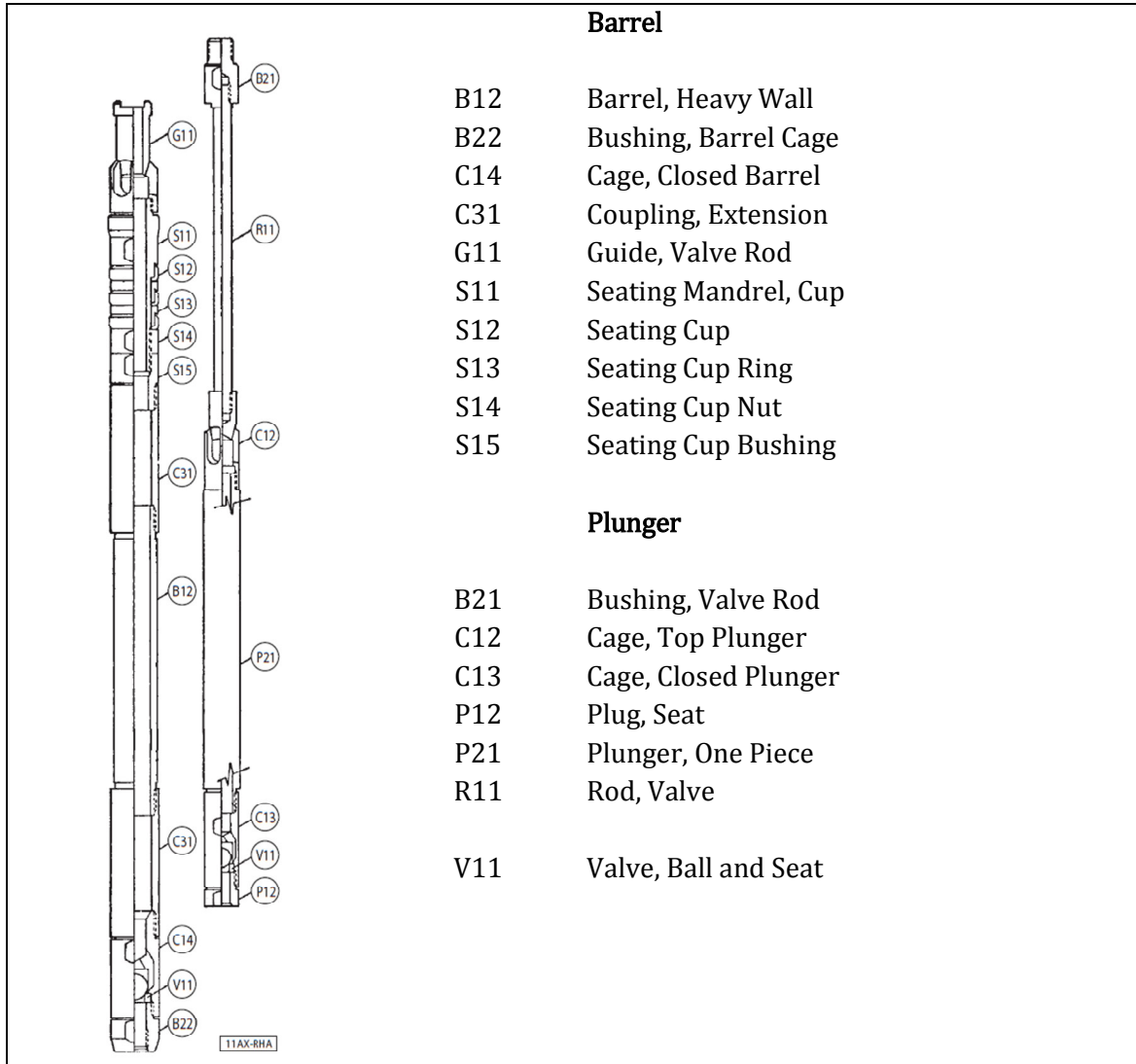


FIGURE 73: PUMP COMPONENTS (93)

The pump plunger defines the moving weight of the downhole pump itself. Its length varies with installation depth and is between 3 and 6 feet. Another important part is the pump barrel (B12). The difference in diameter of pump barrel and pump plunger is called clearance and influences the viscous fluid friction. Its magnitude should be larger than the biggest solid particles in the pumped fluid to prevent excessive wear and abrasion. Of course, the clearance must be small enough to prevent high slippage rates, which reduces production. Slippage is dependent on clearance and additionally on the differential pressure across the plunger. As a result for deeper installations, longer plungers are selected.

Figure 74 shows a schematic sketch of all forces, acting on the plunger during the downstroke. Basically these forces can be divided into three groups:

- Motion independent forces (Coulomb friction, hydrostatic pressure forces, etc.)
- Velocity dependent forces (fluid friction, pressure losses, etc.)
- Acceleration dependent forces (plunger inertia force, fluid inertia force, etc.)

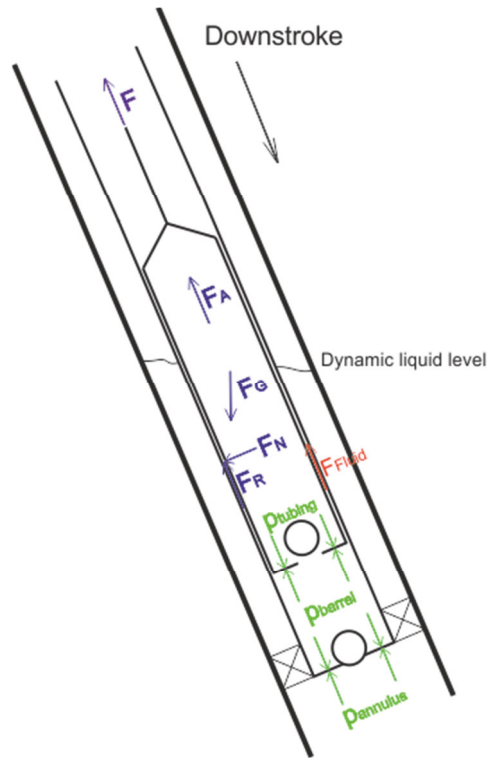


FIGURE 74: FORCES AT THE PLUNGER

5.5.1.1.1 MOTION INDEPENDENT FORCES

This type of forces consist of static forces and forces that occur as a result of the plunger's motion, but its terms are independent on velocity or acceleration (e.g. Coulomb friction)

- Plunger weight: F_p

The plunger weight is a result the plunger's mass and the inclination of the wellbore at the pump installation depth. In a vertical well this force represents the full weight of the plunger m_p . In deviated wellbores the plunger weight is multiplied by the cosine of the inclination.

$$F_p = m_p \cdot g \cdot \cos(\alpha)$$

Eq. 47

- Coulomb friction force: F_R

The Coulomb friction force is a result of the metal to metal contact of the plunger to the barrel. The Coulomb friction force is calculated by the force normal to the observed contact surface and the friction coefficient. The friction is dependent on the surface roughness and the media in the gap between the two surfaces; hence the friction coefficient is different, if water, oil or paraffin is in the gap. The direction of the Coulomb friction force is always in the direction opposite to the motion.

$$F_R = m_p \cdot g \cdot \sin(\alpha) \cdot \mu \quad \text{Eq. 48}$$

- Tubing pressure: F_{tbg}

The tubing pressure is the result of the pressure, required for lifting the liquid – gas mixture in the tubing to the surface and the back pressure at the wellhead p_{wh} . Beside friction pressure losses in the tubing, which are highly dependent on velocity and the mixture properties, the hydrostatic weight of the column has the major influence.

Depending on the pressure regime and the pumped fluid properties, during the lifting process bound gas becomes liberated, which lowers the density of the mixture and reduces the tubing pressure that acts on the plunger.

For known fluid properties, where the gas content is of special importance, the pressure regime of the multiphase mixture can be approximated by using the commercial software PROSPER from Petroleum Experts. The tubing pressure p_{tbg} gives when multiplying with the plunger cross-section A_{plunger} , the load F_{tbg} . This load acts on the plunger during upstroke. During the downstroke this pressure acts as buoyancy effect on the rod's diameter and causes compression of the rod string.

$$F_{\text{tbg}} = p_{\text{tbg}} \cdot A_{\text{plunger}} \quad \text{Eq. 49}$$

- Annulus pressure: F_{csg}

The annulus pressure is a result of the fluid / gas column in the tubing – casing annulus and the casing head pressure. It assists in lifting the pumped mixture, but only during the upstroke. During the downstroke the standing valve is closed and the annulus pressure does not come in contact with the plunger, hence there is no influence of the annulus pressure on the plunger behavior during the downstroke.

$$F_{\text{csg}} = p_{\text{annulus}} \cdot A_{\text{plunger}} \quad \text{Eq. 50}$$

5.5.1.1.2 VELOCITY DEPENDENT FORCES

This type of forces is dependent on the velocity of the system, like fluid friction forces and pressure losses through restrictions.

- Valve flow pressure drop: F_{valve}

The working procedure is based on two valves that are alternately opened and closed during up- and downstroke. The valves itself generate restrictions on the fluid flow.

Within the pumping procedure the pumped fluid is pushed through the standing valve during the upstroke and the travelling valve during the downstroke. In addition the

fluid must pass through the plunger with reduced diameter during the downstroke, which cause an additional pressure drop.

So the complete pressure drop through the valves is the sum of the orifice pressure drop, the pressure drop through the ball valve and for the downstroke the friction pressure drop, caused by the flow through the plunger. The following models are for liquid flow only. Models that account for two phase flow become very complicated, hence single phase flow only is considered, which is valid for full pump conditions. Valve flow pressure drops are of minor importance, thus the overall error stays small.

Orifice pressure drop:

The pressure drop, cause by the orifice is dependent on the diameter restriction, the flow velocity and a so called discharge coefficient C_D , which is geometry and pressure dependent.

Head, m	Diameter of circular orifices, cm						
	0.5	1.0	2.0	5.0	10.0	15.0	30.0
0.1		0.642	0.627	0.606			
0.2	0.657	0.637	0.618	0.604	0.598	0.595	
0.3	0.648	0.630	0.613	0.603	0.598	0.596	0.591
0.4	0.643	0.627	0.611	0.601	0.598	0.597	0.592
0.5	0.638	0.623	0.608	0.601	0.599	0.597	0.594
1	0.629	0.616	0.604	0.600	0.599	0.598	0.597
2	0.619	0.610	0.602	0.599	0.598	0.597	0.596
3	0.612	0.606	0.599	0.597	0.597	0.596	0.595
4	0.609	0.604	0.599	0.597	0.596	0.596	0.595
5	0.606	0.603	0.598	0.596	0.596	0.596	0.594
10	0.599	0.598	0.596	0.595	0.595	0.595	0.594
20	0.595	0.594	0.593	0.593	0.593	0.593	0.593
30	0.593	0.592	0.592	0.592	0.592	0.592	0.592

TABLE 10: SMITH'S COEFFICIENTS OF DISCHARGE FOR CIRCULAR ORIFICES WITH FULL CONTRACTION (94)

According to reference (95) and (96) the pressure drop, caused by a stationary orifice flow can be approximated by

$$\Delta p_{\text{orifice}} = \frac{\rho}{2} \cdot \left(\frac{v_{\text{orifice}}}{C_D} \right)^2 \cdot \left(1 - \frac{d_{\text{orifice}}^4}{d_{\text{plunger}}^4} \right) \tag{Eq. 51}$$

Ball valve pressure drop:

The pressure drop, caused by the ball valve, can be seen as single restriction; hence it can be calculated by

$$\Delta p_{\text{ball valve}} = \xi \cdot \frac{\rho}{2} \cdot v_{\text{orifice}}^2 \tag{Eq. 52}$$

ξ represents the flow restriction coefficient and is dependent on the type of valve.

Part / Diameter (mm)	10 -15	20 - 25	32 - 40	> 50
Slide valve	1	0,5	0,3	0,3
Globe valve	10	7	5	4
Angel seat valve	3,5	3	2,5	2

Angle valve	4	2	2	1,5
Check valve	5	4	4	3,5
No return flap	2	1,5	1,2	1

TABLE 11: FLOW RESTRICTION COEFFICIENTS (97)

Flow through the plunger:

The pressure drop, caused by the flow of the fluid through the plunger, can simply be calculated by using the pipe friction and the Moody diagram. In the first step the flow regime is selected by using the Reynolds number ($Re = \frac{v_{orifice} \cdot d_{orifice} \cdot \rho}{\mu}$) as criterion (98). Laminar flow occurs for Reynolds numbers less than 2100. For larger numbers transition or turbulent flow occurs. In this case the friction coefficient is selected from Figure 75 in dependency of the relative pipe roughness. Finally the pressure drop can be approximated by

$$\Delta p_{plunger} = \frac{f \rho v_{orifice}^2}{2d} \cdot l_{plunger} \tag{Eq. 53}$$

Where f is the friction coefficient, $\Delta p_{plunger}$ the friction pressure loss through the plunger and $l_{plunger}$ the plunger's length.

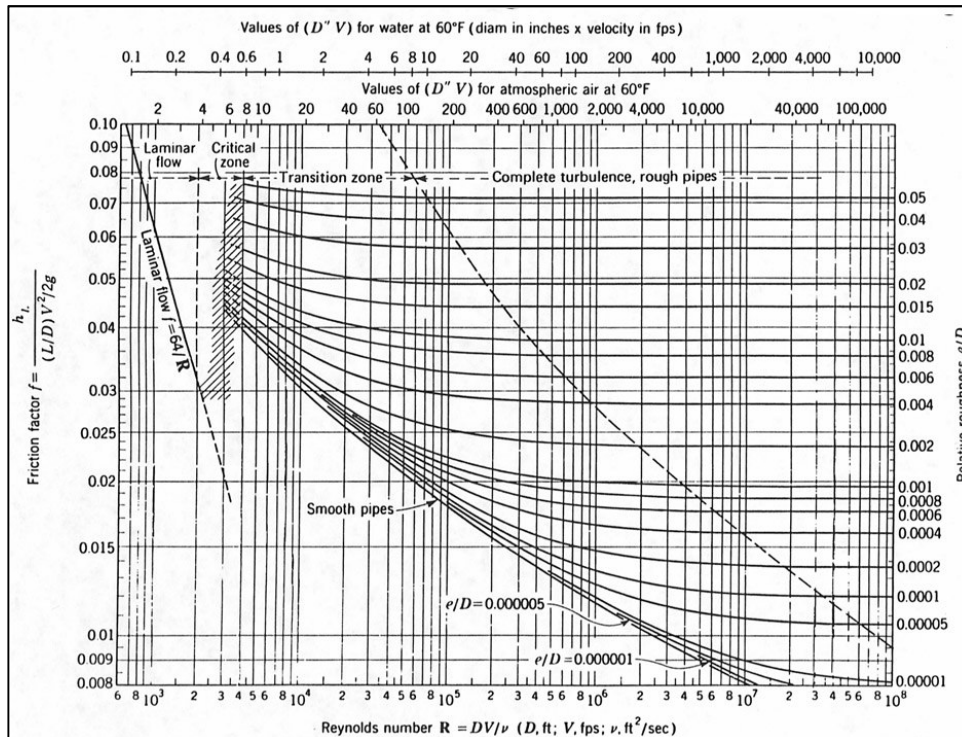


FIGURE 75: MOODY DIAGRAM (99)

The resulting pressure drop is multiplied with the plunger cross-section and gives an additional force to be considered during up- and downstroke. Depending on the orifice diameter, fluid flow rate and the fluid properties, the resulting restriction force can be calculated. Typical values can be seen in Figure 76.

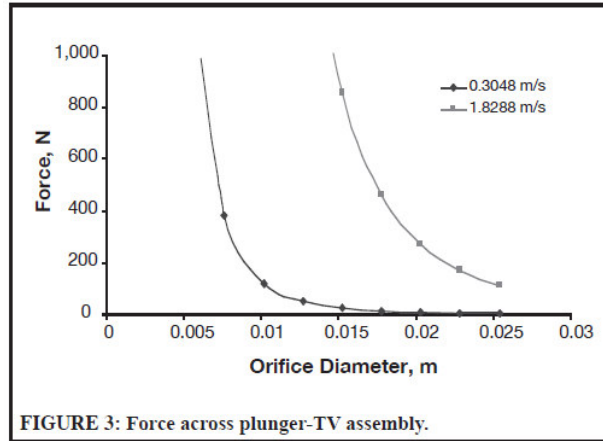


FIGURE 3: Force across plunger-TV assembly.

FIGURE 76: FORCE ACROSS VALVE (100)

- Viscous friction force: F_{viscous}
 The clearance between plunger and barrel is filled with fluid. Due to the relative motion of the plunger to the barrel, a velocity field is generated, which causes fluid friction. Although some fluid is flowing downward through the gap during the upstroke, which is called slippage, the resulting friction force is also in downward direction, because the influence of the upward moving plunger dominates the frictional behavior. For the downstroke the fluid in the gap moves with the plunger downward. The corresponding flow profile can be seen in Figure 77.

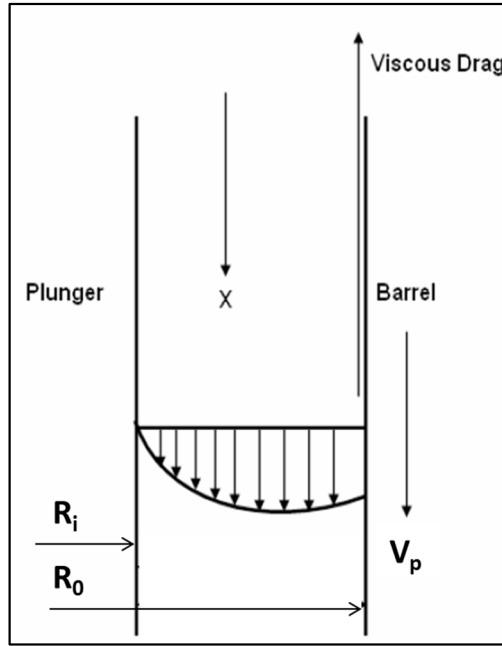


FIGURE 77: VISCIOUS FRICTION PLUNGER / VELOCITY PROFILE (100)

The resulting friction force F_{viscous} , also called viscous drag force, is based on the shear stress on the plunger surface.

$$F_{\text{viscous}} = 2\pi \cdot \tau \cdot R_i \cdot L \tag{Eq. 54}$$

with:

$$\tau = \left[-\frac{R_i \Delta p}{2} + \frac{\Delta p R_i^2}{4r \ln\left(\frac{R_i}{R_0}\right)} - \frac{\Delta p R_0^2}{4r \ln\left(\frac{R_i}{R_0}\right)} + v_p \frac{\mu}{r \ln\left(\frac{R_i}{R_0}\right)} \right] \tag{Eq. 55}$$

Where τ is the shear stress along the plunger surface, Δp is the pressure difference across the plunger, R_i is the plunger outside diameter, R_0 is the barrel inside diameter and v_p is the plunger velocity.

A closer look on $F_{\text{viscous}} = 2\pi \cdot \tau \cdot R_i \cdot L$

Eq. 54 shows that the friction force is highly dependent on the plunger velocity (see Figure 78), the fluid viscosity and the clearance between plunger and barrel.

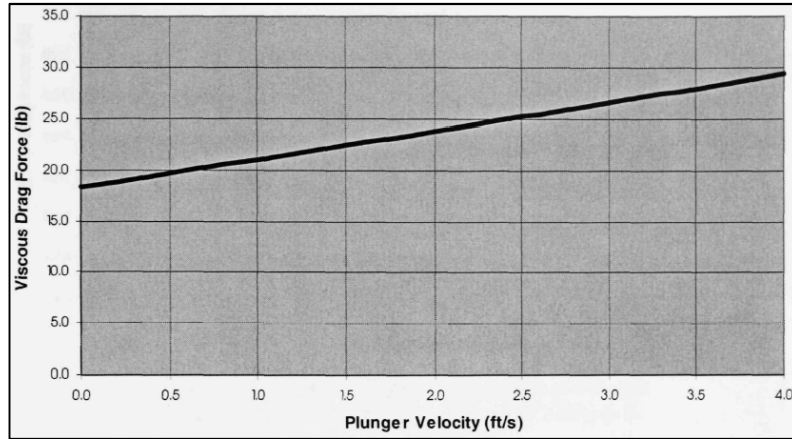


FIGURE 78: VISCOUS FRICTION FORCE AS A FUNCTION OF PLUNGER VELOCITY, A CLEARANCE OF 0.003", 3' PLUNGER LENGTH AND A VISCOSITY OF 7CP (101)

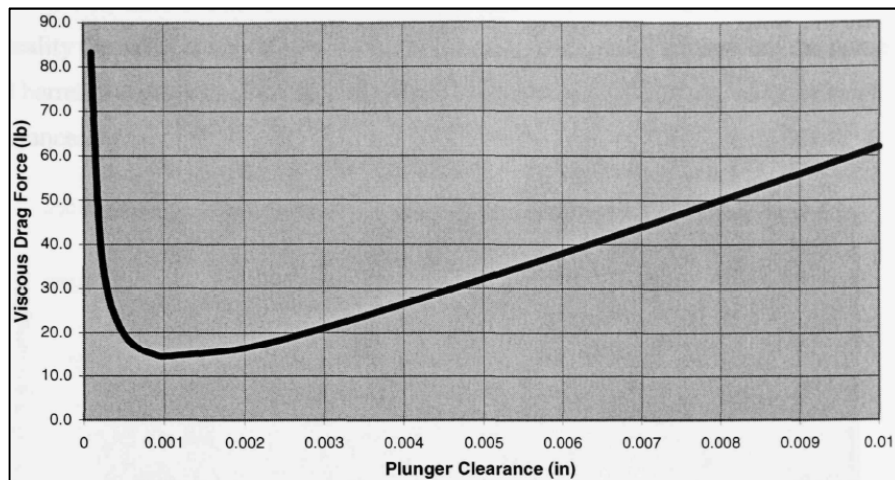


FIGURE 79: VISCOUS FRICTION FORCE AS A FUNCTION OF PLUNGER CLEARANCE (101)

Figure 79 presents the viscous drag force over plunger clearance. A large clearance causes a high liquid rate through the gap. As a result high velocity gradients occur, causing increasing viscous drag forces. Decreasing plunger clearance reduces the liquid rate through the gap drastically, causing also large velocity gradients, as a result of the narrow distance. Hence there is a plunger clearance, causing a minimum viscous drag force (see Figure 79)

- Viscous drag on the tubing walls: $F_{t \text{ drag}}$
 During the upstroke of the pump, there is a relative velocity between the pumped fluid and the inner tubing surface. A relative motion of fluids causes shear forces, which would theoretically cause an additional rod load during the upstroke. In reality the influence of free gas in the tubing and the fact that production also occurs during the downstroke disturb this effect and reduce this influence.

5.5.1.1.3 ACCELERATION DEPENDENT FORCES

This type of forces is dependent on the acceleration of the system, like mass inertia forces.

- Plunger inertia force: $F_{A,p}$

The plunger inertia force is a result of the acceleration of the plunger and acts in the opposite direction of the acceleration.

$$F_{A,p} = -m_p \cdot \frac{\partial z^2}{\partial t^2} @ \text{plunger} \quad \text{Eq. 56}$$

- Fluid inertia force: $F_{A,f}$

This type of force is especially important for group 2 wells. It considers the force, required to accelerate and decelerate the whole fluid column in the tubing, mainly during the upstroke, thus the average density ρ_m of the fluid column has a huge impact on the magnitude of the force.

$$F_{A,f} = -\rho_m \cdot \text{TVD} \cdot \frac{\partial z^2}{\partial t^2} @ \text{plunger} \quad \text{Eq. 57}$$

All of the above described effects are used to describe the minimum and maximum loads of the pumping cycle. The next step is to take a closer look on the transition zones between up- and downstroke of a typical full pump card. These phases of a pumping cycle are dominated by the opening and closing of the standing- and travelling valve. Theoretically these phases are straight, vertical lines in the dynamometer plot. In reality the opening and closing of the valves is not immediate as plunger direction changes because a certain amount of time is required for the process. The shape of the dynamometer card differs between up- and downstroke, which can be seen in Figure 80.

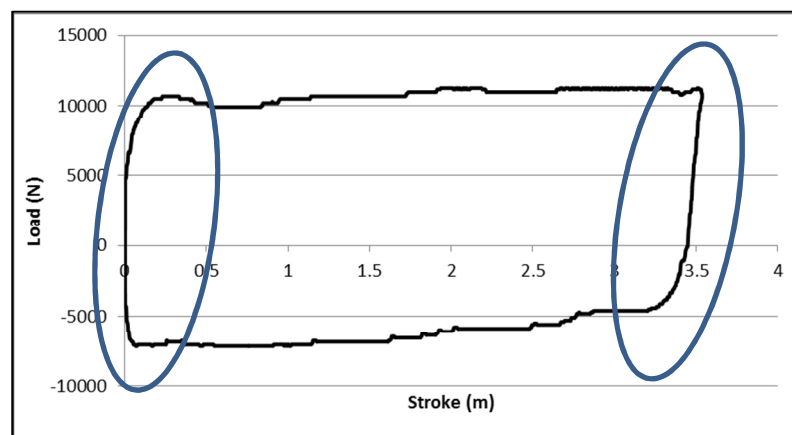


FIGURE 80: TYPICAL DOWNHOLE DYNAMOMETER CARD GENERATED BY RODSTAR

As discussed in chapter 4 the pumping cycle can be broke down into four sections: upstroke, downstroke, transition from downstroke to upstroke and transition from upstroke to downstroke

The load behavior during the up- and downstroke has been discussed extensively in the previous part. At the transition from up- to downstroke and contrariwise the load cannot be transferred immediately, because the valves have to open and close, which takes a while.

5.5.1.1.4 *UPSTROKE*

For the upstroke, the travelling valve is closed, whereas the standing valve is opened. The fluid load is steadily transferred from the tubing string to the rod string. To get a model that is able to represent the real behavior appropriately, the results of multiple real dynamometer card analysis, provided by the industry, are used. Therefore the analyzed data are normalized in a way that the load is between -2000N and 8000N and the stroke length is normalized to 1 meter, as a result of the fact that the measured dynamometer cards belonged

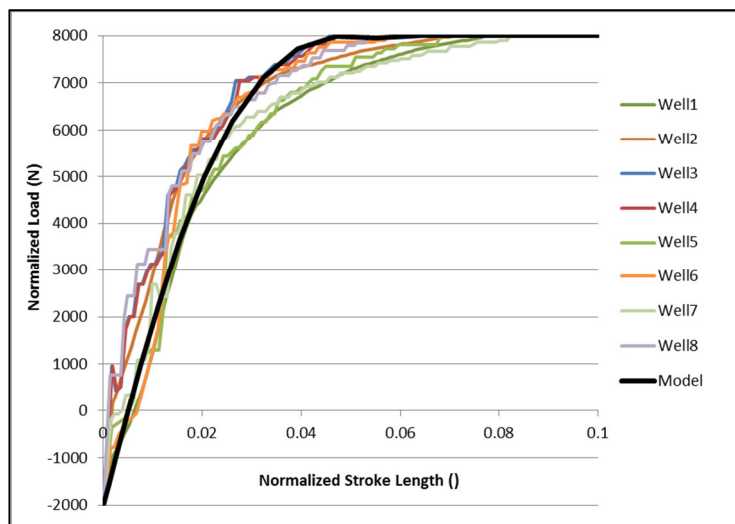


FIGURE 81: VALVE BEHAVIOUR UPSTROKE

Figure 81 shows 8 results of a dynamometer card analysis. The tendency of all eight downhole dynamometers is pretty similar. At the beginning the load change from the tubing string to the rod string goes fast. This phase is followed by a smooth transition to the maximum load. The whole procedure takes about 5 percent of the total stroke length. The exact behavior depends on the wear of the valve and seat as well on the pumped fluid.

The black line represents the result of the designed, empirical model. This model is dependent on minimum and maximum load, as well as the distance to the bottom dead center and the preselected closing distance z_{close} of about 5 percent of the total stroke length.

At the beginning the relative displacement is calculated by:

$$z_{rel} = \frac{z-z(t_1)}{z_{close}} \tag{Eq. 58}$$

At the final step, the actual load $F(t)$ is derived by:

$$F(t) = F(t_1) + [F(t_2) - F(t_1)] \cdot \frac{z}{z_{rel} + \frac{1}{z_{rel}}} \tag{Eq. 59}$$

5.5.1.1.5 DOWNSTROKE

At the transition from the upstroke to the downstroke, the standing valve closes and the travelling valve opens. The fluid load is steadily transferred from the rod string to the tubing string. Due to the fact that the final downhole dynamometer card model should only consider full pumps, no additional effects like gas compression or fluid pound must be considered. The procedure for obtaining the model is basically the same as for the upstroke model. Analyzed downhole dynamometer cards are compared in a normalized plot and the model is matched.

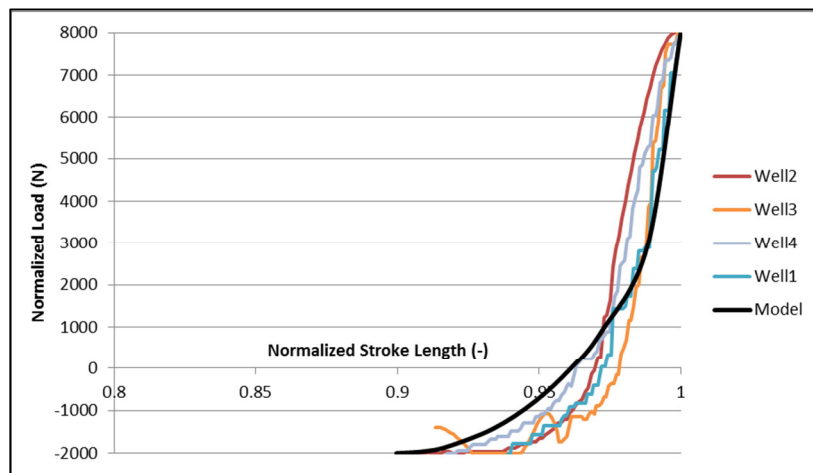


FIGURE 82: VALVE BEHAVIOUR DOWNSTROKE

For the downstroke the z_{close} was detected at about 10 percent of the total stroke length.

$$z_{rel} = \frac{z(t_3)-z}{z_{close}} \tag{Eq. 60}$$

The load is derived by the following equation:

$$F(t) = F(t_3) + [F(t_3) - F(t_2)] \cdot \sin\left(z_{rel} \cdot \frac{\pi}{2}\right)^{\frac{1}{2,5}} \tag{Eq. 61}$$

At the end of this subchapter a complete dynamometer card is artificially generated and a sensitivity analysis is performed for the most influential parameters.

The artificial downhole dynamometer card presented below is generated for a Well OMV 1, which is equipped with a 1,75" insert pump installed at a measured depth of 893 meters with a final inclination of about 25 degrees. The true vertical depth is 877 meters. The pump plunger is connected to a 7/8" sucker rod string. The pump runs with 3,13 strokes per minute and delivers 17,8 m³ of oil per day with a GOR of about 100 m³/sm³ and a water cut (WC) of 85%..

Further data are:

$p_{\text{well head}} = 4 \text{ bar}$	$p_{\text{casing head}} = 4 \text{ bar}$	$d_{\text{orifice}} = 20,67 \text{ mm}$
plunger mass = 30 kg	$v_{\text{oil}} = 0,002 \text{ Pas}$	$\rho_{\text{oil}} = 921 \text{ kg/m}^3$
plunger friction coefficient = 0,3	plunger - barrel clearance = 0,05 mm	

The resulting downhole dynamometer card is presented in Figure 83:

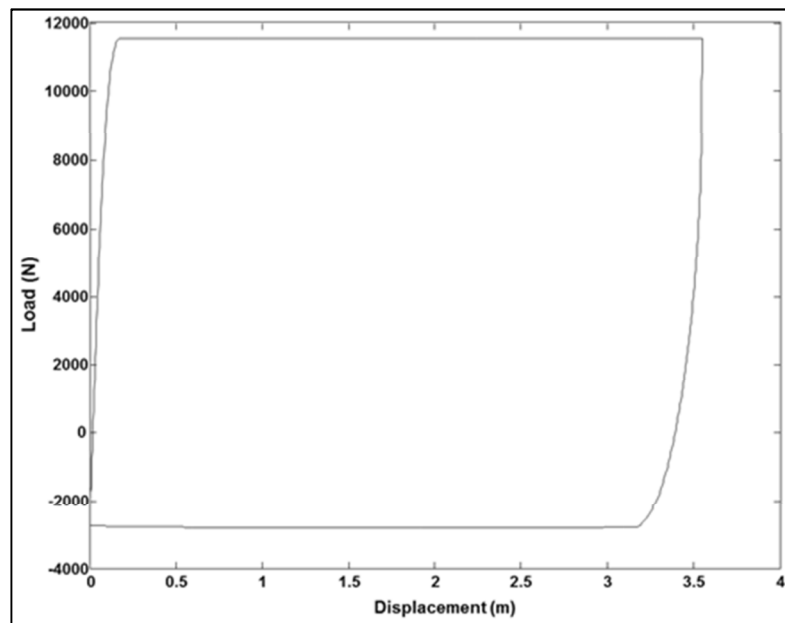


FIGURE 83: ARTIFICIALLY DESIGNED DOWNHOLE DYNAMOMETER CARD

To provide an overview on the most important influencing parameters, a sensitivity analysis is performed. The investigated parameters are: dead oil gravity, water cut, dynamic liquid level, plunger-barrel friction coefficient, strokes per minute and gas – oil ratio

For the sensitivity analysis the parameters are varied by + and - 20 per cent, except the strokes per minute and the water cut. The water cut can become the maximum value of 1. Table 12 summarizes the input parameters for the sensitivity analysis. The vertical lift performance pressures are of major importance and calculated by using the Petroleum Experts PROSPER Software (81).

	Reference	VLP-Pressure	20%	VLP-Pressure	-20%	VLP-Pressure
Oil Gravity	921	72 bar	896	72.1	950	73.6
<i>API - Gravity</i>	22		26.4		17.6	
<i>Dead Oil Viscosity</i>	0.025		0.01		0.1	
Water Cut	0.865	72 bar	1	88.8 bar	0.692	57.2
Dynamic Fluid Level	870m		860m		880m	
Friction Coefficient	0.5		0.6		0.4	
SPM	3.13		3.26		2.85	
<i>Production (m³/day)</i>	24	72 bar	28.8	70.6 bar	19.2	76.9 bar
GOR	100	72 bar	120	69.2 bar	80	77.9 bar

TABLE 12: SENSITIVITY ANALYSIS / PARAMETER SUMMARY

Figure 84 and Figure 85 show the results of the sensitivity analysis for the upstroke, respectively the downstroke in a spider diagram. The blue line represents the reference case, the red line an increase of 20 per cent and the green line a decrease of 20 per cent.

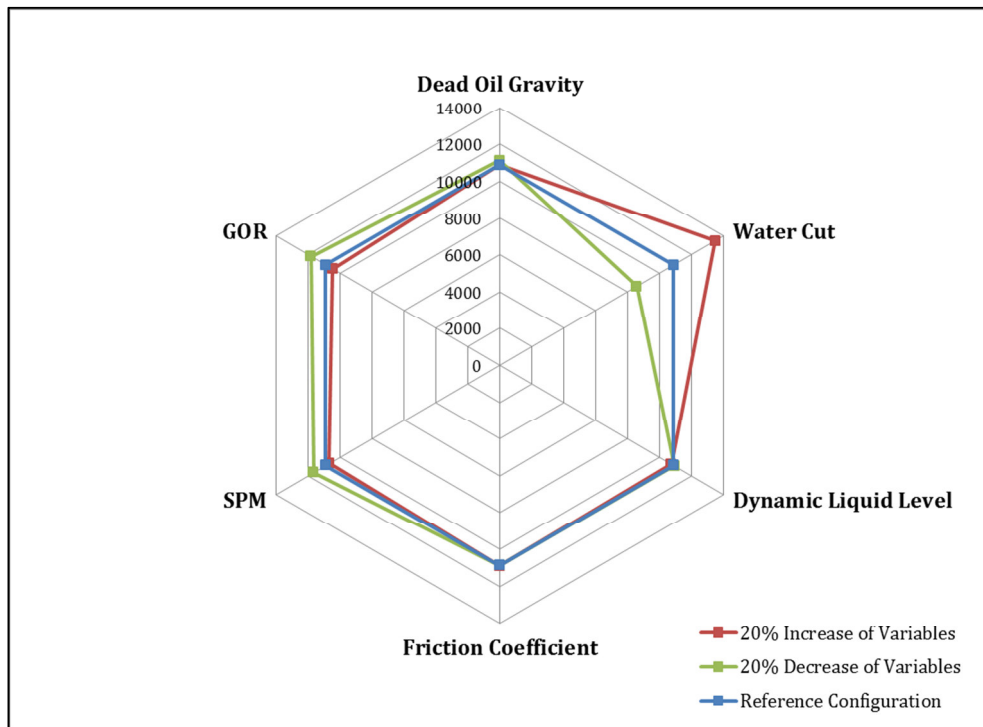


FIGURE 84: SENSITIVITY ANALYSIS / UPSTROKE

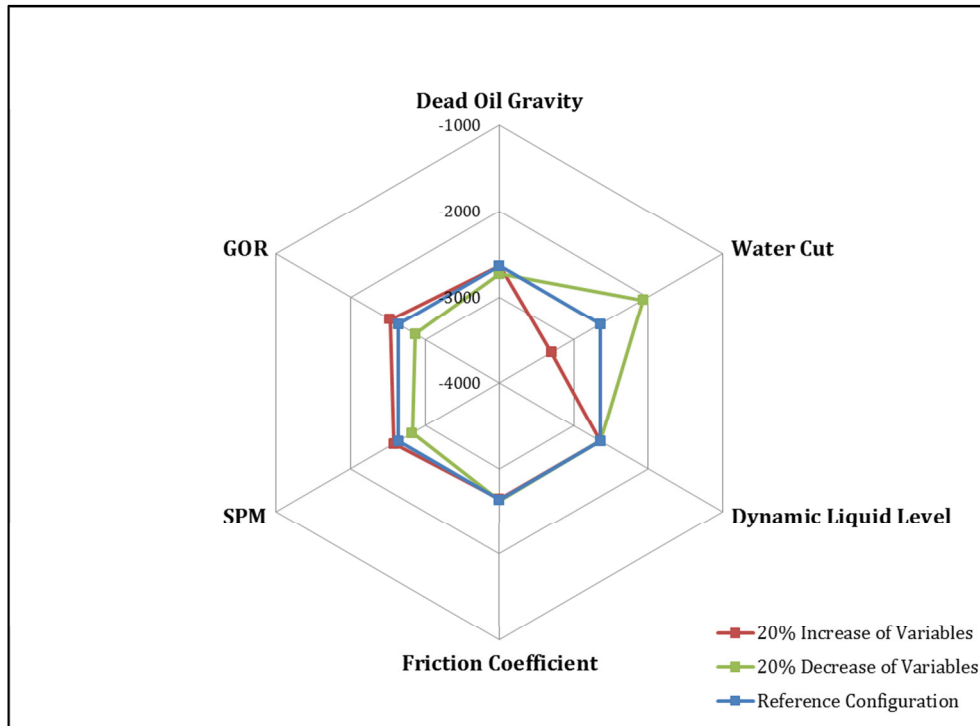


FIGURE 85: SENSITIVITY ANALYSIS / DOWNSTROKE

Both figures show the same tendency. The major influencing parameters are the water cut and the gas-oil ratio. The higher the water cut, the less oil and gas is in the production tubing, hence the overall density increases. A higher gas-oil ratio decreases the density and therefore reduces the required lifting pressure. In conclusion, the pumped fluid properties essentially influence the shape and magnitude of the downhole dynamometer card. The operating conditions themselves are of minor importance.

5.5.2 DOWNHOLE BOUNDARY CONDITION COMPARISON WITH RODSTAR

Today, commercial software based on solving the wave equation is available to estimate and to design sucker rod pumping systems. Such programs also require input variables, respectively boundary conditions, like the motion of the polished rod and the load behavior of the pump plunger. Figure 86 displays the surface (blue curve) and downhole (green curve) dynamometer cards, derived by a commercial software package, based on the data shown above from Well OMV 1. The red lines display the maximum gearbox loading. An intersection of the surface dynamometer card with the red lines indicates a gearbox overloading.

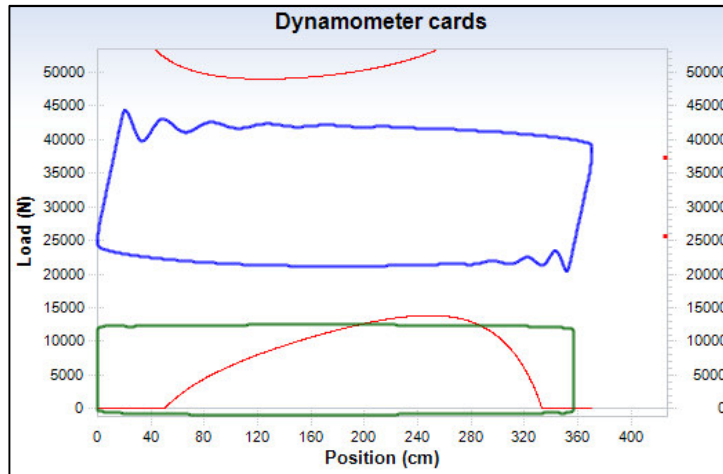


FIGURE 86: COMMERCIAL SOFTWARE / SENSITIVITY ANALYSIS / DOWNSTROKE

The downhole dynamometer card shows a full pump with a maximum load of about 12,4 kN and a minimum load of about -1000N, but the buoyant force, which reduces the minimum load additionally, is not considered in the plot. To get an idea about the match of the commercial downhole dynamometer card and the artificially generated card from the previous subsection, Figure 87 displays a comparison.

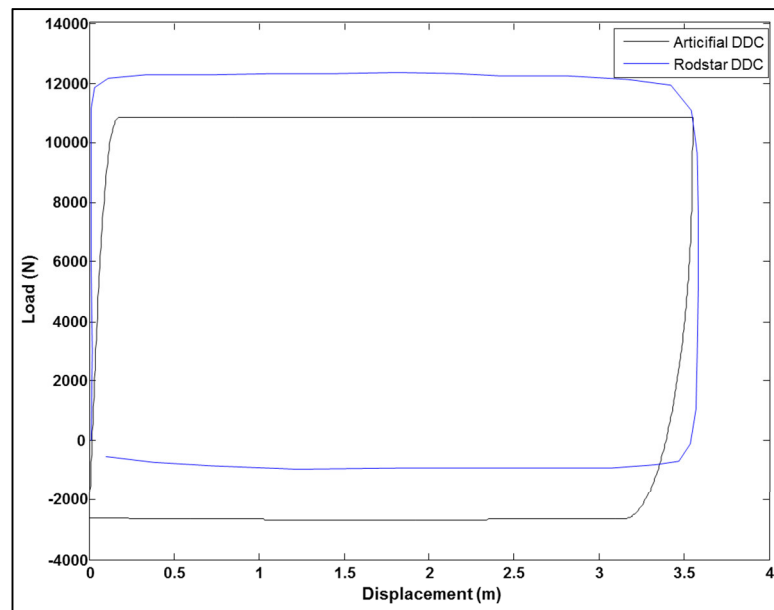


FIGURE 87: COMPARISON RODSTAR DOWNHOLE DYNAMOMETER CARD / ARTIFICIALLY CREATED DOWNHOLE DYNAMOMETER CARD

The match of the above shown DDC's is reasonable, concerning the magnitude of the pump cards, representing the load. This represents the lifted fluid load (102) and is the most important characteristics in terms of energy consumption. However the position of the pump card differs, which is a result of the fact that software programs account differently for buoyancy forces and the placement of the zero load line (103). RODSTAR doesn't show

buoyancy forces in its visualization, but the artificially created DDC does. In addition RODSTAR assumes a higher friction force, resulting in balling of the pump card in the middle of the stroke.

To adjust the artificially DDC, the friction coefficient can be increased to abnormally high values, which could indicate some precipitations of paraffin, or to use a safety margin for the up- and downstroke.

The major findings of this chapter are that the presented theoretical model can be used for predicting the performance of the pump plunger for new installations (no abnormal unknown conditions, like extensive paraffin precipitations, etc.). This model is used as a boundary condition for the simulation presented later. The previous chapters so far presented all theoretical details concerning the working conditions of a common sucker rod pump, based on models. To conclude this chapter, the uncertainties, problems and parameters, used for further analysis are summarized here.

The Svinos model is used for describing the motion of the polished rod because it is the most accurate out of the investigated models and it allows an evaluation of the pump jack kinematics. This model is even able to consider the slip of the electrical engine, as long as the slip over position of the polished rod is provided to the model. This fact is in some kind a limitation, not caused by the model, but the analysis.

Slip of an electrical engine slightly changes the motion of the polished rod and is dependent on the magnitude of the torque, required from the engine. Torque is a result from the polished rod load and the counterweight effect, which depend on the motion of the prime mover. For low slip engines, the slip effect can be neglected, whereas ultra-high slip engines would require an iterative procedure for the system evaluation.

The effect of friction can be split into two parts: fluid friction and coulomb friction. Fluid friction is highly dependent on the SPM and the viscosity of the pumped fluid. The fluid viscosity is again dependent on the composition of the fluid, with the oil phase having the biggest influence. As long as the whole system analysis is performed on wells delivering more than 90 percent water, without excessive precipitations, good results can be obtained by this relative simple fluid friction simulation. The geometry influence is minor. Coulomb friction is mainly dependent on the surface roughness and the presence of solid particles. The higher the solid content and the higher the oil content the higher is the friction coefficient. The major influencing parameter on the pump plunger load is the water cut. The water cut defines the amount oil produced oil, thus the amount of dissolved gas, which lightens the produced column in the tubing, when it starts dissolving from the oil. The higher the water cut, the higher the overall density, hence the load required at the plunger to lift the mixture.

To summarize this chapter the most important parameter is the composition of the pumped fluid with its mixture density. As long as degassed oil is produced, the effect of gas is minor.

6 DOWNHOLE DYNAMOMETER SENSOR MEASUREMENTS

Nowadays, predictive and diagnostic software is used to design and analyze sucker rod pumping systems. These techniques apply simplified models and boundary conditions to describe the behavior of the pumping system. Recent research focused on the accuracy of such design tools, especially the rod – tubing friction in deviated sections and the compressive forces at the pump plunger.

In some cases numerical models are used to describe the behavior of a sucker rod pumping unit. Due to the fact that these models are very complex, a test case is required to check the validity of the numerical approach and settings. In order to get real data, Downhole Dynamometer Sensors were developed and installed along a real operating rod string of a Sucker Rod Pumping system.

This chapter presents a short overview on previous developments and the features of the Downhole Dynamometer Sensor developed at the Montanuniversitaet in cooperation with lilatec (104). It summarizes the properties of the test well and the installation. The measurement procedure and data processing are shown. In the last part the downhole dynamometer card is compared with the RODSTAR results and the artificially generated DDC, derived in the previous chapter.

6.1 SENSORS SO FAR

In the nineteen-nineties efforts have been made by e.g. Albert Glenn Engineering (Longmont, Colorado) (105) to develop electronic downhole load cells, to quantify the results from simulation software programs. These tools contained a load measurement with three full bridge strain gages, located at 120° intervals on the inside diameter of the housing, acceleration sensors in three dimensions and a temperature sensor in the housing (106). Based on the results a database was generated by Sandia National Laboratories (107) for improving the accuracy of predictive and diagnostic software. Evaluations of the database show that often there is a difference how software programs account for buoyancy forces and the placement of the zero load line (103). In addition the importance of considering the effective load instead of the true load for buckling evaluations is shown (108). After futile attempts to get the data from the measurements, performed in the nineties in the US, a Downhole Dynamometer Sensor (DDS) was self-developed to perform accurate measurements of the downhole behavior of the sucker rod string.

The following section presents the DDS development and its field of usage, as well as the field measurement with the data processing.

6.2 DOWNHOLE DYNAMOMETER SENSOR (DDS):

The Downhole Dynamometer Sensor is a self-developed, autonomously working, sealed data logger, which is used to measure the load within the sucker rod string, the motion in three directions and the temperature of the housing. The DDS can be installed with rod couplings directly into the sucker rod string at any position and the rod load is conveyed by the body of the measurement tool. For a full analysis of the sucker rod string it is suggested to install several DDSs at different positions. Therefore it is recommended to position at least two tools at the surface, directly below the polished rod and at least two tools directly above the plunger for redundancy. Additional tools can be placed in between e.g. for deviated wellbores at the deviation from vertical.

The DDS itself is a stainless steel tube with an outside diameter of 43 millimeters, to allow an installation in $2\frac{3}{8}$ tubings and a length without pins of 320 millimeters. The inside dimensions are 30 mm in diameter and 130 mm in length. This chamber contains everything needed for performing and recording measurements, because the DDSs operate independent from surface facilities.

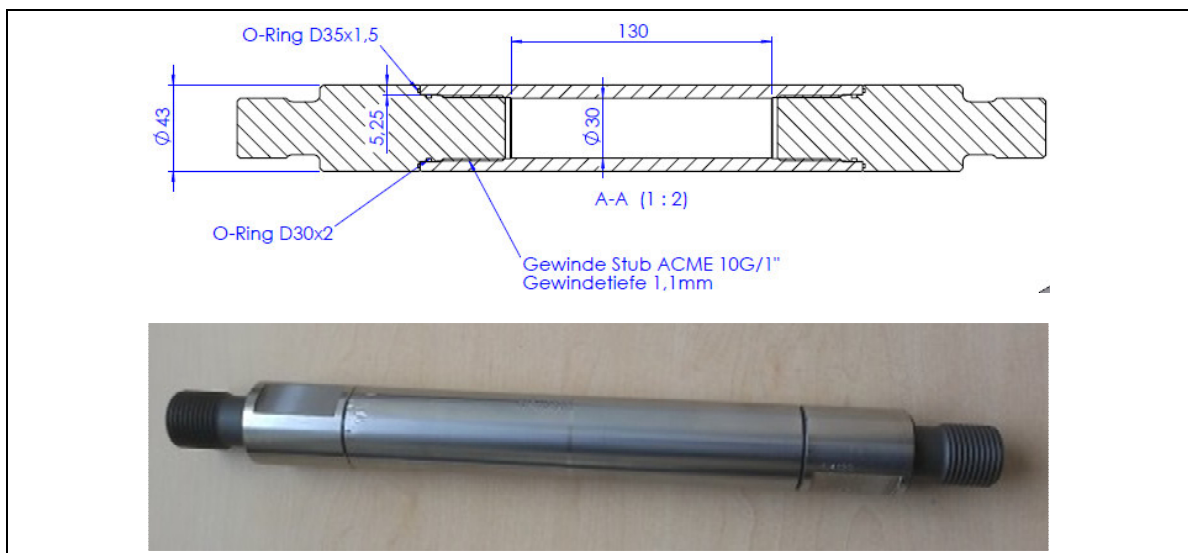


FIGURE 88: DOWNHOLE DYNAMOMETER SENSOR HOUSING (13)

The DDS sensor itself contains four analogous and one digital sensor. The analog sensors are three temperature compensated strain gauges and one temperature sensor. The three strain gauges are positioned at the same axial position, but radially they are shifted by 120 degrees. Beside redundancy, the reason for three strain gauges it to use the measurements to evaluate the rod bending torque in the string.

Figure 89 illustrates the inside of the Downhole Dynamometer Sensor. The circuit board is assembled next to the strain gauges on the one hand due to the limited space and on the other hand to keep the electric cable short and prevent disturbance caused by for instance by the electric supply cable.

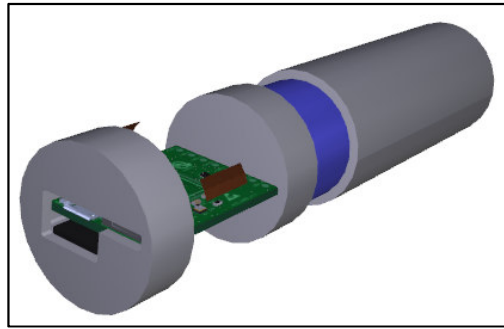


FIGURE 89: ILLUSTRATION OF THE DDS'S ELECTRONIC COMPONENTS (104)

The inner structure of the DDS contains a circuit board and an accumulator, used for energy supply. It is charged via the circuit board and an USB cable. The accumulator is the limiting tool for temperature, because common accumulators can only be used for temperatures up to 60°C. Finally the DDSs chamber is fixed by silicon glue, to prevent the system from failures, caused by vibrations. A schematic of the DDS's electronic components is shown in Figure 90.

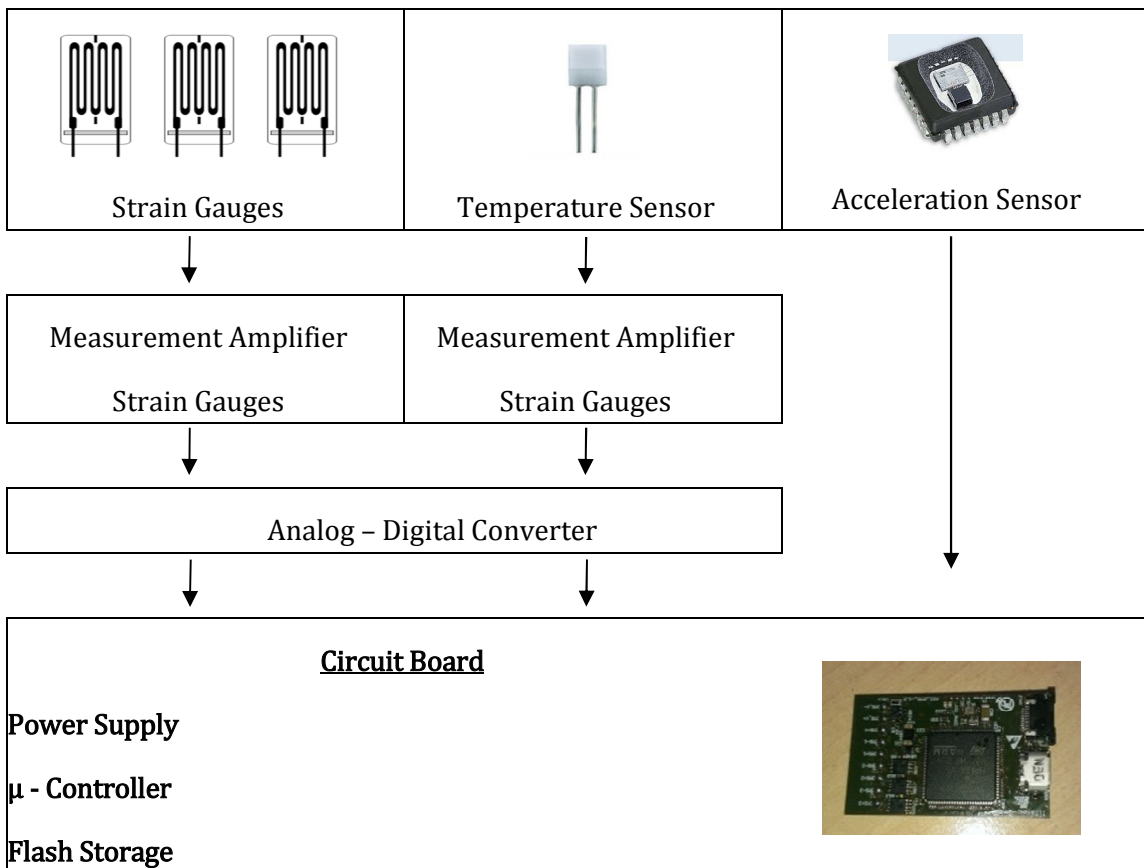


FIGURE 90: SCHEMATIC OF THE DDS'S ELECTRONIC COMPONENTS

The recorded data are stored on an USB flash card and can be recovered via the USB connection. The conversion of the recorded data is not done directly at the tool, but afterwards. The software for the tool itself allows a very comfortable handling. The tool can be programmed to sleep and wake up in time intervals by an alert. After data recording it switched back to sleep mode until the next alert. The software at the microcontroller on the DDS itself is kept relatively simple, to reduce the probability of failures. Hence the stored data at the tool are the measured raw data and require a conversion to the desired units. The analogous sensors deliver Millivolts, which need to be converted to force and temperature, respectively Newton and degrees Celsius. The digital sensor delivers multiples of g, but the actual acceleration is required.

The calibration of each sensor type is done independently, thus the required calibrations are: temperature sensor calibration, strain gauge calibration and acceleration sensor calibration.

6.2.1 TEMPERATURE SENSOR CALIBRATION

The temperature sensor itself is an analogous sensor, which records voltage. To get the conversion to temperature, the DDSs were heated up in 4 steps gradually in a dying stove. The lower limit for testing was ambient temperature, the upper limit the design temperature of the tools, which is about 60°C and limited by the accumulator of the sensor. The whole heating procedure was done very slowly to guarantee an equalization of the sensors and the surrounding temperature. Table 13 shows the readings and the reference temperature of the dying stove.

Reference Temperature	DDT1	DDT2	DDT3	DDT4	DDT6
27 °C	732,5	582	583,5	576,5	577
36,5 °C	753,5	597	599	592	592,5
45 °C	772	612	614,5	607	608
55 °C	793	628,5	631	623,5	624,5

TABLE 13: TEMPERATURE SENSOR CALIBRATION

These data points are fitted, using the least square method. The data points are represented very well by a straight line, hence a linear behavior of the temperature sensor is assumed. Figure 91 summarizes the calibration match of the individual sensors.

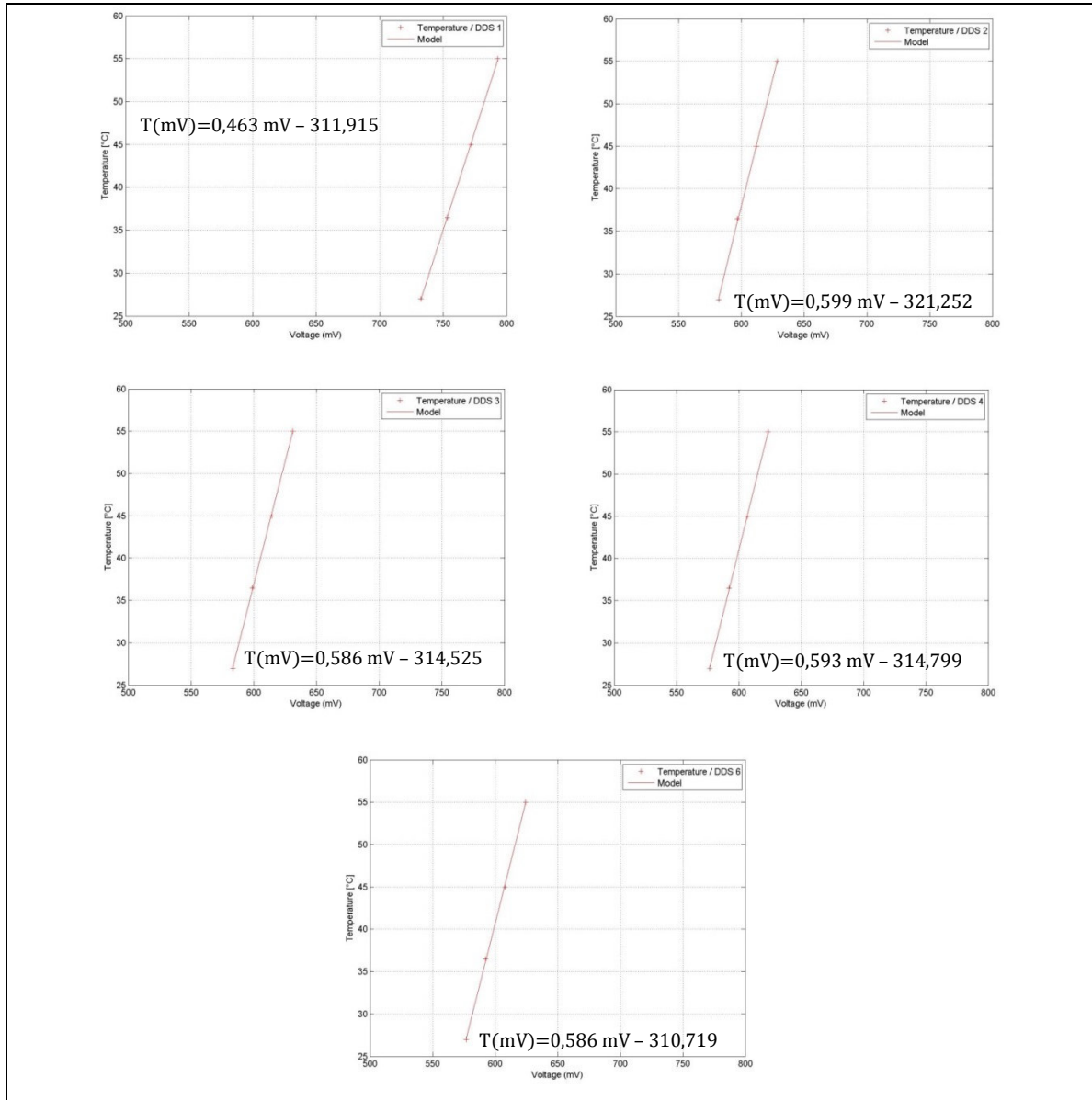


FIGURE 91: TEMPERATURE SENSOR FITTING

The derivation of the calibration coefficients is presented in detail in Appendix E.

6.2.2 ACCELEROMETER CALIBRATION

The DDSs are each equipped with a 3 axes accelerometer, which is directly attached to the circuit board and records multiples of g, the acceleration due to gravity. The objectives of the calibration are to convert the recorded values to “real” acceleration and to correct inaccuracies from assembling. During assembling of the DDS one problem is, that it cannot be guaranteed that the axes of the accelerometer are 100 percent identical with the axes of the DDS.

The calibration of the accelerometer is performed by using the gravitational vector and a horizontal surface. The DDS was positioned on the surface in a way that one axis of the DDS was in line with the gravitational vector and the measured value of this accelerometer direction was recorded. The same process was performed for direction two and three. The calibration is based on a coordinate transformation, using a rotational matrix with nine entries, which returns the acceleration in the axes of the DDS (109). This calibration was done using MatLab and the code is in Appendix E.

In addition filtering of the acceleration data is required. A low pass Chebychev 1 (110) filter seems to be appropriate. The parameters for the filter are:

$$F_{\text{pass}} = 0,15 \text{ Hz} \qquad F_{\text{stop}} = 1,5 \text{ Hz} \qquad A_{\text{pass}} = 1\text{dB} \qquad A_{\text{stop}} = 80\text{dB}$$

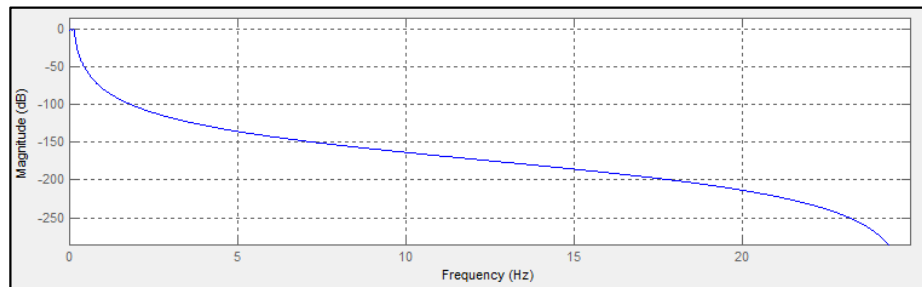


FIGURE 92: CHEBYCHEV 1 - FILTER

Figure 92 shows the behavior of the filter. It indicates a relatively small pass band, followed by a rapid fall in magnitude, which is appropriate for pumping frequencies below 0,1 Hz.

6.2.3 STRAIN GAUGE CALIBRATION

The calibration of the strain gauges must meet the site conditions in the wellbore. This means temperature, fluid pressure and tension, respectively compression. It is not possible to perform a full on-site calibration under the real conditions. As a result the calibration was spitted into two parts: calibration under pure compression or tension and calibration under pure hydrostatic pressure. In addition there is one calibration point from the field test.

The temperature effects need not be considered, because the strain gauges consist of two measurement grids that are shifted by 90 degrees and therefore compensate temperature effects. This fact is also quality checked by comparing the DMS reading for different temperatures but no change of the DMS readings was observed.

6.2.3.1 HYDROSTATIC PRESSURE TEST

The hydrostatic pressure increases in the wellbore from almost zero to relatively high values, very deep in the wellbore. Hydrostatic pressure is acting on the complete surface of the DDS and causes a change in the voltage reading, without a real mechanical compression or tension. As a result the effects of the hydrostatic pressure must be corrected to get valid load readings.

Therefore the Downhole Dynamometer Sensors, in this case sensor 4, was encapsulated and loaded with different pressures, ranging from 0 to 16 MPa with an interval of about 2 MPa. Figure 93 shows the test arrangement.



FIGURE 93: HYDROSTATIC PRESSURE TEST

For the calibration it is important to know if the behavior is linear or not. Therefore the voltage is plotted against hydrostatic fluid pressure. Figure 94 indicates that the increase in voltage is direct proportional to the fluid pressure. Another important observation is that also the slope of the lines is almost identical.

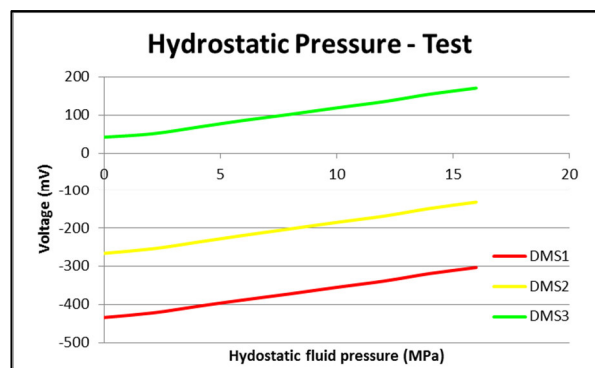


FIGURE 94: HYDROSTATIC PRESSURE TEST CALIBRATION

As a result the hydrostatic pressure and the change in voltage must be corrected to get proper load results, but due to the linearity an emendation is simple.

An additional calibration point was obtained under site conditions at the beginning of the field test, when the complete system was installed but not in operation. The DDS's recorded voltage value is proportional to the static weight of the rod string under buoyant conditions.

During this time period, the tubing and annulus were completely filled with workover fluid ($\rho = 1020 \text{ kg/m}^3$), thus the buoyant force onto the 7/8” sucker rods is about 3550 N.

Table 14 summarizes the weight in air and the buoyant weight, which was seen by the DDS’s in the wellbore:

	Segment length	MD	TVD	Load in air	Load under buoyancy
	<i>m</i>	<i>MD</i>	<i>m</i>	<i>N</i>	<i>N</i>
DDS 1	0.32	902.3	4.0	30409	26859
2 rods	15.24	902.0	4.3	30367	26817
DDS 2	0.32	886.7	19.6	29833	26283
61 rods	464.82	886.4	19.9	29791	26241
DDS 3	0.32	421.6	484.7	13515	9965
52 rods	396.24	421.3	485.0	13473	9923
DDS 4	0.32	25.0	861.3	898	-2652
1 rod	7.62	24.7	861.6	861	-2689
DDS 5	0.32	17.1	869.2	628	-2922
1 rod	7.62	16.8	869.5	591	-2959
DDS 6	0.32	9.2	877.1	358	-3192
1 rod	7.62	8.8	877.5	321	-3229
Plunger	1.2192	1.2	885.1	88	-3462

TABLE 14: WEIGHT OF THE FIELD TEST SUCKER ROD STRING

All calibration curves must go through the individual on site test point to account for the real conditions. These conditions also consider the hydrostatic pressure; hence the correction for the hydrostatic pressure is already included.

6.2.3.2 TENSION AND COMPRESSION TEST

The pure tension respectively compression calibration of the three strain gauges was done by using a rock testing machine, which is able to burden the tool under a specific load. Special adapters were designed to allow assembling of the DDS into the testing machine.



FIGURE 95: ROCK TESTING MACHINE AND DDS

It was desired to do the calibration of the sensors before and after the field test to evaluate changes in the DMS behavior. Due to DDS problems in the development stage it was not

possible to calibrate all sensors before and after the field measurements. Table 15 shows the number and date of the calibration for the DDS's:

Sensor	28.06.	12.07.	04.10.
DDS 1	X		X
DDS 2		X	
DDS 3		X	X
DDS 4			X
DDS 5		X	
DDS 6		X	X

TABLE 15: CALIBRATION DATES

For the calibration procedure itself, a predefined testing procedure was used. The same procedure was used for all six DDSs. The sensors itself were switch on before the installation and fixed by the adapters in the testing machine.

The calibration process itself always started with the compression load case. The load was increased in stages with an increase of 5 kN per second. The first stage started at 0 kN to 50 kN of compression and then the load was kept for a few moments. Afterwards the load was increased to 100 kN compression and then to 150 kN compression. 150 kN were the maximum compressive load in the test. The reduction of the compressive load to zero was performed by the same way. After compression, the tension load case was started. The load stages were principally the same like for the compression case. So the test started from 0 kN to 50 kN tension. After a short hold on period the load was increased to 100 kN and then to 150 kN tension. The reduction of the tensile load to zero was performed by the same way.

Figure 96 shows the load – time profile of the rock testing machine for DDS 3. The left profile shows the compression case and the right profile the tension case.

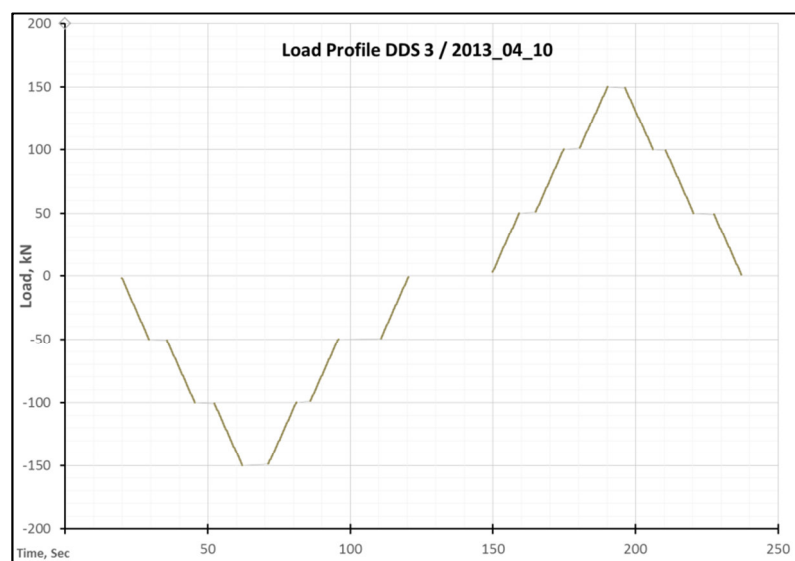


FIGURE 96: ROCK TESTING MACHINE READING

The whole testing cycle was also recorded by all three strain gauges of each DDS. Figure 97 shows the collected data from the DDS 3 and the load from the rock testing machine as a brown line. The pyramid shaped profile on the left represents the compression test and the pyramid shaped profile on the right represents the tension test.

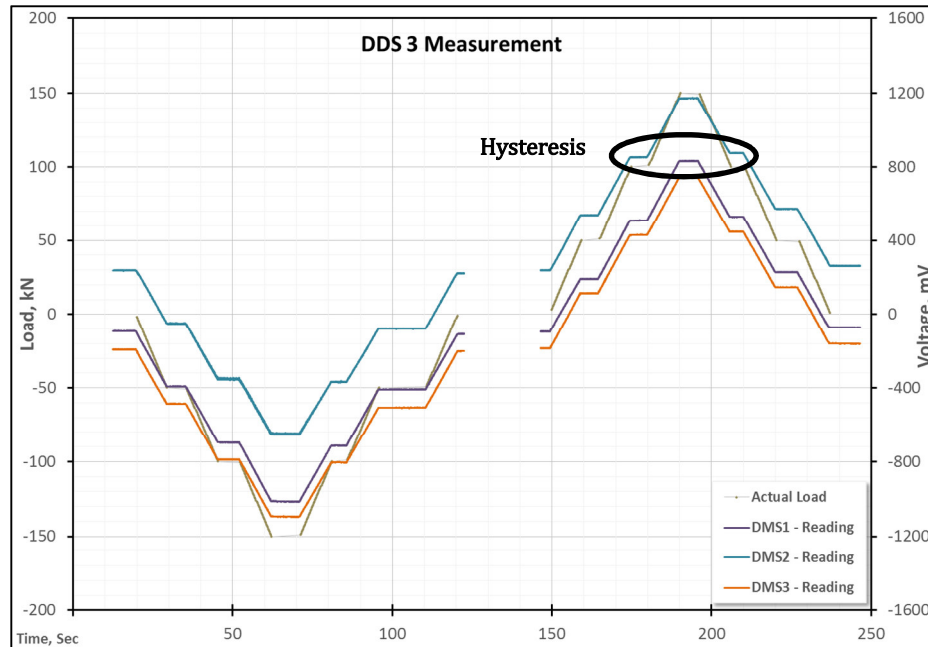


FIGURE 97: DDS READINGS

The figure clearly indicates that the data from the sensors deviate in offset and slope from the data, defined by the rock testing machine. It also can be seen that there is some kind of hysteresis for the load stages. It means the recorded values of the sensor are dependent on the direction from where a specific load value is approached. This fact results in some uncertainties for the measurement.

The next step is the comparison of the DDS readings and the readings from the rock testing machine. The DDS readings are time shifted to exactly overlap the start points for the Downhole Dynamometer Sensors and the rock testing machine. The calibration lines are matched to the analyzed data. In addition the calibration line must go through the on-site test point to account for the field conditions.

Finally this procedure results in a proper value for the fitting and a reasonable hysteresis curve of the calibration lines. Figure 98 shows the fitted rock testing machine and sensor data fitting.

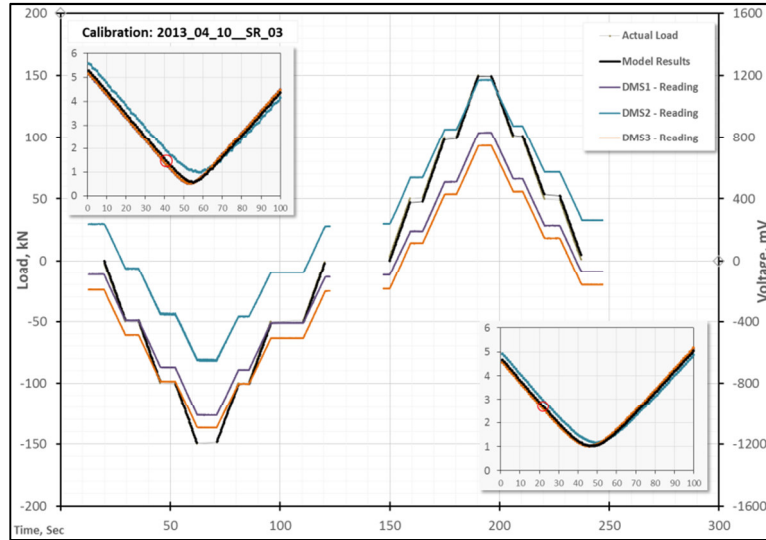


FIGURE 98: ROCK TESTING MACHINE AND DDS – MATCH

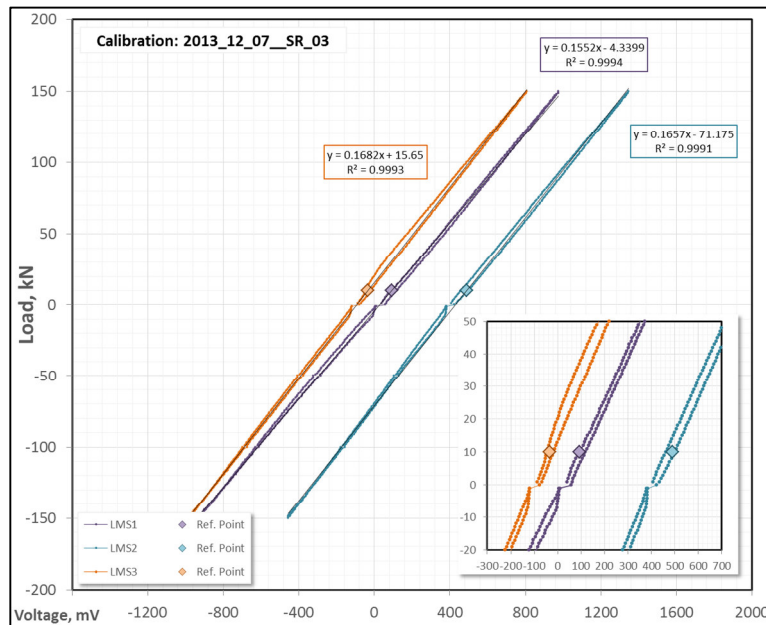


FIGURE 99: CALIBRATION DDS 3 / 2013_12_07

Figure 99 represents the calibration curves for DDS 3 obtained from the calibration on the 12.07.2013. The hysteresis and the correlation coefficients as well as the parameters of the calibration can be seen. Figure 100 demonstrates the results from the 04.10.2013.

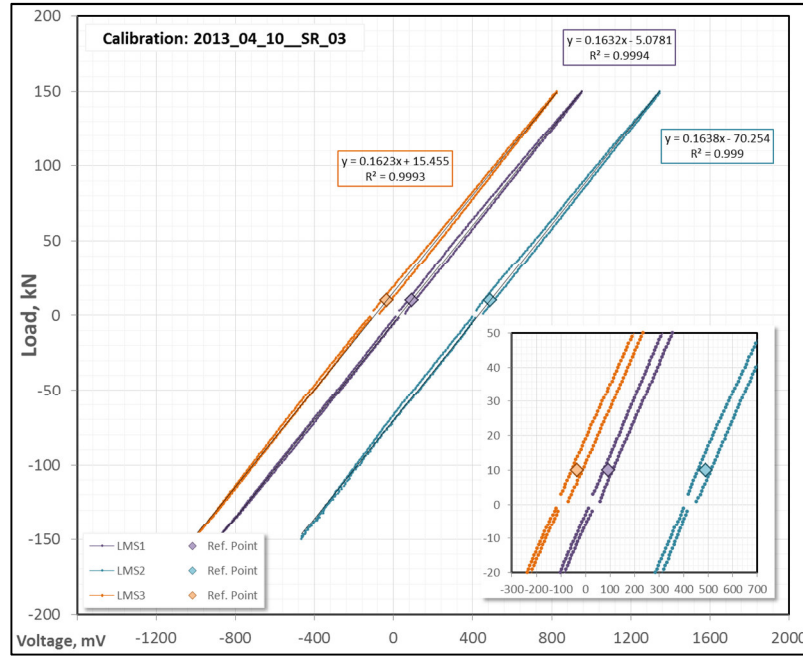


FIGURE 100: CALIBRATION DDS 3 / 2013_04_10

The accuracy of such a calibration is limited, caused by the hysteresis. The converted values could theoretically deviate from the average by about +/- 2 kN (see Figure 101). Due to the fact that during the field test one calibration point can be evaluated relatively exactly, the results get much more accurate. The reason to this is that during the operation the loads are in the range of the “field calibration point”.

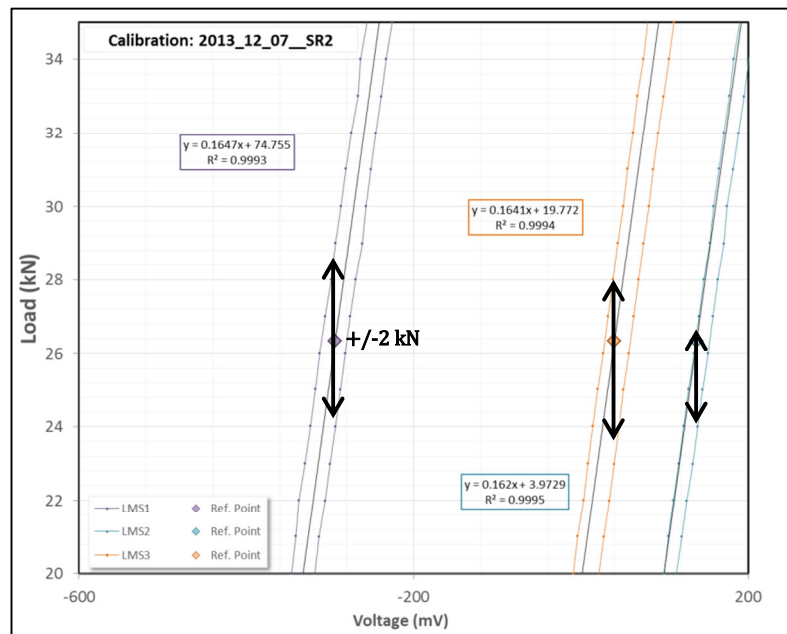


FIGURE 101: ACCURACY OF DDS 2 / 2013_07_12

The comparison of the calibrations shows that the correlation coefficients differ a little bit, nevertheless it makes sense to use the average value for the conversion of the measured data.

The calibration of all Downhole Dynamometer Sensors can be seen in Appendix E. Table 16 summarizes the calibration coefficients, except for sensor 5. Sensor 5 had a runtime error and was not calibrated. The calibration for DMS 2 in DDS 6 could not be performed within the second calibration, because it got loosened during the field test, thus the recorded reading are wrong.

Sensor		28.06.	12.07.	04.10.
DDS 1	DMS 1	-186,6 mV - 14335		-176,6 mV - 12117
	DMS 2	-161,3 mV - 11320		-164,4 mV - 12071
	DMS 3	-171,3 mV - 21159		-167,1 mV - 19974
DDS 2	DMS 1		164,7 mV + 74755	
	DMS 2		162 mV + 3973	
	DMS 3		164,1 mV + 19772	
DDS 3	DMS 1		155,2 mV - 4339	163,2 mV - 5078
	DMS 2		165,7 mV - 71175	163,8 mV - 70254
	DMS 3		168,2 mV + 15650	162,3 mV + 15455
DDS4	DMS 1			160,2 mV + 61244
	DMS 2			162,5 mV + 33321
	DMS 3			167,1 mV - 20976
DDS 6	DMS 1		-162,7 mV + 7029	-166,1 mV + 7242
	DMS 2		-172,5 mV + 2898	-
	DMS 3		-158,7 mV + 12408	-165,4 mV + 13068

TABLE 16: STRAIN GAUGE CALIBRATION PARAMETERS

The objective of the Downhole Dynamometer Sensors is to obtain downhole data from sucker rod pumping systems. These data are later used for a validity check of numerical simulations, needed to simulate the sucker rod string. The constructed and used sensors suffered some limitations due to cost restriction: the temperature had to be lower than 60°C and the maximum load had to be below 150 kN. Therefore a deviated well for the field test with shallow depth, moderate temperatures and production rates was selected in the Vienna Basin. The well with the name OMV 1 is in the vicinity of Gänserndorf.

Weaknesses of the DDS are on one hand the limited storage capacity and energy supply, on the other hand the fact that the sensors have to be disassembled to get the data – so real time monitoring is at the moment impossible.

6.3 WELL OMV 1

The well OMV 1 is an oil well in the district of Gänserndorf in Lower Austria. OMV 1 produces from a reservoir in the Vienna Basin. The reservoir layer is in a depth of about 955 m true vertical depth. It produces 7,7 m³ of reservoir fluid per day, with a water cut of about 85%. The average temperature at reservoir depth is not higher than 40 ° Celsius. The oil density of 920 kg/m³ leads to an API gravity of 22°, which indicates medium heavy oil. The

solution gas ratio is 23 m³ of gas / 1 m³ of produced oil. There are no extensive problems with paraffin precipitations.

The trajectory of OMV 1 starts with a vertical section up to a depth of about 460 meters. There it starts deviating into the south-west direction. In 957 meters TVD the bottom of the well is reached, with an inclination of 28°. (see Figure 102)

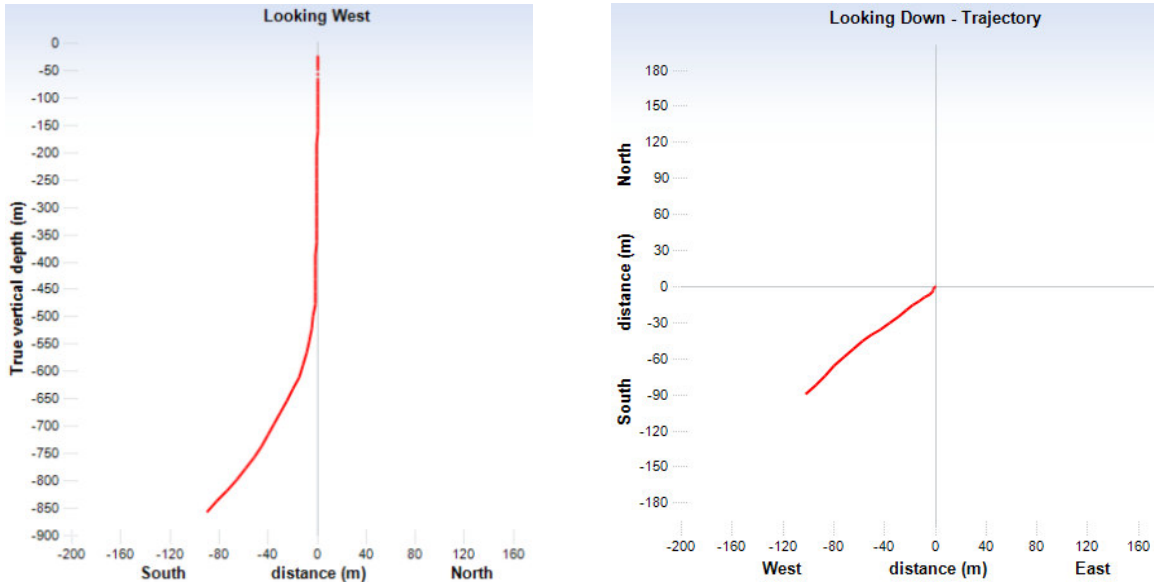


FIGURE 102: TREJECTORY OF WELL OMV 1

At the surface the conventional pump jack C-320D-256-144, with a surface stroke length of about 3,7 meters is installed. A corrosion inhibition system and a rod rotator reduce corrosion and erosion of the downhole equipment. At the well site of well OMV 1 several wells are brought together, thus six pump jacks are next to each other. The pump jack is driven by a variable speed drive controlled asynchronous electrical engine.



FIGURE 103: LOCATION WELL OMV 1

The wellbore is equipped with a non-tapered 2 7/8" tubing string. The tubing is anchored in a TVD of 884 meters. Below the tubing there are a sand anchor and the landing nipples for the insert pump. The big advantage of such insert pumps it, that they can easily be replaced, without pulling the tubing. Therefore only small workover units are required.

6.4 MEASUREMENT PROCEDURE

The implementation of Downhole Dynamometer Sensors is pretty expensive. A workover unit, a lot of equipment, and work force are required for each installation twice – the assembling of the sensors and the dissembling of the sensors, a few weeks later. In addition there are additional costs to be considered, e.g. losses in oil production. Or that during the workover operation a lot of fluids are used to kill the well and to keep the pressure in the well overbalanced. These fluids might travel into the formation and could cause damage to the formation. When the well comes back into production, the water cut at the beginning will be much higher for the first few days, than the water cut before the shut in period.

Due to the relatively high outlay for the field test, as much information as possible should be gained within the test. Therefore in addition to multiple Downhole Dynamometer Sensors at different positions in the rod string, the following measurements are performed:

- Tubing and casing pressure measurement
- Surface dynamometer measurement

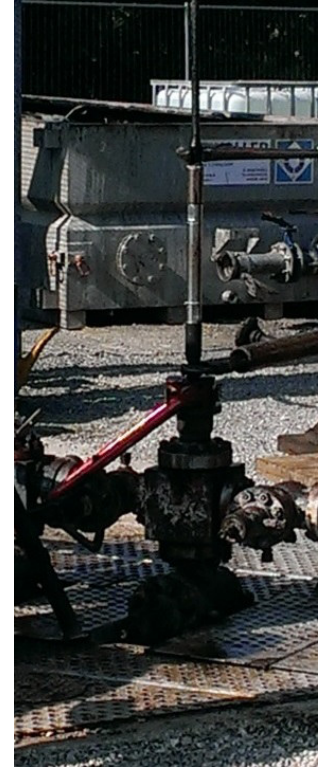


FIGURE 104: DDS INSTALLATION

For the field test six Downhole Dynamometer Sensors were installed in one sucker rod string at different strategic positions:

Sensor 1 and 2 were installed at the top of the rod string, directly below the polished rod. The reason for two sensors at this position was simply back up. If one failed, there would be another one to collect data.

Sensor 4, 5 and 6 were installed directly above the pump plunger at about 880 meters measured depth. The reason again was back up. Without data from this position the test would have been useless and therefore three tools were positioned.

Sensor 3 is installed at a measured depth of about 480 meters. This is a strategic position. If we compare this position with the well trajectory, one can see that the well starts deviating from vertical. The recorded load data from this position, together with the surface and pump data can be used to evaluate the friction coefficient from the vertical and deviated section. Figure 105 indicates the locations of the DDSs installed in well OMV 1.

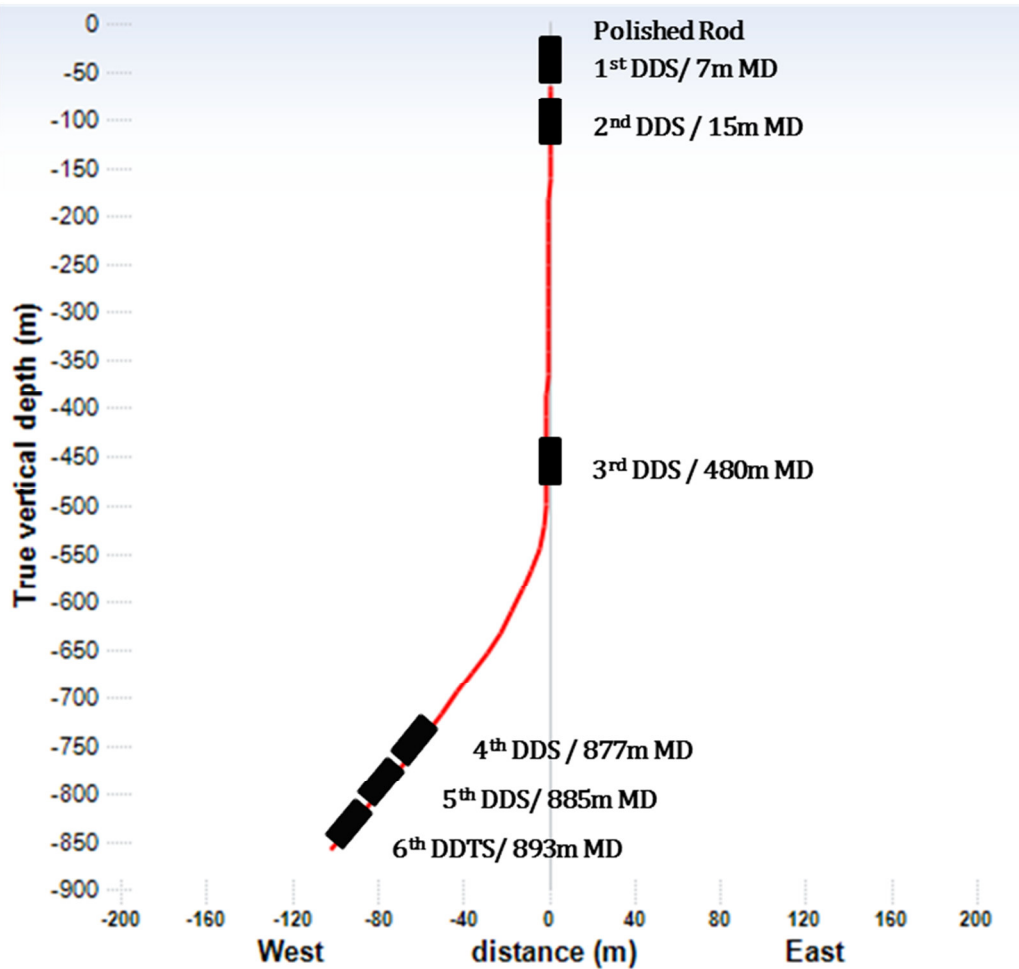


FIGURE 105: POSITION OF THE DOWNHOLE DYNAMOMETER SENSORS IN WELL OMV 1

Test sequence:

An essential design influence is the dynamic behavior of the load within the sucker rod string, which is dependent on the strokes per minute. To get different load cases, the stroke number was changed during the testing period. As a result the test was carried out with different stroke numbers that were not stepped neither by a geometric nor an arithmetic series, with the highest stroke number at the end. The stroke numbers used, vary in a range that the dynamic liquid level in the annulus is materially different, to get essential changes of the dynamic effects of the rod string. The highest number of strokes caused the well to fluid pound.

The DDSs were installed on according the locations, shown in Figure 105. The pumping system went into production two days later at about 11 o'clock.

To reduce the amount of data and to save disk space, the DDSs were programmed to not record data continuously but intermitted. Another advantage is that the received data packages are in handle able sizes. They were programmed to record data for one hour, from 12:00 to 13:00 with 50 Hz and afterwards one hour sleep until 14:00 o'clock. Then they

continued recording and so on. The first measurement was performed on the 22nd of August 2013 at 12 o'clock.

The entire field test period was designed to last about three weeks, because the accumulators of the DDSs are limited in power. At the beginning of the test the workover fluid had to be pumped out of the wellbore, then the liquid level in the tubing – casing annulus stabilizes and all required measurement were performed. After this period the pumping speed was changed. This procedure continued until the final speed was reached.

6.5 DATA PROCESSING AND INTERPRETATION

Data processing is one of the most important steps, when performing measurements. During data processing e.g. undesired noises are removed, conversions are done and the data are prepared for visualization, interpretation and further treatment. Without a proper processing, the measured raw data are pretty useless. Due to the fact that all the data were recorded with 50Hz, a huge amount of data was created by the DDSs.

6.5.1 TEMPERATURE SENSOR

The temperature sensor recorded the housing temperature during the field measurements. Due to the long installation times, it is assumed that the housing temperature is equalized with the pumped fluids temperature. The reason for measuring the temperature was to understand the temperature behavior over time and depth, as well as the temperature gradient in a producing oil well.

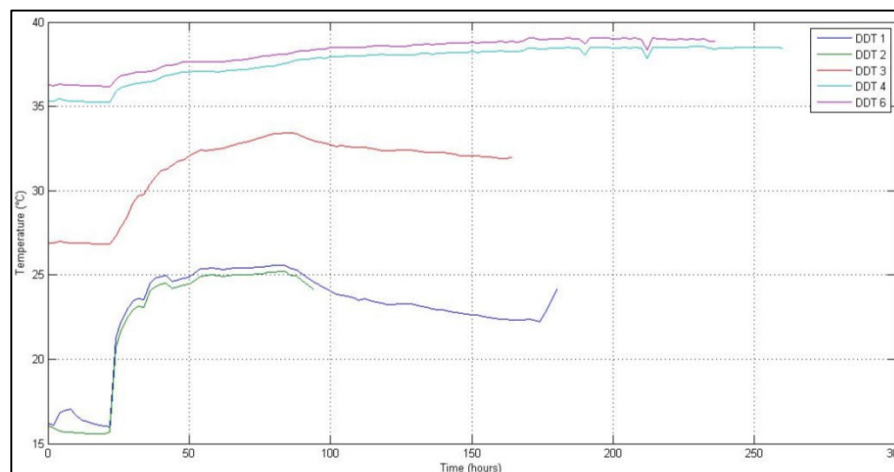


FIGURE 106: TEMPERATURE BEHAVIOR OVER TIME AND DEPTH

Figure 106 shows the temperature behavior over time and depth. At the beginning when the pump was not in operation, the temperature stayed more or less constant, with exception of DDS 1. DDS 1 is installed directly below the polished rod and the 22nd of August was a very hot day; DDS 1 shows the temperature influence of the sun, which is about 1 °C. The geothermal gradient in this region can also be evaluated during this non-operating time. The Sensor surrounding liquids equalize its temperature with the rock behind the

casing, if the duration of non-operation is long enough. Data processing shows a geothermal gradient of 2,3°C / 100m. After 22 hour the pump went into production and started to lift warmer fluid to surface. Due to the fact that the pump plunger is not installed at reservoir depth, there is also a moderate increase in temperature of about 3°C at the pump plunger. At the surface the temperature increased from 15,5°C to 25,5°C. The temperature losses of the pumped fluid during rising are with 13°C and a gradient of 1,44°C/100m very low.

From hour 85 on, the temperature at the shallower locations started to decrease, while the temperature at the pump plunger still increased slightly. This behavior is a result of the falling liquid level in the annulus. As long as there is liquid in the annulus, the energy is conserved. But with falling liquid level, liquid is postponed by expanding gas, which cools the surrounding and transports some heat faster to surface, hence the resulting temperature must decrease. This effect cannot occur at DDS 6, because production requires the liquid level in the annulus at least at the pump plunger, where DDS 6 is installed. The temperature gradient increases to 1,9°C/100m and causes the lifted fluid to lose about 17°C of its temperature during lifting, thus the liquid arrives at surface with about 22°C.

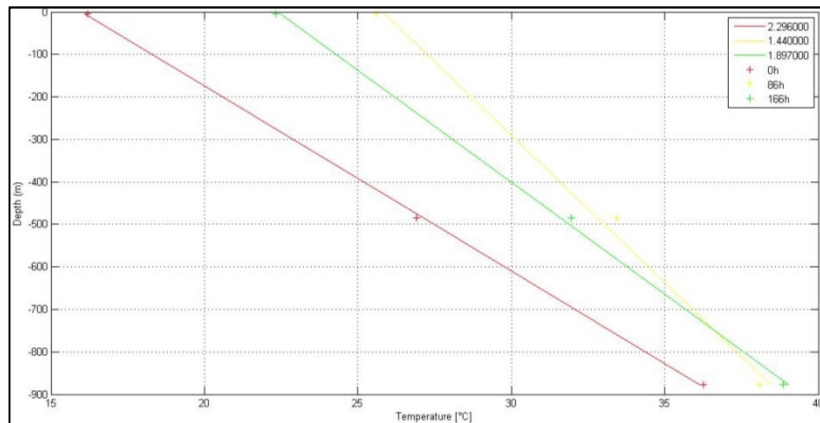


FIGURE 107: GEOTHERMAL GRADIENT BEHAVIOR

6.5.2 ACCELEROMETER SENSOR

The accelerometer sensor data contain 3 acceleration measurements, where the z-axis is in the axial direction of the DDS. This information can be used to evaluate the exact inclination of the wellbore at the sensor positions, simply by calculating the angle to the gravitational vector. Table 17 shows the inclinations of the sensors at final position.

	Measured Depth (m)	Inclination (°)
DDS 1	7	12,8°
DDS 2	15	0°
DDS 3	480	0°
DDS 4	877	26,8°
DDS 6	893	27,8°

TABLE 17: STRAIN GAUGE CALIBRATION PARAMETERS

Sensors 2 to 6 represent the inclination of the wellbore very well. The reading from DDS 1 might indicate that the polished rod is not hanging vertical in the wellbore, but deviated from vertical by 12,8°.

The evaluation of the stroke profile from the acceleration reading requires in addition to a calibration, filtering of the raw data. A sample of the filtered data can be seen in Figure 108. The raw data are in blue and the filtered data in green. It can be seen that the filtered data are reduced by the noise and show a cyclic behavior.

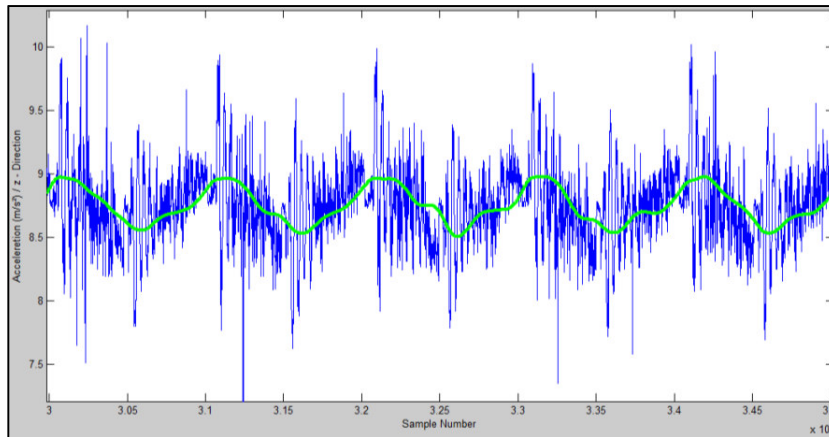


FIGURE 108: ACCELERATION MEASUREMENT SAMPLE

A closer observation of the filtered data displays a phase shift between recorded and processed data, which is normal for filtering.

The second objective for the evaluation of the accelerometer data is the derivation of the stroke profile. For the analysis it is the best way to define the beginning of the upstroke as start point. At this point the acceleration is a maximum. The exact stroke number can be obtained by a Fourier analysis of the strain gauge measurements, presented in the next chapter. Using this information, the samples belonging to one stroke are once integrated to get the velocity profile and a second time to get the displacement. Afterwards a scaling to the assumed stroke length is required. Figure 109 now presents the acceleration -, velocity - and displacement profile for DDS 1:

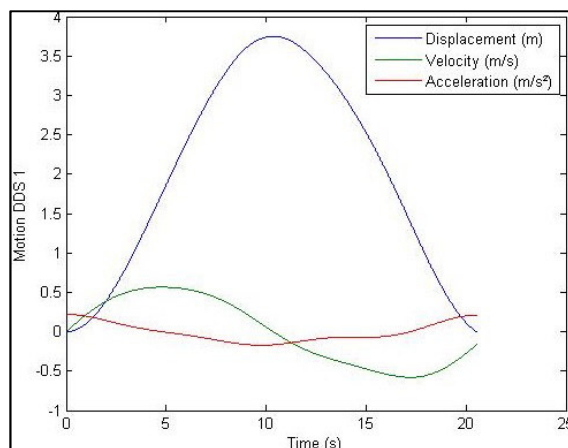


FIGURE 109: MOTION OF DDS 1

Another interesting plot is Figure 110. It shows the behavior of the displacement over depth, for the same stroke. The figure shows that the profiles of the individual sensors are apart from the different stroke lengths pretty similar. The displacement of the deeper sensors is delayed because the motion from the polished rod requires a certain amount of time to reach the position of the sensors.

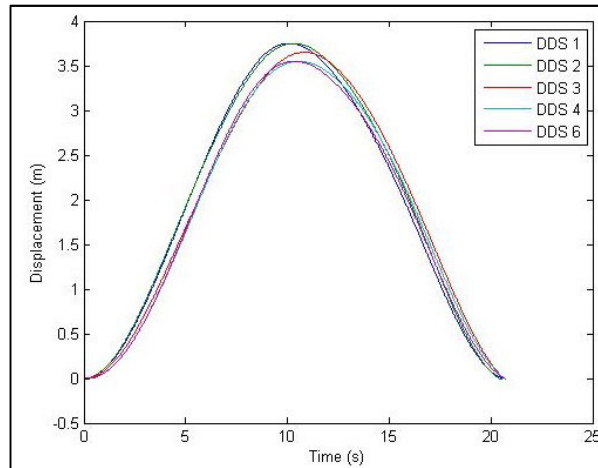


FIGURE 110: DISPLACEMENT COMPARISON DOWNHOLE DYNAMOMETER SENSORS

6.5.3 STRAIN GAUGE SENSOR

The results of the strain gauge measurements are directly used for evaluating the exact pumping speed, the load and the relative bending torque. In addition these data allow an interpretation of the overall pump conditions.

The first step is to evaluate the pumping speed. Figure 111 displays the unconverted strain gauge readings for all three strain gauges.

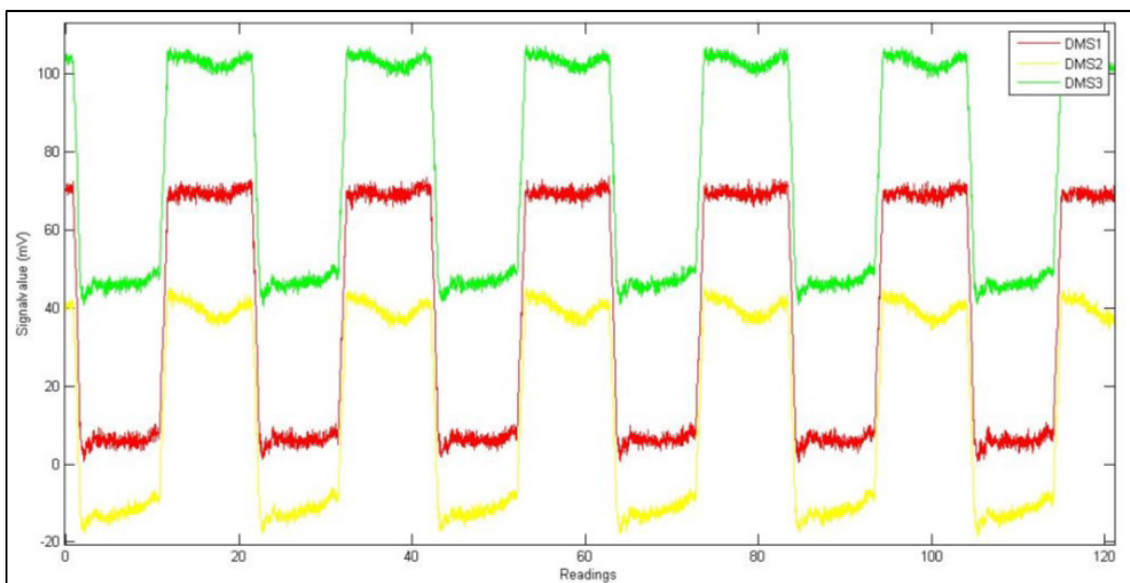


FIGURE 111: UNCONVERTED STRAIN GAUGE READINGS

The signals replicates in a certain time period, which allows using of the Fourier Transformation. It decomposes the signal into angular functions with different frequencies. (Figure 112)

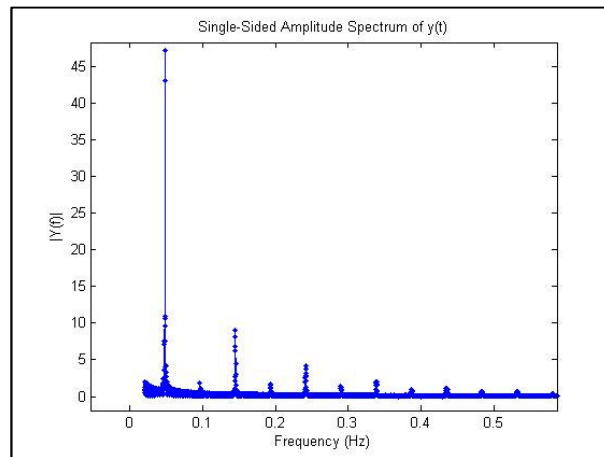


FIGURE 112: FREQUENCY PLOT / SPM - EVALUATION

The highest peak with the lowest frequency represents the repetition frequency of the measurement signal; all others are multiples of the fundamental frequency. This conversion is done for all measurements over time and the strokes per minute behavior can be found (Figure 113).

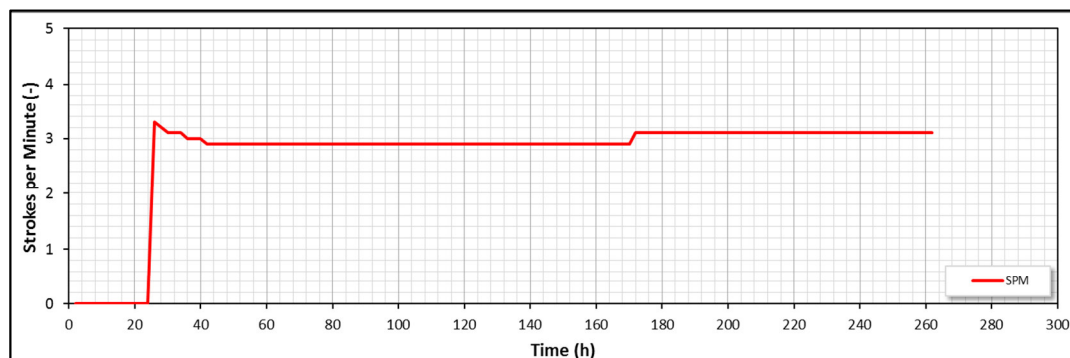


FIGURE 113: SPM BEHAVIOUR OVER TIME

Figure 113 shows that the pump started operation after 24 hours. Afterwards the pump went into production and produced with 3,3 strokes per minute, followed by a reduction of the SPM to 2,9 in the next 20 hours. The reason for this reduction in SPM was the falling liquid level in the annulus. At the beginning of pumping, after a work over job, the annulus is almost completely filled with brine. During the first days of pumping, these liquids are pumped out, until the equilibrium between reservoir pressure and liquid level is reached. This goes along with a reduction of the pumping speed, because the counter pressure at the plunger is steadily reduced and the lifting load increases. After 70 hours the pumping speed was increased to 3,1 strokes per minute and stayed at this level until the end of data recording. The Downhole Dynamometer Sensors performed due to unequally charged accumulators unequal numbers of measurements, summarized in Table 18.

	Hours of Measurement
DDS 1	182
DDS 2	96
DDS 3	166
DDS 4	262
DDS 6	182

TABLE 18: HOUR OF MEASUREMENT / DDS

The analysis of the huge amount of data is started by generating history plots over all measurements of each DDS. Such plots allow quick quality checks of the data and enable a fast interpretation of the operation conditions. Figure 114 presents three history plots at different times. A history plot itself shows the frequency of a measured sample versus measured voltage.

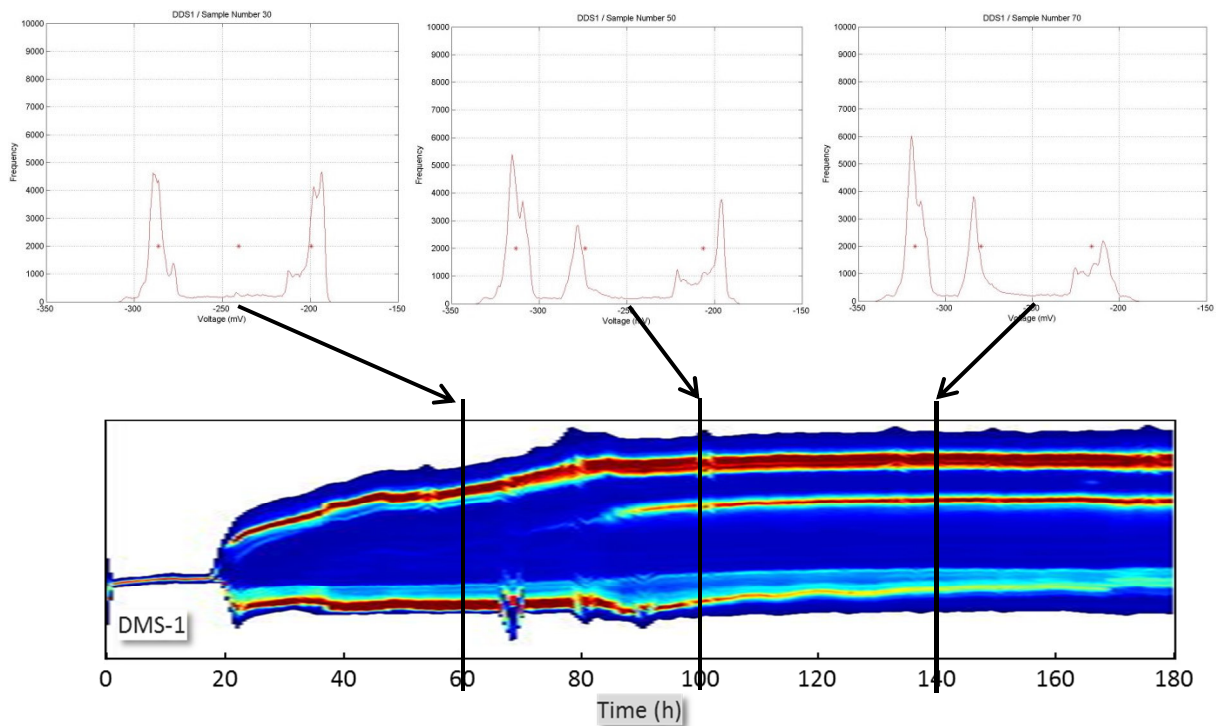


FIGURE 114: HISTORY PLOTS

Figure 114 presents history over time plots for DMS 1 in DDS 1. Red regions indicate a high sample frequency, which means that there are a lot of measured data within this area. The figure above shows that from initially two peaks after about 85 hours a third peak develops, which indicates that the pump starts pumping off. The load increase between hour 20 and 80 confirms the fall of the liquid level in the annulus. The quality check also includes the observation of the lower maxima values. These values represent the behavior of the pump during the downstroke. The previous chapter presented that buoyancy has the major influence, which is in turn highly influenced by the density of the pumped fluid. Hence as long as the liquid level in the annulus falls, the pump is producing more or less the kill fluid

with a high density. Subsequently oil, water and gas, with a lower average density is produced, thus the buoyant force is decreased. In conclusion this means that the lower maxima curve should go a little bit upward, when the liquid level has equalized.

The following section displays the history plots for all Sensors and DMS for a quality check and trend analysis.

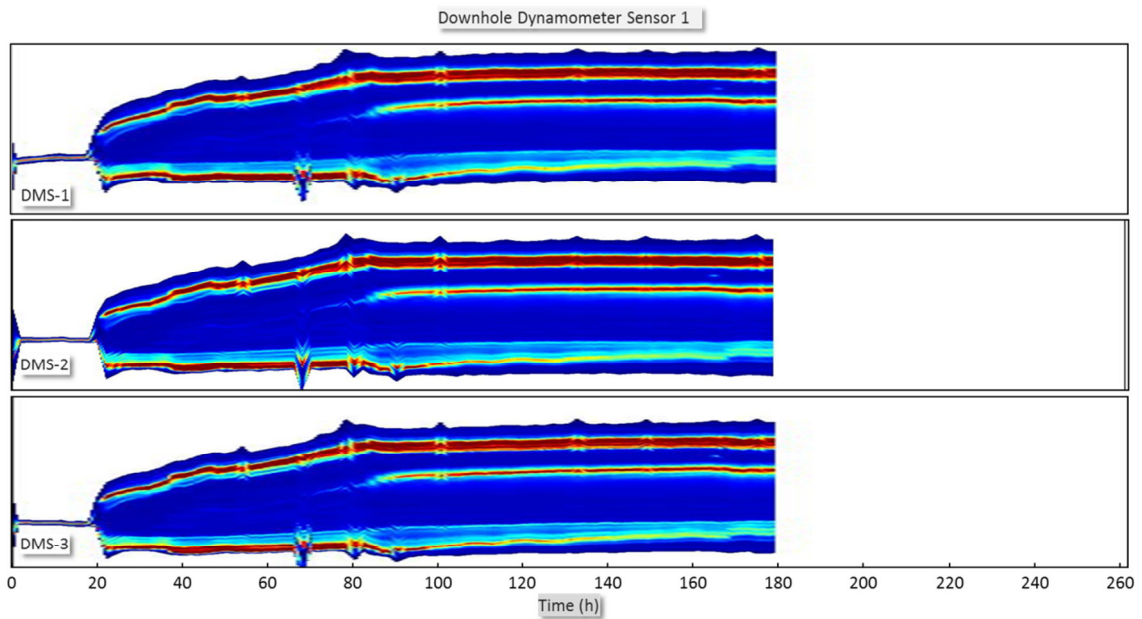


FIGURE 115: HISTORY PLOTS / DDS 1

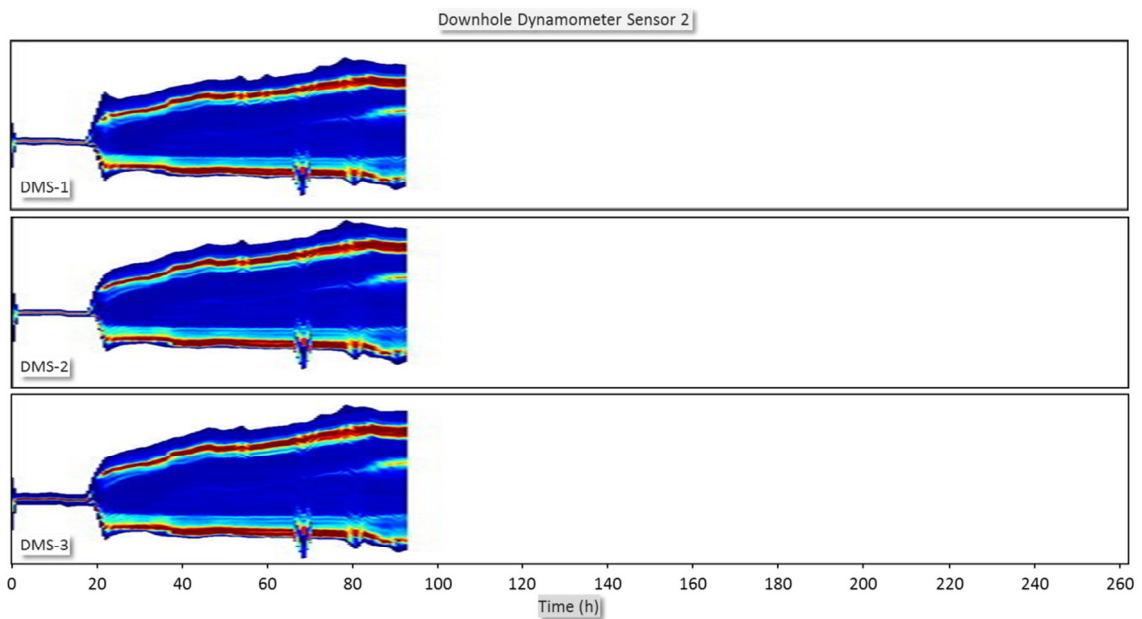


FIGURE 116: HISTORY PLOTS / DDS 2

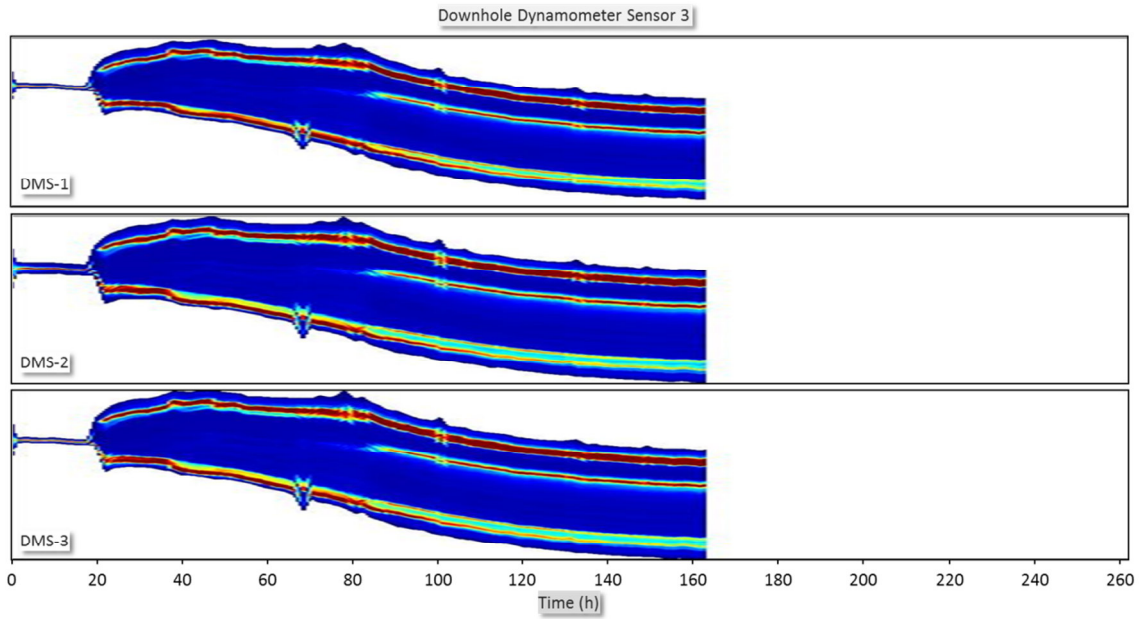


FIGURE 117: HISTORY PLOTS / DDS 3

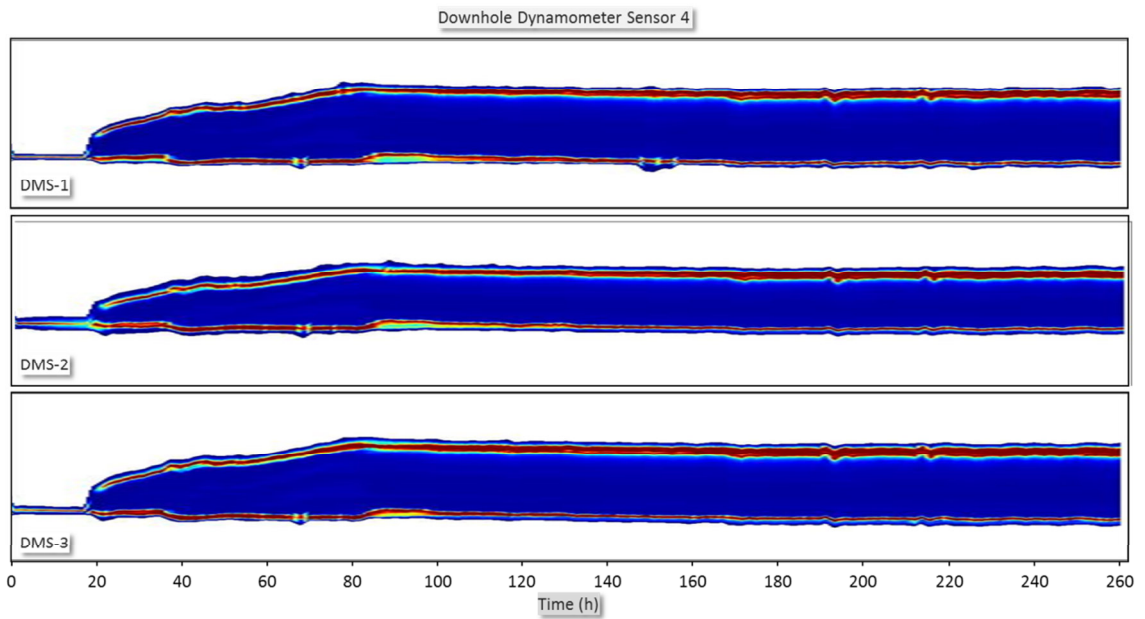


FIGURE 118: HISTORY PLOTS / DDS 4

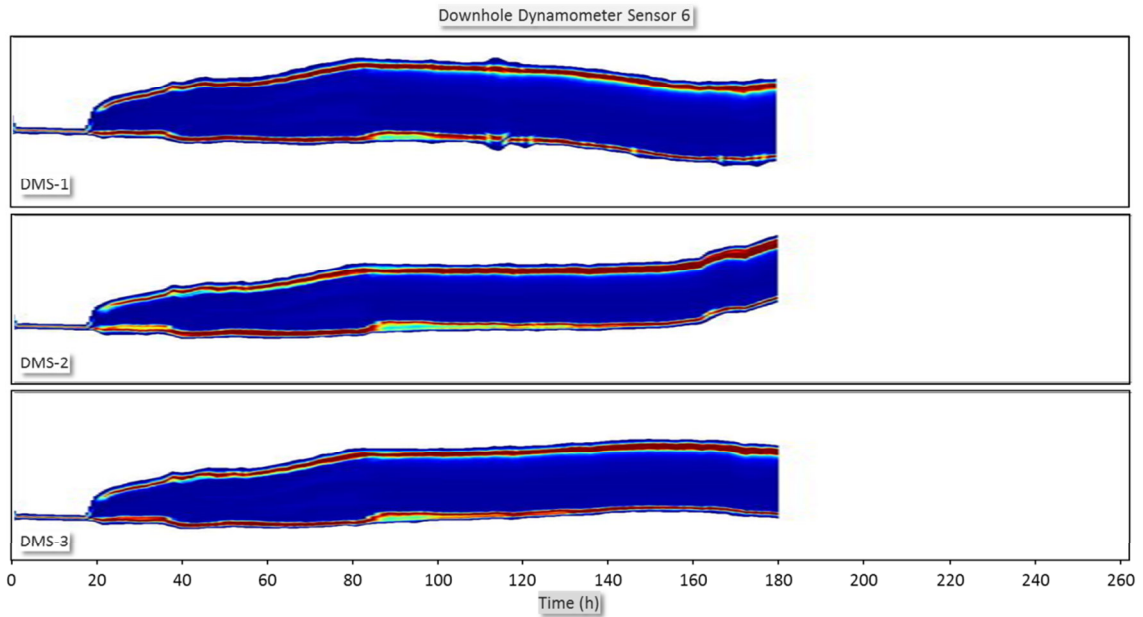


FIGURE 119: HISTORY PLOTS / DDS 6

A quick overview on the figures shows that the behavior of DDS 3 is uninterpretable, as well as the behavior of DDS 6, especially DMS 2, which got loosened during the field measurements. The recording duration of DDS 2 is relatively short, but DDS 1 and DDS 4 show a very good trend. On the basis of the fact that the results of DDS 3 and DD 6 cannot be used, only the remaining sensors DDS 1, DDS 2 and DDS 4 are used for further analysis.

The load in Newton is obtained from the measured data by using the calibration coefficients. The load readings from the three strain gauges are averaged, which gives the normal stress, hence tension or compression. The difference to the average value of the single readings represents the bending stress, which is evaluated in the next subchapter.

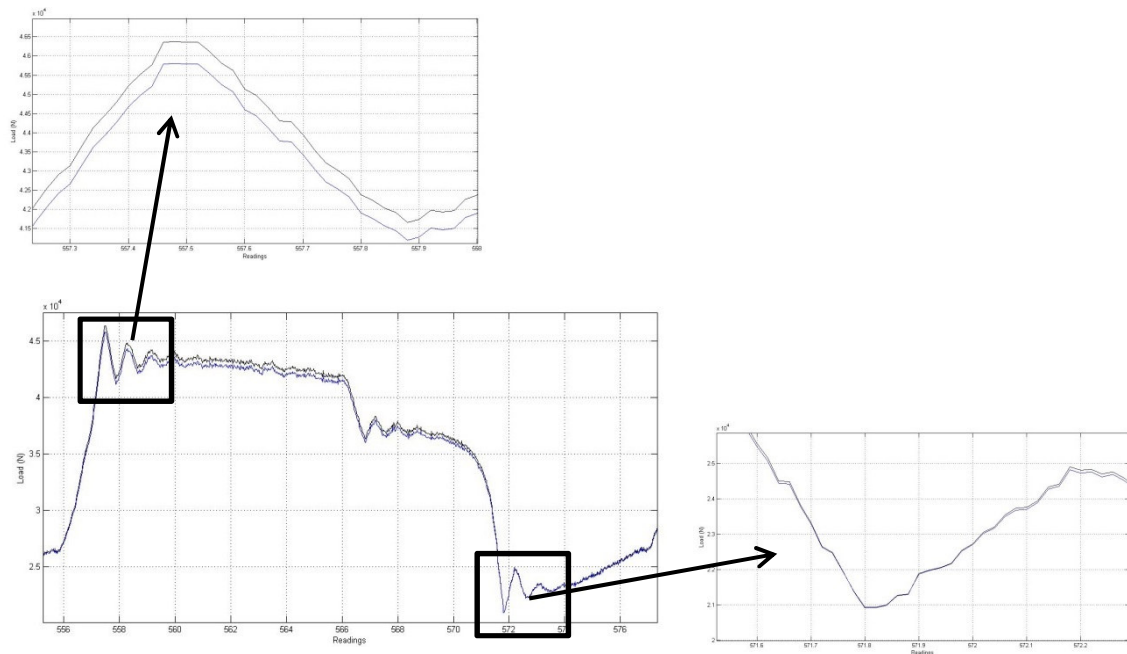


FIGURE 120: RECORDED DATA CONVERSION

The previous plots show the conversion from DDS 4 with the calibration before (black line) and after (blue line) the field measurements. It can be seen that the uncertainties during the upstroke are about 500N and during the downstroke about 10N. As a result the average values, obtained from these calibrations, are used.

The calibration leads to three force readings, one from each strain gauge. Due to their unique arrangement in the sensor, they allow the calculation of the normal load and the bending torque. The normal load is exactly the average of all three loads, as presented in Figure 121 by the black curve.

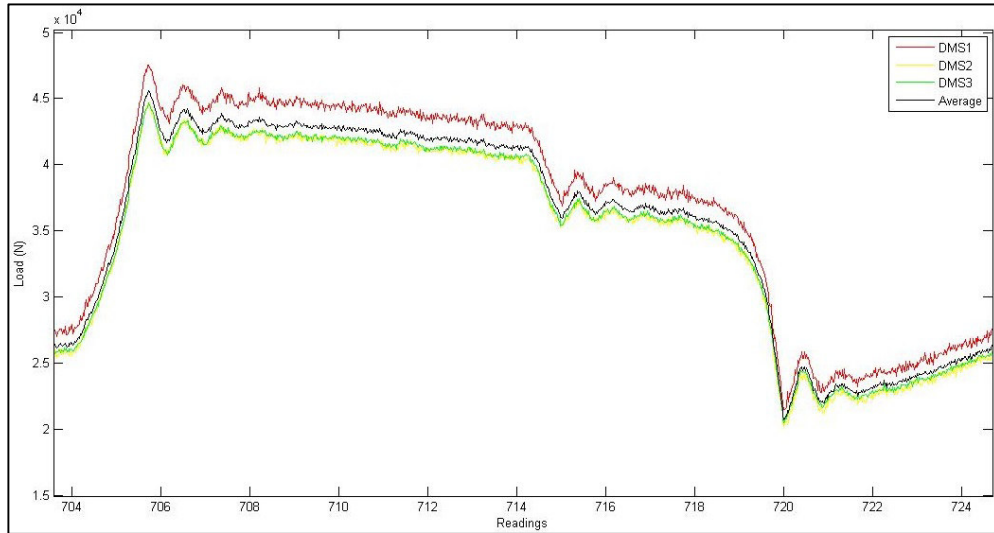


FIGURE 121: LOAD AVERAGING

The three strain gauge readings and their special arrangement also allow the evaluation of the relative bending torque M and the position of the bending axis β in relation to the strain gauges, by the following equation:

$$\sigma = \frac{\text{DMS reading}}{A}$$

$$\sigma = N + M \cdot \frac{A}{W} \sin(\beta)$$

The position of the bending axis primarily depends on the position of the DDS in the sucker rod string, but also on the up- and downstroke. Table 19 summarizes the behavior of the bending axis as well as the bending torque of the DDS 1 for 60, 120 and 180 hours of operation. It can be seen that the location of the bending axis stays more or less constant during one stroke and only changes a little bit with. This is a result of the fact that this sensor is installed in a vertical section of the sucker rod string. The bending torque follows the load.

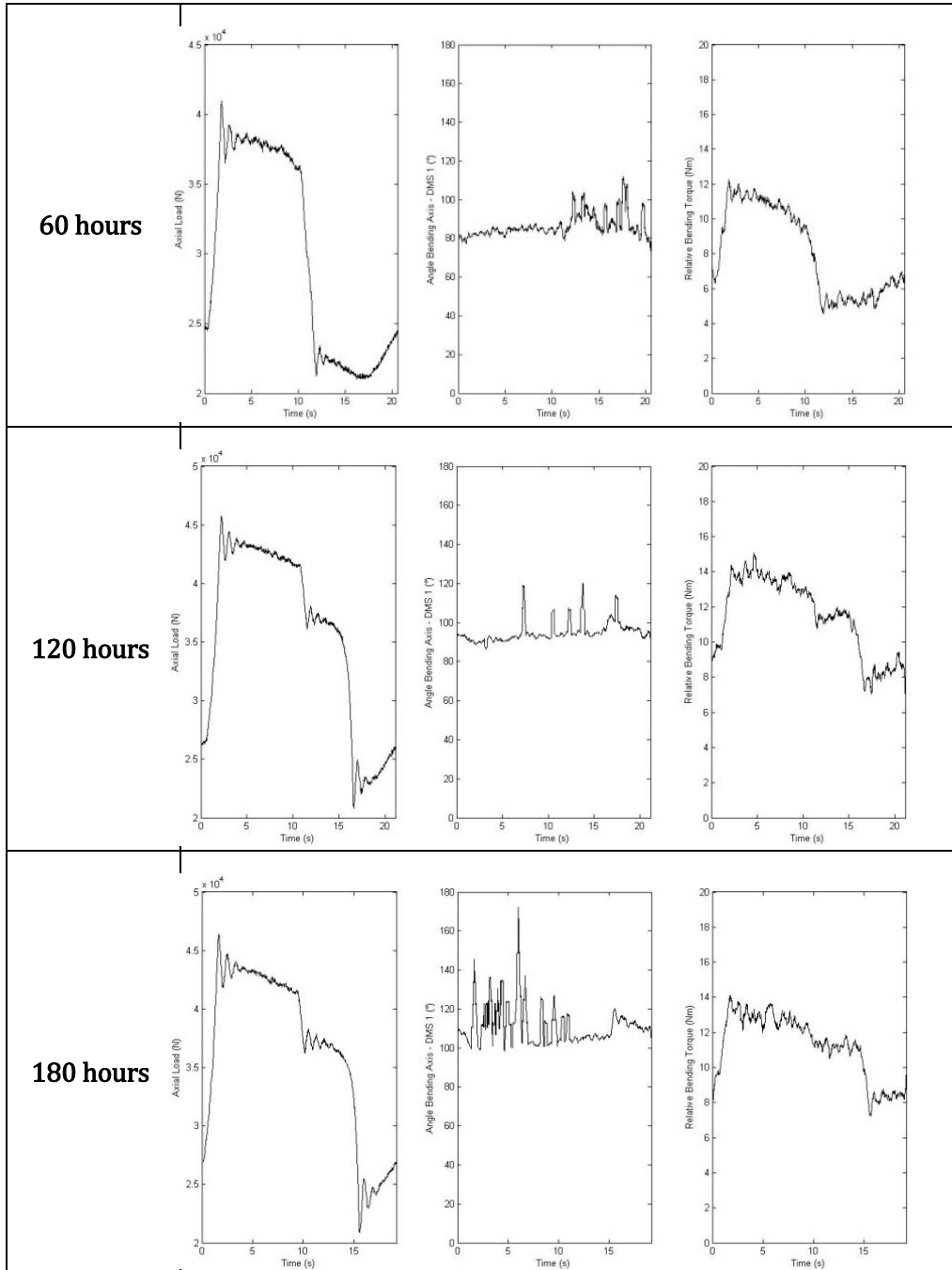


TABLE 19: BENDING AXIS & - TORQUE FOR DDS 1

Table 20 presents the same as Table 19 but for DDS 4. As DDS is installed in an inclined section, the effect of deviation is represented by the bending angle as well. The deviation angle shifts between up- and downstroke by 50 degrees. The magnitude of the bending torque is a little bit higher that for DDS 1.

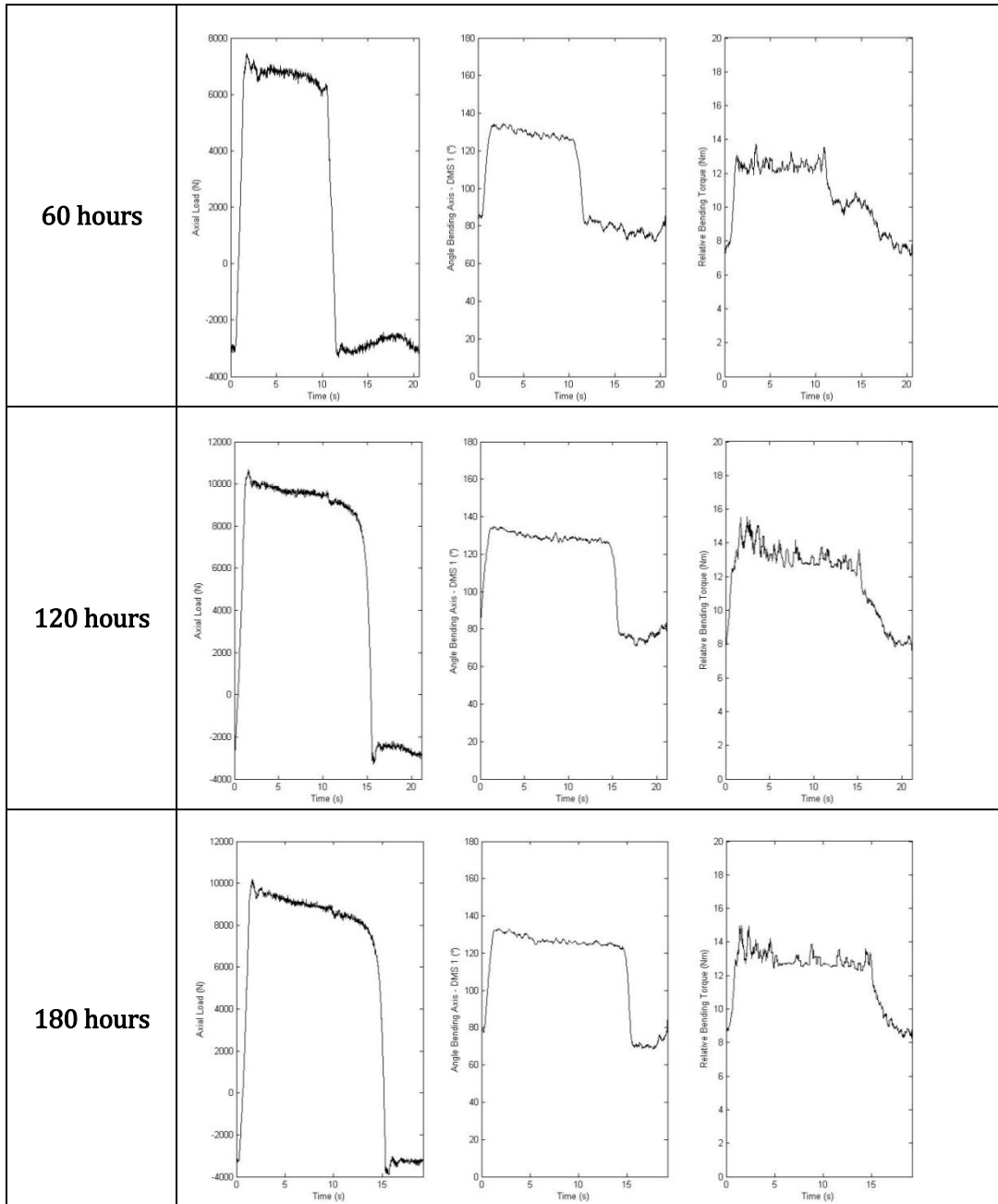


TABLE 20: BENDING AXIS & - TORQUE FOR DDS 4

Finally all the results can be brought together and dynamometer cards can be generated. These cards change their shape, depending on position and time. Figure 122 gives an impression of the dynamometer card shape development for the position at the polished rod (DDS 1) and downhole above the pump plunger (DDS 4) at significant time steps.

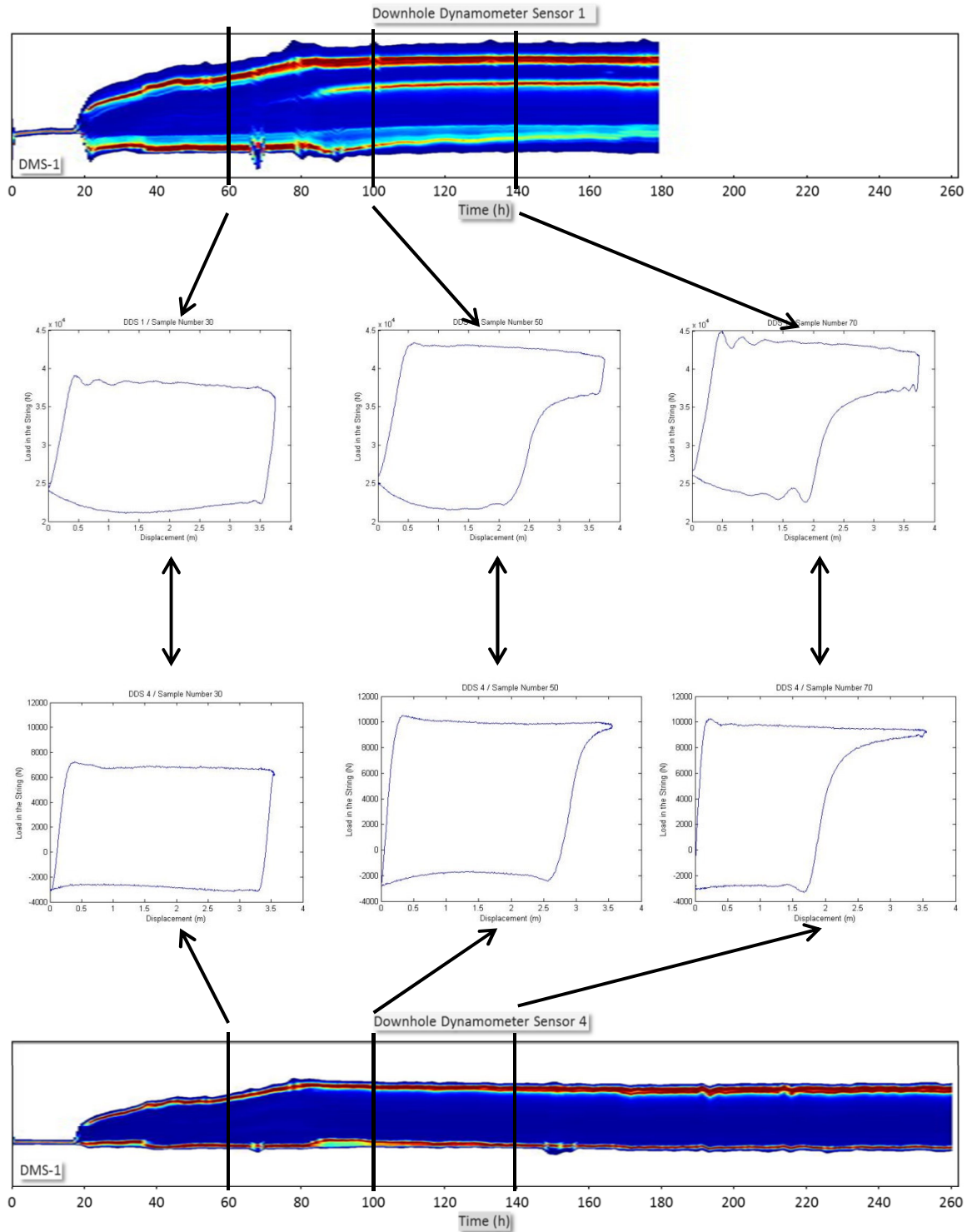


FIGURE 122: MEASURED DYNAMOMETER CARDS

Figure 122 clearly shows the increase in load over time due to the fall of the liquid level in the annulus as well as the formation of the pumped off condition.

The implementation of multiple DDS's along a sucker rod string provides a unique possibility to study its behavior. Beside the interesting temperature distribution and changes during the start after a work over operation, it can be important for the evaluation of paraffin precipitations. The evaluated motion of the pump plunger is a basis for the artificially set forces, which are highly motion dependent.

The most important result is the load profile at different positions and different times, which is used for the verification of the FEA and the adjustment of the friction and damping coefficients.

The major risk that comes along with the Downhole Dynamometer Sensor is the uncertainty caused by the measuring errors, which will be improved by a design adjustment for the next application.

6.6 SURFACE DYNAMOMETER CARD COMPARISON

The performance at the polished rod is checked by oil companies on a regular basis by analog dynamometer measurements, unless there are permanent devices installed at the wellsite for permanent monitoring. Figure 123 presents the comparison of such an analog measurement with the results obtained from the Downhole Dynamometer Sensor 1, which was installed close to the surface, directly below the polished rod. The readings of the analog measurements are about 3000N lower than the readings from DDS1. The reason therefor is not a male working DDS, but a lag in the calibration of the analog measurement systems, used for comparison. This circumstance is normally no problem, because only a qualitative review is for most oil companies satisfying. Except this fact the shape of both curves match.

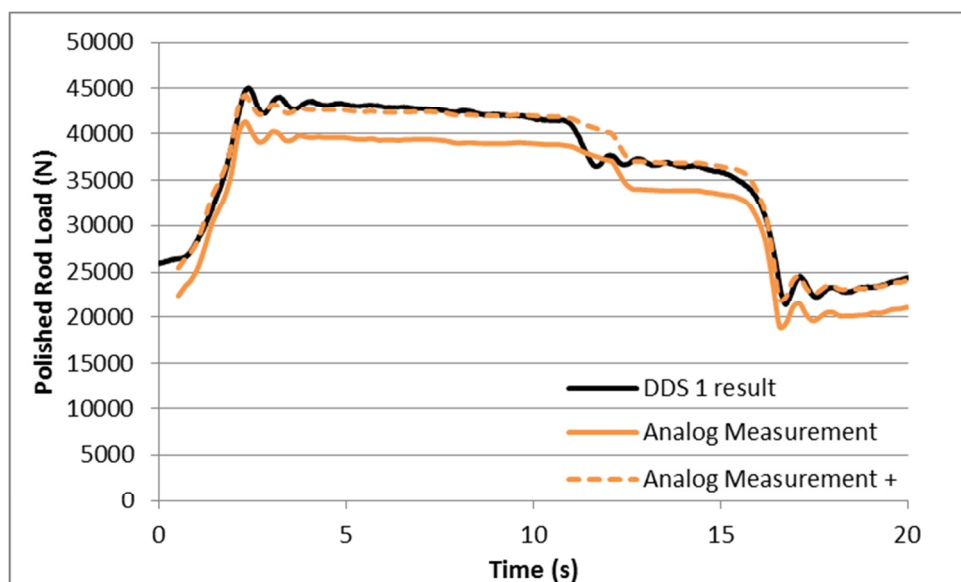


FIGURE 123: SURFACE DYNAMOMETER CARD COMPARISON

6.7 DOWNHOLE DYNAMOMETER CARD COMPARISON

This chapter presents a comparison of the measured downhole dynamometer card and the artificially generated dynamometer card. The gained information is used in the FEM – simulation, to simulate pumping systems, where no measurements were performed.

As a result of the complications with DDS 6, which was installed directly above the pump plunger during the field tests, the measurements performed with DDS 4 are used for this comparison. The most important part of the comparison are the maximum and minimum loads. Figure 124 presents the comparison of these two downhole dynamometer cards in one plot.

It can be seen that the minimum loads of the two pump cards are almost identical. This was reached by applying a relatively high coulomb friction coefficient to the system, which could be the result of some precipitations. This results in the relatively high maximum load of the artificially generated pump card, which doesn't care because of safety reasons.

The measured pump card represents a pump off condition, which is a not desired pump condition. That's the reason why the artificially generated DDC is designed for a full pump, assuming the dynamic liquid level in the tubing – casing annulus slightly above the subsurface pump. This can be sustained for instance for the same well as the measured DDC by an intermitted production.

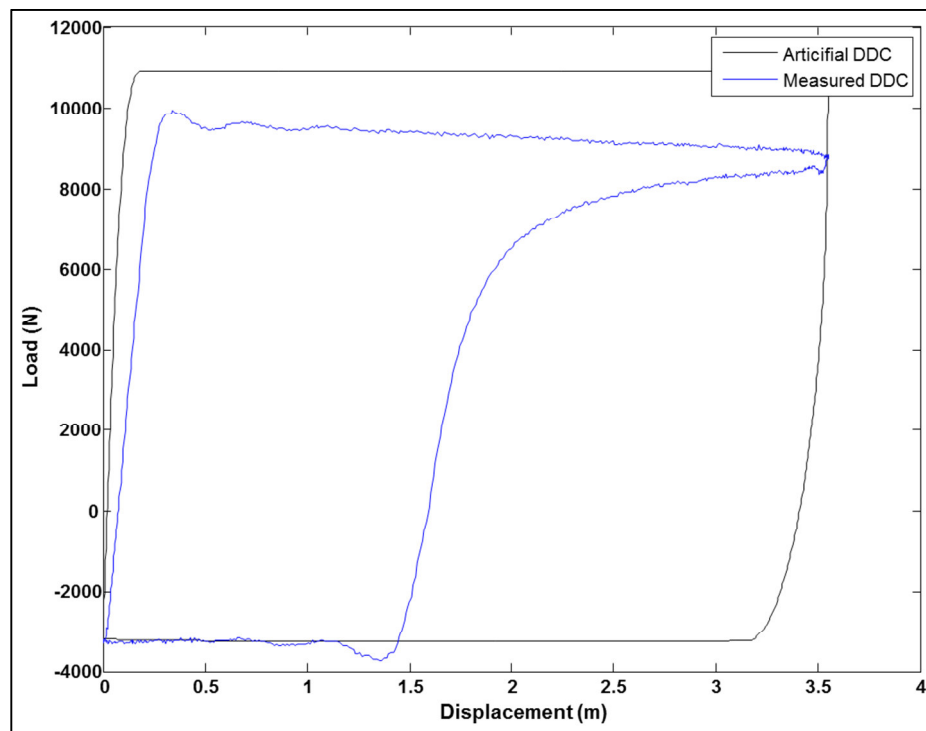


FIGURE 124: DOWNHOLE DYNAMOMETER CARD COMPARISON

After this verification of the downhole boundary model, the artificial pump card allows the approximation of the downhole conditions for different wells and conditions.

7 DYNAMIC FINITE ELEMENTS METHOD ANALYSIS

As discussed in Chapter 5 the sucker rod pumping system is a very complex system – hence only a numerical simulation is able to give precise and realistic results (26). Therefore such simulations are a necessity for obtaining accurate results. A simulation with such a high degree of complexity has so far never been performed.

The rod string of a sucker rod pump is a highly dynamical system. Due to the disproportion between the rod string diameter and the rod string length, even relatively small forces on the rods cause rod stretch or contraction and thus a change in acceleration, velocity and displacement along the sucker rod string. At no position along the sucker rod string, the kinematic behavior is completely the same, as a result of the materials elasticity and the travel speed of sound. For solving this problem, by the nature of the basic second order partial differential equation, always two boundary conditions are required. These boundary conditions can be defined at the polished rod and / or the pump plunger. In general these are represented by displacement and load over time behavior.

This chapter presents an innovative approach for describing and analyzing a sucker rod pumping system with Finite Elements. A special emphasis is laid on the contact definition between rod string and tubing, as well as the dynamic behavior of the rod string.

A FEA software program requires numerous input parameters for performing the analysis, which have to be provided to the solver via the graphical user interface or via an input file, which allow for much more flexibility. The used input files must have a specific structure with special keywords:

1. Mesh definition:
Defines the geometry and the mechanical behavior or bonds of the structure
2. Contact definition:
Defines the contact behavior of the interacting components
3. Material property definition:
Assigns the material's properties to the model
4. Boundary condition and amplitude definition:
Defines or constrains the motion of the system
5. Step definition:
Defines exactly the simulation conditions, like type and duration
6. Load definition:
Defines the actual load of the simulated structure

7.1 INPUT FILE STRUCTURE / DEFINITION

A numerical simulation requires a discretization of the analyzed structure, i.e. the mesh, as well as a boundary condition definition and the specification of numerous effects that occur during the real operation of the system.

This chapter presents how the numerical mesh for the sucker rod string is created, including a tapered rod string with different section lengths and diameters and of course the consideration of rod guides. Stabilization effects as well as the generation of the Input – File, using the programming software PYTHON (111) are shown.

7.1.1 MESH DEFINITION

The numerical mesh is based on nodes and elements, as a result of the geometry to be analyzed. In addition special effects, like fluid stabilization of the rod string must be already considered at this stage. The first part of the meshing process is to define which components of the real system must be considered under which circumstances. For the sucker rod pumping system the following items are considered:

- *Wellbore trajectory:*
Directional trajectories with doglegs, etc. can be simulated
- *Tubing:*
Any tubing size or tapered tubing strings as rigid component, fixed in the center of the wellbore
- *Rod string:*
Tapered rod string with different diameters and section lengths, which are allowed to move freely in the tubing string (sinker bars and the tensioning element can be considered).
The fluid effects in the tubing (friction, stabilization effect) are implemented
- *Rod guides:*
Rod guides can be defined at specified positions along the rod string to guide the rods in the tubing. Each rod string section can have a different number of rod guides per segment.
- *Subsurface pump:*
Different pump sizes are analyzable
- *Operational parameters:*
Any surface stroke length, stroke profile or strokes per minute can be considered

The nodes are based on the wellbore trajectory, which again is a result of the relative position of the reservoir layer and the starting point of the well. Stratified layers in the ground can cause small deviations during the drilling process, called doglegs. After drilling the well a survey of the wellbore is performed to get exact trajectory and geometry data. The data gained by this survey define the center of the wellbore, which acts as reference position for the casing, tubing and sucker rod string at the beginning of the analysis. Wellbore geometry data are often provided as Cartesian coordinates in increments of about 40 meters. This distance is clearly too inaccurate, to directly use it as input for a numerical

simulation. As a result the first step of the mesh generation is to derive a cubic spline, based on the trajectory survey. This spline allows thereafter an exact definition of the wellbore trajectory at any point. Figure 125 presents the trajectory of Well OMV 1, already including the complete length of the sucker rod string.

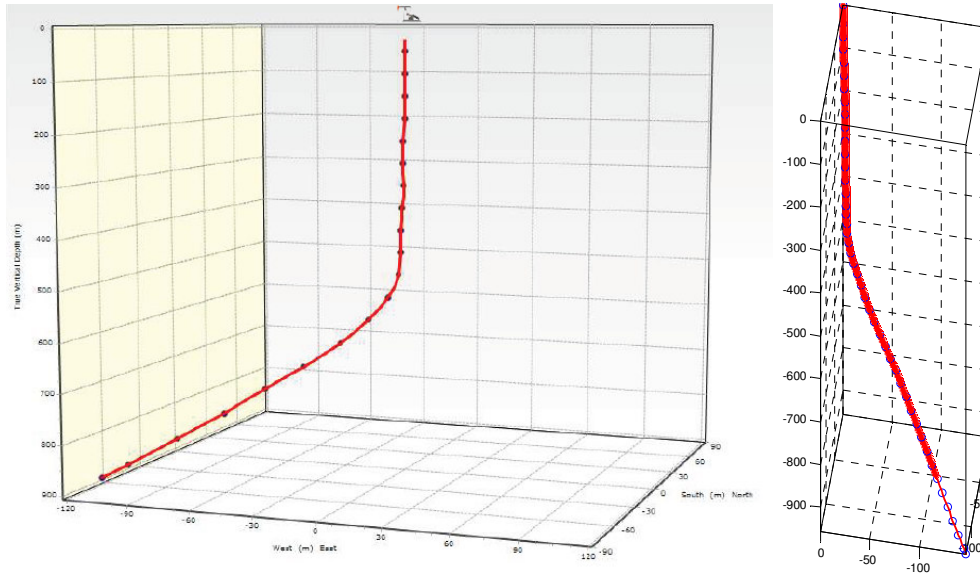


FIGURE 125: TRAJECTORY OF WELL OMV 1

In the field a rod string can be composed out of rod sections with several diameters, a so called tapered rod string. This is a result of different needs at different positions. The conventional design uses sinker bars with heavy weight or sucker rods with bigger diameter at the bottom of the rod string to tension the rod string. The intermediate section uses thin rods to reduce the weight of the overall string. At the top bigger sized rods must be used to support the loads. The elongation and the dynamic behavior of rods with different diameters under the same load differ. As a result the model is composed out of several sections. One section is the continuous length of the portion of the sucker rod string with the same diameter.

The next step is the evaluation of the number of rods per section. In the field in addition to the 25' or 30' long standard sucker rods, so called pony rods, which are rods with shorter lengths, are used to space out the pump. Pony rods are not considered, hence the length of the modelled rod string can differ from the original string by 1 or 2 meters, which is a negligible distance in comparison to a 1000 or 2000 meter long sucker rod string.

Each rod can further be split into segments. The position of the partitioning is dependent on the composition of the rods itself. Nowadays sucker rods are composed out of the steel body and two or four rod guides at special positions, dependent on the oil company's needs. In Figure 61 it can be clearly seen that the rod guides are not equally spaced, especially at the ends of the rod. The general idea is to position a node exactly at the location of the rod guides and exactly at the location between two rod guides, hence four nodes for a rod with two rod guides and eight nodes for a rod with four rod guide. Rods without rod guides, which are rarely used, are defined to have four nodes, equally spaced.

As discussed above, the rod couplings are not exactly in the middle between two rod guides. Hence it is necessary to check if the blanked rod or the rod coupling, which is used for connecting consecutive sucker rods and are of course of bigger diameter than the rod itself, comes in contact with the tubing inner wall. This analysis assumes a sinusoidal shape of the buckled sucker rod string. There are standard and slim-hole couplings available (see Table 21). Table 22 summarizes for the combination of three different tubing sizes (2 3/8", 2 7/8" and 3 1/2") and rod diameters with standard and slim-hole couplings, if contact for sinusoidal buckling occurs at the tubing by the rod coupling.

API Size (in.)	OD (in.)		Weight (lb/kg)	
	Standard	Slimhole	Standard	Slimhole
5/8	1-1/2	1-1/4	1.30 0.59	1.00 0.45
3/4	1-5/8	1-1/2	1.50 0.68	1.26 0.57
7/8	1-13/16	1-5/8	1.80 0.82	1.50 0.68
1	2-3/16	2	2.58 1.17	2.01 0.91
1-1/8	2-3/8	—	3.13 1.42	—

TABLE 21: SIZES OF STANDARD AND SLIMHOLE COUPLINGS (112)

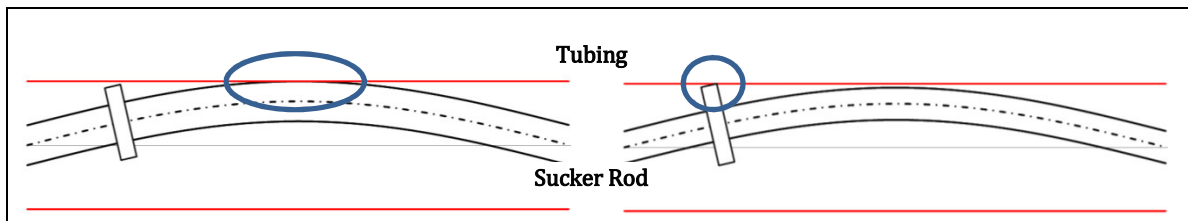


FIGURE 126: TUBING - SUCKER ROD / COUPLING CONTACT

	Standard Coupling	Slim-hole Coupling
2 3/8"		
5/8"	X	
3/4"	X	X
7/8"	X	X
2 7/8"		
5/8"		
3/4"		
7/8"	X	
1"	X	X
3 1/2"		
5/8"		
3/4"		
7/8"		
1"	X	

TABLE 22: TUBING – ROD COUPLING CONTACT

Table 22 indicates that for the small tubing sizes, even the slim-hole couplings get in contact with the inner tubing wall, before the rod itself touches the tubing, when buckling occurs.

As a result the nodes for the numerical mesh must be defined in dependence of the used equipment. Finally to get the Cartesian coordinates of the nodes, the spline is cut into increments, equal in length to the previously evaluated distance between the nodes.

The definition of the elements is based on the created nodes. Each element combines certain nodes and constructs in this way the mesh for the numerical model. This numerical analysis uses the beam element B32, which is a three node quadratic beam in space. Quadratic means that there are two integration points within the element. Figure 127 presents a B32 beam. The three points present the nodes to be connected and the crosses the corresponding integration points. At the integration points stresses within the beam cross-section are evaluated.

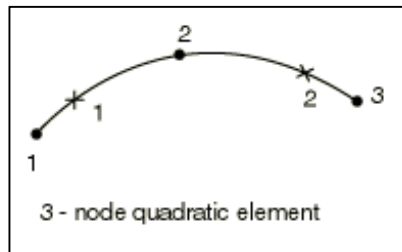


FIGURE 127: B32 BEAM ELEMENT (113)

In addition to the element definition, the beam section must be defined. The beam section defines the shape of the cross-section with its parameters, the beam element cross-section orientation and the material properties.

For the shape definition a circular cross-section is used. A circular section in space consists of 3 points radially and 8 points circumferentially (see Figure 128). Integration point 1 is situated at the center of the beam and is used for output purposes only. Stress outputs are provided at intersections with the surface and the axis 1 and 2, which are represented by the points 3, 7, 11 and 15.

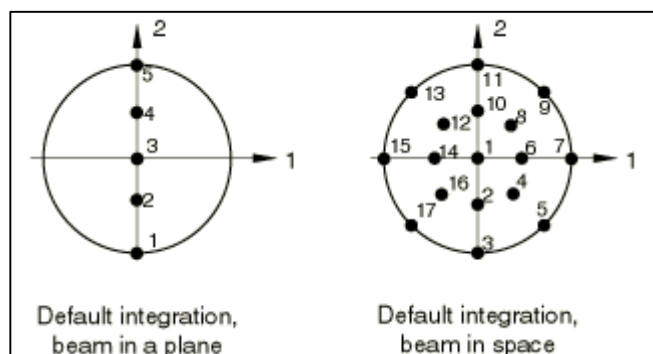


FIGURE 128: CIRCULAR CROSS-SECTION DEFINITION (114)

The beam element cross-section orientation is defined by the vector (t, n_1, n_2) , where t is the tangent to the axis of the element, positive in the direction from the first to the second node of the element, and are basis vectors that define the local 1- and 2-directions of the

cross-section. is referred to as the first beam section axis, and is referred to as the normal to the beam.”(113)

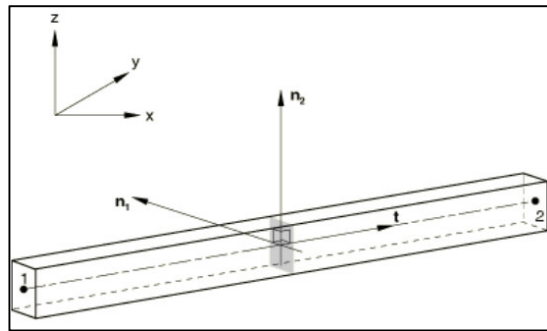


FIGURE 129: BEAM ELEMENT CROSS-SECTION ORIENTATION (115)

All the above presented calculations are done by MATLAB (116), which creates several files, containing the node and element information, required by the Input file. The MATLAB code can be found in Appendix F:

rodnummer_V0.txt	Contains the Cartesian coordinates of the node position
MD_V0.txt	Contains the measured depth of the node position
rodelement1_V0.txt	Contains the element definition of section 1
rodelement2_V0.txt	Contains the element definition of section 2
rodnummerfeder_V0.txt	Contains the definition of the nodes for the spring elements
rodnummerpipe_V0.txt	Contains the definition of the nodes for the tubing string
Tangente_V0.txt	Contains the direction of the tangent of each element
Federkonstante_V0.txt	Contains the spring constant for the spring elements
Fluid_Reibung_V0.txt	Contains the fluid friction amplitude per segment

The following code is the part of the input file, that deals with the mesh definition:

```
*Node, INPUT=rodnummer_V0.txt, nset=n_rod
*Element, ELSET=el_rod1, type=B32, INPUT=rodelement1_V0.txt
*Beam Section, elset=el_rod1, material=steel, poisson=0.3, temperature=GRADIENTS, section=CIRC
0.011
*Nonstructural Mass, elset=el_rod1, units=MASS PER LENGTH
0.4
*Element, ELSET=el_rod2, type=B32, INPUT=rodelement2_V0.txt
*Beam Section, elset=el_rod2, material=steel, poisson=0.3, temperature=GRADIENTS, section=CIRC
0.011
*Nonstructural Mass, elset=el_rod2, units=MASS PER LENGTH
0.4
*Nset, nset=boundaryrodoben
2000
*Nset, nset=force
2468
*Include, INPUT=Federn_Base_Case0.txt
```

A nonstructural mass of 0,4 kg is added to the beam elements, because they do not consider the weight of the rod guides and rod couplings. In addition to the beam elements, spring elements are used to simulate the stabilization effect of the rod surrounding fluid (45). The file *Federn_Base_Case0.txt* contains all required information on the springs that simulate the radial fluid pressure. Due to the fact that the springs are only allowed to balance radial movements of the rod string, their attachment points have to move with the lateral motion of the sucker rod string.

```
*Node, INPUT=rodnummerfeder_V0.txt, nset=nrod_feder
*ELEMENT, type=SPRINGA, elset=feder2
10002, 2002, 4002
*SPRING,ELSET=Feder2
.....
*Nset, nset=Mset
4002,4004,4006,4008,.....
*Nset, nset=Uset
2001,2003,2005,2007,.....
*Nset, nset=Lset
2003,2005,2007,2009,.....
*Equation
3
Mset,1,2.,Uset,1,-1.,Lset,1,-1
3
Mset,2,2.,Uset,2,-1.,Lset,2,-1
3
Mset,3,2.,Uset,3,-1.,Lset,3,-1
*Nset,nset=node2000
2000,
.....
```

7.1.2 CONTACT DEFINITION

During the up- and downstroke the sucker rod string is in continuous interaction with the tubing string. The sliding in the lateral direction causes mainly contact, hence friction between the rod guides and the tubing, but also a movement in radial direction, which can result, depending on its magnitude, in contact between the steel rod and the tubing. As a result realistic friction coefficients for these two material combinations have to be defined.

ABAQUS allows the modelling of the finite-sliding interaction between two pipes by so called tube-to-tube contact elements (ITT31 – Elements) (117). These elements assume a predominant sliding of the inner tube along a predefined slide-line, in most cases defined by the outer tube and a relatively small radial movement. The modeling of the ITT-Elements can be done in four steps: (118)

- Definition of the ITT-Elements
- Interface definition
- Friction definition
- Slide line definition

The interface defines the radial clearance of the outer tube to this slide line, which corresponds to the inner radius of the tubing minus the radius of the sucker rods or the inner radius of the tubing minus the outer radius of the rod guides, respectively.

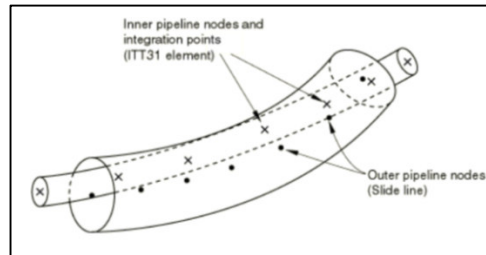


FIGURE 130: ITT-ELEMENT (117)

Therefore MATLAB provides the following input files:

- ittelement_1oP_V0.txt Contact definition at nodes without rod guides/ section 1
- ittelement_1mP_V0.txt Contact definition at nodes with rod guides/ section 1
- ittelement_2oP_V0.txt Contact definition at nodes without rod guides/ section 2
- ittelement_2mP_V0.txt Contact definition at nodes with rod guides/ section 2

The following code represents the contact definition for the FEA:

```
*Element, ELSET=el_itt1oP, type=ITT31, INPUT=ittelement_1oP_V0.txt
*Interface, ELSET=el_itt1oP
0.0198
*Friction
0.2
*Element, ELSET=el_itt1mP, type=ITT31, INPUT=ittelement_1mP_V0.txt
*Interface, ELSET=el_itt1mP
0.001
*Friction
0.12
*Element, ELSET=el_itt2oP, type=ITT31, INPUT=ittelement_2oP_V0.txt
*Interface, ELSET=el_itt2oP
0.0198
*Friction
0.2
*Element, ELSET=el_itt2mP, type=ITT31, INPUT=ittelement_2mP_V0.txt
*Interface, ELSET=el_itt2mP
0.001
*Friction
0.12
*NODE, INPUT=rodnummerpipe_V0.txt, NSET=n_tubing
*SLIDE LINE, ELSET=el_itt1oP, TYPE=parabolic, GENERATE
6000, 6468, 1
*SLIDE LINE, ELSET=el_itt1mP, TYPE=parabolic, GENERATE
6000, 6468, 1
*SLIDE LINE, ELSET=el_itt2oP, TYPE=parabolic, GENERATE
6000, 6468, 1
*SLIDE LINE, ELSET=el_itt2mP, TYPE=parabolic, GENERATE
6000, 6468, 1
```


7.1.3 MATERIAL PROPERTY DEFINITION

The beam elements must be assigned with material properties. Within this thesis only steel sucker rods are considered, is assumed to behave elastic only. In principle a wide range of material behaviors can be defined. The density of steel is 7850 kg/m^3 , the modulus of elasticity is $210\,000 \text{ MPa}$ and the Poisson ratio is $0,3$.

In addition ABAQUS allows the implementation of material damping (119). In dynamic analysis it can be necessary, if energy dissipation sources are missing, to introduce some general damping (Rayleigh damping). It provides a convenient procedure to damp lower (mass-dependent / α) and higher (stiffness-dependent / β) frequencies. The mass dependent damping introduces damping forces that simulate the idea of the model moving through a viscous media, so that any motion of any point in the model causes damping.

Stiffness proportional damping causes damping proportional to the strain rate. The effect is that damping is associated with the material itself, which is proportional to the modulus of elasticity of the used material.

```
*Material, name=steel
*Damping, alpha=0.1, beta=0.04, composite=0.0, structural=0.
*Density
7850.,
*Elastic
2.1e+11, 0.3
```

7.1.4 BOUNDARY CONDITION AND AMPLITUDE DEFINITION

The next section of the input file is the definition of the boundary conditions. In three dimensions each node of a structural element has six degrees of freedom. As the tubing is assumed to be fixed, no motion is allowed, all degrees of freedom are constrained, and hence all nodes belonging to the tubing are fixed by the term ENCASTRE.

The top node of the sucker rod string moves through the stuffing box only in the vertical direction, thus the command ZASYMM is employed to restrict motion in x and y direction. The motion in z-direction is defined by an amplitude function, representing the motion of the polished rod *Hub_90_Base_Case.txt*. Supplementary load amplitude and friction amplitude is defined.

```
*Boundary
n_tubing, ENCASTRE
*Boundary
boundaryrodoben, ZASYMM
*Amplitude, name=Amplitude1, INPUT=Hub_90_Base_Case.txt, time=TOTAL TIME, smooth=0.3
*Amplitude, name=Amplitudeload1, INPUT=Last_plunger_90_Base_Case.txt, time=TOTAL TIME,
smooth=0.3
*Amplitude, name=AmplitudeFriction, INPUT=Fluid_Reibung_Base_Case.txt, time=TOTAL TIME,
smooth=0.3
```

7.1.5 STEP DEFINITION

In ABAQUS the step definition defines the parameters for the simulation procedure. The simulation of the sucker rod system is divided into three steps. The first step does not prescribe any motion – only the gravitational force is applied. This first step simulates three seconds to settle the initial vibrations. Step two and three each represent one complete pumping cycle. Initial effects after starting the simulation can disturb the results of step two. Hence only the results of step three are used for post processing.

The solution algorithm is DYNAMIC implicit with MODERATE DISSIPATION. Moderate dissipation will add larger than default damping and a more aggressive time incrementation to the solution by an accepted reduction of the accuracy. Without this modification a stable simulation result is difficult to achieve.

```
*Step, name=Step_gravity, nlgeom=YES, inc=6000, unsymm=YES, CONVERT SDI=NO
*Dynamic, APPLICATION=MODERATE DISSIPATION
0.1, 3.0, 1e-05, 0.2
.....
*End Step

*Step, name=Step_load, nlgeom=YES, inc=6000, unsymm=YES, CONVERT SDI=NO
*Dynamic, INITIAL=NO, APPLICATION=MODERATE DISSIPATION
0.005, 19.2, 1e-08, 0.3
*CONTROLS, PARAMETERS=TIME INCREMENTATION
```

7.1.6 LOAD DEFINITION

At end of each step definition the actual load definitions is set. The nodes, where load amplitudes are defined, are stated and the type of load, like distributed load or concentrated load are provided to the input file. At the end output properties are set. The load definition for the first step activates only gravity:

```
*Boundary
boundaryrodoben, 3,3, 0
*Dload
, GRAV, 9.81, 0., 0., -1.,
*Output, field, frequency=1, variable=PRESELECT
*Output, history, variable=PRESELECT
```

For the second and third step the plunger load, as a concentrated load is added at the lowest point of the sucker rod string and the viscous friction force is added as distributed load along the complete rod string:

```
*Boundary, amplitude=Amplitude1
```

```

boundaryrodoben, 3, 3, 1.
*Clod, amplitude=Amplitudeload1
force,1, -0.34893
force,2, -0.34056
force,3, -0.87308
*Include,INPUT=Cload_Base_Case0.txt

```

Fluid friction from the previously defined amplitude function is added *Cload_Base_Case0.txt*, as well as the plunger load *Last_plunger_90_Base_Case.txt*.

```

*CLOAD,AMPLITUDE=AmplitudeFriction
node2000,1, -0.00276
node2000,2, -0.01003
node2000,3, -0.99995
.....

```

The complete input file is coded in Python, which allows easy and fast changes of properties and adjustments. (see Appendix F)

7.1.7 SRABS IMPLEMENTATION

The implementation of SRABS into the simulation divided, according to the number of inventions, into two parts.

The first part considers the dynamic liquid level to the pump plunger during the downstroke, instead of the tubing pressure, which is essentially lower and prevents the sucker rod string from buckling for low pumping rates e.g. 8 strokes per minute, depending on the properties of the sucker rod pumping system. The implementation of this effect is done by adjusting the load amplitude at the pump plunger to the new conditions. The ABAQUS input file not to have to be changed at all.

```

*Amplitude, name=Amplitudeload1, INPUT=Last_plunger_90_SRABS_18_3SPMm.txt, time=TOTAL
TIME, smooth=0.3

```

The implementation of the tensioning element, required at higher pumping speeds, is achieved by adding a single sucker rod segment below the pump plunger. The diameter of this section can be adjusted to reach the required mass, but it must not exceed the space in the tubing without leaving a clearance for the liquid to flow into the pump. If the mass must be increased nevertheless, another rod segment can be added below the pump plunger.

The following code shows the sections that must be added to the standard input file to consider SRABS:

```

*Element, ELSET=el_rod3, type=B32, INPUT=rodelement3_V22m.txt
*Beam Section, elset=el_rod3, material=steel, poisson=0.3, temperature=GRADIENTS, section=CIRC
0.01905
*Nonstructural Mass, elset=el_rod3, units=MASS PER LENGTH
10
.....
*Element, ELSET=el_itt3mP, type=ITT31, INPUT=ittlement_3mP_V22m.txt
*Interface, ELSET=el_itt3mP
0.005
*Friction
0.12
.....
*SLIDE LINE, ELSET=el_itt3mP,TYPE=parabolic, GENERATE
6000,6470,1

```

7.2 SIMULATION CASES

The above described numerical simulation model is able to analyze the sucker rod string under various conditions, like trajectory, equipment dimensions, fluid properties and boundary conditions, which makes the model very flexible. This circumstance allows the introduction of three basic simulation cases, important for the application in the oil industry:

- *Sucker Rod String Friction Analysis:*
The rod string friction analysis is used to detect and investigate the friction between the sucker rod string and the tubing. The obtained results can be very useful for increasing the accuracy of further simulations and for finding zones of excessive paraffin precipitations.
- *Diagnostic Analysis:*
The diagnostic analysis is used for investigating the performance of the pump plunger during the operation of the pump on a regular basis. The results are used to optimize the pumping system.
- *Predictive analysis:*
The predictive analysis is used for predicting the performance of new, in the future installed sucker rod pumps and optimizations. The outcome of this analysis is very important for designing the pump, the rod string and the operation conditions.

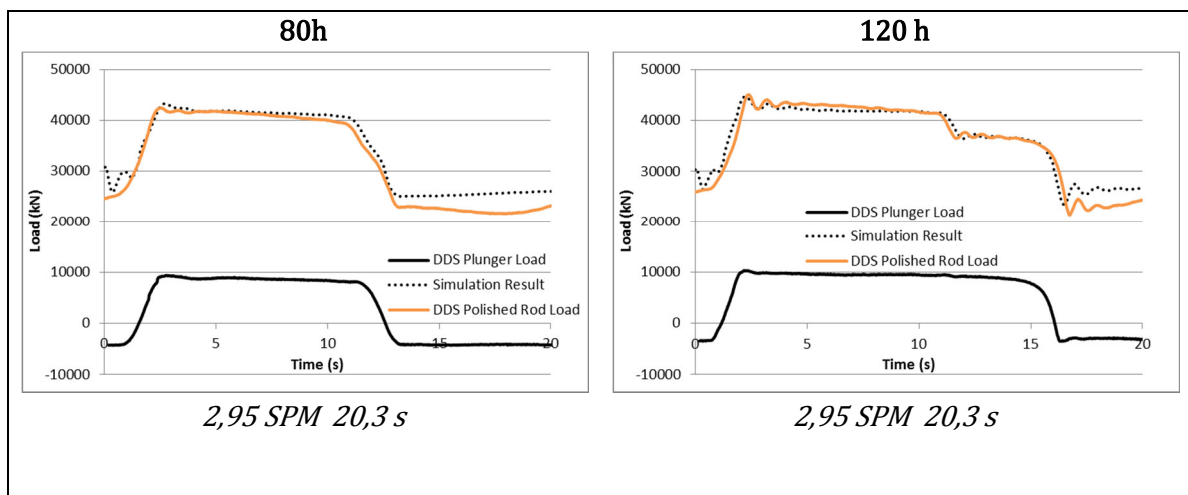
7.2.1 SUCKER ROD STRING FRICTION ANALYSIS

The sucker rod string friction analysis is used to evaluate the Coulomb friction coefficient between tubing and rod guides and the material damping coefficients under real conditions. To obtain appropriate results two sets of load measurements must be available:

- Load behavior at the polished rod:
This load amplitude can be measured by a classical surface dynamometer or a DDS installed close to the surface.
- Load behavior at the pump plunger:
This load amplitude has to be measured by a DDS, installed close to the pump plunger.

The FEA model using the above presented input file provides the basis for the evaluation. The displacement boundary condition at the polished rod is given by the Svinos – model. The DDS measurements, performed at Well OMV 1, provide the required load amplitudes. The simulation uses the measured pump plunger load amplitude. The simulated polished rod load is compared with the measured one. Erratic motion of the simulated load can be reduced by increasing the material damping coefficients.

Simulations for four different times after starting the pump are performed. Figure 131 visualizes the results. The black line at the bottom represents the measured pump plunger load, the orange curve the measured polished rod load and the black, dashed line the simulation result. The pump was operating under pump off condition, which gives the unique possibility to determine the friction coefficient very accurately. The load difference during upstroke and the beginning of the downstroke represents only friction. If the friction coefficient is chosen too high, the simulation result would be higher than the measured results during the upstroke and too low during the downstroke.



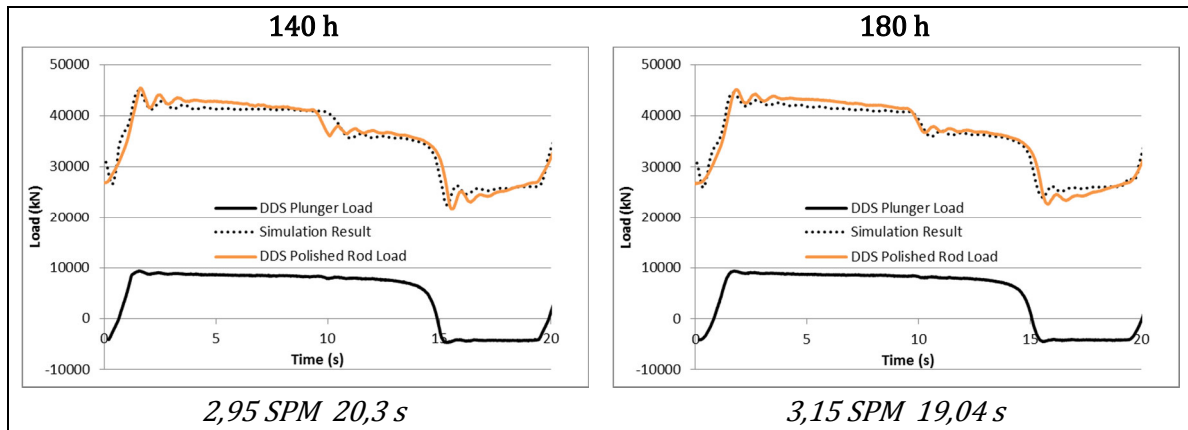


FIGURE 131: SUCKER ROD STRING FRICTION ANALYSIS

Numerous simulations showed that a friction factor of 0,12 should be selected for the interaction tubing – rod guide. The impact of the interaction tubing – rod is minor, hence it is defined with 0,2, which is the common friction coefficient at the interface steel to steel.

This simulation case results in very useful parameters, like friction coefficients and damping coefficients for further simulations and optimizations, with the limitation of required downhole measurements.

7.2.2 DIAGNOSTIC ANALYSIS

This analysis is used to diagnose the performance of running sucker rod pumping systems. The displacement function at the polished rod, as well as the load function at the polished rod is provided by a conventional dynamometer measurement. A limitation of the FEA is that the application for sucker rod pumping requires one boundary condition at the surface, which is the predefined motion of the polished rod and another boundary condition at the pump plunger. As a result the surface load measurement cannot be used directly in the simulation.

To overcome this limitation the plunger load is cut into defined time intervals. An iterative procedure then evaluates the correct load. This procedure assumes at the beginning for each time step a probable plunger force. The selected force is used to simulate the polished rod load, which is in turn compared to the actual measured polished rod load. If the difference between simulated and actual polished rod load is within the chosen accuracy, the simulation continues with the next time step, if not the previously selected plunger load is changed until the required accuracy is obtained.

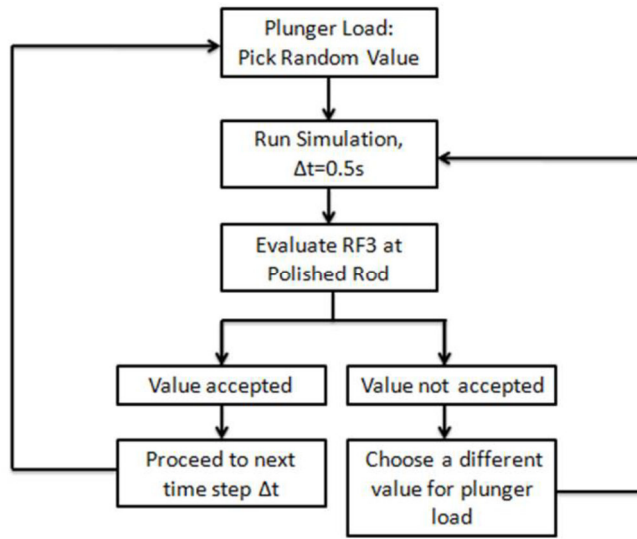


FIGURE 132: DIAGNOSTIC ANALYSIS / ITERATION PRINCIPLE REF (120) PAGE 46

The weakness of the diagnostic analysis is that its results depend on the influencing parameters like the accuracy of the surface dynamometer measurements, fluid friction and Coulomb friction factor. The quality of the measurement can be improved by calibrating the measuring tool. The influence of fluid friction can be handled by improving multiphase fluid friction simulations along the tubing string. The difficulty is the Coulomb friction. It changes with the temperature of the lifted liquid and thus may change during the lift of the sucker rod pumping system as a result of paraffin precipitations or wax depositions. The only way to get reliable data is to use Downhole Dynamometer Sensors in selected wells of the field and spread the gained information to all wells in the same area as a basis for the simulations of pumping systems in the same field.

Figure 133 visualizes the results of the diagnostic simulation. The diagram on the left shows a comparison of the simulated (red line) with the actual polished rod load (green line), whereas the diagram on the right compares the simulated plunger load (red line) with the DDS measurements (blue line). Both indicate that the simulation work satisfying.

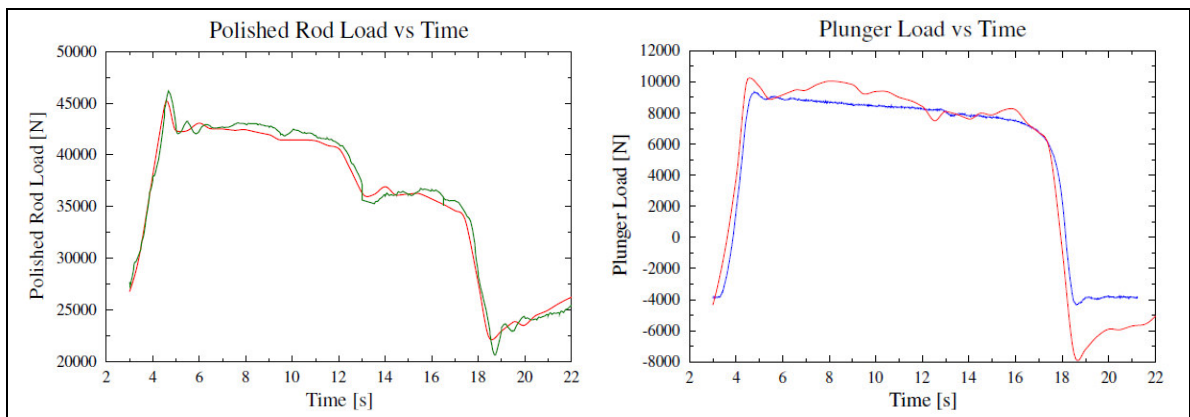


FIGURE 133: DIAGNOSTIC ANALYSIS / SIMULATION RESULTS REF (120) PP 62-64

Figure 134 shows a comparison of the results of the FEA simulation and the commercial XDIAG-D program (121). Globally the shapes of both pump cards match reasonably well, beside the problem that the commercial program does not account for the buoyancy forces in the diagram. That’s the reason why the XDIAG-D pump card shows much higher tensile loads than are actually present, whereas the FEA simulation result presents the actual load at the pump plunger.

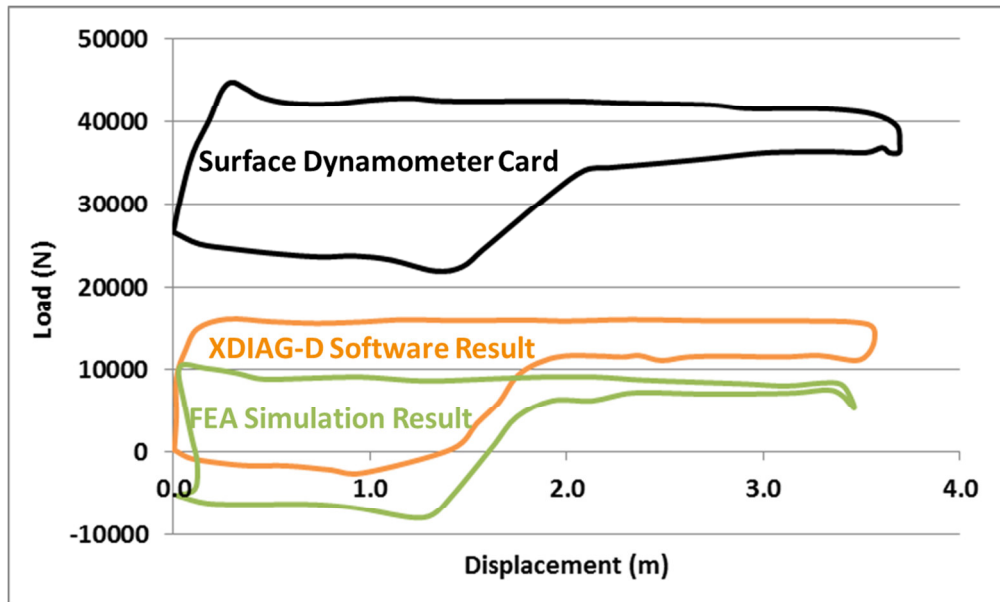


FIGURE 134: DIAGNOSTIC ANALYSIS / XDIAG-D COMPARISON

7.2.3 PREDICTIVE ANALYSIS

The predictive analysis is used to design new pumping systems or to adjust and optimize existing ones, on basis of the findings from the diagnostic analysis. That is why there are no load measurements available and appropriate models must be used. The polished rod motion is again defined by the Svinos model. The pump plunger behavior is defined by the model presented in chapter 5.5. The FEA model is provided with these boundary conditions.

The simulation provides a huge amount of data e.g. stress distributions in the rod string, contact forces, displacements, etc., which are very useful for designing efficient pumping systems. ABAQUS creates only one .odb-output file, where all desired data are stored. To get a comfortable access to these data a PYTHON script rearranges the data and creates the following files:

- Time.dat Links the simulation steps with the simulated time
- ReactionForce.dat Contains the reaction force of the top node
- Displacement_2468.dat Contains the displacement of the pump plunger

And for each time step:

- ContactT.dat Contact force of the rod / rod guides with the tubing
- Displacement.dat Displacement for every rod node
- Stress.dat Stresses of all beam elements

Thereafter two MATLAB files are used for post processing. The first one *CCSVMain.m* (see Appendix G) sorts and rearranges the data. The second file *MCSVMain.m* is responsible for visualizing of the data.

The most important data processing steps are the calculation of the contact friction force between tubing and rod / rod guides, on the basis of the contact normal force times the Coulomb friction coefficient and the stress conversion from N/m^2 to MPa, as well as the absolute displacement evaluation of the rod nodes.

```
tmpC_g=tmpC(:,2:2)*0.2;
tmpC_u=tmpC(:,2:2)*0.12;
```

```
tmpS(2*k-1)=tmpSS(k,2)/10^6;
tmpS(2*k)=tmpSS(k,3)/10^6;
```

```
tmpD=sqrt(tmpD(:,2).^2+tmpD(:,3).^2+tmpD(:,4).^2);
```

The second m-file calculates node velocities; time increments, energy and power consumption, as well as gear box torque and counter weight torque. A detailed explanation of the post processing is provided in the following chapter.

Visualization of the Simulation Results:

This section presents the description of the visualization of the simulation results on the basis of a predictive analysis of Well OMV 1, equipped with a 1,5” insert pump and installed at a measured depth of 893 meters (TVD = 877m).

7/8” rod string (2 rod guides/rod) 3,2 SPM GOR = 100 m³/m³.
 p_{well head} = 4 bar p_{casing head} = 4 bar d_{orifice} = 20,67 mm
 plunger mass = 30 kg v_{oil} = 0,002 Pas ρ_{oil} = 921 kg/m³
 plunger friction coefficient = 0,3 plunger - barrel clearance = 0,05 mm

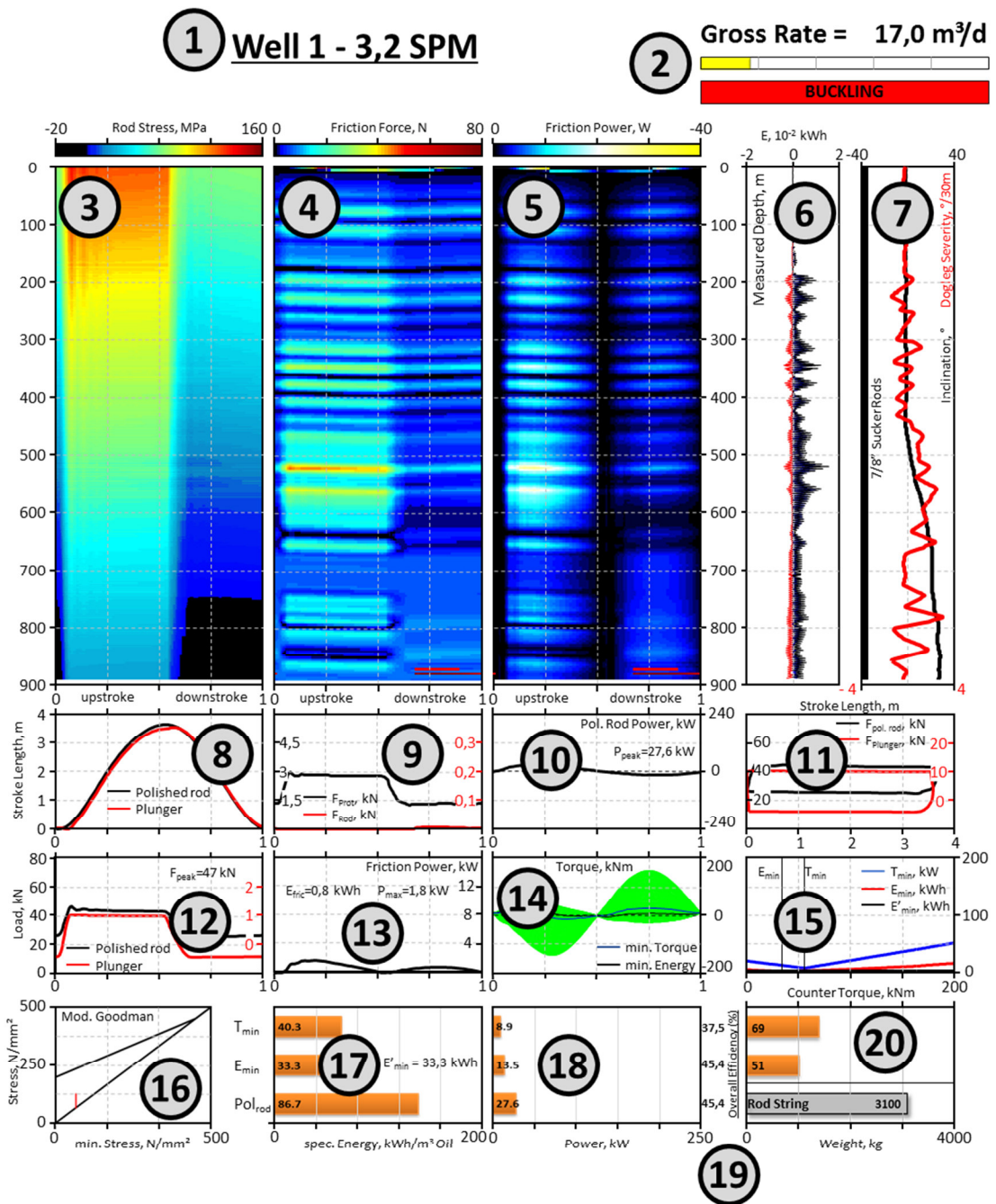


FIGURE 135: SIMULATION RESULT VISUALIZATION

Marker 1:

Marker 1 states all general important information and differentiators to other simulation runs.

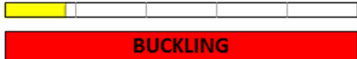
Included are always the name of the well and the number of strokes. Rod size, sinker bars etc. can be included.

1 Well 1 - 3,2 SPM

Marker 2:

Marker 2 states the gross rate of daily oil and water production, as a result of the displaced volume at the pump plunger. It accounts for actual simulated plunger stroke length.

A bar indicates if buckling at any position within the sucker rod string will occur or not.

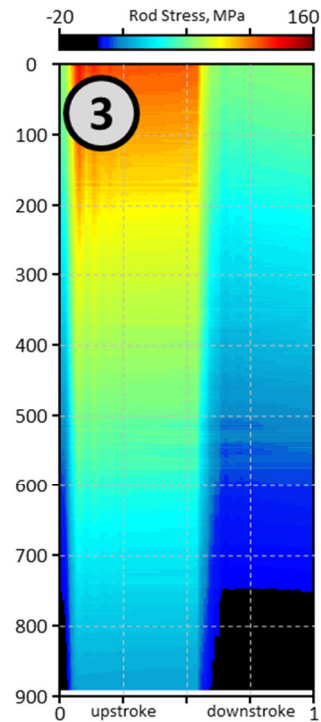
2 Gross Rate = 17,0 m³/d


Marker 3:

Marker 3 visualizes the rod stress at any position during up- and downstroke. The red color indicates regions with high tensile loads, whereas the black region indicates compression of the rod string.

During the upstroke, clearly essentially higher loads occur than during the downstroke. The higher the number of strokes per minute, the higher is the oscillation of the iso-stress lines.

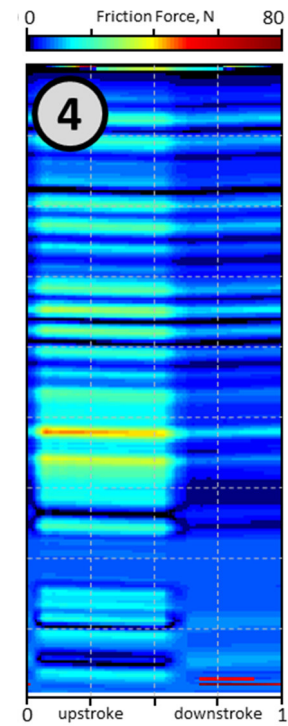
Black areas indicate compression, where buckling might occur.



Marker 4:

Marker 4 presents the friction force at the interaction rod guides and tubing. High friction forces are not necessarily a result of high inclinations, but a result of high dogleg severities.

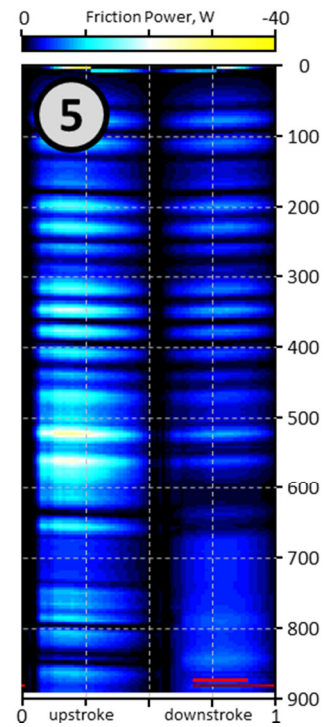
Red bars in addition indicate buckling, which occurs especially at the lower part of the sucker rod string. These red bars also present the time, the duration and the location of buckling along the complete sucker rod string.



Marker 5:

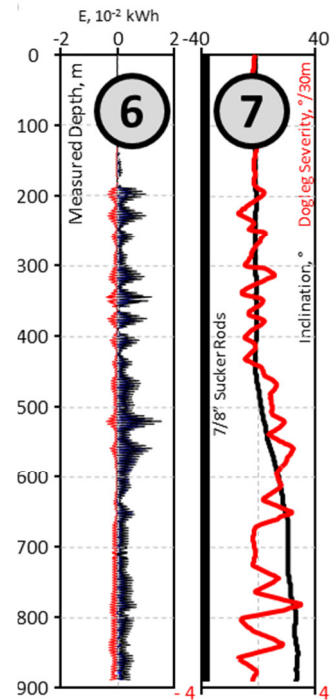
Marker 5 presents the friction power for up- and downstroke for any position within the sucker rod string. The diagram is based on the simulated friction force and the displacement increments. Due to the fact that friction energy cannot be recovered, it is presented as a negative value. The brighter the color, the higher the value.

In addition red bars indicate, like in Marker 4, buckling.



Marker 6:

Marker 6 presents the energy consumed by Coulomb friction, separated for upstroke (red line), downstroke (blue line) and the total pumping cycle (black line), along the total sucker rod string.

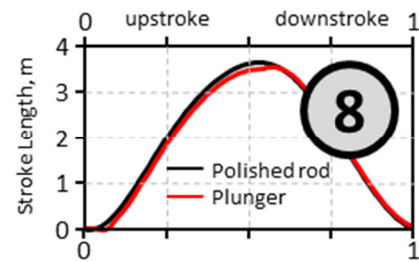


Marker 7:

Marker 7 shows the inclination of wellbore trajectory over depth, the calculated dogleg severity, as well as the composition of the sucker rod string at the very left of this diagram. In the presented case the sucker rod string is only composed out of 7/8" sucker rods. For other cases the sucker rod string is composed by a tapered rod string, sinker bars or SRABS.

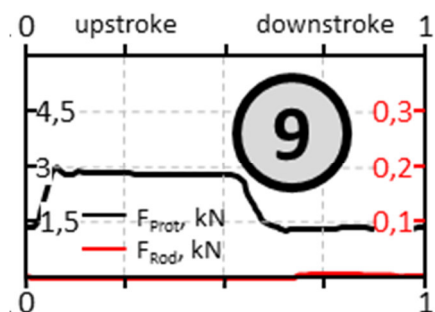
Marker 8:

Marker 8 compares the displacement at the polished rod with the displacement at the pump plunger. The displacement at the pump plunger is important, because it defines the production rate per stroke.



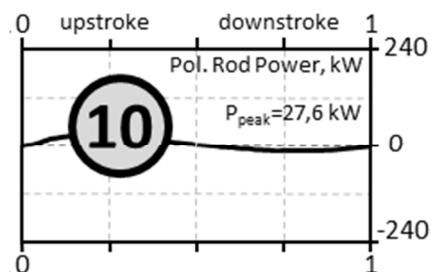
Marker 9:

Marker 9 summarizes the complete friction force of the sucker rod string for up- and downstroke by two lines. The black line indicated the friction between rod guides and tubing, whereas the red line indicated friction between the bare sucker rods and the tubing, which occurs only in the case of buckling.



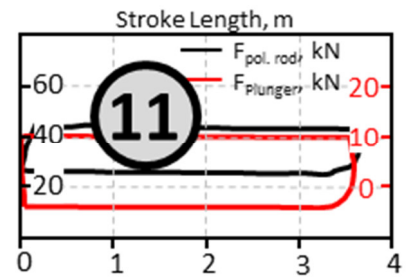
Marker 10:

Marker 10 presents the polished rod power on the basis of the polished rod load, which means that counterbalancing effects of the surface pump jack are not considered. The presented power would be required for e.g. a hydraulic system, where the polished rod is driven directly by a hydraulic cylinder. In addition the peak polished rod power is provided separately.



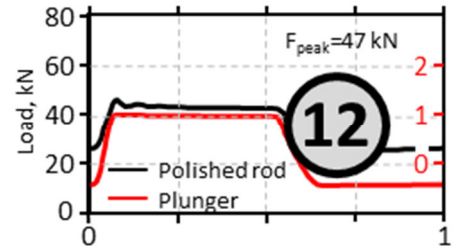
Marker 11:

Marker 11 displays the common dynamometer card representation; hence load over displacement curves for the polished rod (black) and the pump plunger (red).



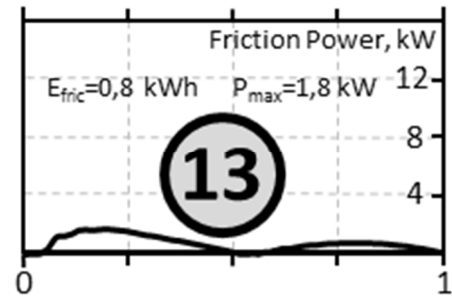
Marker 12:

Marker 12 presents the polished rod load and the plunger load profile over time. The peak load F_{peak} at the polished rod is stated separately.



Marker 13:

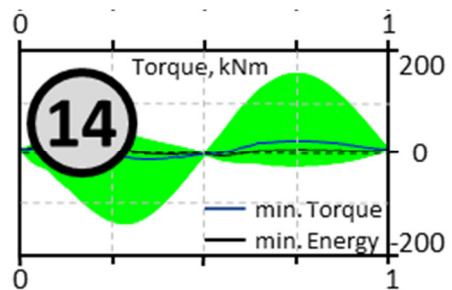
Marker 13 depicts the total friction force versus time behavior. The peak friction power and the energy to overcome the friction are displayed separately.



Marker 14:

Marker 14 shows the counterbalance torque requirements (63) for the pump jack C-320D-256-144. For this pump jack the dimensions and weights are the following: (61)

$A = 4.57\text{m}$, $C = 3.05\text{m}$, $I = 3.05\text{m}$, $P = 3.67\text{m}$, $H = 6.6\text{m}$, $G = 2.82\text{m}$, $R = 1.19\text{m}$



- Structural unbalance $B = -1780\text{ N}$
- Walking Beam W30x173 (114) $m_{Beam} = 260\text{ kg/m}$
- Pitman W8x10 (114) $m_{Pitman} = 15\text{ kg/m}$
- Equalizer beam W24x55 (114) $m_{Equalizer} = 82\text{ kg/m}$
- Cranks $M_{Cranks} = 20000\text{ Nm}$

One can distinguish between three different operation modes of the surface equipment:

Minimum torque: T_{min}

The mass of the counterweights is selected in such a way that the total torque at the crank shaft, resulting from the polished rod load, the torque caused by the structure and the counterweight torque, is a minimum.

Minimum Energy: E_{min}

The mass of the counterweights is selected in such a way that the total energy without energy recovery is a minimum. The crankshaft torque is normally higher than for the minimum torque case.

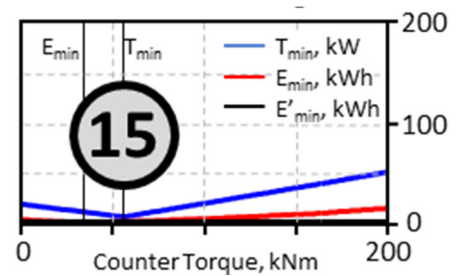
Minimum Energy, recovery: E'_{min}

The mass of the counterweights is selected in such a way that the total energy with energy recovery is a minimum. This case is rarely applicable, because the surface facilities would require special equipment for directing energy back into the supply grid.

Marker 15:

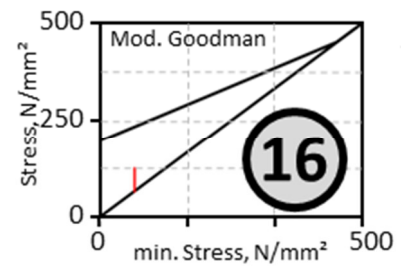
Marker 15 presents the required counterweight torque and the required peak power for all three cases.

- Blue: Minimum torque case
- Red: Minimum energy case
- Black: Minimum energy, recovery case



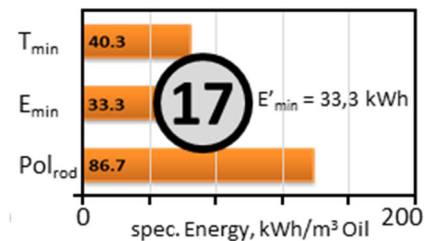
Marker 16:

Marker 16 presents the rod stress in a Modified Goodman Diagram (123). For the analysis rods of API Steel grade D with a minimum tensile strength of 198 MPa are assumed (124). The red line in the diagram indicates the actual load at the polished rod. If a tapered rod string is used, more lines are shown, indicating always the highest load of the corresponding section.



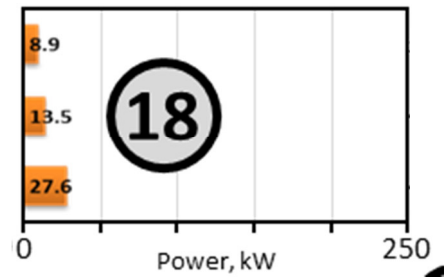
Marker 17:

Marker 17 shows the energy required for lifting one cubic meter of oil for the three cases T_{min} , E_{min} and E'_{min} , as well as the energy at the polished rod Pol_{rod} , where the effect of the pump jack is not included.



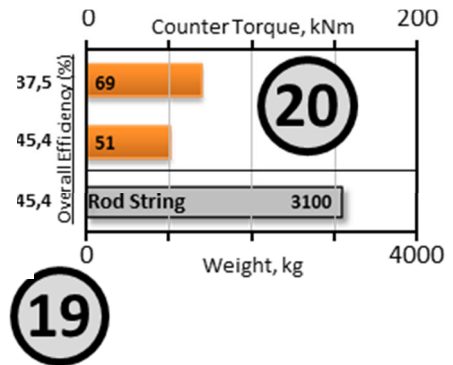
Marker 18:

Marker 18 depicts the peak power, required during one complete pumping cycle, for T_{min} , E_{min} and the Pol_{rod} case.



Marker 19:

Marker 19 points out the overall efficiency of lifting. The required hydraulic power (117) is divided by the energy consumed by the pumping system. The efficiencies of the electrical engine and the gear box are not considered.



Marker 20:

Marker 20 illustrates the required counter torque, which must be provided by the counterweights, for the minimum torque and minimum energy consumption case without energy recovery. The minimum energy consumption case with energy recovery doesn't care on counterweight mass, because the surplus of energy is redirected into the supply grid. In addition the complete rod string weight, as well as the mass of the tensioning element, if applied, is shown.

The preceding chapter presented the simulation setup for the FEA. It is clearly indicated that one basic simulation setup can be used for multiple applications - only small model adjustments are required. The enormous amount of data, generated by this simulation, allows a full analysis of the sucker rod string behavior. Contact forces, separated for rod guides and the rod string allow the evaluation of the friction power and a statement if buckling occurs. The provided motion information is used to calculate energy consumption and power requirements.

In conjunction with pump jack parameters, like transmission ratios, structure sizes and counterweight positions a complete analysis, of energy and power requirements for different operation cases, of the sucker rod pumping system can be performed. Counterweight torque requirements and overall system efficiencies, as well as tensioning element information of SRABS are shown.

8 CASE STUDY

The content of the case study is the investigation of the performance of different rod string compositions under varying operation conditions.

The reference case is based on Well OMV 1 with a 1,5" plunger, a stroke length of 144", 7/8" sucker rods with two rod guides and 3,2 strokes per minute. The resulting production rate is about 17 m³ of liquid per day. The pump jack was not modified during the simulation, which means that the stroke length and the stroke profile will remain constant.

In total the case study was performed for four different production rates: 17 m³, 27 m³, 53 m³ and 83 m³. For each production rate several subcases, containing different sucker rod string compositions, are investigated. A change in the rod string size, especially the valve rod diameter, does only change the total production rate per stroke of a standard pump slightly (see Table 7). The reason therefore is a small difference in the plunger stroke length as a result of the rod string dynamics, which are dependent on the rod string diameter.

Whereas the total production rate for the SRABS pump is due its unique working principle dependent on the plunger rod size – the smaller the plunger rod, the higher the achieved production. For the first attempts it is assumed that the valve rod diameter is equal to the last rod section diameter. To obtain the same production rate using the SRABS pump in comparison to a standard pump, the strokes per minute are slightly higher.

The conventional way to overcome buckling is the usage of sinker bars. To get realistic cases in addition rod strings with sinker bars for standard pumps are evaluated.

A large number of strokes per minute cause high system dynamics and polished rod load. These cases require tapered rod strings, where sections with more than one rod diameter are used. The design of tapered rod strings is a several discussed issue in sucker rod pump optimization. On one hand researches design all sections to get the same safety factor, which could help to balance the fatigue load (126). On the other hand in terms of energy efficiency, it makes sense to load the thin rod sections in the middle of the rod string with a safety factor close to one.

Table 23 summarizes the essential results of the case study in terms of an approximate production rate and required strokes per minute to achieve the production rate, a rod string description, a buckling indicator and the achieved efficiencies under the assumption of minimum torque at the crank shaft.

Rate	SPM	Description	Sinker Bars	SRABS	Buckling	η
~ 17 m ³	3,2	7/8" rods			✓	37,5
	3,2	7/8" rods, 1,5" sinker bars (23m)	✓			37,1
	3,2	5/8" rods			✓	42,2
	4,85	7/8" rods		✓		23,1
	3,87	5/8" rods		✓		38,7
~ 27 m ³	5	7/8" rod string			✓	31,2
	5	7/8" rods, 1,5" sinker bars (30m)	✓			34,4
	5	5/8" rods			✓	38,7
	7,58	7/8" rods		✓		17,9
	5,95	5/8" rods		✓		32,3
~ 53 m ³	10	7/8" rod string			✓	21,5
	10	7/8" rods, 1,5" sinker bars (38m)	✓			21,5
	10	5/8" rods			✓	25,4
	14,6	7/8" rods		✓		11,1
	11,8	7/8" & 5/8" rods		✓		19,6
~ 83 m ³	15	7/8" rods			✓	15,7
	15	7/8" rods, 1,5" sinker bars (53m)	✓			16,6
	15	5/8" rod string			✓	17,5
	22	1 1/8" & 7/8" rods		✓	✓	7,6
	18,3	7/8" rods		✓		9,8

TABLE 23: CASE STUDY / SUMMARY

The results of all simulations can be seen in Appendix G.

The most interesting case is the production rate of 17 m³ per day, because it can be linked directly to the reference case and the highest number of simulation runs was performed for this case. Within the following comparison only the non-buckling designs are discussed, because other designs would obviously never be realized.

The standard pump is equipped with a 7/8" sucker rod string with 23m of 1,5" sinker bars and an overall weight of 3200 kg. The maximum rod stress is about 125 MPa, the peak load is 46,7 kN and the peak power is 9 kW using a maximum counterweight torque of 69 kNm for minimum torque scenario. 1,9 kW thereof are required to overcome the friction of the sucker rod string in the tubing which has its highest magnitude in the built section at about 550 m. The energy consumption is 40,8 kWh per lifted m³ of oil giving an overall efficiency of $\eta = 37,1\%$. The results can be seen in Figure 136.

Using thinner sucker rods would require an inadequate long sinker bar section or a higher number of rod guides per sucker rod, resulting in higher energy losses and erosion due to friction.

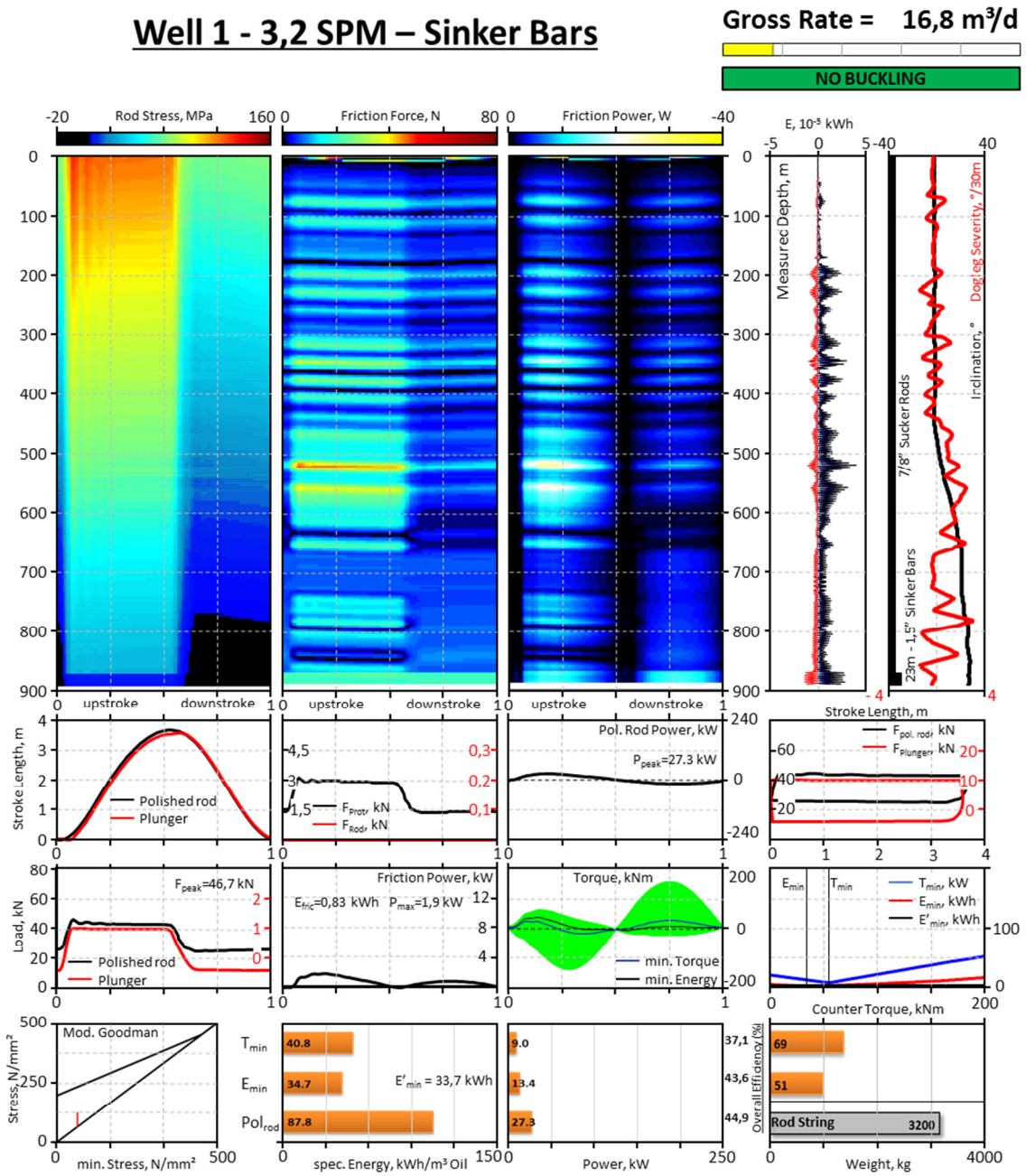


FIGURE 136: STANDARD DESIGN / 3,2 SPM - SINKER BARS

SRABS requires 3,87 SPM to deliver the same amount of liquid as the standard system with 3,2 SPM. As a result of the system’s unique behavior, 5/8” sucker rods can be used for the whole rod string, with a maximum rod stress of about 158 MPa, a peak load of 31,3 kN and a peak power of 8,8 kW using a maximum counterweight torque of 45 kNm. The rod string friction is 1,7 kW. The energy consumption is 39,1 kWh per lifted m³ of oil giving an overall efficiency of $\eta = 38,7\%$ (see Figure 137). Beside the higher efficiency, SRABS comes along with additional advantages. The peak load at the polished rod is lower; hence the load at the pump jack is reduced and the specific energy consumption is lower. Another big advantage

of SRABS is that the friction power as well as the friction forces are lower, which results in reduced wear of the equipment and a higher mean time between failures of the used tubing.

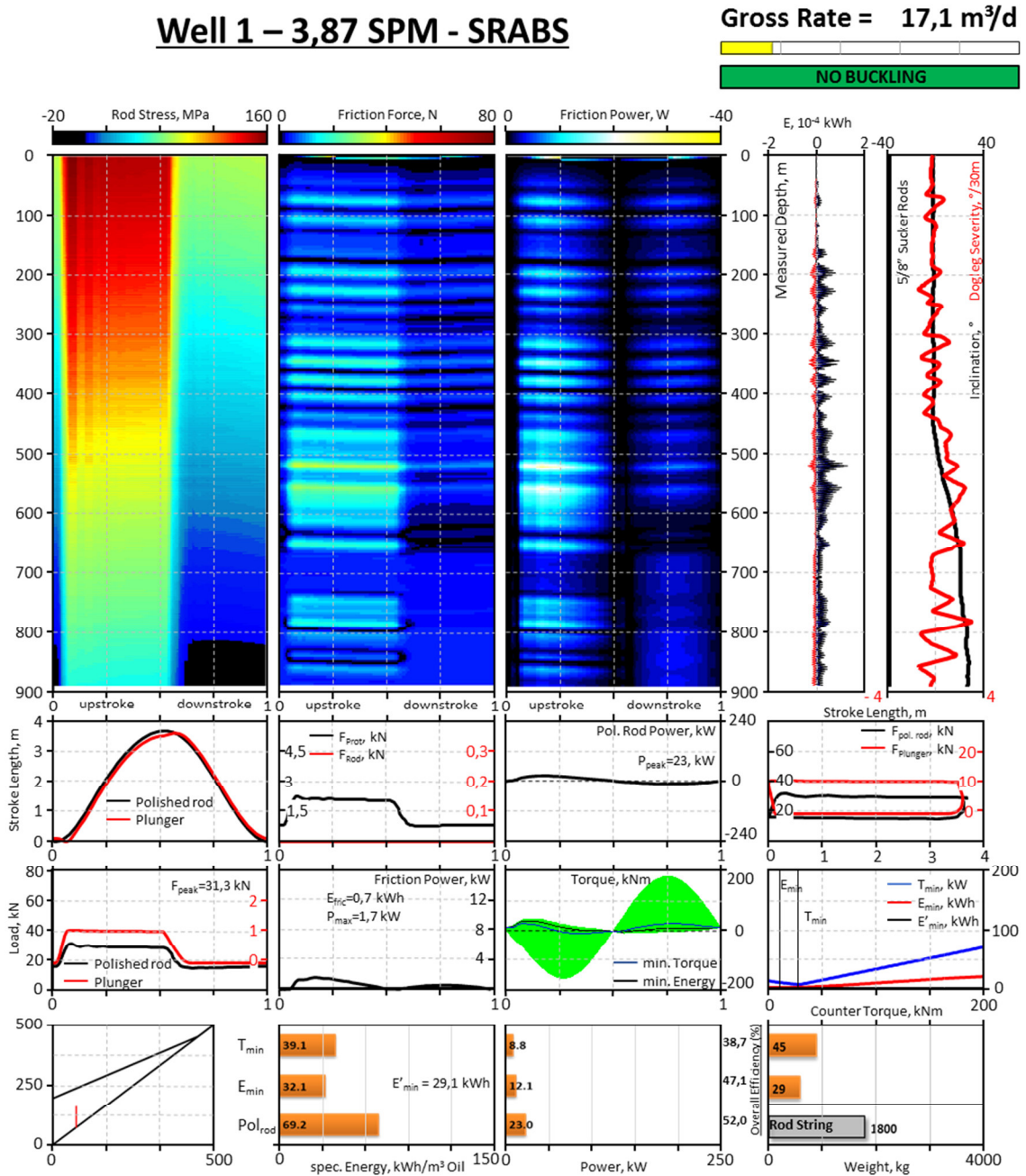


FIGURE 137: SRABS / 3,87 SPM

Increasing the production rate, using the same pump equipment, requires a higher pumping speed. Higher pumping speed is costly in term of energy. That is the reason why for a production of about 27 m³, 53 m³ and 83 m³ per day, the efficiency of the standard design is slightly higher than the efficiency of SRABS, which is illustrated in Figure 138.

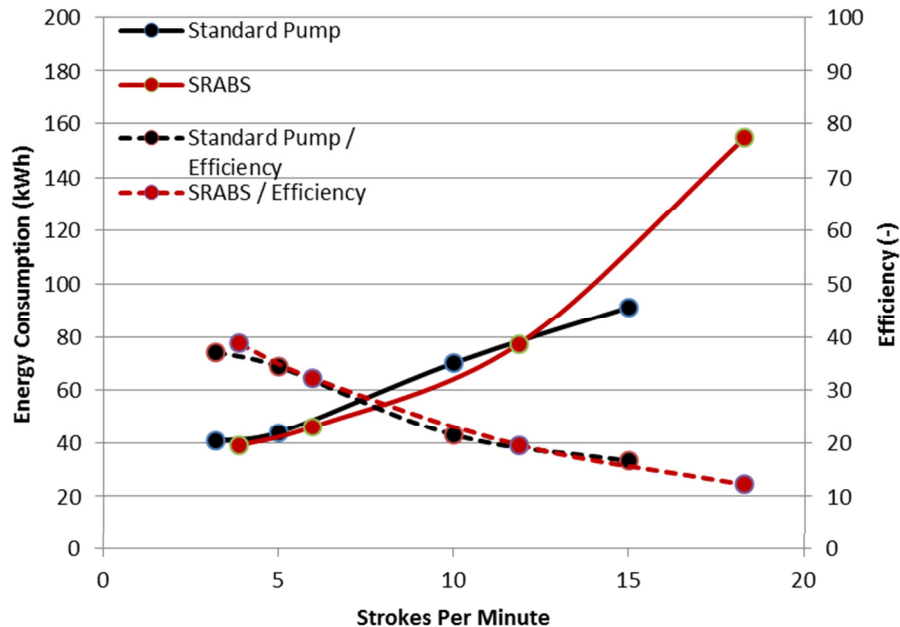


FIGURE 138: ENERGY CONSUMPTION AND EFFICIENCY COMPARISON

Despite the slightly lower efficiency of SRABS causes a better frictional behavior. The peak friction power as well as the friction force are essentially lower for. Due to the lighter rod string, the loading of the pump jack is reduced.

An important finding is that SRABS doesn't require a tensioning element, installed below the pump plunger, for pumping speeds up to 8 SPM (see Figure 198) under the operation conditions presented above. Thereafter, depending on the SPM, a mass of 100 to 200 kg is required to prevent buckling. It is important to know that for e.g. 22 SPM and a mass of 200 kg, the sucker rod string doesn't buckle directly above the pump plunger, but in the area of the highest dogleg severity (see Figure 195).

To increase the efficiency of SRABS, its required strokes per minute must get closer to that of the standard pump. To reach this target the following measures are investigated:

- Pump jack stroke length increase
- Optimization of the plunger rod diameter
- Combination stroke length – plunger rod

Pump Jack Stroke Length Increase:

Standard pump jacks normally allow by having three or four bores in the crankshaft, where the pitmen are fixed in, various stroke lengths. Higher stroke lengths cause a higher speed of the sucker rod string, which can cause problems especially during the downstroke if the critical rod fall velocity is surpassed. The unique design of SRABS allows higher rod fall velocities without buckling in comparison to a standard pump. The stroke length was increased from 144" to 170". The pumping speed was reduced to 3,2 SPM to produce 16,45 m³ of liquid per day. The simulation results show an energy consumption of 40,6 kWh/m³ oil and a total efficiency of 37,1%, which is exactly the same as for the standard pump of Well1. The peak power is with 8,7 kW slightly lower, caused by the reduced friction power.

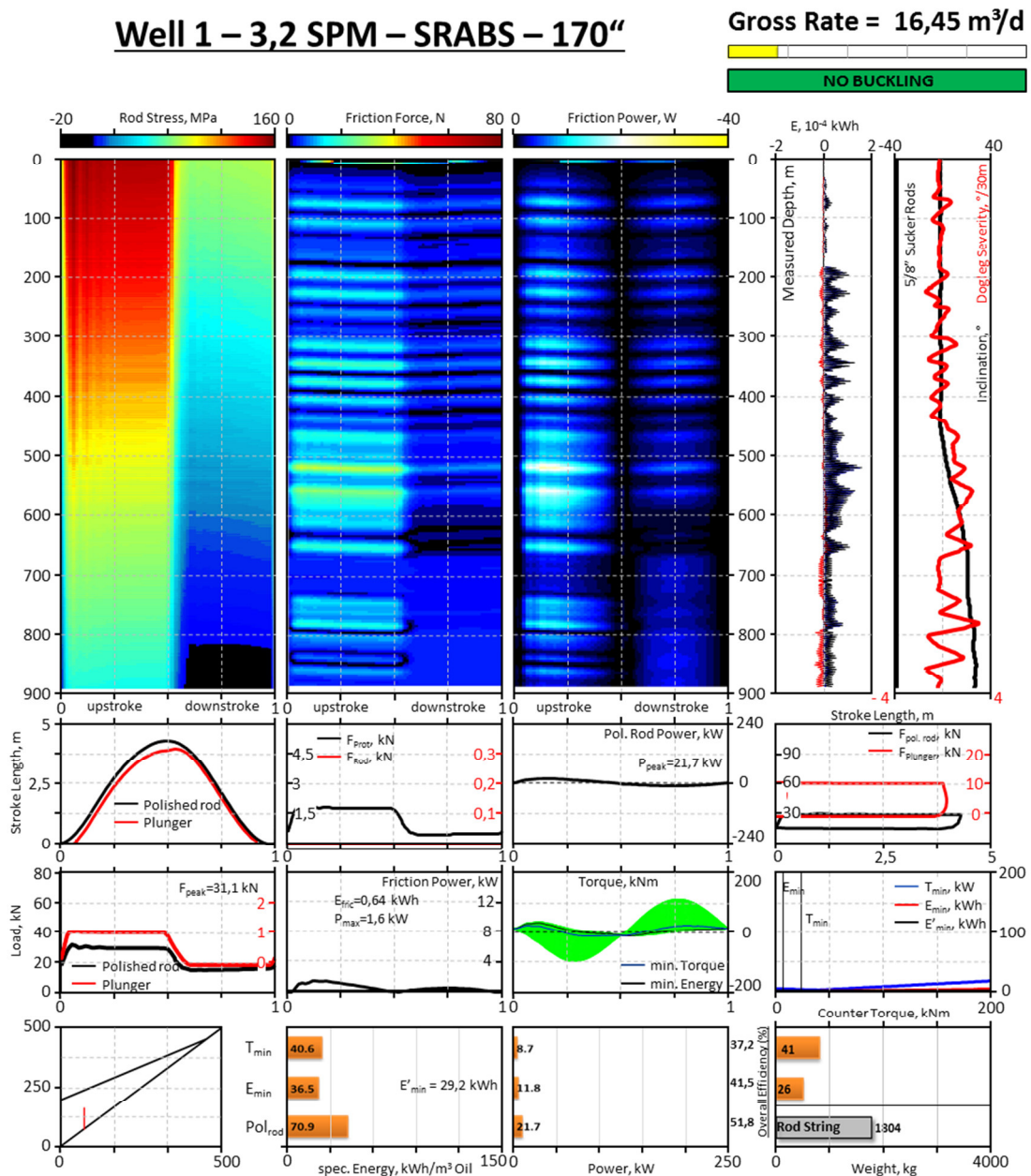


FIGURE 139: SRABS – 3,2 SPM – 170" STROKE LENGTH

Optimization of the Plunger Rod Diameter:

The optimization of the plunger rod diameter is the key to increase the produced volume per upstroke of SRABS, thus reducing the required number of strokes per minute. The plunger rod is stressed by tensile load caused by the fluid load during the upstroke and stressed by compressive load during the downstroke caused by viscous and Coulomb friction. As a result the minimum diameter of the plunger rod is required to prevent its demolition by tension and buckling.

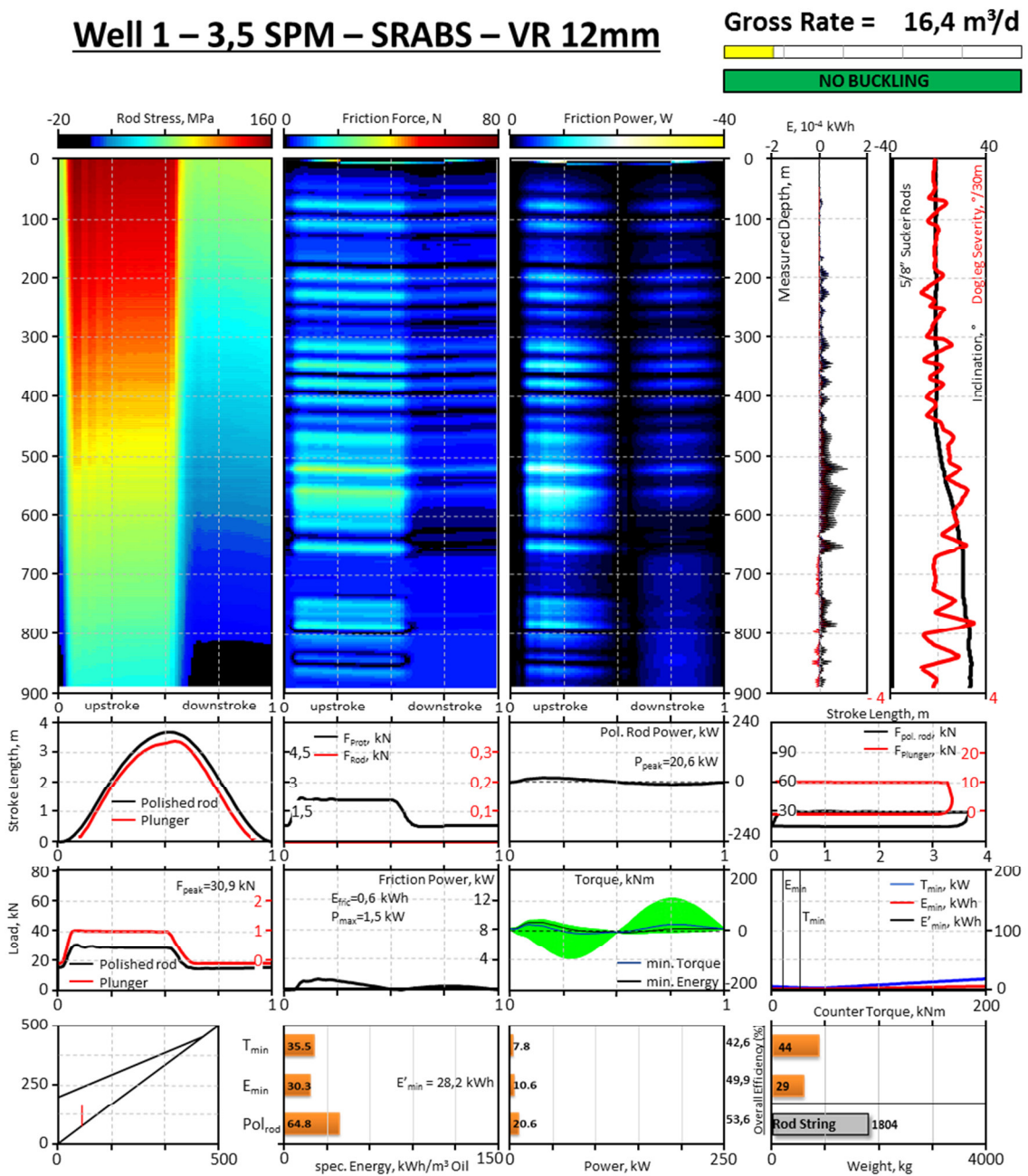


FIGURE 140: SRABS – 3,5 SPM – 12 mm PLUNGER ROD – 5/8" RODS

The usage of high strength, wear-less steel allows the reduction of the plunger rod diameter from the previously selected 5/7" or 7/8" to 12 mm. As a result the production can be increased from 3.07 litres per stroke to 3,25 litres per stroke, allowing a reduction of the pumping speed to 3,5 SPM.

The simulation for 5/8" sucker rods shows that the peak polished rod load can be reduced to 30,9 kN, friction losses are reduced. But the most important findings are that the specific energy consumption is reduced to 35,5 kW/h per m³ of oil giving an overall efficiency of 42,6%.

The usage of 7/8" sucker rods is not necessary, but for comparison simulated. The specific energy consumption is 40,8 kW/h per m³ of oil giving an overall efficiency of 37%.

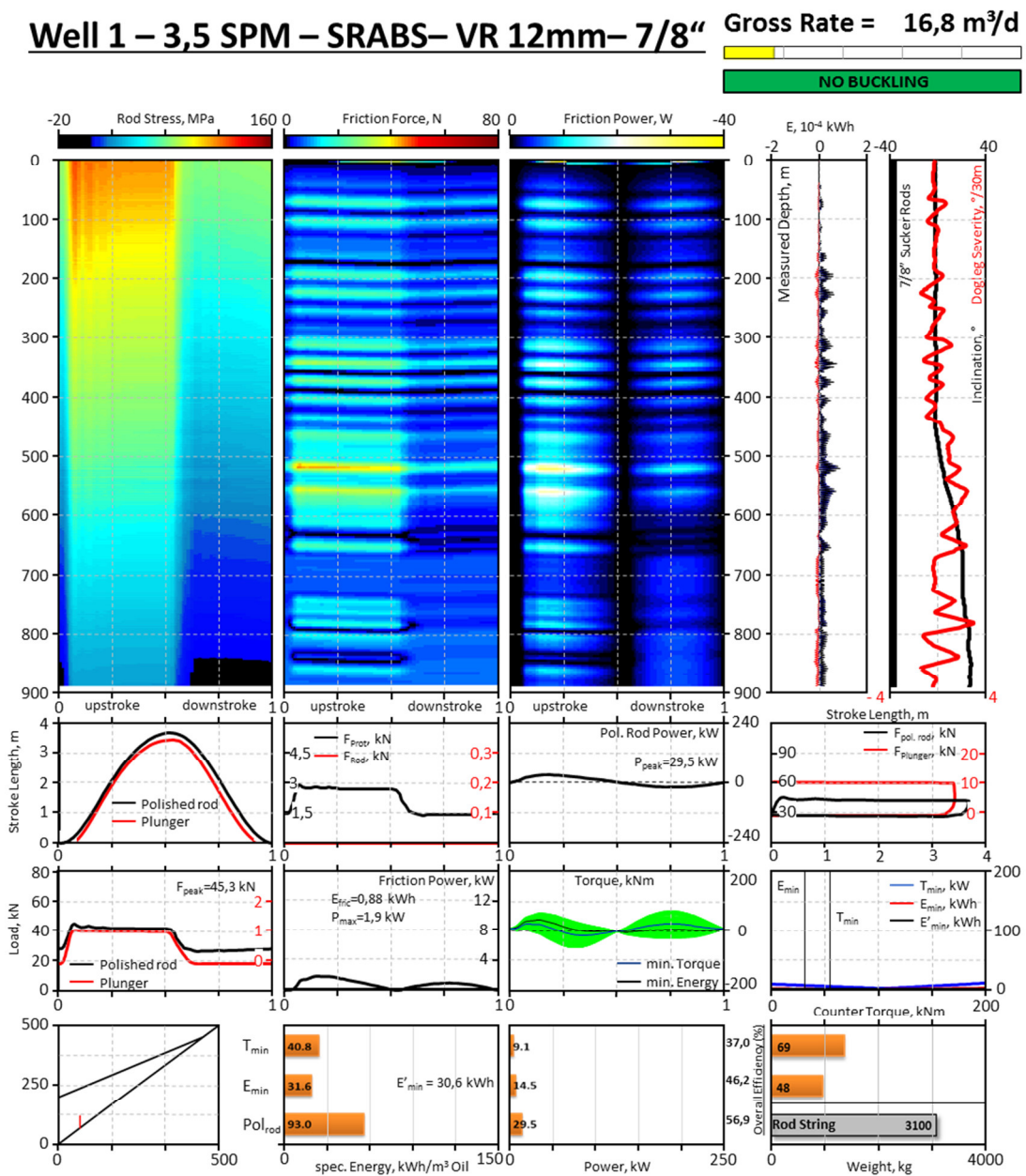


FIGURE 141: SRABS – 3,5 SPM – 12 mm PLUNGER ROD – 7/8" RODS

Combination Stroke Length – Plunger Rod

A combination of a larger stroke length and the optimization of the plunger rod diameter has also been investigated. The SPM is reduced to 3, but the plunger rod diameter must be increased to 13 mm because of buckling problems.

The specific energy consumption of 37,4 kW/h per m³ of oil and an overall efficiency of 40,3% is not as effective as the pure plunger rod optimization. The reason therefor might be the higher velocities and accelerations, caused by the larger stroke length.

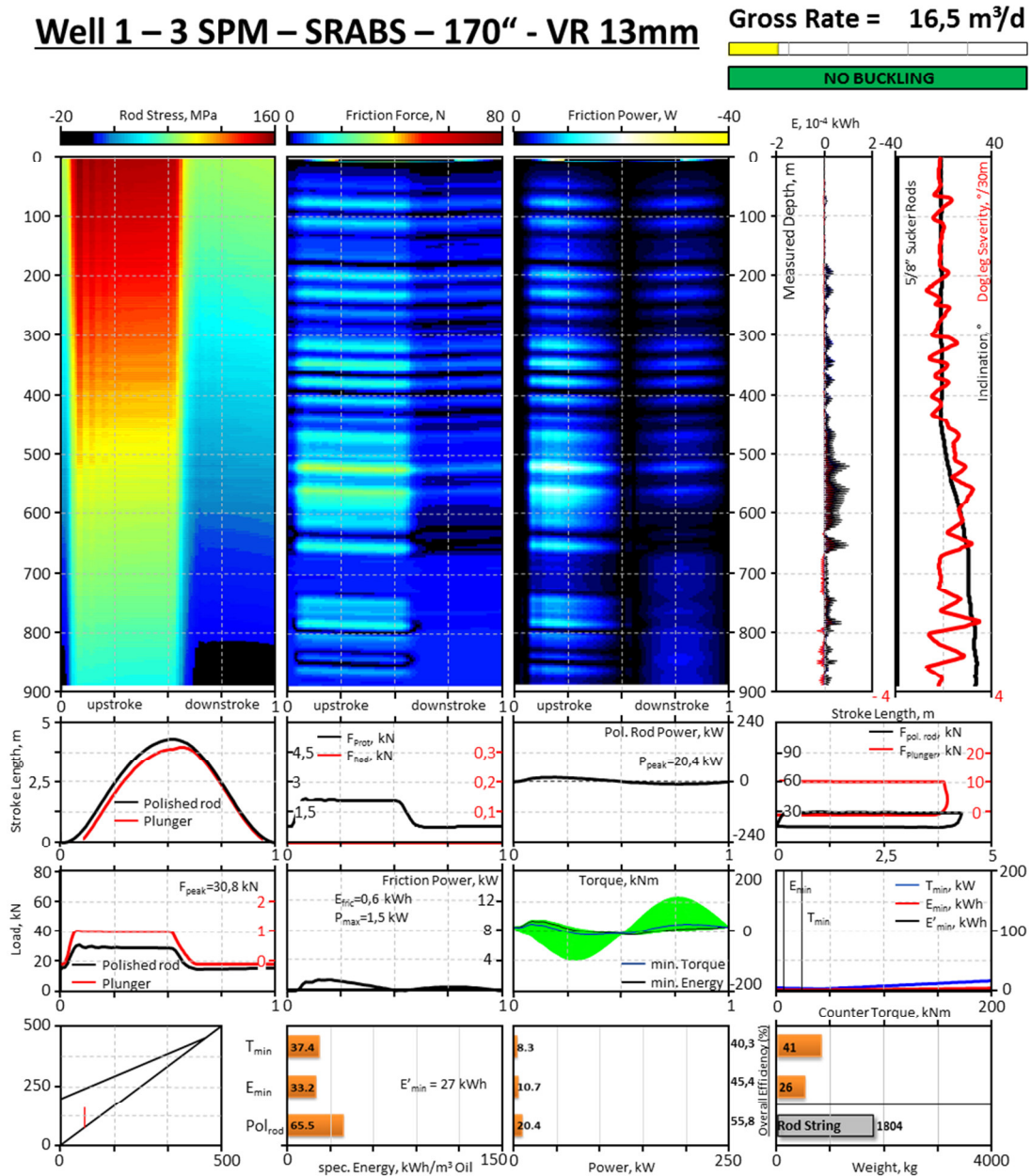


FIGURE 142: SRABS – 3 SPM – 13 mm PLUNGER ROD – 7/8" RODS

Beside the above presented optimizations the influence of rod guides was investigated too. The target was to reduce or even to keep the rod string free from rod guides, especially in the almost vertical sections. The results show that it doesn't make sense to use sucker rod strings without rod guides. At least one or two rod guides per sucker rod should be installed to prevent the contact of the rod string with the tubing. The reasons are radial oscillations, starting even from small deflections from vertical, which cannot be damped from the lifted liquid effective. Figure 202 presents the results for a standard pump and Figure 203 for SRABS. There is no difference in the performance, concerning rod contact.

Summary:

Table 24 shows the impact of the technology advancements in comparison to the reference case.

Description	Energy Consumption (kWh/m ³ oil)	Energy Reduction (%)	Efficiency η
Reference Case	40,8	-	37,1
SRABS	39,1	4,2	38,7
SRABS 170" Stroke Length	40,6	0,5	37,1
SRABS 12 mm Plunger Rod – 5/8" Rods	35,5	13,0	42,6
SRABS 12 mm Plunger Rod – 7/8" Rods	40,8	0,0	37,0
Combi. 170" Stroke Length – 13 mm Plunger Rod	37,4	3,4	40,3

TABLE 24: SRABS CASE STUDY / IMPROVEMENTS

It can be clearly seen that SRABS, using an optimized plunger rod, delivers the highest system efficiency with 42,6% and an energy saving of up to 13 percent in comparison to the reference case with a standard pump.

Table 24 shows that using these technology advancements SRABS overhauls the efficiency of the standard pump (Reference Case) also for higher pumping rates.

9 ECONOMIC EVALUATION OF SRABS

This chapter presents a short economic evaluation based on the data collection and assumptions performed within the Master Thesis “SRABS – An Economic View – Economic evaluation of the technical innovations found through SRABS” (9). The most efficient SRABS case (optimized plunger rod diameter) is compared with the reference system installed in Well OMV 1. The gross liquid production is 16,4 m³/day, having a water cut of 85 per cent. A 1,5” pump plunger is installed at a TVD of about 870m and operating with 3,2 SPM.

The following economic evaluation is based on a 10 years period (3650 days), using a discount factor of 12 percent per year. One major assumption for the following analysis is that the lifetime for the new developed SRABS pump is at least the lifetime of a standard pump. Currently investigations for selecting proper materials for seal faces and the plunger rod guides, which are essential components of the SRABS pump, to prevent erosion or fatigue are performed, but so far the above stated assumptions seem to be justified.

The total costs consist of the following components:

- Mean Time To Repair (MTTR) - Cost of Loss of Production
- Mean Time Between Failure (MTBF)
- Subsurface Equipment Costs
- Electricity Costs

Mean Time To Repair – Costs of Loss of Production:

The MTTR is the time duration required to maintain a system. For workover operations it consists of two components. The first component is the time duration required to get a free workover unit to the well site and planning of the job after an error occurred. Due to the fact that this duration varies a lot with the companies’ utilization, no number is stated at this position. Omitting this time span will result in a more conservative cost comparison of the systems.

The second component is the time duration to repair the system, which includes workover equipment transportation, the performance of the actual job and recommissioning of the pumping system. It is suggested by the industry to select three days for tubing changes and two days for rod changes. But anyway, this time is without oil production and therefore every day costs money.

If the pumping system is not working due to failures, it will not produce oil and revenues are lost. The considered oil price represents the average oil price of the Europe Brent Oil of the last three years and is considered with 402,50 €/m³ oil (9) (127).

Mean Time Between Failure:

The average MTBF is, according to OMV, 1130 days (9) for the lifetime of the tubing in a standard sucker rod system application. Practical experience shows that sucker rods can withstand at least 16 million pumping cycles, thus the actual lifetime of the sucker rods is SPM dependent. For the standard pumping system with 3,2 SPM a lifetime of 3400 day and for SRABS with 3.5 SPM a lifetime of 3150 days can be reached.

Year	Equipment Change After	Standard System	SRABS
1			
2			
3			
4	1130 days	Tubing change	
5			
6			
7	2260 days	Tubing change	Tubing change
8			
9	3150 days		Rod change
10	3390 days	Tubing + Rod change	

TABLE 25: MTBF STANDARD SYSTEM – SRABS COMPARISON

SRABS is able to increase the lifetime of the tubing, but not all tubing failures are purely related to buckling. As a result every second tubing change is also performed for the SRABS installation, as a result of non-buckling related events. If the required changes of tubing and sucker rods are close together, the assumption is that they are changed within one workover operation. Table 25 summarizes the required equipment changes.

The standard system requires three tubing and one rod change, whereas for SRABS only one tubing and rod change is required. The costs for each workover operation, based on OMV (9), are currently considered with 37.600, - €.

Subsurface Equipment Costs:

The subsurface costs consider the costs of the equipment that is installed at the workover jobs, like tubing string, sucker rods, pump, etc. Table 26 lists the individual costs:

Description	Costs
1,5" Insert Pump	2,750 €
2 7/8" Tubing 900 m	6,300 €
7/8" Rods - 5/8" Rods (2 Rod Guides 880 m)	5,750 € / 5,050 €
1,5" Sinker Bars 23 m	800 €

TABLE 26: SUBSURFACE EQUIPMENT COSTS (9)

Electricity:

Electricity costs are a big share of the total costs. More efficient systems can contribute essentially to a total cost reduction. Using 7 Cent/kWh as reference industrial electricity costs for today, the cost development over ten years is the following:

	Electricity Consumption (MWh)	Electricity Costs – Discounted (€)
Standard Pump	37,5	16.624,-
SRABS	33,2	14.723,-

TABLE 27: ELECTRICITY COSTS

The energy consumption of SRABS is 4,3 MWh lower than the energy consumption of the standard system.

Cost Analysis:

The previously discussed influencing parameters are applied on Well OMV 1 for a standard pumping system and for SRABS.

	Standard System	SRABS
Electricity	€ 16,624	€ 14,723
Subsurface Equipment	€ 16,649	€ 7,734
Workover Operations	€ 59,371	€ 34,235
Lost Production	€ 4,640	€ 2,146
Total Costs	€ 97,284	€ 58,838
Revenue	€ 3,252,790	€ 3,310,870
<i>Costs in % of Revenue</i>	3.0	1.8
Production (m ³)	9198	9362
<i>Costs per m³</i>	10.6	6.3

TABLE 28: COST COMPARISON STANDARD SYSTEM - SRABS

For 10 years, the costs for the standard pumping system are 97.284 €, whereas SRABS causes costs of 58.838 €, which is a potential saving of 40 percent. Using SRABS the costs per produced m³ of oil can potentially be reduced from 10,6 € to 6,3 €.

Figure 143 presents the cost distributions for the standard and the SRABS sucker rod pumping systems.

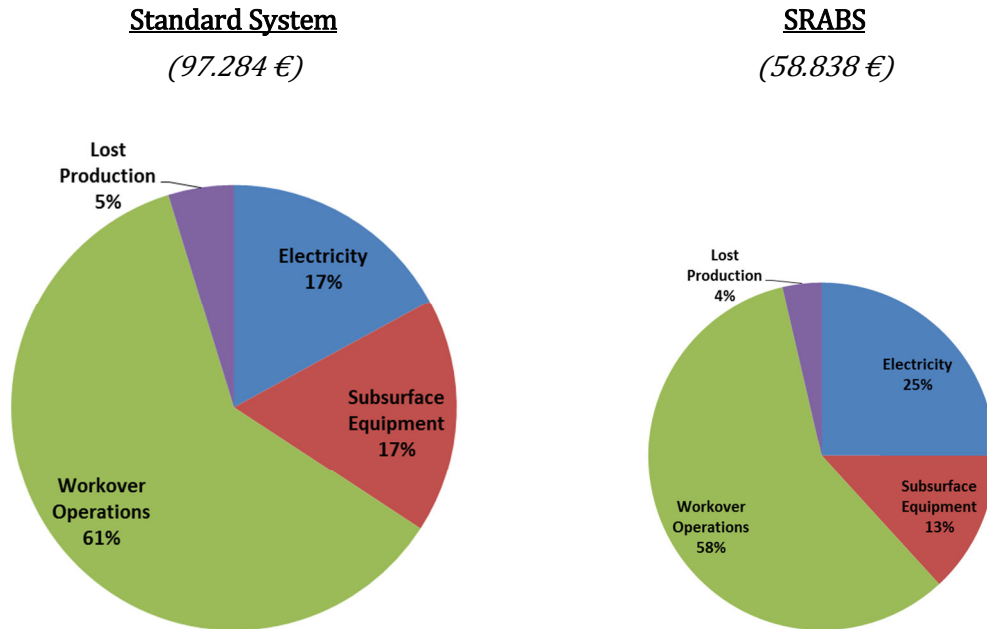


FIGURE 143: COST COMPARISON – STANDARD SYSTEM / SRABS

This economic analysis is a result of parameters, having some uncertainties. An uncertainty is on one hand based on the assumption that the lifetime of the new SRABS pumps is as long as the lifetime of a standard pump, which results in a halving the required number of well interventions. On the other hand a constant oil price is assumed for the next decade. The past shows that the oil price is fluctuating and will not stay constant over the next years.

Another parameter which cannot be expressed in terms of cost is HSE. Experience shows that well interventions belong to the most dangerous operations in the oil business in terms of risk of accidents.

Health: The number of accidents is based on the number of well interventions; hence a reduction of well interventions will directly cause a reduction of injuries of employees or contractors.

Safety: Tubing leaks, caused by buckling for instance, can cause special well interventions. Each intervention comes along with the risk for destroying or in the worst case losing the wellbore. If there is a system in place that reduces fatigue and failures, there is less probability for destroying equipment.

Environment: A reduced number of intervention leads to less emissions, like CO₂, caused by prime movers, trucks, etc..

10 CONCLUSION

In conclusion this thesis discusses the analysis of the performance of sucker rod pumping systems, employing the new patented Sucker Rod Anti-Buckling System, in comparison to standard sucker rod pumping systems. Therefore a powerful software, using a finite element analysis, is used to simulate the dynamic behavior of the sucker rod string. Beside deviated tapered rod strings, the software simulates the performance of additional equipment, like rod guides, sinker bars, tensioning element, etc. under various operation conditions.

Downhole Dynamometer Sensors:

The self-developed downhole dynamometer sensors allow an accurate measurement of the load, temperature and motional behavior of the sucker rod string. The usage of several sensors at predefined positions along the rod string allows, in combination with the developed software, an accurate evaluation of the frictional interaction of sucker rods and tubing and a verification of the simulation results. Beside the temperature profile, the measurements results provide important information of a production well. Sensors that are installed directly above the pump plunger are used to evaluate bucking of the sucker rod string.

Analyzing and optimizing the sucker rod string with developed innovative software:

Predictive analysis and diagnostic analysis of the sucker rod system are performed and the results of the diagnostic simulations are compared with the processed measurements of the self-developed downhole dynamometer sensor, which are able to record the dynamic behavior of the sucker rod string in the field at any desired depth, showing remarkable results.

The predictive analysis is performed for the same well, where the DDS were applied, to investigate the optimization potential of the well OMV 1 and the application of SRABS. Although SRABS produces liquid exclusively during the upstroke, the usage of carefully chosen material causes only a slight increase in the number of strokes per minute for SRABS to deliver the same production rate as a standard pump, without becoming more expensive in equipment or in electricity costs (CAPEX or OPEX). Actually the application of SRABS leads to extraordinary results, concerning the saving potential within sucker rod pumping, based on the performed case study on the selected well:

- Reduced tubing wear because rod string buckling is completely prevented
- Bending stress reversals of the rod string are stopped, causing an increased lifespan of sucker rods
- Up to 8 SPM SRABS does not require an additional tensioning element below the pump plunger
- For higher pumping speeds a tensioning element mass between 50 kg (11 SPM) or 3 m of 2" sinker bars to 200 kg (20 SPM) or 12 m of 2" sinker bars is required
- Electricity consumption is reduced by up to 12 %
- An economic analysis shows an OPEX reduction of 40 % when using SRABS instead of the standard pumping system

The software itself at the moment consists of several independent, but interacting components. The plan is to improve the interaction of the individual parts and to create a user-friendly software package, which can be provided to the industry. At the moment there exists no commercial software that is able to analyze sucker rod pumping systems in such a quality and accuracy, like the developed software.

SRABS Patents:

The effective operation of the patented Sucker Rod Anti-Buckling System is proved and even an additional patent, discussing the beneficial influence of the liquid level in the tubing and the casing – tubing annulus, was developed during the research. The developed software includes the patent's principles and returns a proper analysis of the new sucker rod pump design.

Currently the emphasis of the pump development is laid on the material and geometry selection for the sealing and guiding sections. Therefore a pump testing facility is constructed at the Montanuniversitaet Leoben. The objective is on one hand to test the performance and to increase the efficiency of the new pumping system. On the other hand the tests help to improve the durability of the selected materials. Beside the testing facility allows also testing of other artificial lift systems under various operation conditions. In addition field tests, using beside other measurement systems the self-developed downhole dynamometer sensors, are planned to measure the performance of the new pump design in a real oil well.

Beside the impressive number of benefits, there are still some limitations that come along with SRABS. Comparing to the standard system, SRASBS requires a cylinder valve that allows the passing through of the plunger rod. Therefore additional sealing surfaces and special materials for obtaining a durable plunger rod are required, which can be damaged by unforeseen events as well. Another limitation is that the developed software is only able to analyze wells, having a small GOR, at the moment, but improvements in this direction are in progress.

11 RECOMMENDATIONS

Apart from these achievements in optimizing sucker rod pumping, there is still room for further improvement referring to the following recommendations:

Gas – Fluid Interaction:

The investigated well delivers a very small GOR, hence the importance of the gas influence to the total system is minor. As a result only viscous liquid interaction with the tubing and rods is considered. For application of the simulation on gassy wells, further research is recommended on the fluid – gas interaction with tubing and rods for the whole length of the sucker rod string.

Coulomb Friction Factor:

The Coulomb friction factor between rod guides and tubing as well as rods and tubing is an important input parameter for the Finite Element Analysis and highly dependent on the pumped medium, within borders. The evaluation of the DDS measurements delivers this Coulomb friction factor for exactly for the prevailing conditions of the selected well during the timespan of the measurement. The friction factor might also be used for pumps operating in the same field, but wellbore situations can change fast, thus also the friction factor. It is recommended to install DDSs in various wells to get a database for friction coefficient under different conditions.

Continuous Rod String:

Developments especially in the material sector allow technology changes or adaptations in sucker rod pumping. The usage of a steel cable instead of single rods as continuous rod string could simplify maintenance and increase safety. SRABS might be able to be driven by a steel cable. It is recommended to run simulations using a steel cable instead rods with or without guides and after success to perform a field test.

Asymmetric Stroke Profile:

The usage of frequency converters for electrical motors even allows the change of the motor speed during one pumping cycle. Lower speed during the upstroke reduces the dynamic load on the system and higher speed during the downstroke catches the cycle duration. Standard pumps do not allow fast downstroke velocities because of buckling, but SRABS does. As a result in addition to lower total loads, no negative torque and the system becomes even more efficient.

BIBLIOGRAPHY

1. **U.S., Energy Information Administration.** Short Term Energy Outlook. 01/2014.
2. **J.D. Clegg, S.M. Bucaram, N.W. Heln Jr.** Recommendations and Comparisons for Selecting Artificial-Lift Methods. SPE 24834, December 1983.
3. **Rigzone.** How Does Artificial Lift Work? Webpage, www.rigzone.com/training/insight.asp, 23rd July 2015.
4. **M.Alemi, H.Jalalifar.** A prediction to the best artificial lift method selection on the basis of TOPSIS model. Journal of Petroleum and Gas Engineering Vol. 1(1), pp 009-015, March 2010.
5. **Halliburton.** Artificial Lift Systems and The 5 P's Webpage. halliburtonblog.com/artificial-lift-and-the-5-ps, 23rd July 2015.
6. **H.Rischmüller.** Oil Production with Subsurface Sucker Rod Pumps. Ternitz, Austria : Schöller Bleckmann GmbH, January 1989.
7. **H.B.Bradley.** Petroleum Engineering Handbook. Richardson, Texas, USA : Society of Petroleum Engineers, February 1992. Third Edition.
8. **Upstreampumping.** Tubing Anchor Catcher Application and Operation. Webpage, 20th June 2015.
9. **J.Wiedorn.** Economic evaluation of the technical innovations found through SRABS. Master Thesis, Montanuniversitaet Leoben, March 2015.
10. **J.F.Lea, H.V.Nickens.** *Selection of Artificial Lift*. SPE Mid-Continent Operations Symposium held in Oklahoma City : s.n., March 28-31, 1999. SPE 52157.
11. **H.Hofstätter.** A pumping device for pumping fluid. Patent Nr. PCT/EP2008/004373, Montanuniversitaet Leoben, June 2008.
12. **C.Langbauer.** A pumping device for pumping fluids. Patent candidate M1686, Intellectual Property Office Great Britain, Application No: GB1420640.3, 19th May 2015.
13. **W.Ebenhöh.** Ebenhöh GmbH. Himberg bei Wien, 2014.
14. **Skillman.** DownStroke, Public Executive Summary. LLC of Kelle, TX.
15. **American Oil & Gas Historical Society.** All Pumped Up – Oilfield Technology. ["aoghs.org/oilfield-technologies/all-pumped-up-oil-production-technology"](http://aoghs.org/oilfield-technologies/all-pumped-up-oil-production-technology). s.l. : Webpage, 14th February 2014.

16. **Texas State Historical Association.** Exxon Company, U.S.A. Webpage, tshaonline.org/handbook/online/articles/doi04, 21st June 2015.
17. **Lufkin.** Picture of an automated Pump Jack. Webpage, www.lufkin.com, July 2014.
18. **G.Takacs.** Sucker Rod Pumping Manual. PenWell Corporation, ISBN 0-878 14-892-2, 2003.
19. **S.G.Gibbs.** Predicting the Behaviour of Sucker Rod Pumping Systems. SPE 588, SPE Rocky Mountain Regional Meeting, May 27-28, 1963, Denver.
20. **C.Langbauer.** Antibuckling System in Sucker Rod Pumps. Montanuniversitaet Leoben, Master Thesis, May 2011.
21. **S.G.Gibbs.** Method of Determining Sucker Rod Performance. Houston, Texas, 26.09.1966 : s.n. Vol. US Patent Nr. 3343409.
22. **John, Fritz.** Partial Differential Equations. 4. Auflage, Springer Verlag 1982, Page 9.
23. **J.E.Chacin.** A Numerical Approach tot he Diagnosis of Sucker Rod Pumping Installations and Ist Verification With Downhole Pump Field Measurements. SPE 18829, SPE Production Symposium held in Oklahoma City, March 13-14,1989.
24. **S.G.Gibbs, A.B.Neely.** Computer Diagnosis of Down-Hole Conditions In Sucker Rod Pumping Wells. SPE Annual Fall Meeting, Denver, Oct 3-6, 1965.
25. **T.A.Everitt, J.W.Jennings.** An Improved Finite-Difference Calculation of Downhole Dynamometer Cards for Sucker-Rod Pumps. SPE Annual Technical Conference and Exhibition held in Houston, Oct 2-5 1988.
26. **D.J.Schafer, J.W.Jennings.** An Investigation of Analytical and Numerical Sucker Rod Pumping Mathematical Models. SPE 62nd Annual Technical Conference and Exhibition, Dallas, September 27-30, 1987.
27. **D.R.Doty, Z.Schmidt.** An Improved Model for Sucker Rod Pumping. SPE of AIME, February 1983, San Antonio.
28. **H.A.Tripp, J.J.Kilgore.** A Comparison Between Predicted and Measured Walking Beam Pump Parameters. SPE 20671, 65th Annual Technical Conference and Exhibition of SPE held in Oklahoma, LA, September 23-26, 1990.
29. **A.Kodabandeh, S.Miska.** A New Approach for Modeling Fluid Inertia Effects on Sucker-Rod Pump Performance and Design. SPE 24329, SPE Rocky Mountain Regional Meeting held in Casper, Wyoming, May 18-21, 1992.
30. **M.L.Bergeron.** Methode Graphique Generale De Calcul Des Propagations D'ondes Planes. Bulletin de juillet-août. Extrait des Mémoires de la Société des Ingénieurs Civils de France, 1937.

31. **S.A.Lukasiewicz.** Dynamic Behavior of the Sucker Rod String in the Inclined Well. SPE 21665, Production Operations Symposium held in Oklahoma City, Oklahoma, April 7-9,1991.
32. **G.W.Wang, S.S.Rahman, G.Y.Yang.** An Improved Model for the Sucker Rod Pumping System. 11th Australasian Fluid Mechanics Conference, University of Tasmania, Hobart, Australia, 14-18 December 1992.
33. **P.A.Lollback, G.Y.Wang and S.S.Rahman.** An alternative approach of sucker – rod dynamics in vertical and deviated wells. School of Applied Science, The University of New South Wales, Sydney, 18th September 1996.
34. **B.G.Galerkin.** On electrical circuits for the approximate solution of the Laplace equation. Vestnik Inzh., 19 (1915) pp. 897–908.
35. **J.Xu.** A Method for Diagnosing the Performance of Sucker Rod String in Straight Inclined Wells. SPE 26970, Tonji University, Latin America/Caribbean Petroleum Engineering Conference held in Buenos Aires, Argentina, 27-29 April 1994.
36. —. A New Approach to the Analysis of Deviated Rod-Pumped Wells. SPE 28697, International Petroleum Conference and Exhibition of Mexico held in Veracruz, 10-13 October 1994.
37. **C.Lanczos.** The Variational Principles of Mechanics (4th ed.). New York, Dover Publications Inc. p. 92, ISBN 0-486-65067-7, 1970.
38. **M.H.Hojjati, S.A.Lukasiewicz.** Modelling of Sucker Rod String. JCPT, December 2005, Volume 44, No 12.
39. **J.J.DaCunha, S.G.Gibbs.** Modeling a Finite-Length Sucker Rod Using the Semi-Infinite Wave Equation and a Proff to Gibbs’ Conjecture. SPE 108762, SPE Annual Technical Conference and Exhibition held in Anaheim, California, 11-14 November 2007.
40. **B.Li, X.Wang.** The Research of Vibration Characteristic about Sucker Rod String. Applied Mechanics and Materials, Vols. 130-134 (2012), pp 2789-2794, Switzerland.
41. **M.Jiang, K.Dong.** Dynamic Instability of Slender Sucker Rod String Vibration Characteristic Research. Advanced Materials Research Vols 550-553 (2012) pp 3173-3179, Switzerland, 2012.
42. **Y.Yang, J.Watson and S.Dubljevic.** Modeling and Dynamic Analysis of the Wave Equation on Sucker-Rod Pumping System. SPE 159593, University of Alberta, Annual Technical Conference and Exhibition held in San Antonio, Texas, 8-10 October 2012.
43. **A.P.Araujo Junior, A.L.Maitelli.** Determination of Dynamometer Cards from Deviated Wells. SPE 173970 MS, SPE Artificial Lift Conference – Latin America and Caribbean held in Salvador, Brazil, 27-28 May 2015.
44. **R.O.Costa.** Bombeamento mecanico alternative em pocos direcionais. MS Thesis, Universidade Estadual de Campinas, 1995.

45. **R.Schmidt.** Mechanik – Festigkeitslehre, Vorlesungsskriptum. Lehrstuhl und Institut für Allgemeine Mechanik, RWTH Aachen, 2008.
46. **Maschinenbau-Wissen.** Knicken - Eulersche Knickfälle. Webpage, www.maschinenbau-wissen.de/skript3/mechanik/festigkeitslehre/134-knicken-euler, 25th June 2015.
47. **A.Böge.** Handbuch Maschinenbau, Grundlagen und Anwendung der Maschinenbau-Technik. 20.Auflage, ISBN 978-3-8348-1025-0, Page D57.
48. **F.Jablonski.** Stabilität (Knicken von Stäben). Vorlesungsunterlagen, Technische Mechanik – Strukturmechanik, Universität Bremen.
49. **A.Lubinski.** A Study of the Buckling of Rotary Drilling Strings. presented at the spring meeting, Mid-Continent District, Division of Production. Oklahoma City, Barnsdall Research Corp., Tulsa, March 1950.
50. **R.F.Mitchell.** Tubing Buckling – The State of the Art. SPE 104267, SPE Annual Technical Conference and Exhibition held in San Antonio, Texas, 24-27 September 2006.
51. **S.A.Lukasiewicz, C.Knight.** On Lateral and Helical Buckling of a Rod in a Tubing. University of Calgary, Journal of Petroleum Technology, Vol 44, No.3, March 2006.
52. **J.B.Cheatham, P.D.Patillo.** Helical Postbuckling Configuration of a Weightless Column Under the Action of an Axial Load. SPE Journal, Vol. 24, pp. 467-472, August 1984.
53. **Y.W.Kwon.** Analysis of Helical Buckling. SPE 14729, SPE Drilling Engineering, pp. 211-216, June 1988.
54. **R.F.Mitchell.** Simple Frictional Analysis of Helical Buckling of Tubing. SPE Drilling Engineering, Vol. 1, No. 6, pp. 457-465, December 1986.
55. **J.F.Lea, P.D.Patillo, W.R.Studenmund.** *Interpretation of Calculated Forces on Sucker Rods.* Production Operations Symposium held in Oklahoma City : s.n., March 21-23, 1993.
56. **R.F.Mitchell.** Lateral Buckling of Pipe With Connectors in Horizontal Wells. SPE 84950, IADC Drilling Conference, New Orleans, 23-25 February 2003.
57. **R.Dawson, P.R.Paslay.** Drillpipe Buckling in Inclined Holes. JPT, October 1984.
58. **Y.C.Chen, Y.H.Lin.** Tubular and Casing Buckling in Horizontal Wells. SPE 19176-PA, Journal of Petroleum Technology, 1990.
59. **G.Gao, S.Miska.** *Effects of Boundary Conditions and Friction on Static Buckling of Pipe in Horizontal Well.* SPE/IADC Drilling Conference, Orlando, Florida, USA, 4-6 March 2008.
60. **R.F.Mitchell, T.Weltzin.** Lateral Buckling – The Key to Lockup . SPE 139824, IADC Drilling Conference and Exhibition, Amsterdam, 9th March 2011.
61. **M.Hajianmaleki, J.S.Daily.** Critical-Buckling-Load Assessment of Drillstrings in Different Wellbores by Use of the Explicite Finite-Element method. SPE 166592, SPE Drilling and Completion, pp. 256-264, June 2014.

62. **Dassault Systems.** ABAQUS – Finite Element Analysis Software. www.3ds.com/products-services/simulia/products/abaqus, 28th June 2015 : s.n.
63. **J.D.Clegg.** High Rate Artificial Lift. JPT, March 1988, page 277-282.
64. **S.G.Gibbs.** A Review of Methods for Design and Analysis of Rod Pumping Installations. SPE 9980, International Petroleum Exhibition and Technical Symposium held in Beijing, March 18-26, 1982 : s.n.
65. **C.Burgstaller.** Newly Developed Automatic Fluid Level Control System. Gas Well Deliquification Conference 28-29 Sep. 2011.
66. **Lufkin.** Pump Jack Types. Webpage, www.lufkin.com/index.php/products-a-services/oilfield/beam-pumping-unit, 29th June 2015.
67. **H.E.Gray.** Kinematics of Oil-well Pumping Units. Shell Development Company, Houston, Texas, March 1963.
68. **Lufkin, Oilfield Products Group.** General Catalog. Houston, Texas, 2008-2009.
69. **API Standard.** Specification for Pumping Units 11E. 1st May, 2009.
70. **J.G.Svinos.** Exact Kinematic Analysis of Pumping Units. Gulf Research & Development Co. Dallas 1983.
71. **Siamoil Company.** Surface Digital Dynamometer Measurement Tool. Webpage, www.siamoil.ru/en/tools/dynamometers/siddos-automat-3, 29th June 2015.
72. **OMV.** Analogous Dynamometer Card. Exploration and Production Austria, Gänserndorf, December 2011.
73. **S.G.Gibbs.** Computing Gearbox Trque and Motor Loading for Beam Pumping Units with Consideration of Inertia Effects. SPE-AIME, Nabla Corp.,September 1975.
74. **Knowledge Construction.** Steel section tables. www.constructionknowledge.net, April 2014.
75. **J.R.Eickmeier.** Diagnostic Analysis of Dynamometer Cards. Petroleum Transaction, pp. 97 – 106, January 1967.
76. **L.W.Lake.** Petroleum Engineering Handbook—Vol. IV. ISBN 978-1-55563-135-2, Page IV-458.
77. **B.Klein.** FEM – Grundlagen und Anwendungen der Finite-Elemente-Methode im Maschinen- und Fahrzeugbeu. Springer Vieweg, ISBN 978-3-8348-1603-0, 9. Auflage.
78. **FEA Optimization.** Stresses on an element cube. www.fea-optimization.com, July 2014.
79. **D.Gross, W.Hauger.** Technische Mechanik 2 . Springer, ISBN 3-540-64147-5.

80. **Globalstressengineers.** List of finite element software packages . Webpage, www.globalstressengineers.info/2013/02/list-of-finite-element-software-packages, 26th of July 2015.
81. **Petroleum Experts.** Prosper Software. www.petex.com/products/?ssi=3, Webpage, 29th of June.
82. **OpenFoam.** Open Field Operation And Manipulation. www.openfoam.com, Webpage, 29th June 2015.
83. **B.Howard, H.D.Beggs.** Petroleum Engineering Handbook, Chapter 22, Oil System Correlations. *3rd Version, ISBN 1-55.563-010-3, 1987.*
84. **OpenFoam.** CFD - Solver. Webpage, openfoam.org/features/standard-solvers, 12th June 2014.
85. **OpenFoamWiki.** OpenFOAM_guide/The_PISO_algorithm_in_OpenFOAM. Webpage, openfoamwiki.net/index.php, 12th June 2014.
86. **S.W.Long, E.J.Smith.** *Total Downhole Friction From Downhole Dynamometer Analysis.* SPE 67274, Oklahoma, 24-27 March 2001.
87. **H.Hofstätter.** Advanced Well Completion. Montanuniversitaet Leoben, Lecture Notes, 2014.
88. **V.L.Popov.** Das Coulombsche Reibungsgesetz. ISBN 978-3-540-88836-9, Springer Berlin Heidelberg, pp 131-152, 2009.
89. **CANAM Pipe and Supply.** Rod Guides. Rod Guide Brochure, July 2014.
90. **Theta Oilfield Services.** RODSTAR - Design and Simulation Software for Deviated and Vertical Rod Pumping Systems. Webpage, www.doverals.com/theta/en/gn/products/rodstar, 1st July 2015.
91. **J.G.Svinos.** Rod Pumping Optimization - Course Material. Gänserndorf, October 2013.
92. **W.Gilbert.** An Oil-Well Pump Dynagraph. Drilling and Production Practice, New York, API-36-094, 1 January 1936.
93. **API Standard.** Specification for Subsurface Sucker Rod Pumps and Fittings. API Specification 11AX, 12th Edition, June 2012.
94. **E.F.Brater.** Handbook of Hydraulics. 7th Edition, ISBN 0-07-007247-7.
95. **A.Schenkoff.** Druckverlust an Blenden in einer oszillierenden Rohrströmung. Dissertation, Wuppertal 1991.
96. **H.H.Bengtson.** Differential Pressure Flow Meter Background . *SunCam Publication 2011.*
97. **FH Wolfenbüttel.** Druckverlust in Armaturen. Daterpool IFHK.

98. **Wikipedia.org**. Reynolds-Zahl. Webpage, de.wikipedia.org/wiki/Reynolds-Zahl, 1st July 2015.
99. **Virginia Tech**. Fluid Flows In Nature. University Webpage, www.dept.aoe.vt.edu/~jschetz/fluidnature/unit07/ffin1.jpg, 28th July 2015.
100. **H.Nickens, J.F.Lea**. Downhole Beam Pump Operation: Slippage and Buckling Forces Transmitted to the Rod String. *Journal of Canadian Petroleum Technology*, May 2005, Volume 44, No.5.
101. **R.K.Chambliss**. Plunger Leakage and viscous Drag for Beam Pump Systems. Master Thesis, Texas Tech University, August 2001, page 41 ff.
102. **O.L.Rowin, J.N.McCoc**. Pump Intake Pressure Determined From Fluid Levels, Dynamometers, and Valve-Test Measurements. 10th Canadian International Petroleum Conference, Calgary, 16-18 June 2009.
103. **R.L.Soza**. Review of Downhole Dynamometer Testing. SPE 35217, Permian Basin Oil & Gas Recovery Conference held in Midland, 27-29 March 1996.
104. **Lilatec GmbH**. Creative innovations for our future. www.lilatec.com, Schloßberg 39, 8463 Leutschach.
105. **G.D.Albert**. Downhole Dynamometer Update. Paper presented at the Southwestern Short Course 42nd Annual Meeting, Lubbock, Texas, 19-20 April 1995.
106. **J.R.Waggoner**. Insight from the Downhole Dynamometer Database. Sandia National Laboratories, Albuquerque, New Mexico, 31st January 1997.
107. **Sandia National Laboratories**. Subsidiary of Lockheed Martin Corporation. Webpage, www.sandia.gov/media/dynamo.htm, 3rd July 2015.
108. **J.R.Waggoner**. Development of the Downhole Dynamometer Database. SPE 60768, SPE Production Operations Symposium held in Oklahoma City, 9-11 March 1997.
109. **Wikipedia.org**. Drehmatrix Webpage. de.wikipedia.org/wiki/Drehmatrix, 3rd July 2015.
110. **L.D.Paarmann**. Design and Analysis of Analog Filters - A Signal Processing Perspective. ISBN: 978-0-7923-7373-5, Pages 131-153, 2001.
111. **Python Software Foundation**. Python. Webpage, www.python.org, 4th July 2015.
112. **Weatherford International**. Weatherford Sucker Rods Brochure. 2003 - 2009.
113. **Abaqus 6.13 Documentation**. Beam element library. Chapter 29.3.8.
114. —. Beam cross-section library. Chapter 29.3.9.
115. —. Beam element cross-section orientation. Chapter 29.3.4.

116. **The MathWorks, Inc.** Matlab. Webpage, de.mathworks.com/products/matlab, 4th July 2015.
117. **Abaqus 6.13 Documentation.** Tube-to-tube contact elements. Chapter 31.3.1.
118. **L.Hansen.** Modeling Tube-to-Tube contact in Abaqus using Part and Instance. www.lhe.no, 2010.
119. **Abaqus 6.13 Documentation .** Material damping . Chapter 26.1.1.
120. **P.Eisner.** Incremental plunger force evaluation for predicting sucker rod buckling. Master Thesis, Montanuniversitaet Leoben, June 2015.
121. **Theta Oilfield Services.** XDIAG - Expert Diagnostic Analysis of Deviated and Vertical Rod Pumping Systems. Webpage, www.doverals.com/theta/en/gn/products/xdiag, 5th July 2015.
122. **Construction Knowledge.** Steel Section Tables. Webpage, www.constructionknowledge.net, 5th July 2015.
123. **K.E.Brown.** Artificial Lift Methods 2a. Penn Well Books, ISBN 0-87814-031-X(v.1) Page 26.
124. **Tenaris .** Sucker Rods Product General Catalogue.pdf. Webpage, www.tenaris.com/en/Products/SuckerRods/BeamPumping.aspx, 5th July 2015.
125. **G.Takacs.** Ways to Obtain Optimum Power Efficiency of Artificial Lift Installations. SPE 126544, SPE Oil and Gas Conference and Exhibition held in Mumbai, India, 20-22 January 2010.
126. **G.Takacs, M.Gajda.** The Ultimate Sucker-Rod String Design Procedure. SPE 170588 SPE Annual Technical Conference and Exhibition held in Amsterdam, The Netherlands, 27-29 October 2014.
127. **Statista.** Average Annual Spot Price of Brent Crude Oil. Webpage, www.statista.com/statistics/209641/average-annual-spot-price-of-wti-and-brent-crude-oil, 26th of August 2015.
128. **H.D.Beggs.** Production Optimization using Nodal Analysis. ISBN 0-930972-14-7, 2nd Edition, Page 62, May 2003.
129. **Österreichs Energie .** Industriestrompreise im europäischen Vergleich . Webpage, oesterreichsenergie.at/daten-fakten/statistik/Strompreis.html, 12th August 2015.

NOMENCLATURE

A	Cross-section of the sucker rod (m^2)
a	Velocity of sound in the sucker rods (m/s)
$a^*(\theta)$	Dimensionless acceleration of the polished rod (-)
A_{pass}	Pass band Chebychev 1 filter amplitude (Hz)
$A_{plunger}$	Plunger cross-section (m^2)
C, G, H, I, K, L, R, P	Pump jack geometry dimensions (m)
C_D	Valve discharge coefficient (-)
$D(\omega t)$	Dynamic polished rod load function (N)
$d_{orifice}$	Orifice diameter of the valve (m)
$d_{plunger}$	Plunger diameter (m)
F_{A_f}	Fluid inertia force caused by liquid column acceleration (N)
F_{A_p}	Plunger inertia force caused by plunger acceleration (N)
$F_{crh,h}$	Critical helical buckling load, horizontal rod (N)
F_{crh}	Critical helical buckling load, vertical rod (N)
$F_{crl,h}$	Critical lateral buckling load, horizontal rod (N)
F_{crl}	Critical lateral buckling load, vertical rod (N)
f	Pipe friction coefficient (-)
F_A	Inertia force (N)
F_{cf}	Viscous friction force (N/m)

F_{csg}	Plunger load, caused by the annular pressure (N)
F_D	Viscous damping force (N)
F_P	Plunger weight force (N)
F_{pass}	Pass band Chebychev 1 filter frequency (Hz)
F_R	Coulomb friction force (N)
f_r	Rod tension (N/mm ²)
F_{rf}	Friction force between rod and tubing (N/m)
F_{rt}	Friction force between coupling and tubing (N/m)
F_{stop}	Stop frequency Chebychev 1 filter amplitude (Hz)
F_{stop}	Stop frequency Chebychev 1 frequency (Hz)
$F_{t drag}$	Viscous drag force on the tubing walls (N)
F_{tbg}	Tubing pressure times plunger cross-section force (N)
F_{tbg}	Plunger load, caused by the tubing pressure (N)
F_{valve}	Force on the plunger causes by liquid flow through the valve (N)
$F_{viscous}$	Viscous friction force at the plunger (N)
F_x	Force in the rod cross-section at position x (N)
F_{x+dx}	Force in the rod cross-section at position x + dx (N)
g	Acceleration due to gravity (m/s ²)
h_1	Liquid level in the tubing (m)
h_2	Dynamic liquid level in the casing – tubing annulus (m)
I	Moment of inertia (m ⁴)
I_B	Moment of inertia of all oscillating components (m ⁴)
I_g	Moment of inertia of all rotating components (m ⁴)

L_h	Length of the rod section supposed to buckle (m)
l_{plunger}	Plunger length (m)
L	Total length of the sucker rod string (m)
$L(\omega t)$	Total polished rod load function (N)
L_1, L_2, L_3, L_4, L_5	Geometric dimensions of the pump jack (m)
M	Maximum torque of the counter weights (Nm)
m_p	Plunger weight (kg)
n	Index for the number of Fourier coefficients (-)
n_n	Traverse normal force caused by tubing contact (N)
n_p	Traverse normal force, caused by fluid pressure (N)
n_t	Viscous damping coefficient in lateral direction (-)
O_n, P_n, O'_n, P'_n	Factors (-)
p	Surrounding liquid pressure (Pa)
p_{annulus}	Annular pressure (Pa)
PRL	Polished rod load (N)
p_{tbg}	Tubing pressure (Pa)
p_{wh}	Wellhead pressure (Pa)
Δp	Pressure difference across the plunger (Pa)
$\Delta p_{\text{plunger}}$	Friction pressure loss through the plunger (Pa)
R	Radius of the actual curvature of the bended rod (m)
r	Radius of the sucker rod (m)
R_1, R_2, R_3, R_4	Crank shaft hole positions (m)

Re	Reynolds number
R_{α}	Radius of the curvature of the unloaded rod in the wellbore (m)
R_0	Barrel inside diameter (m)
R_i	Plunger outside diameter (m)
r_T	Inside diameter of the tubing (m)
s	Measured length along the curved rod (m)
S	Force in cross-section of the curved rod (N)
$s^*(\theta)$	Dimensionless position of the polished rod (-)
$s(\theta)$	Position of the polished rod in dependency of the crank angle θ (m)
S.U.	Structural Unbalance (N)
t	Time (s)
T.F.	Torque Factor (-)
t_1	Time where standing valve is closed and travelling valve is opened – end of downstroke (s)
t_2	Time where standing valve is opened and travelling valve is closed (s)
t_3	Time where standing valve is opened and travelling valve is closed – end of upstroke (s)
t_4	Time where standing valve is closed and travelling valve is opened (s)
T_{eff}	Effective tensile force (N)
T_{true}	True tensile force (N)
$T_{counter\ weight}$	Counter weight torque (Nm)
$U(\omega t)$	Polished rod displacement function (m)
$v^*(\theta)$	Dimensionless velocity of the polished rod (-)

v_{orifice}	Flow velocity through valve (m/s)
v_p	Plunger velocity (m/s)
v_r	Velocity of the rod (m/s)
w	Traverse displacement of the rod (m)
w_r	Total buoyant weight of the sucker rod string (kg)
x	Observed position (m)
z	Displacement of the sucker rod string in z – direction (m)
z_{close}	Preselected closing distance of plunger valve (m)
γ	Counterbalance offset angle ($^{\circ}$)
ϵ	Strain in the sucker rod (-)
ν	Dimensionless damping coefficient, defined by Gibbs (-)
ξ	Flow restriction coefficient (-)
ρ	Density of the lifted fluid (kg/m^3)
τ	Shear stress along the plunger surface (N/mm^2)
φ	Inclination of the rod string ($^{\circ}$)
ω	Angular velocity of the pump jack (rad/s)
v_0, v_n, δ_n	Fourier Coefficients (-)
ρ_m	Average density of the fluid column (kg/m^3)
$\sigma_0, \sigma_n, \tau_n$	Fourier Coefficients (-)
μ	Coulomb friction coefficient (-)

LIST OF ABBREVIATIONS

B.D.C.	Bottom Dead Center
BOPD	Barrel of Oil per Day
BWPD	Barrel of Water per Day
CFD	Computational Fluid Dynamics
DDS	Downhole Dynamometer Sensor
DMS	Strain Gauge Measurement
ESP	Electric Submersible Pump
FEA	Finite Element Analysis
FEM	Finite Element Method
GL	Gas Lift System
GOR	Gas – Oil Ratio
HP	Hydraulic Pump
HSE	Health, Safety and Environment
IPR	Inflow Performance Relationship
ITT	Tube-to-Tube Contact Element
MD	Measured Depth
MTBF	Meantime Between Failure
MTTR	Mean Time to Repair
PCP	Progressive Cavity Pump

PRL	Polished Rod Load
RPM	Rotations per Minute
S.U.	Structural Unbalance
SPM	Strokes per Minute
SRABS	Sucker Rod Anti-Buckling System
SRP	Sucker Rod Pump
T.D.C.	Top Dead Center
T.F.	Torque Factor
TVD	True Vertical Depth
VLP	Vertical Lift Performance
WC	Water Cut

LIST OF FIGURES

Figure 1: World Liquid Fuels Production and Consumption Balance	1
Figure 2: Inflow Performance Relation Ship	2
Figure 3: Usage of different Artificial Lift Methods in the U.S.	3
Figure 4: Hydraulic Horsepower Efficiency Comparisons for the major Artificial Lift – Methods	3
Figure 5: Sucker Rod Pump	5
Figure 6: Schematic Representation of the Pumping Cycle	7
Figure 7: Schematic of a Buckled Rod String	8
Figure 8: History of typical Beam Pump Operation: Failures per Year with approximate associated costs	9
Figure 9: Typical distribution of failures among the Beam Pump System Components	10
Figure 10: Liquid Loads on Plunger Rod	11
Figure 11: Reverse SRABS Pump Design	12
Figure 12: Patent Drawing of a Historic SRP System	13
Figure 13: Simplex Pumping Jack	13
Figure 14: Walter Trout’s Revolutionary Prototype	14
Figure 15: Automated Pump Jack	14
Figure 16: Production versus Lifting Depth	16
Figure 17: Forces acting on a vertical Rod Segment	18
Figure 18: Beam Pumping Unit Shown as a Four-bar Linkage	19
Figure 19: Typical Pump Dynagraph Showing Valve Operation	20
Figure 20: Comparison of numerical and analytical Diagnostic Models	22
Figure 21: Comparison of Bottomhole Pump Dynagraph	23
Figure 22: Force Balance in Direction of Motion	25
Figure 23: Deflected Sucker Rod String	26

Figure 24: Euler Buckling Cases 29

Figure 25: Buckling Stress in dependence of the Slenderness λ for the Steel S235JR..... 30

Figure 26: Shape of a Buckled Structure 30

Figure 27: Shape of Lateral Buckling..... 31

Figure 28: Lateral Buckling Deformation 31

Figure 29: Shape of Helical Buckling 32

Figure 30: Helical Buckling Deformation 32

Figure 31: Force on Rod due to Fluid Pressure 33

Figure 32: Block Diagramm – Polished Rod 39

Figure 33: Pump Jack Types 39

Figure 34: Four – bar Linkage System / Gray 40

Figure 35: Displacement - polished rod / Gray – Lufkin C 228 D 200 144 - 144” Stroke Length..... 42

Figure 36: Normalized Displacement of the Polished Rod / Gray..... 42

Figure 37: Normalized Polished Rod Behavior after Gray 43

Figure 38: Normalized Polished Rod Behavior / Different Pump Jack Types 44

Figure 39: Nomenclature of the Conventional Pumping Unit 45

Figure 40: Polished Rod Motion..... 47

Figure 41: Normalized Polished Rod Behavior / Svinos..... 47

Figure 42: Comparison Gray / Svinos 47

Figure 43: Surface Digital Measurement Tool 48

Figure 44: Normalized Plot / Surface Measurement..... 49

Figure 45: Velocity/ Acceleration Comparison..... 49

Figure 46: Dynamometer Card Representation..... 50

Figure 47: Analogous Dynamometer Card 51

Figure 48: Load Function Derivation 51

Figure 49: Crank Shaft Torque from Polished Rod Load..... 52

Figure 50: Crankshaft Torque from Counterweights 53

Figure 51: Total Crankshaft Torque..... 54

Figure 52: Prime Mover Torque 55

Figure 53: Block Diagram / Sucker Rod String Evaluation 56

Figure 54: Stresses on an Element Cube 57

Figure 55: Slice Distortions / Displacements 58

Figure 56: External and Body Forces / X-Axis 59

Figure 57: Up- and Downstroke Production at the Plunger 63

Figure 58: Up- and Downstroke Production at the Wellhead 63

Figure 59: Pressure Traverse Curve for Well OMV 1 and different GOR's 64

Figure 60: Rod Guide Geometry 65

Figure 61: Rod Guide Assembly 65

Figure 62: Open Foam Mesh / Rod Guide Detail 66

Figure 63: Viscosity of Oil, Water and Gas 66

Figure 64: Viscous Drag for 0,005 Pas 67

Figure 65: Viscous Drag Simulation for 3 Strokes Per Minute 68

Figure 66: Maximum Friction Force on Rods and Tubing / Sensitivity Analysis 69

Figure 67: 2 7/8" – 7/8" Rod Guide 70

Figure 69: Tubing Erosion and Leakage caused by Rod Guides 71

Figure 69: 0° and 45° Rod Guide Orientation 71

Figure 70: Summary Friction Coefficient Experiment 72

Figure 71: Full Pump – Dynamometer Card 74

Figure 72: Group 2 Dynamometer Card 75

Figure 73: Pump Components 77

Figure 74: Forces at the Plunger 78

Figure 75: Moody Diagram 81

Figure 76: Force across Valve 82

Figure 77: Viscous Friction Plunger / Velocity Profile 83

Figure 78: Viscous Friction Force as a Function of Plunger Velcocity, a Clearance of 0.003", 3' Plunger Length and a Vicosity of 7cp 84

Figure 79: Viscous Friction Force as a Function of Plunger Clearance 84

Figure 80: Typical Downhole Dynamometer Card generated by Rodstar 85

Figure 81: Valve Behaviour Upstroke 86

Figure 82: Valve Behaviour Downstroke..... 87

Figure 83: Artificially designed Downhole Dynamometer Card 88

Figure 84: Sensitivity Analysis / Upstroke 89

Figure 85: Sensitivity Analysis / Downstroke 90

Figure 86: Commercial Software / Sensitivity Analysis / Downstroke 91

Figure 87: Comparision Rodstar Downhole Dynamometer Card / Artificially created Downhole Dynamometer Card 91

Figure 88: Downhole Dynamometer Sensor Housing 94

Figure 89: Illustration of the DDS's Electronic Components 95

Figure 90: Schematic of the DDS's Electronic Components 95

Figure 91: Temperature Sensor Fitting..... 97

Figure 92: Chebychev 1 - Filter 98

Figure 93: Hydrostatic Pressure Test..... 99

Figure 94: Hydrostatic Pressure Test Calibration..... 99

Figure 95: Rock Testing Machine and DDS 100

Figure 96: Rock Testing Machine Reading..... 101

Figure 97: DDS Readings 102

Figure 98: Rock Testing Machine and DDS – Match..... 103

Figure 99: Calibration DDS 3 / 2013_12_07 103

Figure 100: Calibration DDS 3 / 2013_04_10 104

Figure 101: Accuracy of DDS 2 / 2013_07_12 104

Figure 102: Trejectory of Well OMV 1 106

Figure 103: Location Well OMV 1 106

Figure 104: DDS Installation..... 107

Figure 105: Position of the Downhole Dynamometer Sensors in Well OMV 1 108

Figure 106: Temperature Behavior over Time and Depth..... 109

Figure 107: Geothermal Gradient Behavior 110

Figure 108: Acceleration Measurement Sample..... 111

Figure 109: Motion of DDS 1..... 111

Figure 110: Displacement Comparison Downhole Dynamometer Sensors 112

Figure 111: Unconverted Strain Gauge Readings 112

Figure 112: Frequency plot / SPM - Evaluation..... 113

Figure 113: SPM Behaviour over Time..... 113

Figure 114: History Plots..... 114

Figure 115: History Plots / DDS 1 115

Figure 116: History Plots / DDS 2..... 115

Figure 117: History Plots / DDS 3..... 116

Figure 118: History Plots / DDS 4..... 116

Figure 119: History Plots / DDS 6..... 117

Figure 120: Recorded Data Conversion 117

Figure 121: Load Averaging..... 118

Figure 122: Measured Dynamometer Cards 121

Figure 123: Surface Dynamometer Card Comparison 122

Figure 124: Downhole Dynamometer Card Comparison..... 123

Figure 125: Trajectory of Well OMV 1 127

Figure 126: Tubing - Sucker Rod / Coupling Contact..... 128

Figure 127: B32 Beam Element 129

Figure 128: Circular Cross-section Definition 129

Figure 129: Beam Element Cross-section Orientation 130

Figure 130: ITT-Element 132

Figure 131: Sucker Rod String Friction Analysis..... 138

Figure 132: Diagnostic Analysis / Iteration Principle 139

Figure 133: Diagnostic Analysis / Simulation Results 139

Figure 134: Diagnostic Analysis / XDIAG-D Comparison..... 140

Figure 135: Simulation Result Visualization..... 142

Figure 136: Standard Design / 3,2 SPM - Sinker Bars 151

Figure 137: SRABS / 3,87 SPM..... 152

Figure 138: Energy Consumption and Efficiency Comparison 153

Figure 139: SRABS – 3,2 SPM – 170” Stroke Length 154

Figure 140: SRABS – 3,5 SPM – 12 mm Plunger Rod – 5/8” Rods..... 155

Figure 141: SRABS – 3,5 SPM – 12 mm Plunger Rod – 7/8” Rods..... 156

Figure 142: SRABS – 3 SPM – 13 mm Plunger Rod – 7/8” Rods 157

Figure 143: Cost Comparison – Standard System / SRABS..... 162

Figure 144: Viscous Drag Simulation for 3 Strokes Per Minute 199

Figure 145: Influence of Mixture Viscosity on Viscous Drag 200

Figure 146: Influence of Tubing Diameter on Viscous Drag..... 200

Figure 147: Influence of Rod Diameter on Viscous Drag 201

Figure 148: Influence of the Stroke Length on Viscous Drag 201

Figure 149: Influence of Strokes Per Minute on Viscous Drag 202

Figure 150: Rod Guide with attached Weight..... 203

Figure 151: Friction Coefficient Distribution / Dry Tubing / Static Friction..... 204

Figure 152: Friction Coefficient Distribution / Dry Tubing / Kinetic Friction..... 204

Figure 153: Friction Coefficient Distribution / Water Wet Tubing / Static Friction 205

Figure 154: Friction Coefficient Distribution / Water Wet Tubing / Kinetic Friction..... 205

Figure 155: Friction Coefficient Distribution / Oil Wet Tubing / Static Friction..... 206

Figure 156: Friction Coefficient Distribution / Oil Wet Tubing / Kinetic Friction..... 206

Figure 157: Friction Coefficient Distribution / Oil Wet Tubing / Static Friction..... 207

Figure 158: Friction Coefficient Distribution / Oil Wet Tubing / Kinetic Friction..... 207

Figure 159: Friction Coefficient Distribution / Hot Oil in Tubing / Static Friction..... 208

Figure 160: Gas Interference - Card..... 210

Figure 161: Fluid Pound - Card 211

Figure 162: Tubing Stretch - Card 211

Figure 163: Excessive Friction - Card 212

Figure 164: Rock Testing Machine and DDS 1 – Match 2013_28_06 215

Figure 165: Calibration DDS 1 / 2013_28_06 215

Figure 166: Rock Testing Machine and DDS 1 – Match 2013_04_10 216

Figure 167: Calibration DDS 1 / 2013_04_10 216

Figure 168: Rock Testing Machine and DDS 2 – Match 2013_12_07 217

Figure 169: Calibration DDS 2 / 2013_12_07 217

Figure 170: Rock Testing Machine and DDS 3 – Match 2013_12_07 218

Figure 171: Calibration DDS 3 / 2013_12_07 218

Figure 172: Rock Testing Machine and DDS 3 – Match 2013_04_10 219

Figure 173: Calibration DDS 3 / 2013_04_10 219

Figure 174: Rock Testing Machine and DDS 4 – Match 2013_04_10 220

Figure 175: Calibration DDS 4 / 2013_04_10 220

Figure 176: Rock Testing Machine and DDS 6 – Match 2013_12_07 221

Figure 177: Calibration DDS 6 / 2013_12_07 221

Figure 178: Rock Testing Machine and DDS 6 – Match 2013_04_10 222

Figure 179: Calibration DDS 6 / 2013_04_10 222

Figure 180: Well 1 – 3,2 SPM 247

Figure 181: Well OMV 1 – 5 SPM 248

Figure 182: Well OMV 1 – 10 SPM 249

Figure 183: Well OMV 1 – 15 SPM 250

Figure 184: Well OMV 1 – 3,2 SPM / Sinker Bars 251

Figure 185: Well OMV 1 – 5 SPM / Sinker Bars 252

Figure 186: Well OMV 1 – 10 SPM / Sinker Bars 253

Figure 187: Well OMV 1 – 15 SPM / Sinker Bars 254

Figure 188: Well OMV 1 – 3,2 SPM / 5/8” Rods 255

Figure 189: Well OMV 1 – 5 SPM / 5/8” Rods 256

Figure 190: Well OMV 1 – 10 SPM / 5/8” – 7/8” Rods 257

Figure 191: Well OMV 1 – 15 SPM / 5/8” – 7/8” Rods 258

Figure 192: Well OMV 1 – 4,85 SPM / SRABS – 7/8” Rods..... 259

Figure 193: Well OMV 1 – 7,58 SPM / SRABS – 7/8” Rods..... 260

Figure 194: Well OMV 1 – 14,6 SPM / SRABS – 7/8” Rods..... 261

Figure 195: Well OMV 1 – 22 SPM / SRABS – 7/8” & 1 1/8” Rods..... 262

Figure 196: Well OMV 1 – 3,87 SPM / SRABS – 5/8” Rods..... 263

Figure 197: Well OMV 1 – 5,95 SPM / SRABS – 5/8” Rods..... 264

Figure 198: Well OMV 1 – 8 SPM / SRABS – 5/8” Rods..... 265

Figure 199: Well OMV 1 – 11,85 SPM / SRABS – 5/8” & 7/8” Rods 266

Figure 200: Well OMV 1 – 11,85 SPM / SRABS – 5/8” & 7/8” Rods - Mass..... 267

Figure 201: Well OMV 1 – 18,3 SPM / SRABS – 7/8” Rods - Mass..... 268

Figure 202: Well OMV 1 – 3,2 SPM / Sinker Bars – No Rod Guides 269

Figure 203: Well OMV 1 – 3,87 SPM / SRABS – No Rod Guides 270

LIST OF TABLES

Table 1: MTBF for SRPs of an Austrian Oil Company	9
Table 2: Comparison of Rod Pumped Wells USA/USSR	15
Table 3: SRP Design Options	38
Table 4: Lufkin - Pump Jack Dimensions	40
Table 5: Geometric Dimensions / Conventional Units	48
Table 6: Pump Jack Components Dimensions	54
Table 7: Relationship Upstroke to Downstroke Production.....	62
Table 8: Equivalent Rod Guide Diameter.....	65
Table 9: Friction Coefficients / CANAM Pipe & Supply.....	72
Table 10: Smith's Coefficients of Discharge for Circular Orifices with Full Contraction	80
Table 11: Flow Restriction Coefficients	81
Table 12: Sensitivity Analysis / Parameter summary.....	89
Table 13: Temperature Sensor Calibration	96
Table 14: Weight of the Field Test Sucker Rod String.....	100
Table 15: Calibration Dates	101
Table 16: Strain Gauge Calibration Parameters.....	105
Table 17: Strain Gauge Calibration Parameters.....	110
Table 18: Hour of Measurement / DDS	114
Table 19: Bending Axis & - Torque for DDS 1.....	119
Table 20: Bending Axis & - Torque for DDS 4.....	120
Table 21: Sizes of Standard and Slimhole Couplings	128
Table 22: Tubing – Rod Coupling Contact	128
Table 23: Case Study / Summary	150
Table 24: SRABS Case Study / Improvements.....	158

Table 25: MTBF Standard System – SRABS Comparison 160

Table 26: Subsurface Equipment Costs 160

Table 27: Electricity Costs..... 161

Table 28: Cost Comparison Standard System - SRABS 161

APPENDIX A

Load Function Generation / Polished Rod

The following MatLab code enables to derive the load function at the polished rod from a common dynamometer measurement.

```
function surface_boundary_svinos

% Import geometric dimensions
DatenFile='Dynamometer_svinos_V3.xls';
Blatt='Pir86_1';
A = xlsread(DatenFile,Blatt,'L4');
C = xlsread(DatenFile,Blatt,'L5');
I = xlsread(DatenFile,Blatt,'L6');
P = xlsread(DatenFile,Blatt,'L7');
H = xlsread(DatenFile,Blatt,'L8');
G = xlsread(DatenFile,Blatt,'L9');
R = xlsread(DatenFile,Blatt,'L10');
startwert = xlsread(DatenFile,Blatt,'L12');
ufeld=xlsread(DatenFile,Blatt,'G2:G200');
ffeld=xlsread(DatenFile,Blatt,'H2:H200');

hubzahl=xlsread(DatenFile,Blatt,'L13');
T=60/hubzahl;
omega=2*pi/T;

K=((H-G)^2+I^2)^0.5;
d=asin(I/K);

%Reference data - scaling
phip=linspace(0,2*pi,121);

theta2=2*pi-phip+d;
L=sqrt(K^2+R^2-2*K*R*cos(theta2));

for i=1:length(theta2)
    if ((0<theta2(i))&&(theta2(i)<pi))||((theta2(i)>2*pi)
        j(i)=1;
    else
        j(i)=-1;
    end
end

beta=acos((L.^2+K^2-R^2)/2/K/L).*j;

theta4=acos((P^2-C^2-L.^2)/2/C/L)-beta;
uref=A.*(theta4-pi/2-d);

theta2p=2*pi/T;
theta3=acos((P^2+L.^2-C^2)/2/P/L)-beta;
theta3p=R*theta2p/P*sin(theta4-theta2)/sin(theta3-theta4);
theta4p=R*theta2p/C*sin(theta3-theta2)/sin(theta3-theta4);

theta4pp=theta4p.*((theta2p-theta3p).*cot(theta2-theta3)-(theta3p-theta4p).*cot(theta3-theta4));

VR=(theta4p*A)'
AR=(theta4pp*A)'

ufeld=ufeld+min(uref);
```

%Position determination

```

phi=startwert;
for k=1:length(ufeld)
    usoll=ufeld(k);
    abgleich=1;
k;
    while abgleich>0.0001
        theta2i=2*pi-phi+d;
        Li=sqrt(K^2+R^2-2*K*R*cos(theta2i));
        if ((0<theta2i)&&(theta2i<pi))||(theta2i>2*pi)
            j=1;
        else
            j=-1;
        end

        betai=acos((Li^2+K^2-R^2)/2/K/Li)*j;
        theta4i=acos((P^2-C^2-Li^2)/2/C/Li)-betai;
        uneu=A*(theta4i-pi/2-d);

        abgleich=abs(usoll-uneu);
        phi=phi+0.00001;
    end

    phifeld(k)=phi;
    ufeldneu(k)=uneu;

end
phifeld;
Tfeld=phifeld/omega;
tp=phip/omega;

hub=max(uref)-min(uref)

%Interpolation of equal interval scaled points
fneu(1)=ffeld(length(ffeld)-1)+(ffeld(length(ffeld))-ffeld(length(ffeld)-1))/(Tfeld(length(Tfeld))-Tfeld(length(Tfeld)-1))*(T-Tfeld(length(Tfeld)-1));

for i=2:length(tp)

    for k=2:length(Tfeld)
        if tp(i)<=Tfeld(k)&&tp(i)>=Tfeld(k-1)
            fneu(i)=ffeld(k-1)+(ffeld(k)-ffeld(k-1))/(Tfeld(k)-Tfeld(k-1))*(tp(i)-Tfeld(k-1));
        end
    end
end

subplot(2,2,1)
plot(ufeld,ffeld,ufeld,ffeld,'*',uref,fneu,''),grid on, xlabel("Displacement [m]"),ylabel("Force [N]"),axis tight
subplot(2,2,2)
plot(tp,uref,Tfeld,ufeldneu,Tfeld,ufeld,'*'),grid on, ylabel("Displacement [m]"),xlabel("Time [s]"),axis tight
subplot(2,2,3)
plot(Tfeld,ffeld,Tfeld,ffeld,'*',tp,fneu,''),grid on, xlabel("Time [s]"),ylabel("Force [N]"),axis tight
subplot(2,2,4)
plot(tp,uref),grid on, ylabel("Displacement [m]"),xlabel("Time [s]"),axis tight

```

```

function motor

%Polished rod load
load('1_90.mat')

A = 4.57;
C = 3.05;
I = 3.05;
P = 3.67;
H = 6.6;
G = 2.82;
R = 1.19;

B=-1780;%Structural unbalance

%Walking Beam W30x173
l_beam=C+A;
mb=260*l_beam; %beam mass 260kg/m
%Pitman W8x10 (geschätzt)
l_pitman=P;
mp=15*l_pitman*2; %pitman mass
%Equalizer W24x55 (geschätzt)
l_equalizer=1;
me=82*l_equalizer;%equalizer beam
%Horsehead
l_head=5;%geschätzt
mh=(mb*(l_beam/2-C)-B*A/9.81-(me+mp)*C)/l_head; %horse head mass
%Crank
Mc=38000; %cranks Nm
lc=3;
mc=Mc/9.81*2;
%Counterweight
l_counter=2.5;%geschätzt
mcounter=2*660;%Counterweight 2540

%oszillating structures
mo=mb+mh+me+mp/2;
lo=(me+mp/2)*C^2+mh*l_head^2+1/12*mb*l_beam^2+mb*(l_beam/2-C)^2;

%rotating structure
Mrot=Mc+mp/2*R*9.81;
Irot=mp/2*R^2+1/3*mc*lc^2;
Mcounter=mcounter*9.81*(lc-l_counter);
lcounter=mcounter*(lc-l_counter)^2;

%%Hub Svinos
SPM=60/n*50;
T=60/SPM;
omega=2*pi/T;
K=((H-G)^2+I^2)^0.5;
d=asin(I/K)-0.0405;
gamma=d-acos(((P+R)^2+K^2-C^2)/2/K/(R+P));

%Referenzdaten - Skalierung
phip=linspace(0,2*pi,n); %0 bei top
theta2=2*pi-phip+d;
L=sqrt(K^2+R^2-2*K*R*cos(theta2));
for i=1:length(theta2)
    if ((0<theta2(i))&&(theta2(i)<pi))||((theta2(i)>2*pi)
        j(i)=1;
    else
        j(i)=-1;
    end
end

```

```

end
end
beta=acos((L.^2+K^2-R^2)/2/K./L).*j;
theta3=acos((P^2-C^2+L.^2)/2/P./L)-beta;
theta4=acos((P^2-C^2-L.^2)/2/C./L)-beta;

theta2p=omega;%linspace(0,0,n);
theta3p=R.*theta2p./P.*sin(theta4-theta2)./sin(theta3-theta4);
theta4p=R.*theta2p./C.*sin(theta3-theta2)./sin(theta3-theta4);

theta2pp=linspace(0,0,n);
theta4pp=theta4.*(theta2pp./theta2p-(theta3p-theta4p)./tan(theta3-theta4)+(theta2p-theta3p)./tan(theta2-theta3));
VR=A*theta4p;
TF=VR./theta2p;

Tload=-TF.*DMS_average;
Tstructure=-Mrot*sin(hip-gamma)-Irot*theta2pp-B*TF+TF*Io/A.*theta4pp;
Tcounter=-Mcounter*sin(hip-gamma)-Icounter*theta2pp;
Total=Tload+Tstructure+Tcounter;

f=20;%Hz
n=f*60

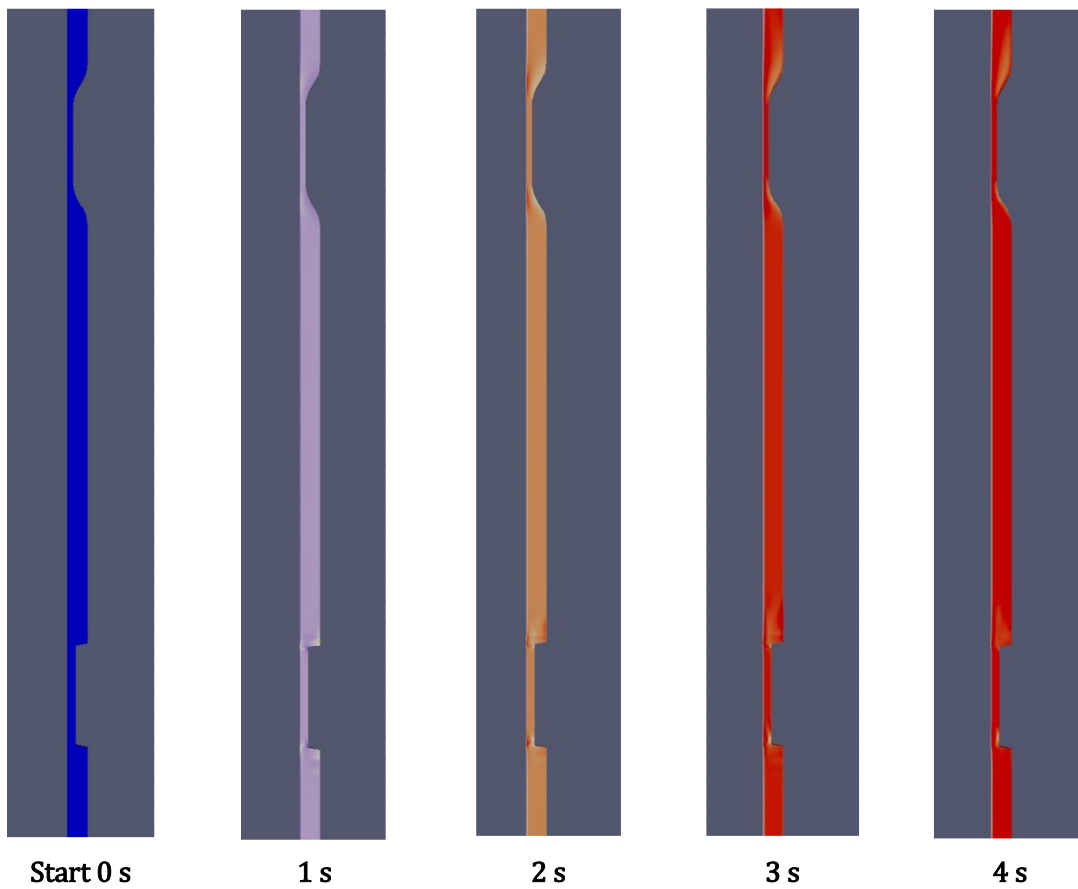
i_ges=n/(60/(length(t_plot)/50))
Mmotor=Total/i_ges;
hip=hip/pi*180;

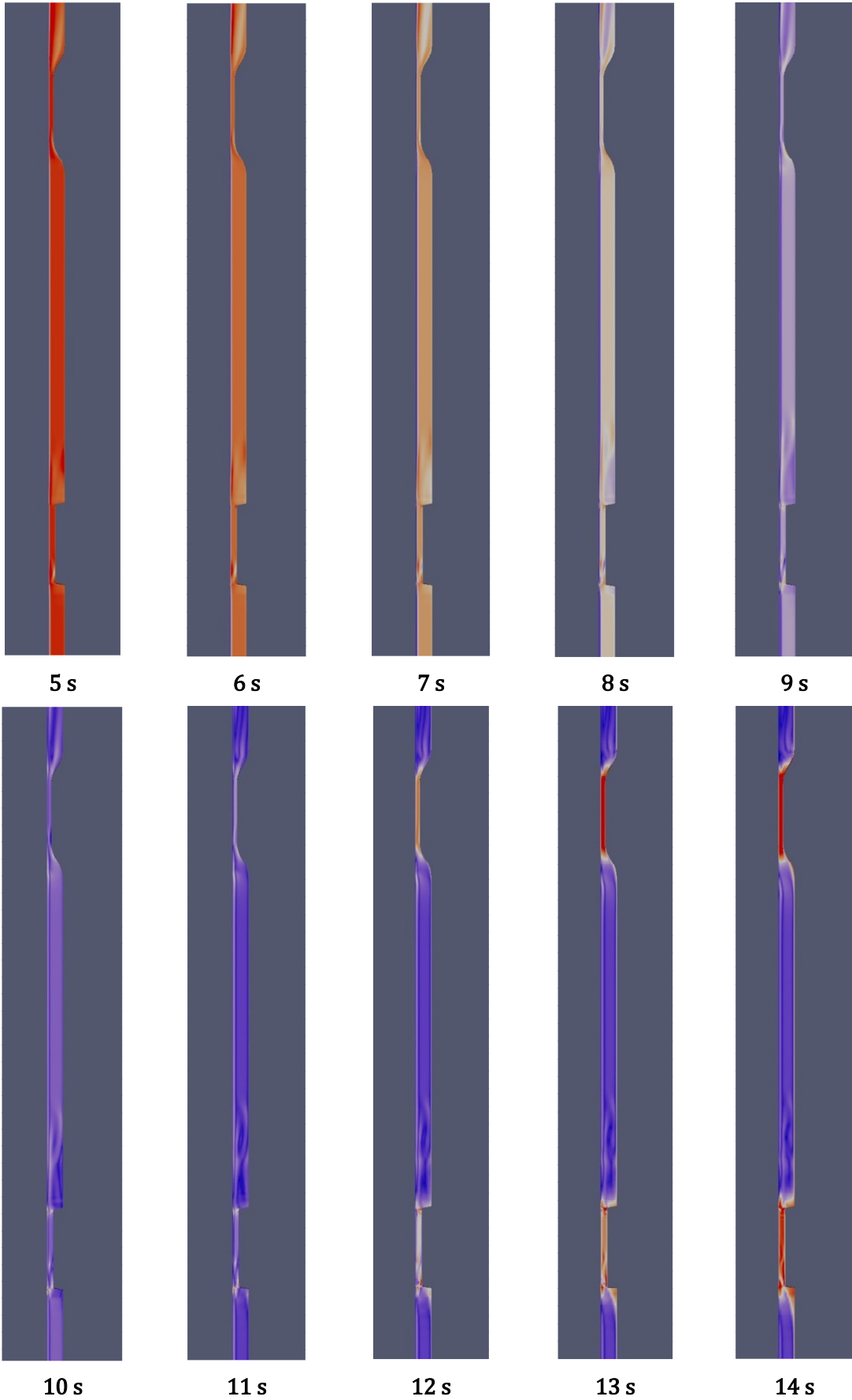
figure
plot(hip,Mmotor),grid on,xlabel('Crank angle (°)'),ylabel('Motor Torque (Nm)'),xlim([0 360]),title('Prime mover torque')

```


APPENDIX B

Appendix B contains the results of the OpenFoam Rod / Tubing Fluid interaction simulation.





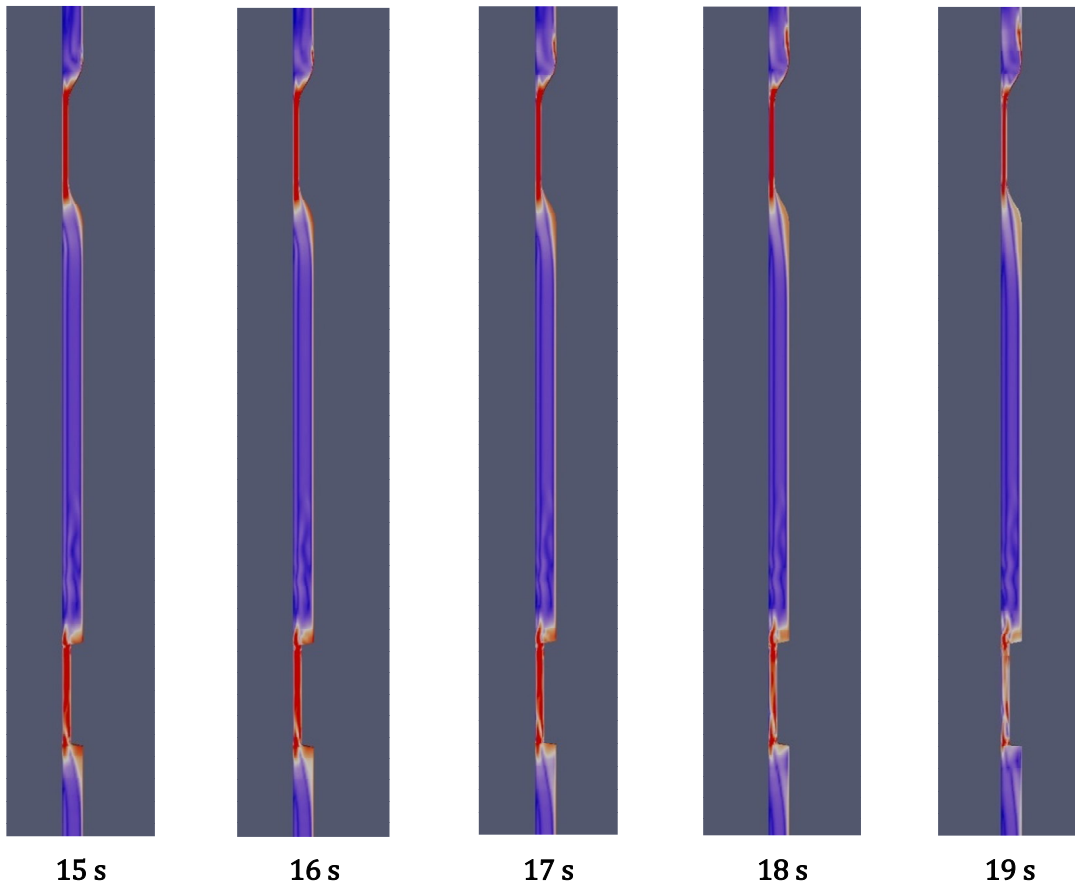


FIGURE 144: VISCOUS DRAG SIMULATION FOR 3 STROKES PER MINUTE

The following section contains the results of the sensitivity analysis performed on the

- mixture density
- tubing diameter
- rod diameter
- stroke length
- strokes per minute

Mixture viscosity:

As mentioned in a previous chapter, the oil viscosity has the biggest influence on the mixture viscosity. The oil viscosity itself depends on parameters like pressure and temperature, as well as oil density and dissolved amount of gas. The extreme values for the mixture viscosity are in one hand pure water, with a viscosity of 0,001 Pas and on the other hand pure oil, with a viscosity of 0,05 Pas. In reality there is no upper limit for the oil viscosity, especially when there are problems with paraffin precipitations.

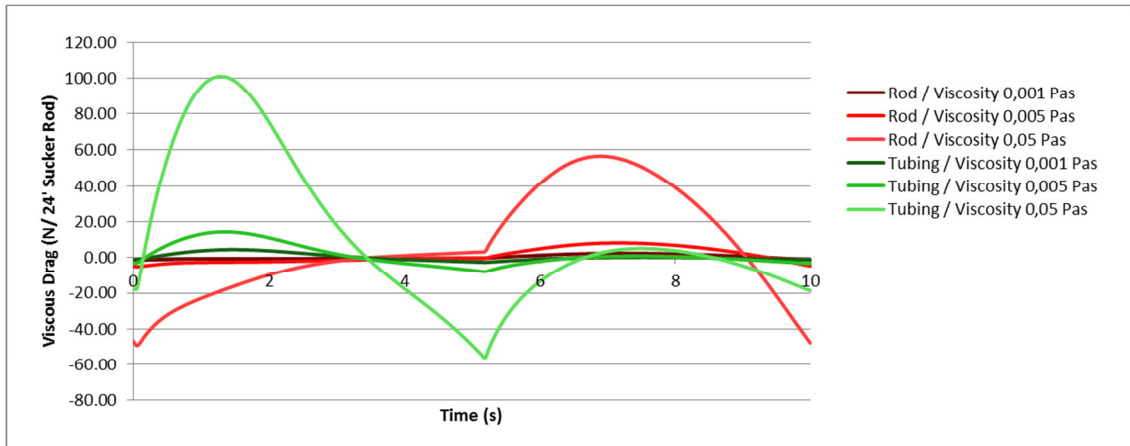


FIGURE 145: INFLUENCE OF MIXTURE VISCOSITY ON VISCOUS DRAG

The magnitude of the viscosity significantly influences the viscous drag. It reaches values higher than 100N during the upstroke.

Tubing diameter:

A change of the tubing diameter requires a change of the protector size. The bigger the tubing, the lower the viscous drag, especially during the downstroke.

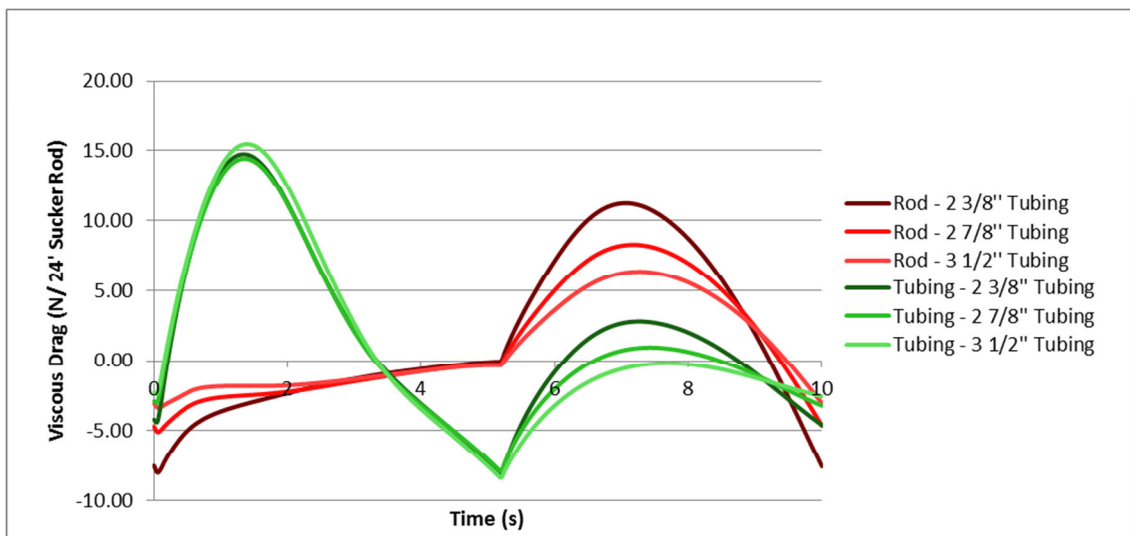


FIGURE 146: INFLUENCE OF TUBING DIAMETER ON VISCOUS DRAG

Rod diameter:

The bigger the rod diameter, the higher the fluid velocities and the higher the viscous drag. Bigger rods require bigger couplings, which cause an additional restriction. The influence can be seen in Figure 147. The major difference to the reference case is again during the downstroke, which is in the range of a multiplier of 2.

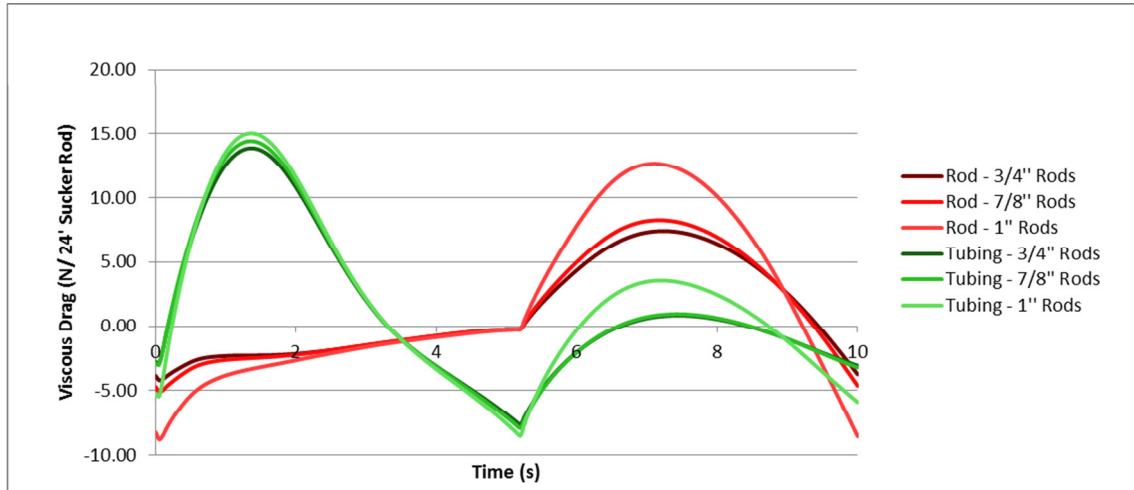


FIGURE 147: INFLUENCE OF ROD DIAMETER ON VISCOUS DRAG

Stroke length:

An increase of the stroke length under the same strokes per minute increases the average fluid velocity and higher velocities cause higher viscous drag.

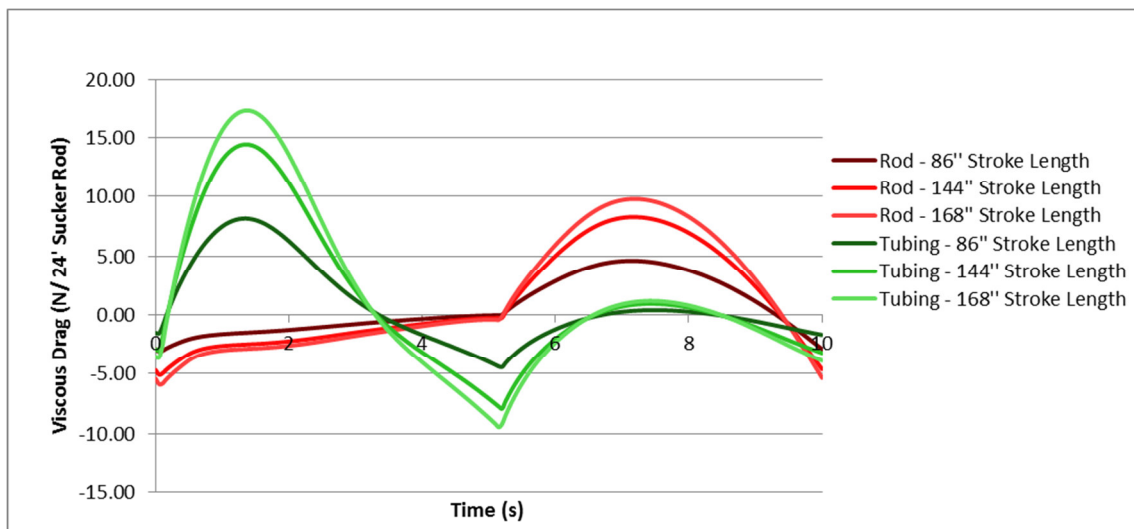


FIGURE 148: INFLUENCE OF THE STROKE LENGTH ON VISCOUS DRAG

Strokes per minute:

The effect of changing the strokes per minute is almost the same like a change in stroke length. More strokes per minute cause higher fluid velocities and thus a higher viscous drag. Figure 149 looks a little bit confusing. The reason therefore is that the curve for 12 SPM repeats 4 times during on cycle of the 3 SPM curve, but the influence of the SPM is clearly indicated by Figure 149.

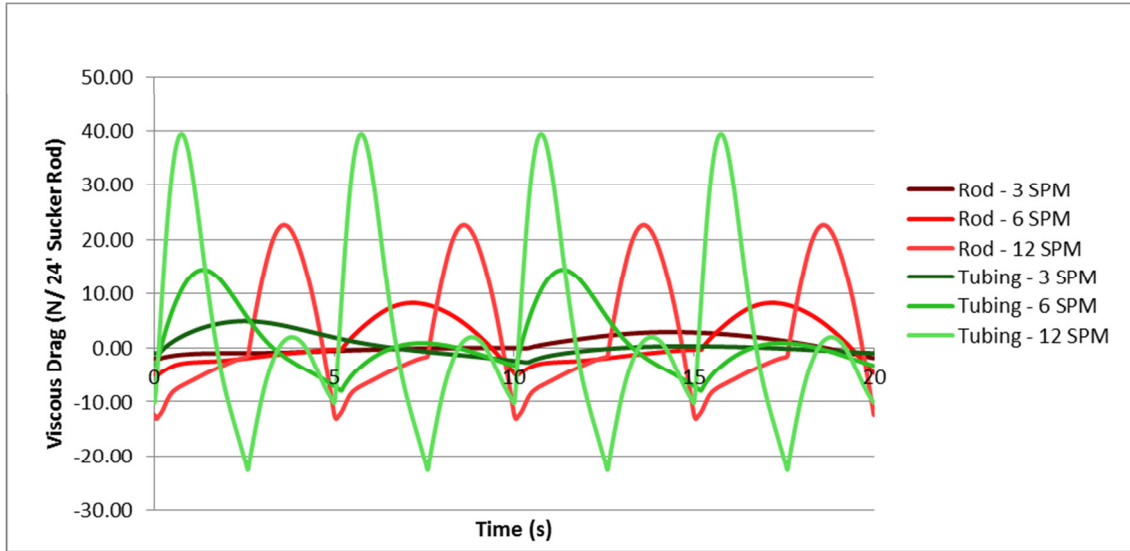


FIGURE 149: INFLUENCE OF STROKES PER MINUTE ON VISCOUS DRAG

APPENDIX C

The following section presents the full details, including the frequency plots of the static and kinetic friction experiments, including statistical evaluations.

Dry Tubing

The experiments started with the dry tubing friction tests. The dry tubing tests were carried out with three different normal forces of 19, 35 and 55 Newton by taking the basic rod guide and attaching some different weights on it.

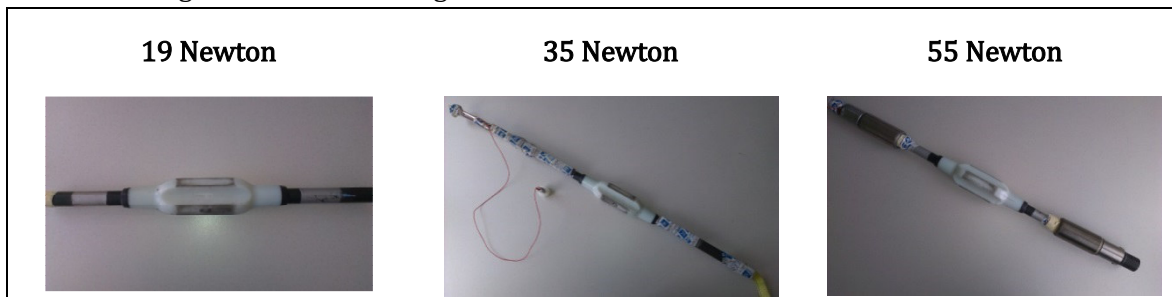


FIGURE 150: ROD GUIDE WITH ATTACHED WEIGHT

At the beginning the static friction tests were performed. The first test series showed that there was some pollution on the tubing walls, because the average friction coefficient of one series was reduced by the continued experiments at the beginning. As a result the first couple of tests are not included in the analysis, because in reality there are such pollutions indeed, but they are removed by the protectors very quickly. The experiments showed that after about 100 repetitions, the surface pollutions were removed effectively.

Another interesting finding was that the friction coefficient is not independent on the contact surface. The tests with 0° , which means that a full rod guides rib is in contact with the tubing, showed higher friction coefficient than a 45° rotated rod guides. Nevertheless nobody can predict how the protectors are oriented in a wellbore. Therefore the statistic average between these two cases is used. The analysis is done, using a history plot and a standard normal distribution with mean and standard deviation.

Figure 151 present the result for the static and dynamic friction coefficient. The standard deviation of the static friction coefficient is wider as a result of the above explained problems with the surface pollution.

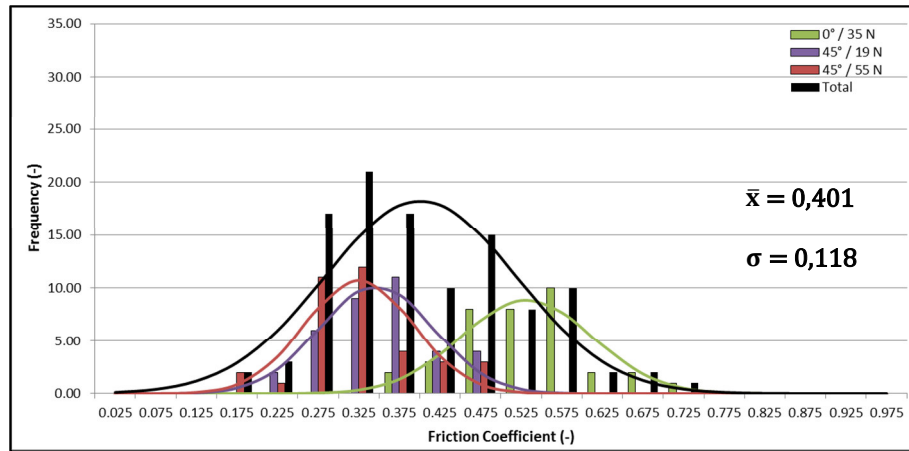


FIGURE 151: FRICTION COEFFICIENT DISTRIBUTION / DRY TUBING / STATIC FRICTION

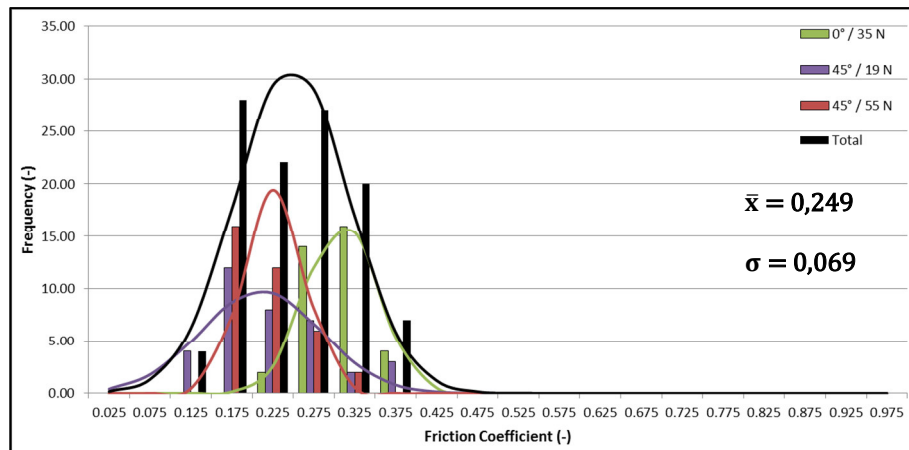


FIGURE 152: FRICTION COEFFICIENT DISTRIBUTION / DRY TUBING / KINETIC FRICTION

Water Wet Tubing

For these test series the tubing was filled with a certain amount of water to wet the sliding surface completely. The testing and evaluation procedure is completely the same like for the dry tubing test. The static friction tests show average values of about 0,288 with a standard deviation of 0,051 in comparison to 0,25 and 0,042 for the kinetic friction tests.

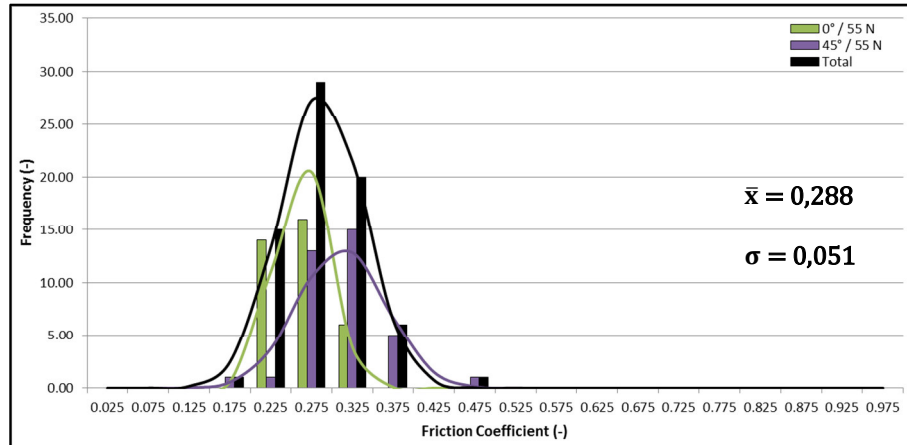


FIGURE 153: FRICTION COEFFICIENT DISTRIBUTION / WATER WET TUBING / STATIC FRICTION

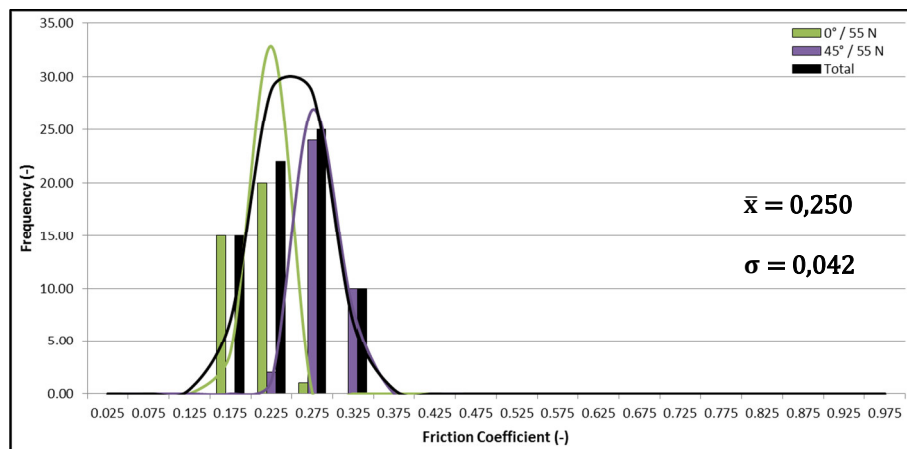


FIGURE 154: FRICTION COEFFICIENT DISTRIBUTION / WATER WET TUBING / KINETIC FRICTION

Oil Wet Tubing

For these test series the tubing was filled with crude oil of a viscosity of about 5 cp at 20°C. The results show that the oil increases, in comparison to water, the static friction coefficient drastically by about 0,15. The kinetic friction coefficient is increased as well, but only at a smaller magnitude.

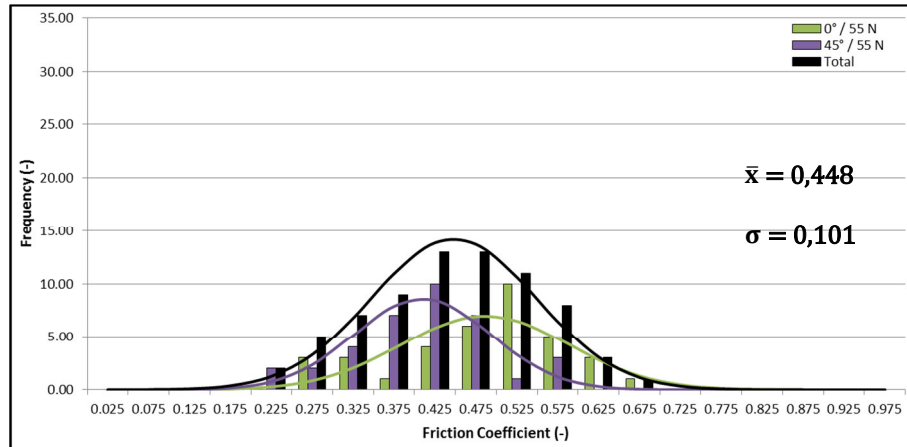


FIGURE 155: FRICTION COEFFICIENT DISTRIBUTION / OIL WET TUBING / STATIC FRICTION

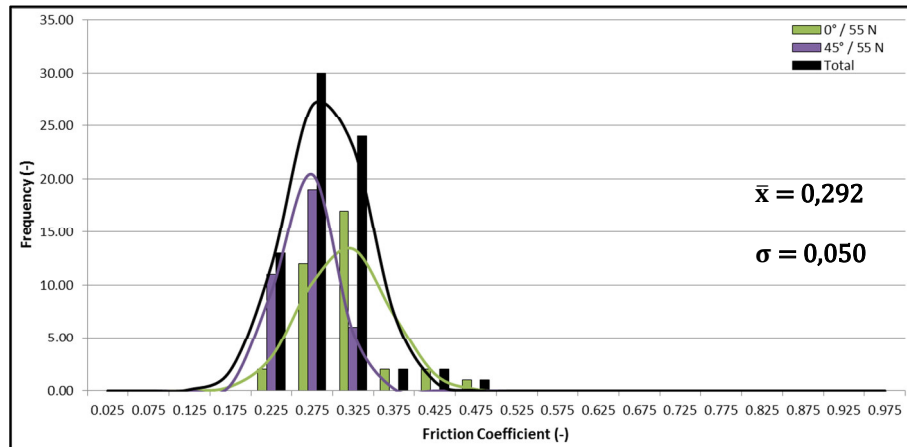


FIGURE 156: FRICTION COEFFICIENT DISTRIBUTION / OIL WET TUBING / KINETIC FRICTION

Oil Wet Tubing with Formation Sand

In a real well often sand accompanies the pumped liquid. To show the influence of formation sand on the friction coefficients 65g of formation sand was added to 100ml of oil. The analysis shows friction coefficient in between those obtained by water and pure oil. This could mean that the sand acts like spheres in a bearing to reduce the friction. Nevertheless it does not mean that sand in the pumped liquid is favorable, because in most cases it is very hard sand with a lot of quartz components, which erode the tubing, especially when it is between the tubing and the rod guides.

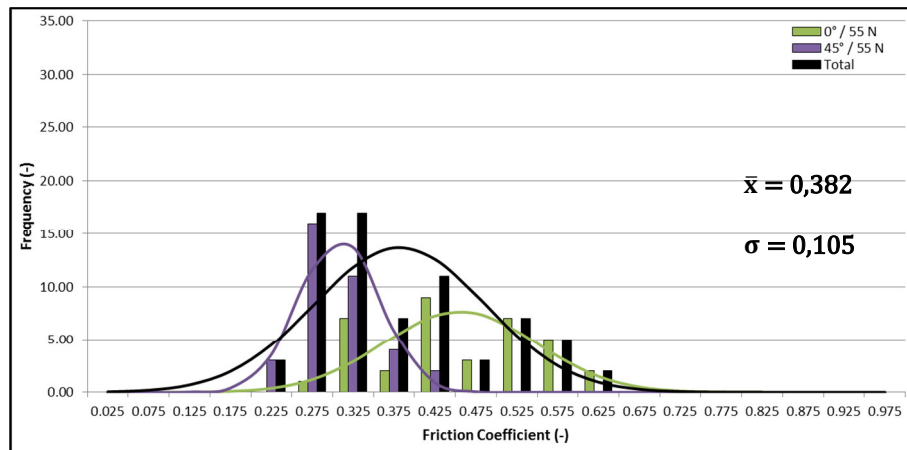


FIGURE 157: FRICTION COEFFICIENT DISTRIBUTION / OIL WET TUBING / STATIC FRICTION

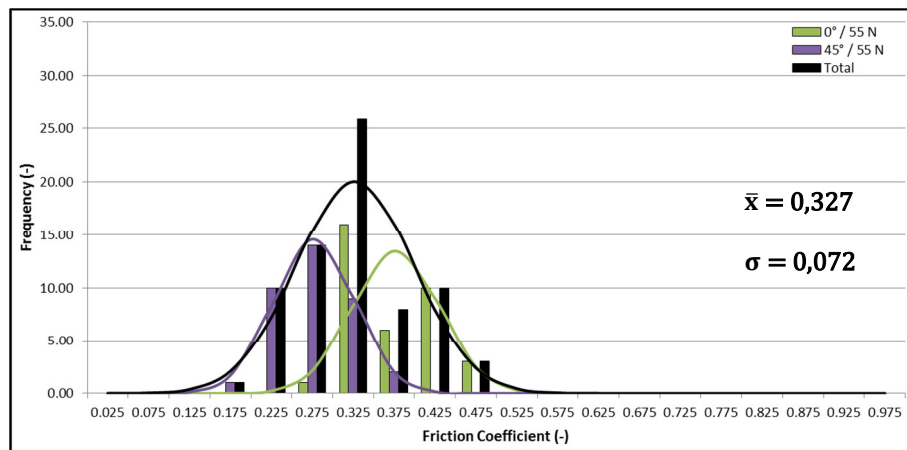


FIGURE 158: FRICTION COEFFICIENT DISTRIBUTION / OIL WET TUBING / KINETIC FRICTION

Hot Oil in Tubing

So far all tests were performed under ambient temperature of about 20°C. To get an idea of the friction coefficients at elevated temperatures one test series was done under a temperature of about 45°C for the static friction coefficients. Beside the viscosity was measured. For the heated oil it was 7cp and 5cp under ambient temperature.

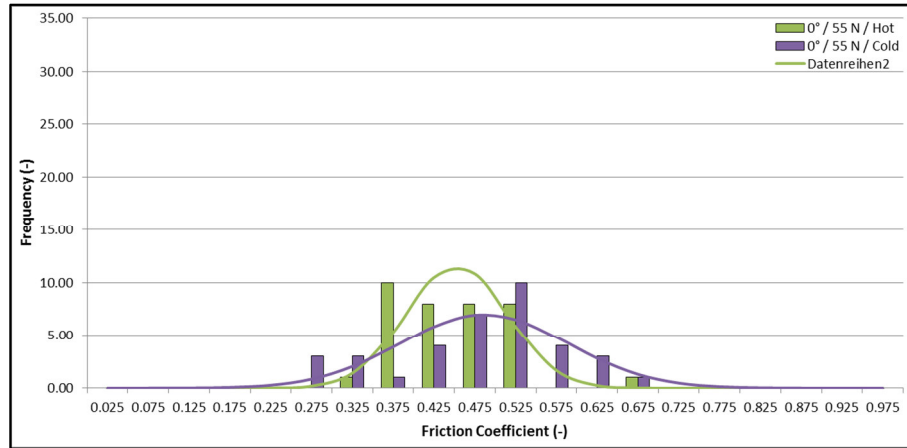


FIGURE 159: FRICTION COEFFICIENT DISTRIBUTION / HOT OIL IN TUBING / STATIC FRICTION

The analysis in Figure 159 shows that the average friction coefficient is reduced slightly from 0,48 to 0,45 for the same normal force of 55N.

APPENDIX D

Appendix D describes the different operating modes of a sucker rod pump in detail.

Gas Interference

Figure 160 presents a typical downhole dynamometer card that shows gas interference. Gas interference will occur, if the pressure in the pump barrel is below the bubble point pressure of the pumped fluid. Dissolved gas from the oil gets liberated and disturbs the pumping process by lowering its efficiency, or in extreme cases even prevents pumping of fluids, which is well known under the expression “gas locked pump”.

The shape of the downhole dynamometer card is a result of the fact that the gas in the pump barrel is compressed and decompressed. To open or close valves, there must be a pressure difference, respectively a force difference, across the standing and travelling valve. To enable an opening of the standing valve during the closed travelling valve and a fluid flow into the barrel during the upstroke, the pressure in the pump barrel must be lower than the intake pressure below the standing valve. This process can require a certain upward displacement of the plunger, causing a reduction of the barrel pressure by the expansion of the free gas and a gradually load shift from the tubing string to the rod string (A). If there was no gas in the pump barrel, as in the case of a full pump, the pressure drop would immediately and the standing valve would open as soon as the plunger starts moving upward. Within the interval (B) and (C) the barrel is filled with new liquid – gas mixture from the wellbore and the load almost remains constant, since it is mainly dependent on the fluid level in the tubing. With point (C) the maximum stroke is reached and the plunger starts moving downwards. Both valves are closed. Now the pressure in the pump barrel must be increased until it exceeds the pressure of the fluid in the tubing, acting atop the plunger, to open the travelling valve. With the downward motion of the plunger, the pressure inside the barrel is increased, which causes a decrease of the plunger load and at a certain point an opening of the travelling valve. Thereby the fluid from the barrel can flow into the tubing to be produced (F), the plunger moves back to its lowest position and the cycle starts again.

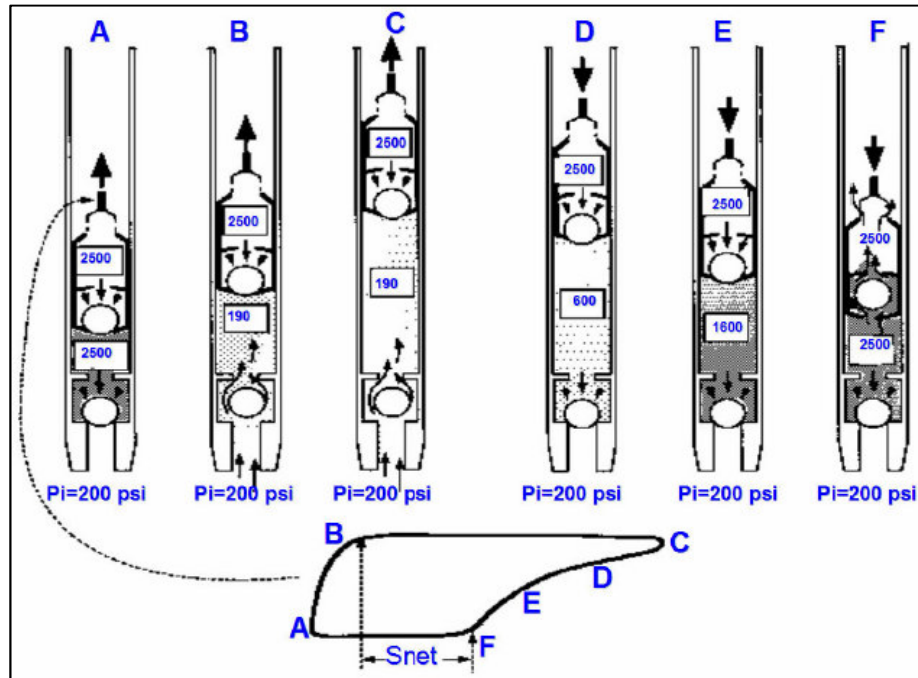


FIGURE 160: GAS INTERFERENCE - CARD (91)

Fluid Pound

Figure 161 shows what happens when the pump is pounding fluid, which occurs when the intake pressure is too low to completely fill the pump barrel with fluid. Fluid pound comes along with low pressure gas in the pump barrel. At the beginning of the upstroke, the load is transferred from the tubing string to the rod string, there is a small effect due to gas compression but afterwards the load stays almost constant until point B is reached. During this sequence the pump barrel cannot be filled completely with fluid due to a too low intake pressure. As a result the travelling valve is not opened immediately when the downstroke starts. Since there is no liquid in the upper portion of the pump barrel but gas, the travelling valve continues to carry the fluid load and it remains closed until the plunger hits the liquid surface. Immediately the travelling valve opens, the load is shifted to the tubing string and the plunger slides through the liquid to its lowermost position. The hit of the plunger often occurs at positions, where the plunger is close to its maximum velocity. As a result there are shocks, travelling through the system, causing a lot of problems that come along with fluid pound.

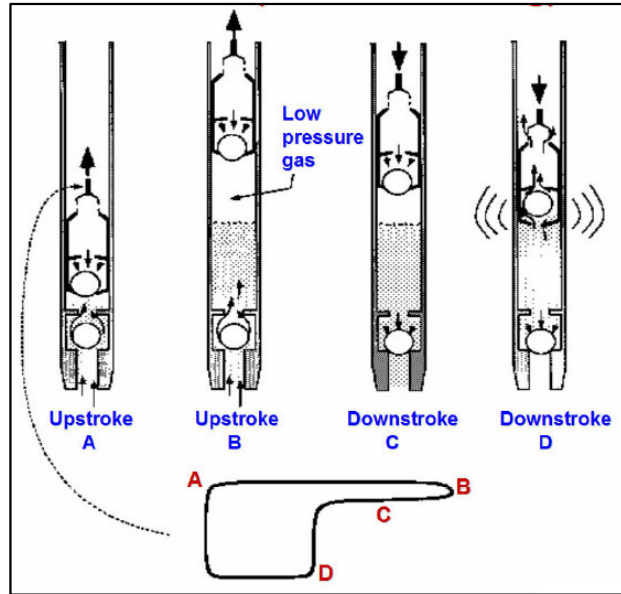


FIGURE 161: FLUID POUND - CARD (91)

Tubing stretch

The fact anchored tubing or non-anchored has an essential influence on the shape of the downhole dynamometer card. When the load on the non-anchored tubing string or rod string is increased or reduced the string reacts with a change in length and a gradually load shift, which occurs twice during one pumping cycle.

During the upstroke, point (A) to (C), the travelling valve closes and the standing valve opens. Due to the gradual load shift from the tubing to the rods, the tubing returns to its initial position. Thereby it moves a certain distance upwards with the pump plunger, which results in a deflection of the downhole pump card from horizontal. During the downstroke the vice versa effect of this principle occurs.

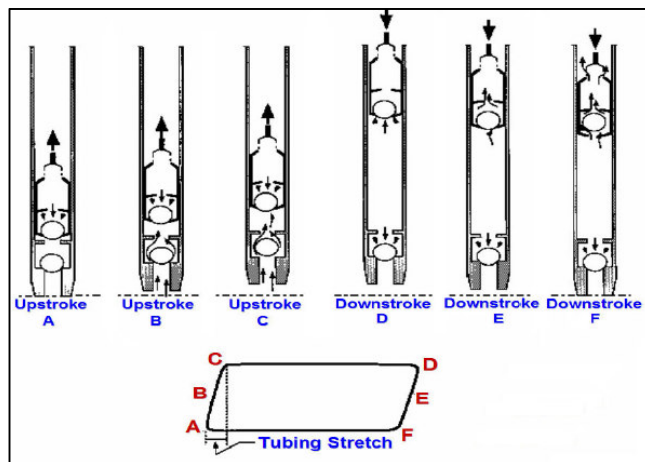


FIGURE 162: TUBING STRETCH - CARD (91)

Excessive Friction

The pump plunger is closely fitted to the pump barrel. The clearance, which is the distance between the inside diameter of the barrel and the outside diameter of the pump plunger, has to be optimized to reduce the viscous friction, coulomb friction and wear, which increases with deceasing clearance and to reduce the slippage, which increases with increasing clearance and causes a reduction of the volumetric efficiency.

Some reservoir fluids have the peculiarity to generate undesired paraffin precipitations at certain surrounding conditions, which can cause in collaboration with sand to excessive friction, if the precipitations are located at the barrel walls. Figure 163 shows how the downhole dynamometer card changes if excessive friction acts on the pump plunger.

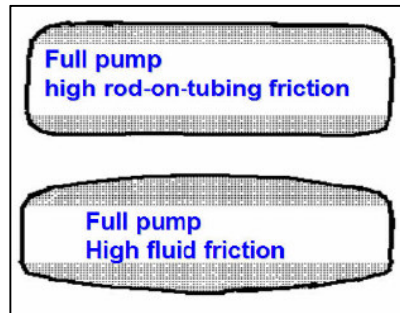


FIGURE 163: EXCESSIVE FRICTION - CARD (83)

APPENDIX E

Temperature Sensor Calibration

The following MatLab code shows the temperature sensor calibration:

```
function [a] = T_Kalibrierung(Nummer)

y=[27 36.5 45 55];

%Kalibrierung Sensor 1
if Nummer==1
    x=[732.5 753.5 772 793];
end
%Kalibrierung Sensor 2
if Nummer==2
    x=[582 597 612 628.5];
end
%Kalibrierung Sensor 3
if Nummer==3
    x=[583.5 599 614.5 631];
end

%Kalibrierung Sensor 4
if Nummer==4
    x=[576.5 592 607 623.5];
end

%Kalibrierung Sensor 6
if Nummer==6
    x=[577 592.5 608 624.5];
end

for i=1:1
    a(i,:)=polyfit(x(i,:),y,1);
    f(i,:)=polyval(a(i,:),x(i,:));
end

plot(x(1,:),y,'+r',x(1,:),f(1,:),'red'), grid on, xlabel('Voltage (mV)'),ylabel('Temperature [°C]'), hold on;
legend('T');
```

Accelerometer Calibration

The following MatLab code shows the accelerometer calibration:

```
function [y]=Acceleration_Kalibrierung(Nummer,wert)

if Nummer == 1
    A=[0.999 -.05 -.036 0 0 0 0 0; 0 0 0 0.999 -.05 -.036 0 0 0; 0 0 0 0 0 0.999 -.05 -.036;
        -.047 -.999 -.047 0 0 0 0 0; 0 0 0 -.047 -.999 -.019 0 0 0; 0 0 0 0 0 -.47 -.999 -.019;
        -.02 -.049 .999 0 0 0 0 0; 0 0 0 -.02 -.049 .999 0 0 0; 0 0 0 0 0 -.02 -.049 .999];
    B=[1 0 0 0 1 0 0 0 1]';
end

if Nummer == 2
    A=[0.999 -.005 -.048 0 0 0 0 0; 0 0 0 0.999 -.0005 -.048 0 0 0; 0 0 0 0 0 0.999 -.005 -.048;
        -.029 -.998 -.048 0 0 0 0 0; 0 0 0 -.029 -.998 -.048 0 0 0; 0 0 0 0 0 -.29 -.998 -.048;
        .01 0 0.99 0 0 0 0 0; 0 0 0 .01 0.99 0 0 0; 0 0 0 0 0 .01 0 .99];
```

```

B=[1 0 0 0 1 0 0 0 1]';
end

if Nummer == 3
A=[0.999 .01 -0.034 0 0 0 0 0 0; 0 0 0 0.999 -.01 -.034 0 0 0; 0 0 0 0 0 0 .999 .01 -.034;
.02 .9997 .015 0 0 0 0 0 0; 0 0 0 .02 .9997 .015 0 0 0; 0 0 0 0 0 0 .02 -.9997 -.015;
.015 .019 .9997 0 0 0 0 0 0; 0 0 0 .015 0.019 .9997 0 0 0; 0 0 0 0 0 0 .015 0.019 .9997];
B=[1 0 0 0 1 0 0 0 1]';
end

if Nummer == 4
A=[0.9997 .015 -0.02 0 0 0 0 0 0; 0 0 0 0.9997 .015 -.02 0 0 0; 0 0 0 0 0 0 .9997 .015 -.02;
.019 .999 .029 0 0 0 0 0 0; 0 0 0 .019 .999 .029 0 0 0; 0 0 0 0 0 0 .019 .999 .029;
0 0 1 0 0 0 0 0; 0 0 0 0 0 1 0 0 0; 0 0 0 0 0 0 0 0 1];
B=[1 0 0 0 1 0 0 0 1]';
end

if Nummer == 5
A=[0.999 .043 0.014 0 0 0 0 0 0; 0 0 0 0.999 .043 .014 0 0 0; 0 0 0 0 0 0 .999 .043 .014;
.005 .99998 .005 0 0 0 0 0 0; 0 0 0 .005 .99998 .005 0 0 0; 0 0 0 0 0 0 .005 .99998 .005;
.005 .005 .99998 0 0 0 0 0 0; 0 0 0 .005 .005 .99998 0 0 0; 0 0 0 0 0 0 .005 .005 .99998];
B=[1 0 0 0 1 0 0 0 1]';
end

if Nummer == 6
A=[0.9996 0 -0.029 0 0 0 0 0 0; 0 0 0 0.9996 0 -0.029 0 0 0; 0 0 0 0 0 0 0.9996 0 -0.029;
-.019 -.9996 -.019 0 0 0 0 0 0; 0 0 0 -.019 -.9996 -.019 0 0 0; 0 0 0 0 0 -.019 -.9996 -.019;
.005 .005 .99998 0 0 0 0 0 0; 0 0 0 .005 .005 .99998 0 0 0; 0 0 0 0 0 0 .005 .005 .99998];
B=[1 0 0 0 1 0 0 0 1]';
end

x=A\B;

K=[x(1) x(2) x(3);x(4) x(5) x(6); x(7) x(8) x(9)];

y=K*wert';

```

Strain Gauge Calibration

The following figures present the strain gauge calibration for all Downhole Dynamometer Sensors.

Downhole Dynamometer Sensor 1

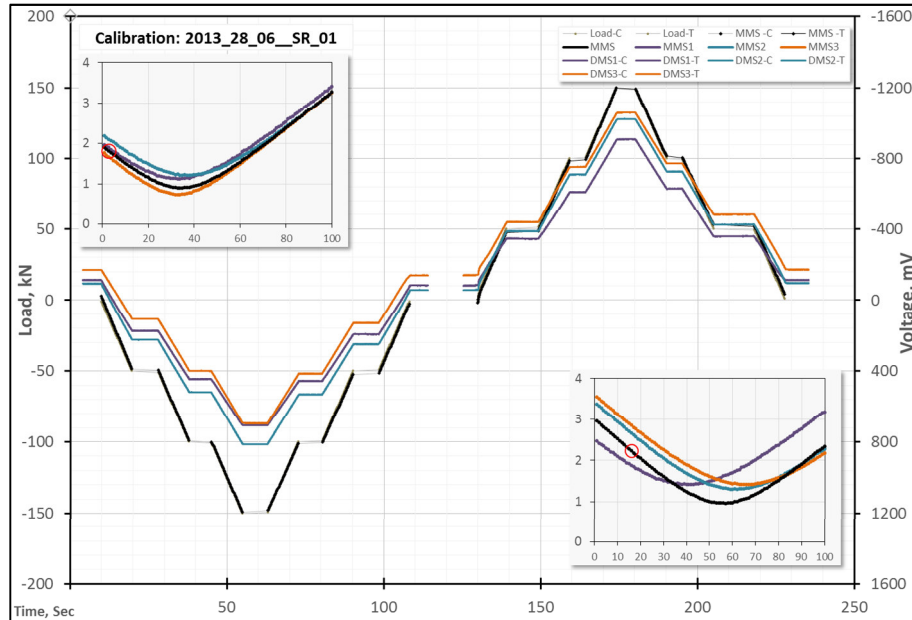


FIGURE 164: ROCK TESTING MACHINE AND DDS 1 – MATCH 2013_28_06

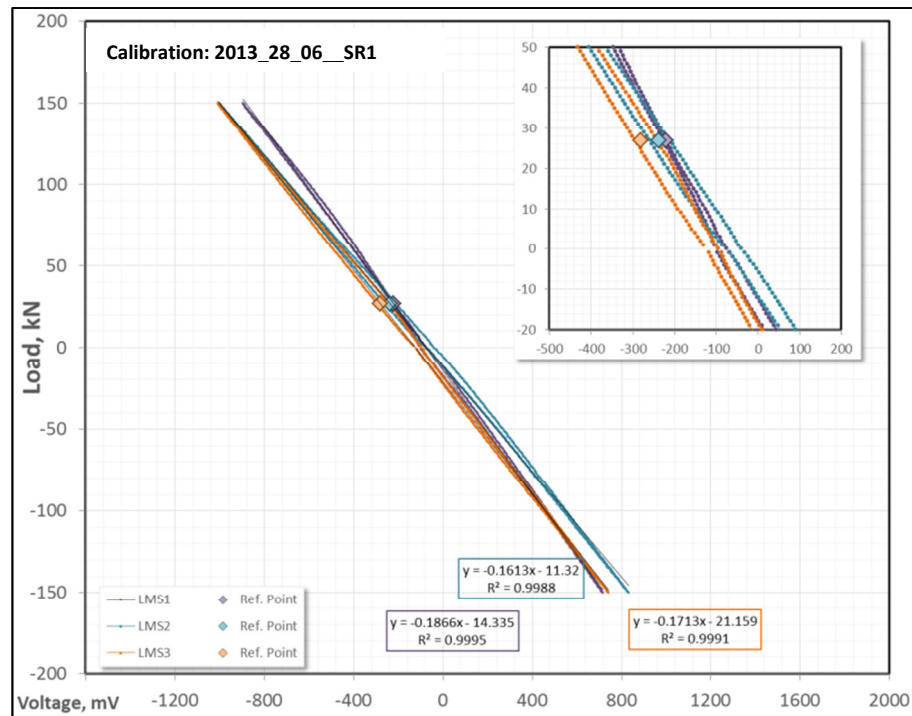


FIGURE 165: CALIBRATION DDS 1 / 2013_28_06

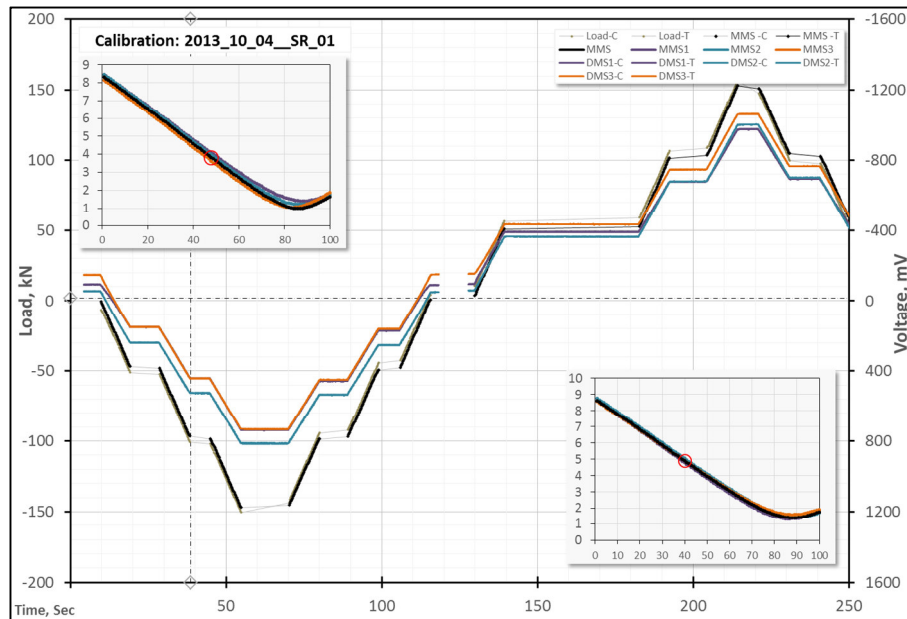


FIGURE 166: ROCK TESTING MACHINE AND DDS 1 – MATCH 2013_04_10

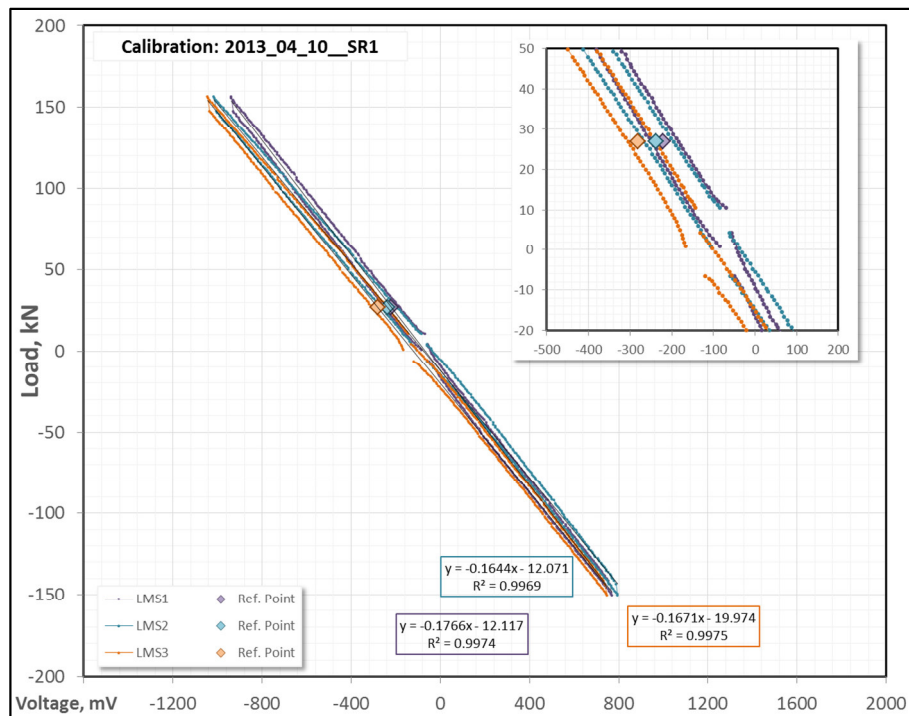


FIGURE 167: CALIBRATION DDS 1 / 2013_04_10

Downhole Dynamometer Sensor 2

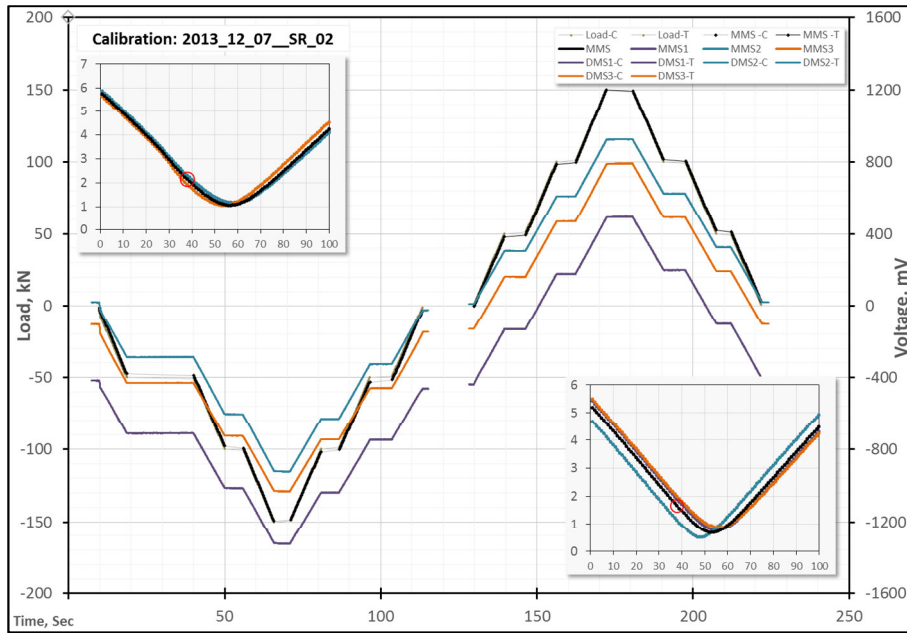


FIGURE 168: ROCK TESTING MACHINE AND DDS 2 – MATCH 2013_12_07

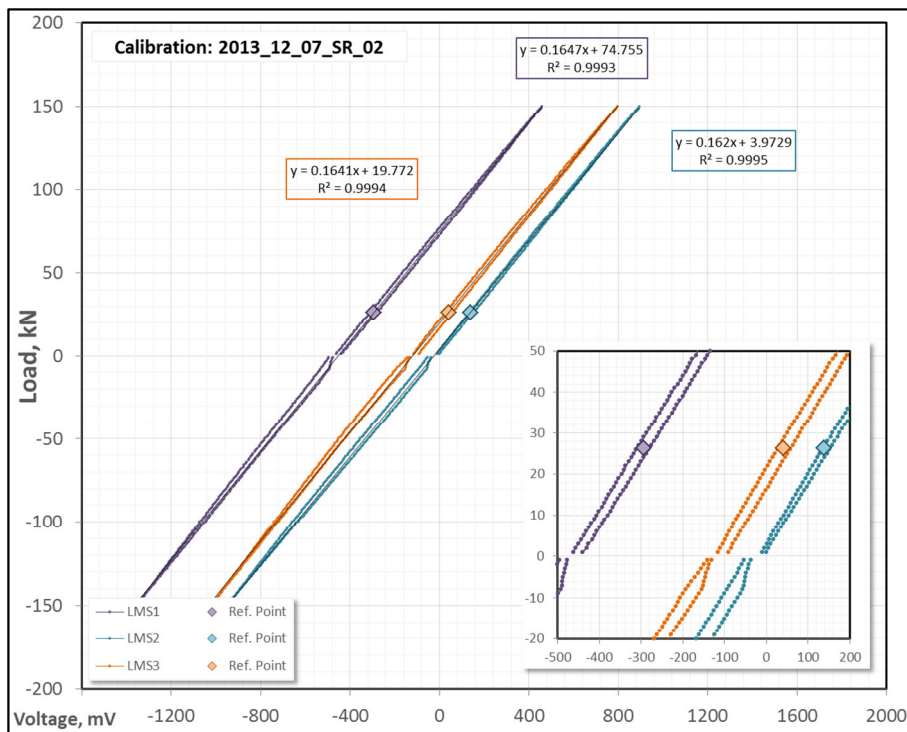


FIGURE 169: CALIBRATION DDS 2 / 2013_12_07

Downhole Dynamometer Sensor 3

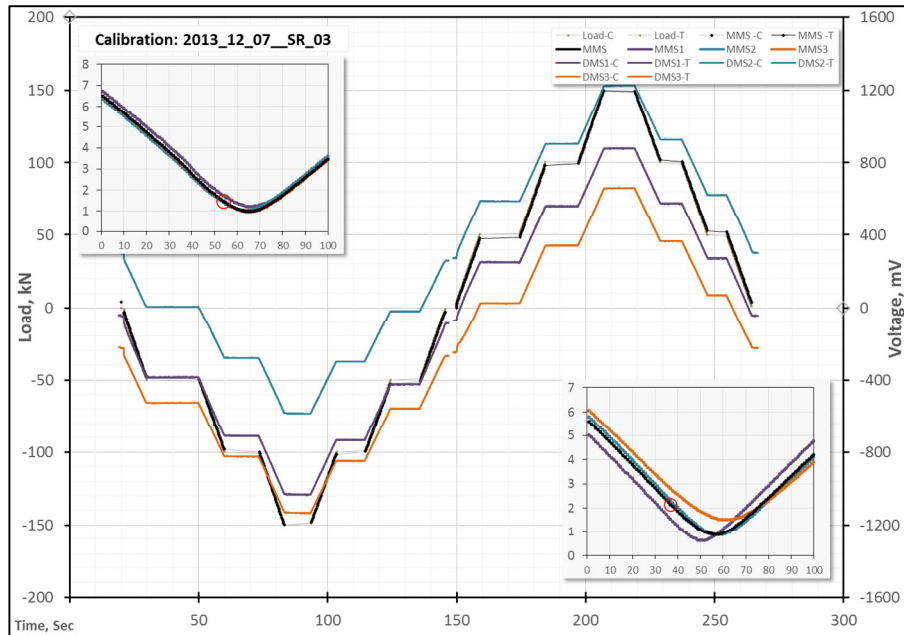


FIGURE 170: ROCK TESTING MACHINE AND DDS 3 – MATCH 2013_12_07

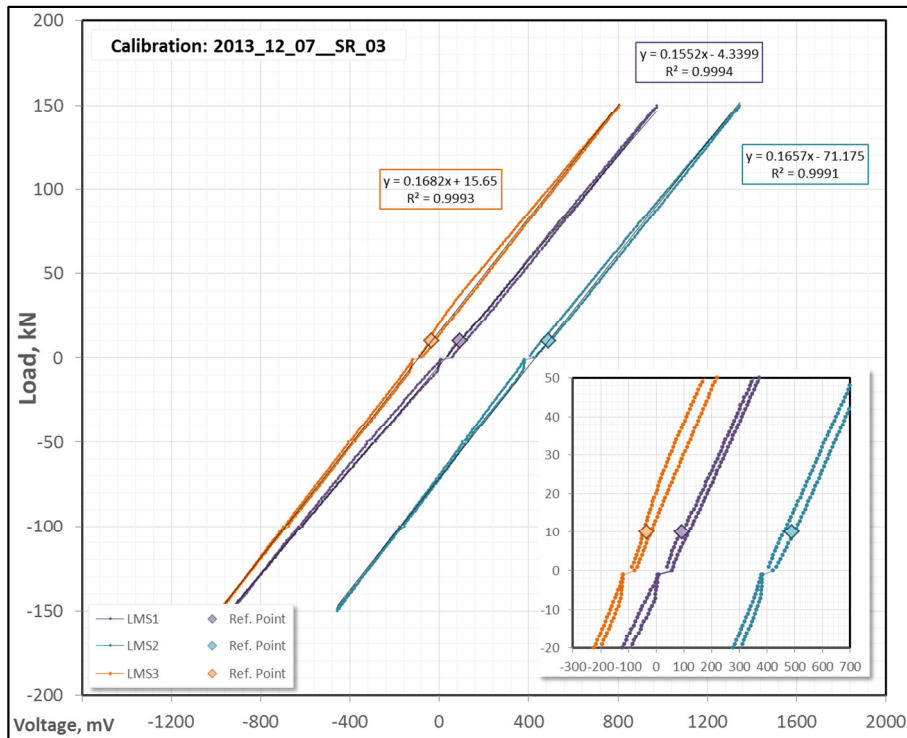


FIGURE 171: CALIBRATION DDS 3 / 2013_12_07

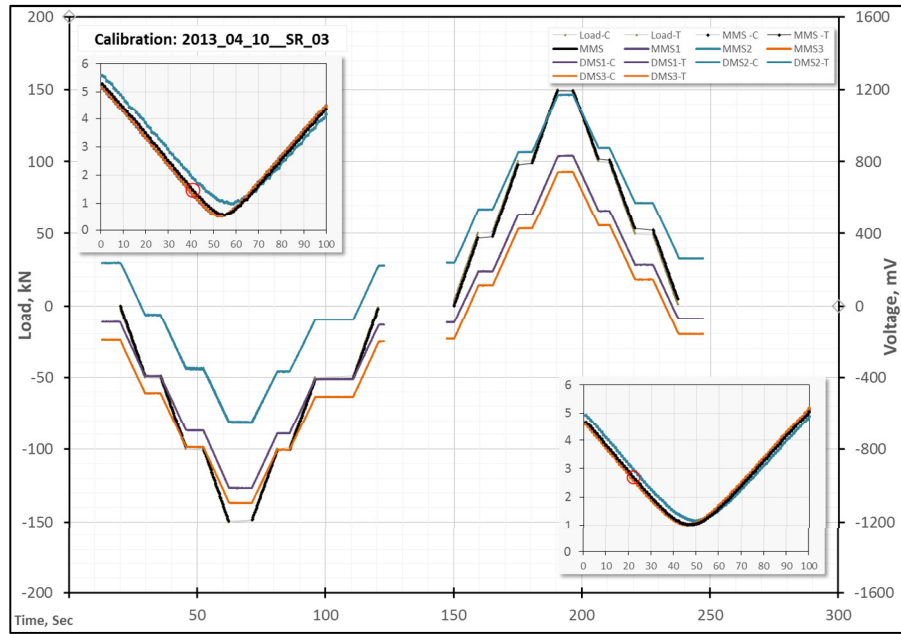


FIGURE 172: ROCK TESTING MACHINE AND DDS 3 - MATCH 2013_04_10

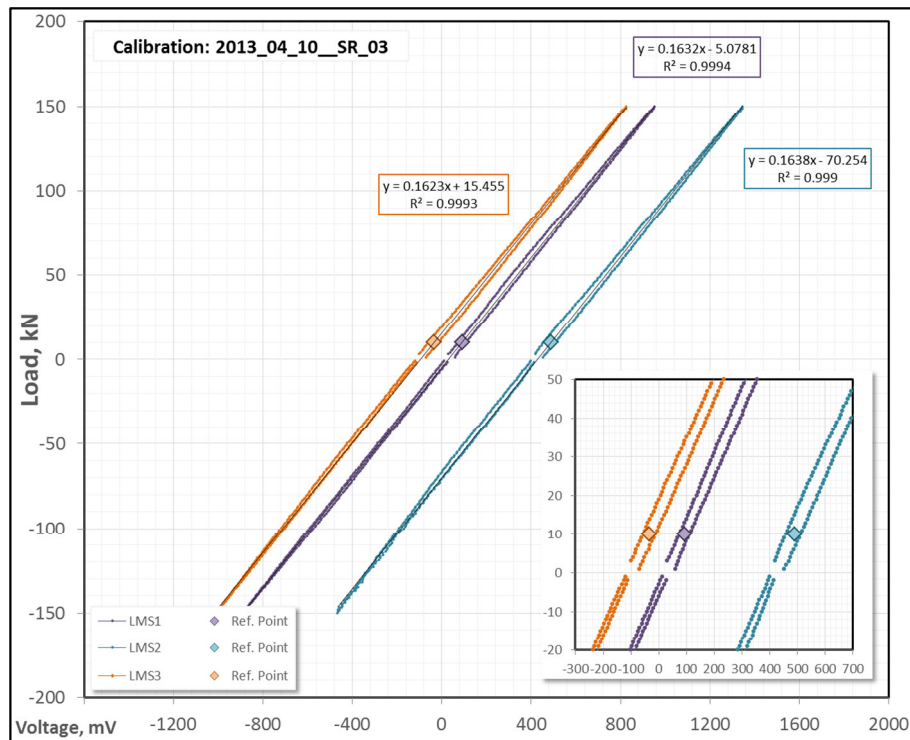


FIGURE 173: CALIBRATION DDS 3 / 2013_04_10

Downhole Dynamometer Sensor 4

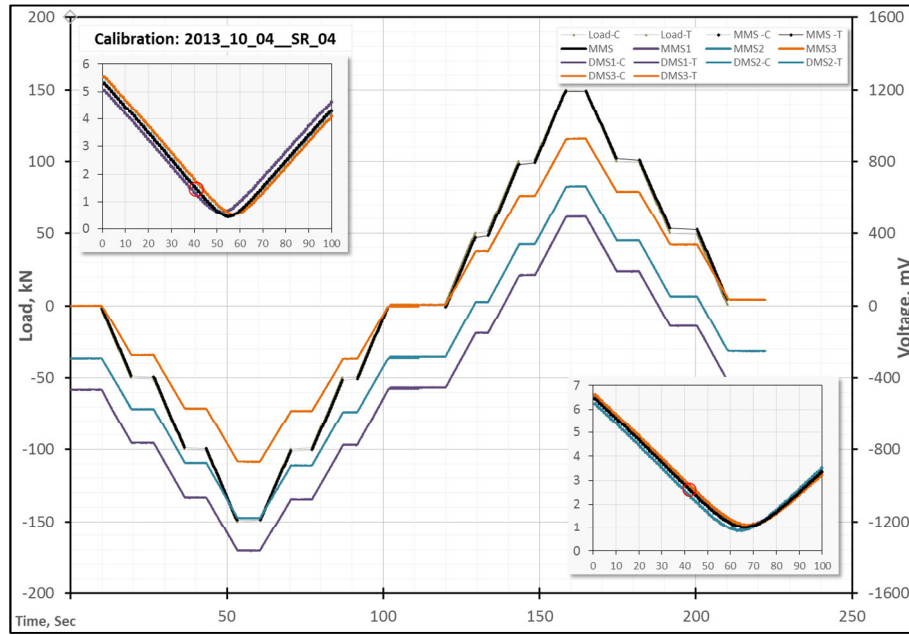


FIGURE 174: ROCK TESTING MACHINE AND DDS 4 – MATCH 2013_04_10

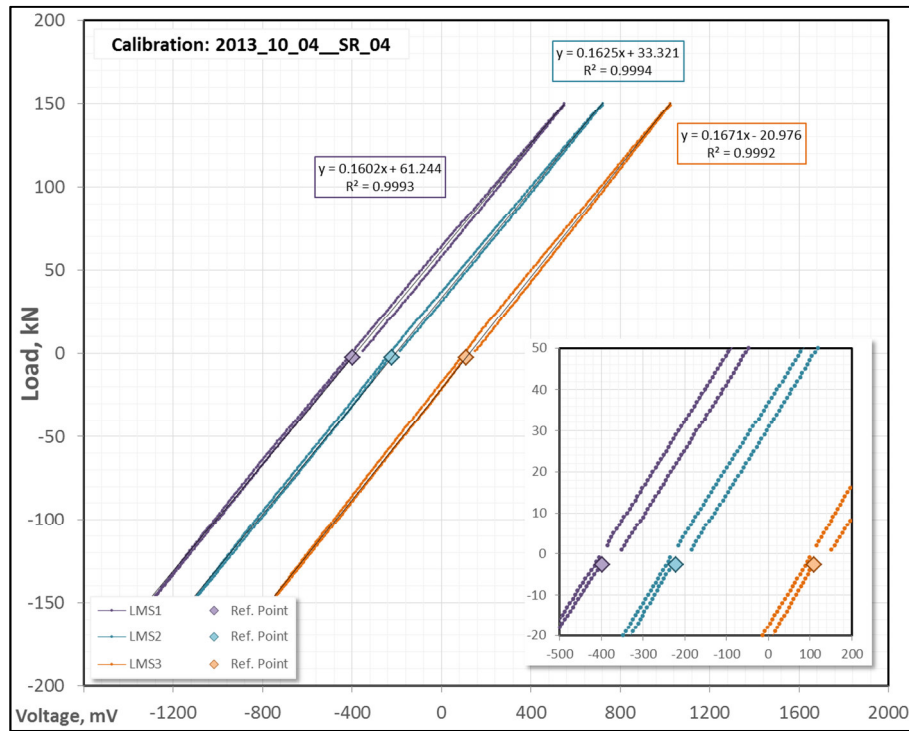


FIGURE 175: CALIBRATION DDS 4 / 2013_04_10

Downhole Dynamometer Sensor 6

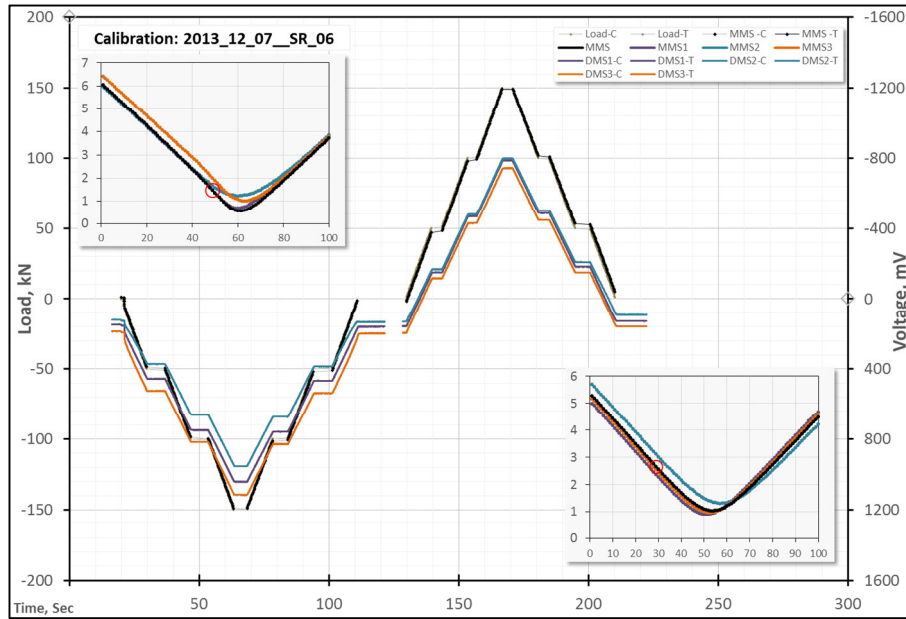


FIGURE 176: ROCK TESTING MACHINE AND DDS 6 – MATCH 2013_12_07

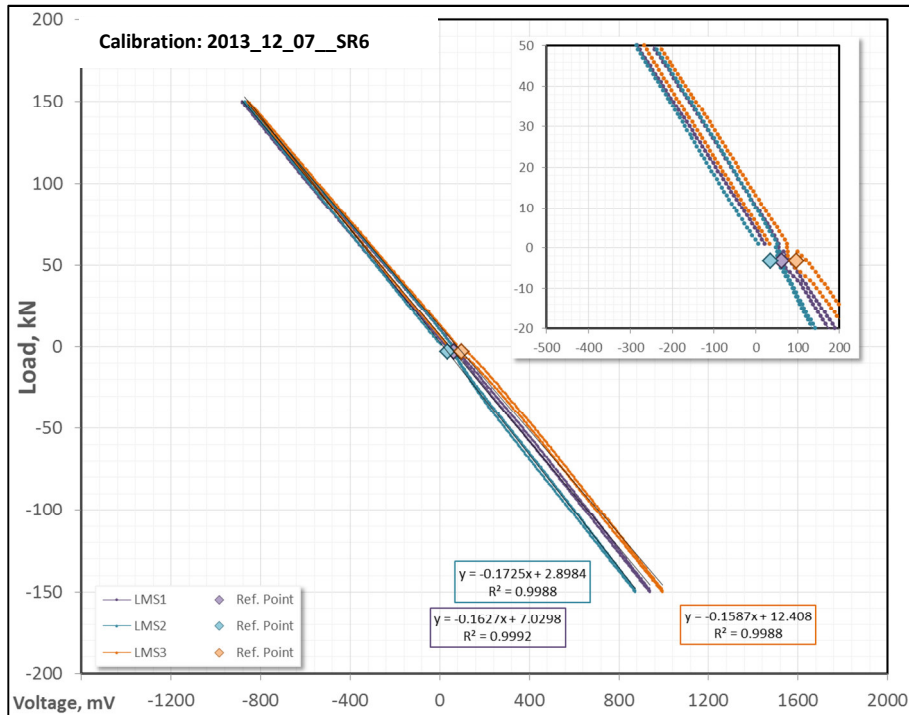


FIGURE 177: CALIBRATION DDS 6 / 2013_12_07

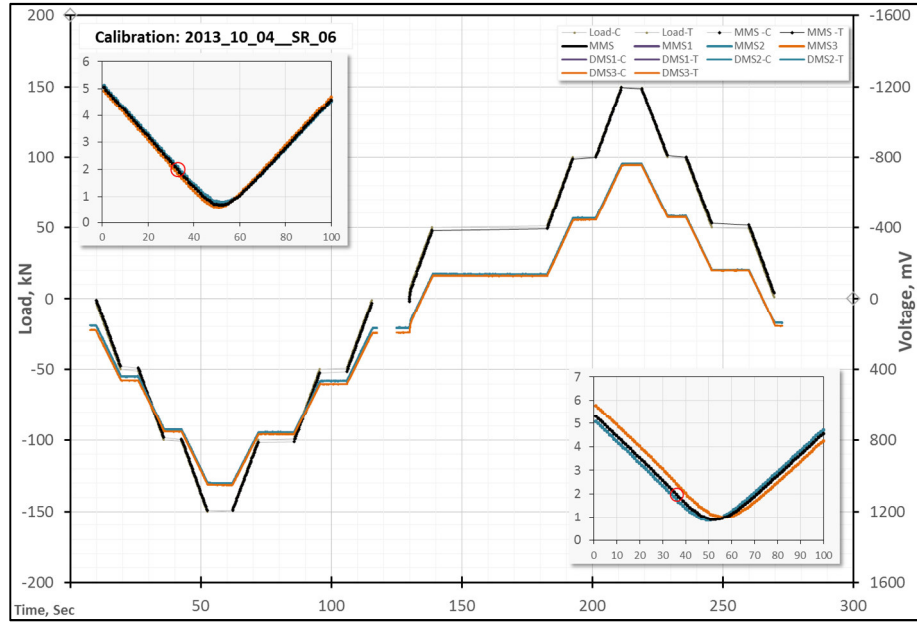


FIGURE 178: ROCK TESTING MACHINE AND DDS 6 – MATCH 2013_04_10

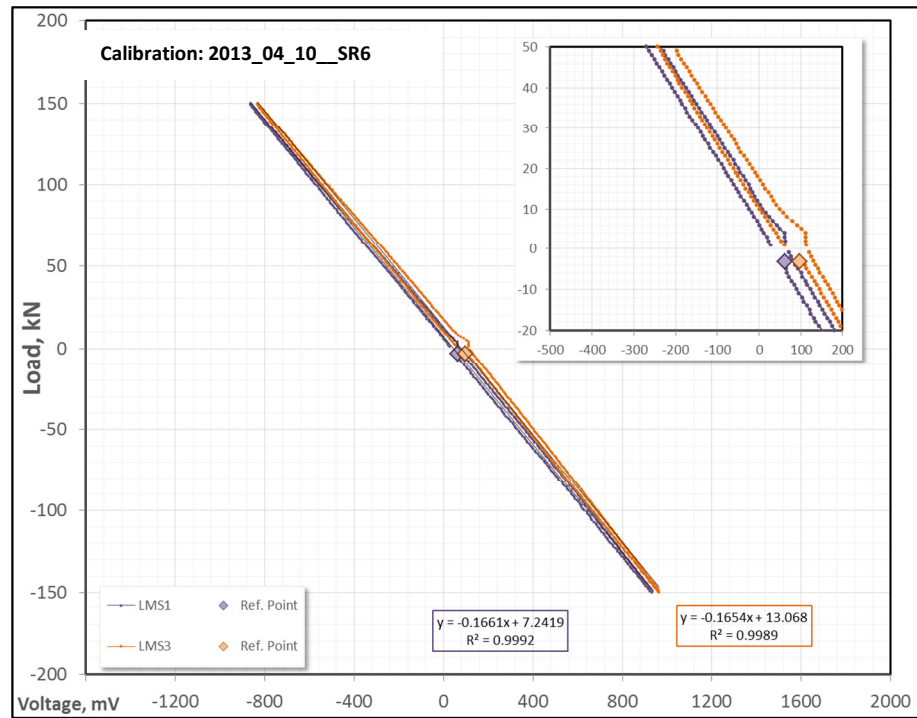


FIGURE 179: CALIBRATION DDS 6 / 2013_04_10

APPENDIX F

This Appendix contains the code and part of the files used for creating the nodes and elements for the FEA.

```
function Knoten_Elemente_ITT_V1

[FileName,PathName,FilterIndex] = uigetfile({'*.xls'},'Data File','D:\Eigene Dateien\A_Petroleum\Bohrlochverlauf1.xls');

ans = inputdlg({'Bezeichnung','x','y','z','MD','Gestänge','Gestängedurchmesser'},'Datenfeld',1,{'000086','G','H','F','E','C','D'});
DatenFile = [PathName FileName];
[num txt raw] = xlsread(DatenFile, 'Koordinaten', 'A1:A4000');
[row,col]=find(strcmp(ans{1},txt)==1);

ans=[ans; int2str(row(1)); int2str(row(length(row)))];

xCol = [ans{2} ans{8} ':' ans{2} ans{9}];
yCol = [ans{3} ans{8} ':' ans{3} ans{9}];
zCol = [ans{4} ans{8} ':' ans{4} ans{9}];
Gestaenge = [ans{6} ans{8} ':' ans{6} ans{9}];
Gestaengedurchmesser = [ans{7} ans{8} ':' ans{7} ans{9}];

x = transpose( xlsread(DatenFile, 'Koordinaten', xCol));
y = transpose( xlsread(DatenFile, 'Koordinaten', yCol));
z = transpose(-xlsread(DatenFile, 'Koordinaten', zCol));
rods = transpose(xlsread(DatenFile, 'Koordinaten', Gestaenge));
radius_rods = transpose(xlsread(DatenFile, 'Koordinaten', Gestaengedurchmesser))*25.4/2000;

rods = [481.5 411.5];
radius_rods = [0.01111, 0.01111];

%Gestängedefinition
segment_length=linspace(7.62,7.62,length(rods)); %Rodsegmentlänge je Abschnitt
protector_anzahl=linspace(2,2,length(rods)); %Protektoranzahl
abstand0p=[0.25 0.5 0.75 1];
abstand2p=[0.2428 0.5 0.7572 1];
abstand4p=[0.0788 0.2074 0.336 0.4646 0.5932 0.7218 0.8504 1];

anzahl_segmente=round(rods./segment_length) %Rodanzahl

figure(1), cla
plot3(x,y,z,'bo','LineWidth',1); hold on; grid on; box on; axis equal

%Generierung des Splines
xyz=[x;y;z];
fn=cscvn(xyz); %Ermittlung der Splines
fnplt(fn,'r',2)
dpp = fnder(fn); %Spline ableiten

%Abstandsvektor Rod - Protektor

for j=1:length(anzahl_segmente)
    zl=0;
    if protector_anzahl(j)==0
        abstand=abstand0p*segment_length(j);
    end
    if protector_anzahl(j)==2
        abstand=abstand2p*segment_length(j);
    end
    if protector_anzahl(j)==4
        abstand=abstand4p*segment_length(j);
    end
end
```

```

end

for i=1:anzahl_segmente(j)
    for k=1:length(abstand)
        zl=k+(i-1)*length(abstand);
        lengthvektor(j,zl)=abstand(k)+segment_length(j)*(i-1);
    end
end
end

%Parameteregenerierung Rod
Q=0; %numerisch integrierte Länge
Q_Rest(1)=0; %Restlänge im Parameterbereich
Q_RestAbschnitt=0; %Restlänge
p=[0]; %iterierter Parameterwert
k=1; %Abschnittszähler / Parameternummer
Q_vektor1=[0]; %Längensammler
p_vektor1=[0]; %Parameterwert der Knoten am Rod
%zr=1;

for j=1:length(anzahl_segmente)

    if protector_anzahl(j)==0
        anzahl=2;
    end
    if protector_anzahl(j)==2
        anzahl=2;
    end
    if protector_anzahl(j)==4
        anzahl=4;
    end

    for i=1:2*anzahl_segmente(j)*anzahl

        while abs(Q-lengthvektor(j,i)-Q_RestAbschnitt(j))>0.1

            Q=Q_Rest+quad(@myfun,0,p(i),1e-6,0,dpp.coefs,1+3*(k-1));
            p(i)=p(i)+0.01;

            if (fn.breaks(k+1)-fn.breaks(k))<p(i)
                Q_Rest=Q;
                k=k+1;
                p(i)=0;
            end
        end
        Q_vektor(i)=Q; %Längensammler Segmente
        p_vektor(i)=fn.breaks(k)+p(i); %Parametersammler
        p(i+1)=p(i);
        Q_RestAbschnitt(j+1)=Q;
    end

    Q_vektor1=[Q_vektor1 Q_vektor];
    Q_vektor=[];
    p_vektor1=[p_vektor1 p_vektor]; %Parameterwert der Knoten am Rod
    p_vektor=[];
end

pr_wert=fnval(fn,p_vektor1); %Koordinaten der Knoten am Rod
plot3(pr_wert(1,:),pr_wert(2,:),pr_wert(3,:),'r*');

[T,N,B,k,t] = frenet(pr_wert(1,:),pr_wert(2,:),pr_wert(3,:)); %Dreibein rods

%_____
% Abaqus Ausgabe in txt- Dateien / - vor x achse

%Rodnummern
counterr=1:1:length(pr_wert');
counterr=counterr+1999;
collr=[counterr' pr_wert'];

fileID = fopen('rodnummer_Pir86_V0.txt','w+');
fprintf(fileID,'%6.0f %8.5f %8.5f %10.5f\r\n',collr');

```

```

fclose(fileID);

%Daten für Auswertung
T_h=sqrt(T(:,1).^2+T(:,2).^2);
Incl=abs(atan(T_h./T(:,3)))*180/pi;

DS(1)=0;
for i=1:length(Incl)-1
    DS(i+1)=(Incl(i+1)-Incl(i))/3.8*30;
end

collmd=[counterr' Q_vektor1' Incl DS'];
fileID = fopen('MD_V0.txt','w+');
fprintf(fileID,'%6.0f,%8.5f,%8.5f,%8.5f\r\n',collmd');
fclose(fileID);

%Elementgenerierung Rod
%1. Abschnitt
%-----
if protector_anzahl(1)==0
    anzahl=2;
end
if protector_anzahl(1)==2
    anzahl=2;
end
if protector_anzahl(1)==4
    anzahl=4;
end

for i=1:(2*anzahl*anzahl_segmente(1))/2
    k=i*2;
    elgenrod1(i,:)=[i,k-1+1999,k+1999,k+1+1999];
end

fileID = fopen('rodelement1_Pir86_V0.txt','w+');
fprintf(fileID,'%6.0f,%6.0f,%6.0f,%6.0f\r\n',elgenrod1');
fclose(fileID);

%ITT Elemente Segment 1 ohne Protektoren
for ii=1:(length(elgenrod1(:,1))+1)*anzahl/2
    itt1oP(ii,:)=[7998+2*ii,1998+2*ii];
end
%ITT Elemente Segment 1 mit Protektoren
for ii=1:length(elgenrod1(:,1))*anzahl/2
    itt1mP(ii,:)=[7999+2*ii,1999+2*ii];
end
if length(rods)==1
    itt1oP(end,:)=[];
    itt1mP(ii+1,:)=[7999+2*ii+1,1999+2*ii+1];
end

fileID = fopen('ittelement_Pir86_1oP_V0.txt','w+');
fprintf(fileID,'%6.0f,%6.0f\r\n',itt1oP');
fclose(fileID);
fileID = fopen('ittelement_Pir86_1mP_V0.txt','w+');
fprintf(fileID,'%6.0f,%6.0f\r\n',itt1mP');
fclose(fileID);

%2.Abschnitt
%-----
if length(rods)>=2
    if protector_anzahl(2)==0
        anzahl=2;
    end
    if protector_anzahl(2)==2
        anzahl=2;
    end
    if protector_anzahl(2)==4
        anzahl=4;
    end

    for j=i+1:(i+anzahl*anzahl_segmente(2))

```

```

k=j*2-2;
elgenrod2(j-i,:)=j,k+1+1999,k+1999+2,k+1+1999+2];
end
length(elgenrod2)
fileID = fopen('rodelement2_Pir86_V0.txt','w+');
fprintf(fileID,'%6.0f,%6.0f,%6.0f,%6.0f\r\n',elgenrod2');
fclose(fileID);

%ITT Elemente Segment 2 ohne Protektoren
for jj=1:(length(elgenrod2(:,1))*anzahl/2)
    itt2oP(jj,:)=[itt1oP(end,1)+2*jj,itt1oP(end,2)+2*jj];
end
%ITT Elemente Segment 2 mit Protektoren
for jj=1:length(elgenrod2(:,1))*anzahl/2
    itt2mP(jj,:)=[itt1mP(end,1)+2*jj,itt1mP(end,2)+2*jj];
end

if length(rods)==2
    itt2oP(end,:)=[];
    itt2mP(jj+1,:)=[itt1mP(end,1)+2*jj+1,itt1mP(end,2)+2*jj+1];
end
fileID = fopen('itttelement_Pir86_2oP_V0.txt','w+');
fprintf(fileID,'%6.0f,%6.0f\r\n',itt2oP');
fclose(fileID);
fileID = fopen('itttelement_Pir86_2mP_V0.txt','w+');
fprintf(fileID,'%6.0f,%6.0f\r\n',itt2mP');
fclose(fileID);
end

%Rodnummern / Haltepunkt für Federn
counterr=1:1:length(pr_wert');
counterr=counterr+3999;
pr_wert_feder=pr_wert;
pr_wert_feder(3,:)=pr_wert_feder(3,)+0.0001;
collr=[counterr' pr_wert_feder'];

fileID = fopen('rodnummerfeder_Pir86_V0.txt','w+');
fprintf(fileID,'%6.0f,%8.5f,%8.5f,%10.5f\r\n',collr');
fclose(fileID);

%Rodnummern / Pipe Elemente
counterr=1:1:length(pr_wert');
counterr=counterr+5999;
pr_wert_feder=pr_wert;
pr_wert_feder(3,:)=pr_wert_feder(3,);
collr=[counterr' pr_wert_feder'];

fileID = fopen('rodnummerpipe_Pir86_V0.txt','w+');
fprintf(fileID,'%6.0f,%8.5f,%8.5f,%10.5f\r\n',collr');
fclose(fileID);

%Flüssigkeitsreibung
Time = xlsread('Auswertung.xls','SPM','A3:A403');
F_rod = xlsread('Auswertung.xls','SPM','E3:E403');
Laenge(1)=0;
for i=1:length(Q_vektor1)-1
    Laenge(i+1)=Q_vektor1(i+1)-Q_vektor1(i);
end

Time=[Time', (Time(end)+Time(2:end))'];
Time=3+Time/20*19.2;
F_rod=[F_rod',F_rod(2:end)'];
F_rod=F_rod/7.62*mean(Laenge);

fileID = fopen('Fluid_Reibung_V0.txt','w+');
fprintf(fileID,'%10.5f,%10.5f\r\n',[Time F_rod]);
fclose(fileID);

%Generierung Tangentenvektor
Tangente=[T(:,1),T(:,2),T(:,3)];

fileID = fopen('Tangente_Pir86_V0.txt','w+');

```

```

fprintf(fileID, '%10.5f,%10.5f,%10.5f\r\n', Tangente');
fclose(fileID);

%Ermittlung der Federkonstanten
Dichte=880; %Mittlere Dichte
a=3.6;
r=0.011;
for i=1:length(pr_wert')
    c(i)=-2*r^2*pi*Dichte*9.81/a*pr_wert(3,i);
end

fileID = fopen('Federkonstante_Pir86_V0.txt','w+');
fprintf(fileID, '%6.0f\r\n', c);
fclose(fileID);

```

ABAQUS Input File:

```

*Heading
*Preprint, echo=NO, model=NO, history=NO, contact=YES
*Node, INPUT=rodnummer_Pir86_V0.txt, nset=n_rod
*Element, ELSET=el_rod1, type=B32, INPUT=rodelement1_Pir86_V0.txt
*Beam Section, elset=el_rod1, material=steel, poisson=0.3, temperature=GRADIENTS, section=CIRC
0.011
*Nonstructural Mass, elset=el_rod1, units=MASS PER LENGTH
0.4
*Element, ELSET=el_rod2, type=B32, INPUT=rodelement2_Pir86_V0.txt
*Beam Section, elset=el_rod2, material=steel, poisson=0.3, temperature=GRADIENTS, section=CIRC
0.011
*Nonstructural Mass, elset=el_rod2, units=MASS PER LENGTH
0.4
*Nset, nset=boundaryrodoben
2000
*Nset, nset=force
2468
*Include, INPUT=Federn_Pir86_Base_Case0.txt
*Element, ELSET=el_itt1oP, type=ITT31, INPUT=ittelelement_Pir86_1oP_V0.txt
*Interface, ELSET=el_itt1oP
0.0198
*Friction
0.2
*Element, ELSET=el_itt1mP, type=ITT31, INPUT=ittelelement_Pir86_1mP_V0.txt
*Interface, ELSET=el_itt1mP
0.001
*Friction
0.12
*Element, ELSET=el_itt2oP, type=ITT31, INPUT=ittelelement_Pir86_2oP_V0.txt
*Interface, ELSET=el_itt2oP
0.0198
*Friction
0.2

```

```

*Element, ELSET=el_itt2mP, type=ITT31, INPUT=ittelement_Pir86_2mP_V0.txt
*Interface, ELSET=el_itt2mP
0.001
*Friction
0.12
*NODE, INPUT=rodnummerpipe_Pir86_V0.txt,NSET=n_tubing
*SLIDE LINE, ELSET=el_itt1oP,TYPE=parabolic, GENERATE
6000, 6468,1
*SLIDE LINE, ELSET=el_itt1mP,TYPE=parabolic, GENERATE
6000, 6468,1
*SLIDE LINE, ELSET=el_itt2oP,TYPE=parabolic, GENERATE
6000, 6468,1
*SLIDE LINE, ELSET=el_itt2mP,TYPE=parabolic, GENERATE
6000, 6468,1
*Material, name=steel
*Damping, alpha=0.1, beta=0.04, composite=0.0, structural=0.
*Density
7850.,
*Elastic
2.1e+11, 0.3
*Amplitude, name=Amplitude1, INPUT=Hub_Pir86_90_Base_Case.txt, time=TOTAL TIME,
smooth=0.3
*Amplitude, name=Amplitudeload1, INPUT=Last_Pir86_plunger_90_Base_Case.txt, time=TOTAL
TIME, smooth=0.3
*Amplitude, name=AmplitudeFriction, INPUT=Fluid_Reibung_Base_Case.txt, time=TOTAL TIME,
smooth=0.3
*Boundary
n_tubing, ENCASTRE
*Boundary
boundaryrodoben, ZASYMM
** -----
*Step, name=Step_gravity, nlgeom=YES, inc=6000, unsymm=YES, CONVERT SDI=NO
*Dynamic, APPLICATION=MODERATE DISSIPATION
0.1,3.0000,1e-05,0.2
*Boundary
boundaryrodoben, 3,3, 0
*Dload
, GRAV, 9.81, 0., 0., -1.,
*Output, field, frequency=1, variable=PRESELECT
*Output, history, variable=PRESELECT
*End Step
*Step, name=Step_1load, nlgeom=YES, inc=6000, unsymm=YES, CONVERT SDI=NO
*Dynamic, INITIAL=NO, APPLICATION=MODERATE DISSIPATION
0.005,19.2,1e-08,0.2
*CONTROLS, PARAMETERS=TIME INCREMENTATION
*Boundary, amplitude=Amplitude1
boundaryrodoben, 3, 3, 1.
*Clod, amplitude=Amplitudeload1
force,1, -0.34893
force,2, -0.34056

```



```

force,3, -0.87308
*Include,INPUT=Cload_Pir86_Base_Case0.txt
*Output, field, frequency=1, variable=PRESELECT
*Contact Output, variable=ALL
*Output, history, variable=PRESELECT
*End Step
*Step, name=Step_load, nlgeom=YES, inc=6000, unsymm=YES, CONVERT SDI=NO
*Dynamic, INITIAL=NO, APPLICATION=MODERATE DISSIPATION
0.005,19.2,1e-08,0.3
*CONTROLS, PARAMETERS=TIME INCREMENTATION
*Boundary, amplitude=Amplitude1
boundaryrodoben, 3, 3, 1.
*Cload, amplitude=Amplitudeload1
force,1, -0.34893
force,2, -0.34056
force,3, -0.87308
*Include,INPUT=Cload_Pir86_Base_Case0.txt
*Output, field, frequency=1, variable=PRESELECT
*Contact Output, variable=ALL
*Output, history, variable=PRESELECT
*End Step

```

Python code:

```

import csv
import os.path

Path_home=(' /home/clangb')
os.chdir(' /home/clangb')

file = open('Pir86_Base_Case.inp', 'w')
V=0
reibung_rod=0.2
reibung_protektoren=0.12

file.write("""*Heading
*Preprint, echo=NO, model=NO, history=NO, contact=YES\n""")
file.write(*Node, INPUT=rodnummer_Pir86_V{0}.txt, nset=n_rod\n'.format(V))
#1. Gestänge
file.write(*Element, ELSET=el_rod1, type=B32, INPUT=rodelement1_Pir86_V{0}.txt\n'.format(V))
file.write("""*Beam Section, elset=el_rod1, material=steel, poisson=0.3, temperature=GRADIENTS,
section=CIRC
0.011
*Nonstructural Mass, elset=el_rod1, units=MASS PER LENGTH
0.7\n""")
#2. Gestänge
file.write(*Element, ELSET=el_rod2, type=B32, INPUT=rodelement2_Pir86_V{0}.txt\n'.format(V))

```

```

file.write('*Beam Section, elset=el_rod2, material=steel, poisson=0.3, temperature=GRADIENTS,
section=CIRC
0.011
*Nonstructural Mass, elset=el_rod2, units=MASS PER LENGTH
0.7\n''')
file.write('*Include,INPUT=Federn_Pir86_Base_Case{0}.txt\n'.format(V))
#1.ITT
file.write('*Element, ELSET=el_itt1oP, type=ITT31,
INPUT=ittelelement_Pir86_1oP_V{0}.txt\n'.format(V))
file.write('*Interface, ELSET=el_itt1oP
0.0198
*Friction\n''')
file.write('{0}\n'.format(reibung_rod))
file.write('*Element, ELSET=el_itt1mP, type=ITT31,
INPUT=ittelelement_Pir86_1mP_V{0}.txt\n'.format(V))
file.write('*Interface, ELSET=el_itt1mP
0.001
*Friction\n''')
file.write('{0}\n'.format(reibung_protektoren))
#2.ITT
file.write('*Element, ELSET=el_itt2oP, type=ITT31,
INPUT=ittelelement_Pir86_2oP_V{0}.txt\n'.format(V))
file.write('*Interface, ELSET=el_itt2oP
0.0198
*Friction\n''')
file.write('{0}\n'.format(reibung_rod))
file.write('*Element, ELSET=el_itt2mP, type=ITT31,
INPUT=ittelelement_Pir86_2mP_V{0}.txt\n'.format(V))
file.write('*Interface, ELSET=el_itt2mP
0.001
*Friction\n''')
file.write('{0}\n'.format(reibung_protektoren))
#-----
file.write('*NODE, INPUT=rodnummerpipe_Pir86_V{0}.txt,NSET=n_tubing\n'.format(V))
file.write('*SLIDE LINE, ELSET=el_itt1oP,TYPE=parabolic, GENERATE\n')
inputfile = open('rodnummerpipe_Pir86_V{0}.txt'.format(V))
reader = csv.reader(inputfile, delimiter=',', lineterminator='')
t = [x[0] for x in reader]
file.write('{0},{1},1 \n'.format(t[0],t[len(t)-1]))
file.write('*SLIDE LINE, ELSET=el_itt1mP,TYPE=parabolic, GENERATE\n')
inputfile = open('rodnummerpipe_Pir86_V{0}.txt'.format(V))
reader = csv.reader(inputfile, delimiter=',', lineterminator='')
t = [x[0] for x in reader]
file.write('{0},{1},1 \n'.format(t[0],t[len(t)-1]))
file.write('*SLIDE LINE, ELSET=el_itt2oP,TYPE=parabolic, GENERATE\n')
inputfile = open('rodnummerpipe_Pir86_V{0}.txt'.format(V))
reader = csv.reader(inputfile, delimiter=',', lineterminator='')
t = [x[0] for x in reader]
file.write('{0},{1},1 \n'.format(t[0],t[len(t)-1]))
file.write('*SLIDE LINE, ELSET=el_itt2mP,TYPE=parabolic, GENERATE\n')

```

```

inputfile = open('rodnummerpipe_Pir86_V{0}.txt'.format(V))
reader = csv.reader(inputfile, delimiter=',', lineterminator='')
t = [x[0] for x in reader]
file.write('{0},{1},1 \n'.format(t[0],t[len(t)-1]))

inputfile = open('rodnummer_Pir86_V{0}.txt'.format(V))
reader = csv.reader(inputfile, delimiter=',', lineterminator='')
rod = [x[0] for x in reader]

file.write('*Nset, nset=boundaryrodoben\n')
file.write('{0}\n'.format(rod[0]))
file.write('*Nset, nset=force\n')
file.write('{0}\n'.format(rod[len(rod) - 1]))

file.write('*Amplitude, name=Amplitude1, INPUT=Hub_Pir86_90_Base_Case.txt, time=TOTAL TIME,
smooth=0.3\n')
file.write('*Amplitude, name=Amplitudeload1, INPUT=Last_Pir86_plunger_90_Base_Case.txt,
time=TOTAL TIME, smooth=0.3\n')
file.write('*Amplitude, name=AmplitudeFriction, INPUT=Fluid_Reibung_Base_Case.txt, time=TOTAL
TIME, smooth=0.3\n')

file.write('*Material, name=steel
*Damping, alpha=0.1, beta=0.04, composite=0.0, structural=0.
*Density
7850.,
*Elastic
2.1e+11, 0.3
*Boundary
n_tubing, ENCASTRE
*Boundary
boundaryrodoben, ZASYMM
** -----\n")

file.write('*Step, name=Step_gravity, nlgeom=YES, inc=6000, unsymm=YES, CONVERT SDI=NO\n')
file.write('*Dynamic, APPLICATION=MODERATE DISSIPATION\n')
inputfile = open('Hub_Pir86_90_Base_Case.txt')
reader = csv.reader(inputfile, delimiter=',', lineterminator='')
t = [x[0] for x in reader]
file.write('0.1,{0},1e-05,0.2\n'.format(t[0]))

file.write('*Boundary
boundaryrodoben, 3,3, 0
*Dload
,GRAV, 9.81, 0., 0.,-1.,
*Output, field, frequency=1, variable=PRESELECT
*Output, history, variable=PRESELECT
*End Step\n")

```

```

file.write("""*Step, name=Step_1load, nlgeom=YES, inc=6000, unsymm=YES, CONVERT SDI=NO
*Dynamic, INITIAL=NO, APPLICATION=MODERATE DISSIPATION
0.005, 19.2, 1e-08, 0.2
*CONTROLS, PARAMETERS=TIME INCREMENTATION
*Boundary, amplitude=Amplitude1
boundaryrodoben, 3, 3, 1.\n""")

file.write(*Clload, amplitude=Amplitudeload1\n')

inputfile = open("Tangente_Pir86_V{0}.txt".format(V))
reader = csv.reader(inputfile, delimiter=',', lineterminator='')
t = [(x[0], x[1], x[2]) for x in reader]

file.write('force,1,{0}\n'.format(t[len(t)-1][0]))
file.write('force,2,{0}\n'.format(t[len(t)-1][1]))
file.write('force,3,{0}\n'.format(t[len(t)-1][2]))
file.write(*Include, INPUT=Clload_Pir86_Base_Case{0}.txt\n'.format(V))
file.write("""*Output, field, frequency=1, variable=PRESELECT
*Contact Output, variable=ALL
*Output, history, variable=PRESELECT
*End Step\n""")

file.write("""*Step, name=Step_load, nlgeom=YES, inc=6000, unsymm=YES, CONVERT SDI=NO
*Dynamic, INITIAL=NO, APPLICATION=MODERATE DISSIPATION
0.005, 19.2, 1e-08, 0.3
*CONTROLS, PARAMETERS=TIME INCREMENTATION
*Boundary, amplitude=Amplitude1
boundaryrodoben, 3, 3, 1.\n""")

file.write(*Clload, amplitude=Amplitudeload1\n')

inputfile = open("Tangente_Pir86_V{0}.txt".format(V))
reader = csv.reader(inputfile, delimiter=',', lineterminator='')
t = [(x[0], x[1], x[2]) for x in reader]

file.write('force,1,{0}\n'.format(t[len(t)-1][0]))
file.write('force,2,{0}\n'.format(t[len(t)-1][1]))
file.write('force,3,{0}\n'.format(t[len(t)-1][2]))
file.write(*Include, INPUT=Clload_Pir86_Base_Case{0}.txt\n'.format(V))
file.write("""*Output, field, frequency=1, variable=PRESELECT
*Contact Output, variable=ALL
*Output, history, variable=PRESELECT
*End Step\n""")

file.close()
#-----
file1 = open('Federn_Pir86_Base_Case{0}.txt'.format(V), 'w')

file1.write(*Node, INPUT=rodnummerfeder_Pir86_V{0}.txt, nset=nrod_feder\n'.format(V))

```

```

inputfile = open('rodnummerfeder_Pir86_V{0}.txt'.format(V))
reader = csv.reader(inputfile, delimiter=',', lineterminator='')

t = [x[0] for x in reader]

inputfile = open('Federkonstante_Pir86_V{0}.txt'.format(V))
reader1 = csv.reader(inputfile, delimiter=',', lineterminator='')

f = [y[0] for y in reader1]

for i in range(2, len(t)-2, 2):
    file1.write('*ELEMENT, type=SPRINGA, elset=feder{0}\n'.format(i))
    zahler=str(10000+i)
    file1.write('{0},{1},{2}\n'.format(str(10000+i),rod[i],t[i]))
    file1.write('*SPRING,ELSET=Feder{0}\n'.format(i))
    file1.write('\n{0}.\n'.format(f[i]))

file1.write('*Nset, nset=Mset\n')
knoten = [t[i].strip() for i in range(2, len(t)-2, 2)]
for i in range(0, len(knoten)):
    file1.write(knoten[i])
    if ((i + 1) % 16) == 0:
        file1.write('\n')
    else:
        file1.write(',')

inputfile = open('rodnummer_Pir86_V{0}.txt'.format(V))
reader2 = csv.reader(inputfile, delimiter=',', lineterminator='')
rodnummer = [x[0] for x in reader2]

file1.write('\n*Nset, nset=Uset\n')
knoten = [rodnummer[i].strip() for i in range(1, len(rodnummer)-2, 2)]
for i in range(0, len(knoten)):
    file1.write(knoten[i])
    if ((i + 1) % 16) == 0:
        file1.write('\n')
    else:
        file1.write(',')

file1.write('\n*Nset, nset=Lset\n')
knoten = [rodnummer[i].strip() for i in range(3, len(rodnummer)-1, 2)]

for i in range(0, len(knoten)):
    file1.write(knoten[i])
    if ((i + 1) % 16) == 0:
        file1.write('\n')
    else:
        file1.write(',')
file1.write('\n')

```

```

file1.write('*Equation
3
Mset,1,2.,Uset,1,-1.,Lset,1,-1
3
Mset,2,2.,Uset,2,-1.,Lset,2,-1
3
Mset,3,2.,Uset,3,-1.,Lset,3,-1\n")

#Knotenbeschriftung
for i in range(0, len(t)):
    file1.write('*Nset,nset=node{0}\n'.format(2000+i))
    file1.write('{0},\n'.format(2000+i))
file1.close()

#-----
file2 = open('Clod_Pir86_Base_Case{0}.txt'.format(V), 'w')

inputfile = open('Tangente_Pir86_V{0}.txt'.format(V))
reader = csv.reader(inputfile, delimiter=',', lineterminator='')
U = [(x[0], x[1], x[2]) for x in reader]
#reader = csv.reader(inputfile, delimiter=',', lineterminator='')
#V = [y[1] for y in reader]
#W = [z[2] for z in reader]

for i in range(0, len(U)):
    file2.write('*CLOAD,AMPLITUDE=AmplitudeFriction\n')
    file2.write('node{0},1,{1}\n'.format(2000+i,U[i][0]))
    file2.write('node{0},2,{1}\n'.format(2000+i,U[i][1]))
    file2.write('node{0},3,{1}\n'.format(2000+i,U[i][2]))

file2.close()

```

APPENDIX G

Python script:

```

import os.path
from time import*
import odbAccess

def createPath(path):
    if not os.path.isdir(path):
        os.makedirs(path)

os.chdir('/home/clangb/Z_Base_Case_3_2SPMoP')
homeDir=os.getcwd()
myOdb = odbAccess.openOdb(path='Pir86_Base_Case_3_2SPMoP.odb')

outputDir=os.path.join(homeDir,'Pir86_Base_Case_3_2SPMoP')
createPath(outputDir)
os.chdir(outputDir)

Step=myOdb.steps['Step_load']

FileRF=open('ReactionForce.dat','w')
FileRF.write('Time,\t RF x,\t RF y,\t RF z,\t\n')
FileTime=open('Time.dat','w')
FileTime.write('Step,\t Time,\t\n')
FileDisp=open('Displacement_2468.dat','w')
FileDisp.write('Node Label,\tDisplacement x,\tDisplacement y,\tDisplacement z,\n')

print('Start Bearbeitung')

for u in range(0,len(Step.frames),1):

    print('Start Zeitschritt', u)

    Frames=Step.frames[u]
    Times=Step.frames[u].frameValue

    #Reaction force node 2000
    #Step-Zeit
    ReactionForce = Frames.fieldOutputs['RF'].values[0]
    FileRF.write('%10f,\t %10f,\t %10f,\t %10f,\t\n' %
(Times,ReactionForce.data[0],ReactionForce.data[1],ReactionForce.data[2]))
    FileTime.write('%10i,\t %10f,\t\n' % (u,Times))

    #Displacement node 2468

```

```

Displacement=Frames.fieldOutputs['U'].values[468]
FileDisp.write('%10f,\t%10f,\t%10f,\t%10f\t\n' %
(Times,Displacement.data[0],Displacement.data[1],Displacement.data[2]))

#Folder für jeden step
writeDir=os.path.join(outputDir,'%d'%(u))
createPath(writeDir)
os.chdir(writeDir)
print("Write Dir =", writeDir)

FileContactT=open('ContactT.dat','w')
FileContactT.write('Element Label,\tNormal Force\n')
FileStress=open('Stress.dat','w')
FileStress.write('Element Label,\tPoint 1,\tPoint 2,\t\n')
FileDispl=open('Displacement.dat','w')
FileDispl.write('Node Label,\tDisplacement x,\tDisplacement y,\tDisplacement z,\n')

#ContactT
for k in range(1872,2341):
    ContactNorm=Frames.fieldOutputs['S'].values[k]
    FileContactT.write('%i,\t%10f\t\n' % (ContactNorm.elementLabel-6000,ContactNorm.data[0]))
FileContactT.close()

#Disp
for j in range(0,469):
    Displ=Frames.fieldOutputs['U'].values[j]
    FileDispl.write('%i,\t%10f,\t%10f,\t%10f\t\n' %
(Displ.nodeLabel,Displ.data[0],Displ.data[1],Displ.data[2]))
FileDispl.close()

#Stress
for l in range(0,468,2):
    Stress1=Frames.fieldOutputs['S'].values[l]
    Stress2=Frames.fieldOutputs['S'].values[l+1]
    FileStress.write('%i,\t%10i,\t%10i\t\n' %
(Stress1.elementLabel,Stress1.data[0],Stress2.data[0]))
FileStress.close()

FileRF.close()
FileTime.close()
FileDisp.close()

```


Matlab file 1:

```

% Class for csv data management
classdef CCSVMain
    properties (Access=public)
        Version = 'CSX 0.00'; %
        datapath = '\Pir86_SRABS_18_3SPMm\';
    end
    methods (Access=public)
        function [dataC_complete,dataCg,dataCu,dataD,dataS,dataD_unten] = ReadAll(this)
            tic;
            for qdir=1:77;%100;%76%164%60%62%64%78%77%74%101

                path=[this.datapath num2str(qdir-1) '\'];
                tmpC_complete = csvread([path 'ContactT.dat'],1);
                tmpC = csvread([path 'ContactT.dat'],1);
                tmpD = csvread([path 'Displacement.dat'],1);
                tmpSS = csvread([path 'Stress.dat'],1);

                vector=[];
                for i=1:length(tmpC_complete(:,2))
                    if rem(i,2)
                        vector=[vector 0.2];
                    else
                        vector=[vector 0.12];
                    end
                end
                tmpC_complete=tmpC_complete(:,2).*vector';

                tmpC(end,:)=[];
                tmpC_g=tmpC(:,2:2)*0.2;
                tmpC_g(2:2:end)=[];
                tmpC_u=tmpC(:,2:2)*0.12;
                tmpC_u(1:2:end)=[];

                for k=1:size(tmpSS,1)
                    if k==1
                        tmpS(2*k-1)=tmpSS(k,3)/10^6;
                        tmpS(2*k)=tmpSS(k,3)/10^6;
                    else
                        tmpS(2*k-1)=tmpSS(k,2)/10^6;
                        tmpS(2*k)=tmpSS(k,3)/10^6;
                    end
                end

                dataC_complete(:,qdir)=tmpC_complete;
                dataCg(:,qdir)=tmpC_g(:,1:1);
                dataCu(:,qdir)=tmpC_u(:,1:1);
                dataD_unten(:,qdir)=tmpD(:,:);
            end
        end
    end
end

```

```

tmpD=sqrt(tmpD(:,2).^2+tmpD(:,3).^2+tmpD(:,4).^2);
dataD(:,qdir)=tmpD(:);

dataS(:,qdir)=tmpS';
%
end
toc
end
function hndl = PlotXXX(this,X,Y,data,XLabel,YLabel,Title,map)
figure1 = figure('Colormap',map);
hndl = surf(X,Y,data,'EdgeColor','none'),hold on;
axis xy; axis tight;
T=60/18.3;
axis([0 T -900 0]);
set(gca,'xtick',[],'ytick',[]);
end
end
end

```

MatLab File 2:

```

oCM=CCSVMain;
[dataC_complete,dataC_g,dataC_u,dataD,dataS,dataD_unten]=oCM.ReadAll();
size(dataC_complete)

MD = csvread(['.\Pir86_SRABS_18_3SPMm\MD_V22m.txt'],0);
Time = csvread(['.\Pir86_SRABS_18_3SPMm\Time.dat'],1);
ReactionForce = csvread(['.\Pir86_SRABS_18_3SPMm\ReactionForce.dat'],1);
Anzahl=length(Time);

for i=1:468
    dataD_unten(i,2,:)=dataD_unten(i,2,:)-min(dataD_unten(i,2,:));
    dataD_unten(i,3,:)=dataD_unten(i,3,:)-min(dataD_unten(i,3,:));
    dataD_unten(i,4,:)=dataD_unten(i,4,:)-min(dataD_unten(i,4,:));
end

for i=1:Anzahl
    dataD_ampl(:,i)=sqrt(dataD_unten(:,2,i).^2+dataD_unten(:,3,i).^2+dataD_unten(:,4,i).^2);
end

for i=1:length(Time)-1
    diff_dataD(:,i)=(dataD_ampl(:,i+1)-dataD_ampl(:,i))/(Time(i+1,2)-Time(i,2));
    Zykl_P(i)=(dataD(1,i+1)-dataD(1,i))*sqrt(abs(ReactionForce(i,4))^2+abs(ReactionForce(i,3))^2
+abs(ReactionForce(i,2))^2)/(Time(i+1,2)-Time(i,2));
    dT(i)=Time(i+1,2)-Time(i,2);
end

```

```

dataC_complete(:,Anzahl)=[];
size(diff_dataD);
power=dataC_complete.*diff_dataD;
power(end,:)=[];

for i=1:length(power(:,1))/2
    power_u(i,:)=power(2*i-1,:);
    power_g(i,:)=power(2*i,:);
end

T=60/18.3;
dr=7/8;

%Bohrlochverlauf
h=figure
plot(MD(:,3),-MD(:,2),'black','LineWidth',1.5),axis([-40 40 -900 0]),hold on
plot(MD(:,4)*10,-MD(:,2),'red','LineWidth',1.5)
set(gca,'xtick',[],'ytick',[])
pbaspect([1.6,9,1])
link=strcat('Inclination.jpeg');
saveas(gcf(),link,'jpeg')
close(h)

%Spannungen im Gestänge
for i=1:length(MD(:,1))-1
    Stress_MD(i)=(MD(i,2)+MD(i+1,2))/2;
end

map=[0 0 0;0 0 0;0 0, .....];

h=oCM.PlotXXX(Time(:,2),-Stress_MD(:),squeeze(dataS(:,1,:)),'MD (m)','Time (s)','Stress in Sucker
Rods (MPa)',map);
pbaspect([3.6,9,1])
link=strcat('Stress.jpeg');
saveas(gcf(),link,'jpeg')
k=(squeeze(dataS(:,1,:)));
% Reaktionskraft an der Polierstange4
h=figure
axes1 = axes('Parent',h,'YTick',[20000 30000 40000 50000 60000]);
xlim(axes1,[0 T]);
ylim(axes1,[0 80000]);
box(axes1,'on');
hold(axes1,'all');
plot(Time(:,2),ReactionForce(:,4),'black','LineWidth',1.5,'Parent',axes1),set(gca,'xtick',[],'ytick',[]);
pbaspect([3.6,2,1])
axes2 = axes('Parent',h,'YTick',[-10000 0 10000 20000 30000],'YAxisLocation','right','YColor',[0 0
0],'ColorOrder',[0 0.5 0;1 0 0;0 0.75 0.75;0.75 0 0.75;0.75 0.75 0;0.25 0.25 0.25;0 0 1],'Color','none');
xlim(axes2,[0 T]);
ylim(axes2,[-10000 30000]);
hold(axes2,'all');

```

```

plot(Time(:,2),squeeze(dataS(468,1,:))*(dr*25.4)^2*pi/4,'red','LineWidth',1.5,'Parent',axes2),set(gca,'xtick',[],'ytick',[])
pbaspect([3.6,2,1])
link=strcat('ReactionForce.jpeg');
saveas(gcf(),link,'jpeg')
max(ReactionForce(:,4))

```

%Dynamometer Kurven

```

h=figure
axes1 = axes('Parent',h,'YTick',[20000 30000 40000 50000 60000]);
xlim(axes1,[0 4]);
ylim(axes1,[0 120000]);
box(axes1,'on');
hold(axes1,'all');
plot(squeeze(dataD_ampl(1,:)),ReactionForce(:,4),'black','LineWidth',1.5,'Parent',axes1),set(gca,'xtick',[],'ytick',[])
pbaspect([3.6,2,1])
axes2 = axes('Parent',h,'YTick',[-10000 0 10000 20000 30000],'YAxisLocation','right','YColor',[0 0 0],'ColorOrder',[0 0.5 0;1 0 0;0 0.75 0.75;0.75 0 0.75;0.75 0.75 0;0.25 0.25 0.25;0 0 1],'Color','none');
xlim(axes2,[0 4]);
ylim(axes2,[-10000 30000]);
hold(axes2,'all');
plot(squeeze(dataD_ampl(469,:)),squeeze(dataS(468,1,:))*(dr*25.4)^2*pi/4,'red','LineWidth',1.5,'Parent',axes2),set(gca,'xtick',[],'ytick',[])
pbaspect([3.6,2,1])
link=strcat('Dyno.jpeg');
saveas(gcf(),link,'jpeg')

```

```

MD(end,:)=[];
MD_g=-MD(:,2);
MD_u=-MD(:,2);
MD_g(2:2:end)=[];
MD_u(1:2:end)=[];
Time1=Time(:,2);
Time1(end)=[];

```

%Bewegung und Geschwindigkeit Polierstange und Plunger

```

h=figure
plot(Time(:,2),squeeze(dataD_ampl(1,:)),'black','LineWidth',1.5),hold on,axis([0 T 0 4]),set(gca,'xtick',[],'ytick',[])
plot(Time(:,2),squeeze(dataD_ampl(469,:)),'red','LineWidth',1.5),hold on,axis([0 T 0 4]),set(gca,'xtick',[],'ytick',[])
pbaspect([3.6,2,1])
link=strcat('U_V.jpeg');
saveas(gcf(),link,'jpeg')

```

%Leistung an der Polierstange

```

h=figure
plot(Time1,Zykl_P/1000,'black','LineWidth',1.5),axis([0 T -240 240])
pbaspect([3.6,2,1])

```

```

link=strcat('PRP.jpeg');
saveas(gcf(),link,'jpeg')

%Torque am Getriebeausgang - Minimum! kW
Pmax_c=max(Zykl_P)/1000;

%Energie ohne Rückgewinnung
sumEo=0;
for i=1:length(dT)
    if Zykl_P(i)>0
        sumEo=sumEo+Zykl_P(i)*dT(i);
    end
end
E_o=sumEo*60/T*60*2.778*10^-7

%Energie mit Rückgewinnung
sumEm=0;
for i=1:length(dT)-1
    sumEm=sumEm+Zykl_P(i)*dT(i);
end
E_m=sumEm*60/T*60*2.778*10^-7

%Reibung Rod Guides
h=figure
FF_p=sum(squeeze(dataC_u(:,1,:)));
plot(Time(:,2),FF_p,'black','LineWidth',1.5),axis([0 T 0 6000]),set(gca,'xtick',[],'ytick',[])
pbaspect([10,2,1])
link=strcat('Friction Guides.jpeg');
saveas(gcf(),link,'jpeg')

h=figure
FF_r=sum(squeeze(dataC_g(:,1,:)));
plot(Time(:,2),FF_r,'red','LineWidth',1.5),axis([0 T 0 1600]),set(gca,'xtick',[],'ytick',[])
pbaspect([3.6,2,1])
link=strcat('Friction Rods1.jpeg');
saveas(gcf(),link,'jpeg')

map=[0 0 0;0 0 0.5;0 0 1; ..... ];
h=oCM.PlotXXX(Time(:,2),MD_u(:,1,:),squeeze(dataC_u(:,1,:)),'MD (m)','Time (s)','Friction Rod Guides
(N)',map);
pbaspect([3.6,9,1])
link=strcat('Friction Rod Guides.jpeg');
saveas(gcf(),link,'jpeg')

% momentane Reibungleistung
map=[0 0 0; ....];
h=oCM.PlotXXX(Time1,MD_u,squeeze(abs(power_g)),'MD (m)','Time (s)','Actual Friction Power /
Rod Guides (W)',map);
pbaspect([3.6,9,1])
link=strcat('Reibleistung_rod_guides.jpeg');

```

```

saveas(gcf(),link,'jpeg')

% %Reibleistung über Zeit
h=figure
P=abs(sum(power));
plot(Time1,P/1000,'black','LineWidth',1.5),axis([0 T 0 16])
pbaspect([3.6,2,1])
link=strcat('Reibleistung über Zeit.jpeg');
saveas(gcf(),link,'jpeg')
Pfr_max=max(P)

sumEf=0;
for i=1:length(dT)-1
    sumEf=sumEf+(P(i))*dT(i);
end
E_f=sumEf*60/T*60*2.778*10^-7

% Reibenergie über Tiefe
h=figure
power_t=power;

for i=1:length(Time)-1
    power_t(i,:)=power_t(i,:).*dT(i);
end

%Reibung Upstroke
P2=power_t*60/T*60*2.778*10^-7;
P2(33:76,:)=[];
P2=sum(P2,1);
plot(P2/1000,-MD(:,2),'blue','LineWidth',1),hold on
pbaspect([2,10,1])

%Reibung Downstroke
P3=power_t*60/T*60*2.778*10^-7;
P3(1:33,:)=[];
P3=sum(P3,1);
plot(P3/1000,-MD(:,2),'red','LineWidth',1),hold on
pbaspect([2,10,1])

P1=abs(P2)+abs(P3);
plot(P1/1000,-MD(:,2),'black','LineWidth',1),hold on
pbaspect([2,10,1])
link=strcat('Reibleistung über Tiefe.jpeg');
saveas(gcf(),link,'jpeg')
set(gca,'xtick',[],'ytick',[])

map=[1 1 1;1 0 0; .....];
h=oCM.PlotXXX(Time(:,2),MD_g(:),squeeze(dataC_g(:,1,:)), 'MD (m)', 'Time (s)', 'Friction Rods (N)',map);
pbaspect([3.6,9,1])

```

```

link=strcat('Friction Rods.jpeg');
saveas(gcf(),link,'jpeg')

map=[1 0 0;.....];
h=ocm.PlotXXX(Time1,MD_g,squeeze(power_u),'MD (m)','Time (s)','Actual Friction Power / Rods
(W)',map);
pbaspect([3.6,9,1])
link=strcat('Reibleistung_rods.jpeg');
saveas(gcf(),link,'jpeg')

%Polished rod load
Pmax_c=[];
E_o=[];
E_m=[];

for kk=0:155

A = 4.57;
C = 3.05;
I = 3.05;
P = 3.67;
H = 6.6;
G = 2.82;
R = 1.19;

B=-1780;%Structural unbalance

%Walking Beam W30x173
l_beam=C+A;
mb=260*l_beam; %beam mass 260kg/m
%Pitman W8x10 (geschätzt)
l_pitman=P;
mp=15*l_pitman*2; %pitman mass
%Equalizer W24x55 (geschätzt)
l_equalizer=1;
me=82*l_equalizer; %equalizer beam
%Horsehead
l_head=5; %geschätzt
mh=(mb*(l_beam/2-C)-B*A/9.81-(me+mp)*C)/l_head; %horse head mass
%Crank
Mc=20000; %7/8" Mc=45000 5/8" 30000
lc=2.3;
mc=Mc/9.81*2/lc;
%Counterweight
l_counter=3; %geschätzt 3,
mcounter=2*kk*20;%320; %Counterweight 7.58/620 - 4.85/470 - 10/700 - 15/1030
%oscillating structures
mo=mb+mh+me+mp/2;
lo=(me+mp/2)*C^2+mh*l_head^2+1/12*mb*l_beam^2+mb*(l_beam/2-C)^2;

```

```

%rotating structure
Mrot=Mc+mp/2*R*9.81;
Irot=mp/2*R^2+1/3*mc*lc^2;
Mcounter(kk+1)=mcounter*9.81*(l_counter);
Icounter=mcounter*(l_counter)^2;

%Anzahl Datenpunkte
n=1000;

%%Hub Svinos
SPM=60/T;
omega=2*pi/T;
K=((H-G)^2+I^2)^0.5;
d=asin(I/K)-0.0405;
gamma=d-acos(((P+R)^2+K^2-C^2)/2/K/(R+P));

%Referenzdaten - Skalierung
phip=linspace(0,2*pi,n); %0 bei top

theta2=2*pi-phip+d;
L=sqrt(K^2+R^2-2*K*R*cos(theta2));
for i=1:length(theta2)
    if ((0<theta2(i))&&(theta2(i)<pi))||((theta2(i)>2*pi)
        j(i)=1;
    else
        j(i)=-1;
    end
end
beta=acos((L.^2+K^2-R^2)/2/K./L).*j;
theta3=acos((P^2-C^2+L.^2)/2/P./L)-beta;
theta4=acos((P^2-C^2-L.^2)/2/C./L)-beta;

theta2p=omega;%linspace(0,0,n);
theta3p=R.*theta2p./P.*sin(theta4-theta2)./sin(theta3-theta4);
theta4p=R.*theta2p./C.*sin(theta3-theta2)./sin(theta3-theta4);

theta2pp=linspace(0,0,n);
theta4pp=theta4.*(theta2pp./theta2p-(theta3p-theta4p)./tan(theta3-theta4)+(theta2p-
theta3p)./tan(theta2-theta3));
VR=A*theta4p;
TF=VR./theta2p;

omega1=2*pi/T.*Time(:,2);
RF_inter= interp1(omega1,ReactionForce(:,4),phip);

Tload=-TF.*RF_inter;
Tstructure=-Mrot*sin(phip-gamma)-Irot*theta2pp-B*TF+TF*Io/A.*theta4pp;
Tcounter=-Mcounter(kk+1)*sin(phip-gamma)-Icounter*theta2pp;
Total(kk+1,:)=Tload+Tcounter+Tstructure;

```



```

pkip=kip/pi*180;

T_plot=linspace(0,T,length(Total(1,:)));
plot(T_plot,Total(kk+1,:),'g'),hold on

%Leistung P=M.w
for i=1:length(Total(kk+1,:))
    P(i)=Total(kk+1,i)*2*pi*SPM/60;
end

%Torque am Getriebeausgang - Minimum! kW
Pmax_c(kk+1)=max(P)/1000;

%Energie ohne Rückgewinnung
sumEo=0;
for i=1:length(P)-1
    if P(i)>0
        sumEo=sumEo+P(i)*T/1000;
    end
end
E_o(kk+1)=sumEo*SPM*60*2.778*10^-7;

%Energie mit Rückgewinnung
sumEm=0;

for i=1:length(P)-1
    sumEm=sumEm+P(i)*T/1000;
end

E_m(kk+1)=sumEm*SPM*60*2.778*10^-7;

%min torque
[c,d]=min(Pmax_c);
Mcounter1=(Mcounter(d-1)+Mc)/1000;

%min energy
[a,b]=min(E_o);
Mcounter2=(Mcounter(b-1)+Mc)/1000;

plot(T_plot,Total(b:),'black',T_plot,Total(d:),'b'),xlim([0 T]),ylim([-200000 200000])
pbaspect([3.6,2,1])
set(gca,'xtick',[],'ytick',[])

figure
M_plot=linspace(Mc,200000,length(Pmax_c));
plot(M_plot,Pmax_c,'b','LineWidth',1.5),hold on,axis([Mc 200000 0 400])
plot(M_plot,E_o,'r','LineWidth',1.5),hold on,axis([Mc 200000 0 400])
plot(M_plot,E_m,'black','LineWidth',1.5),hold on,axis([Mc 200000 0 400])

```

```
x1=[Mcounter1 Mcounter1]*1000;  
x2=[Mcounter2 Mcounter2]*1000;  
y_werte=[0 400];  
  
plot(x1,y_werte,'black',x2,y_werte,'black')  
  
pbaspect([3.6,2,1])  
set(gca,'xtick',[],'ytick',[])
```

APPENDIX H

In the following section all simulation results are presented:

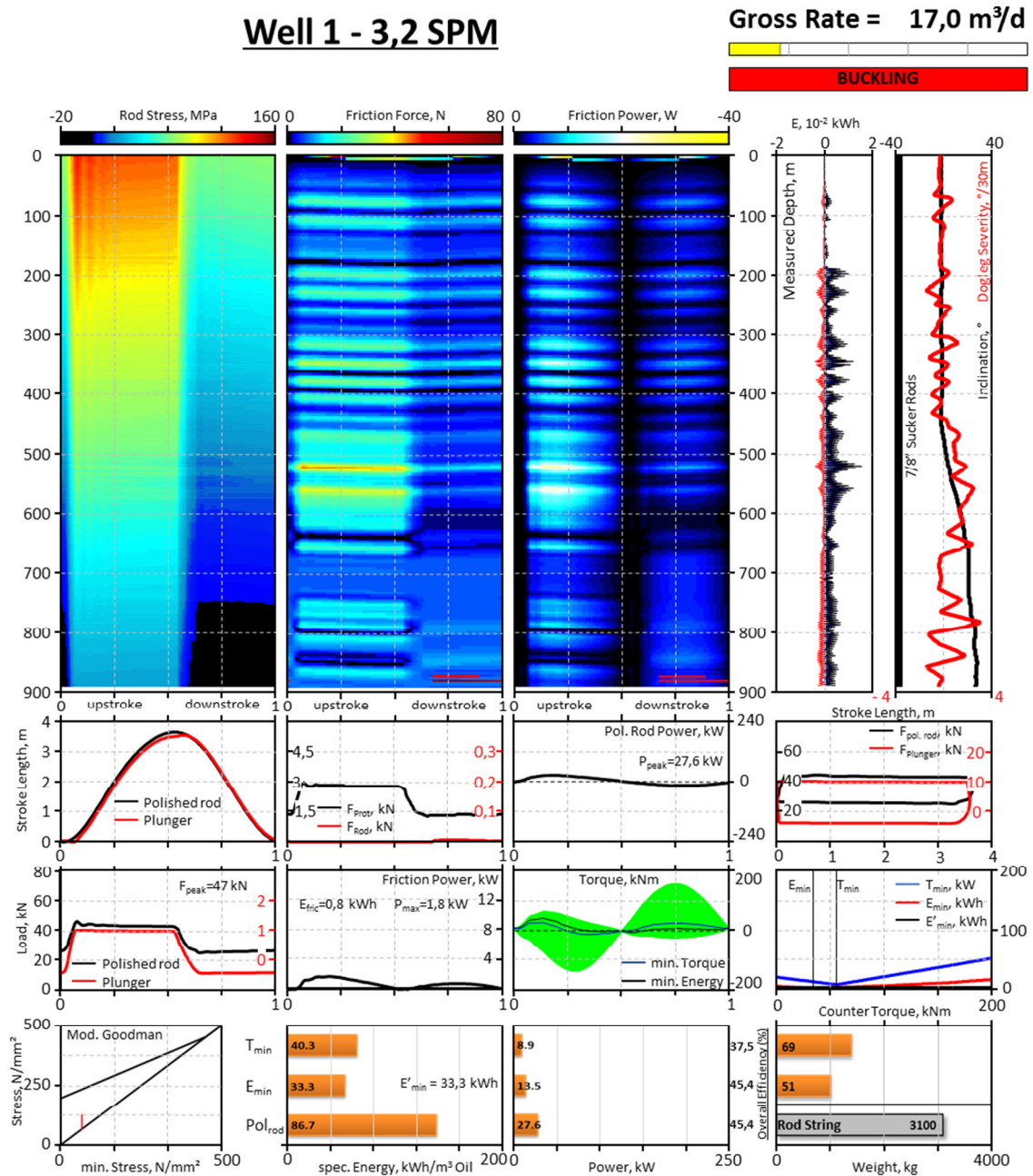


FIGURE 180: WELL 1 - 3,2 SPM

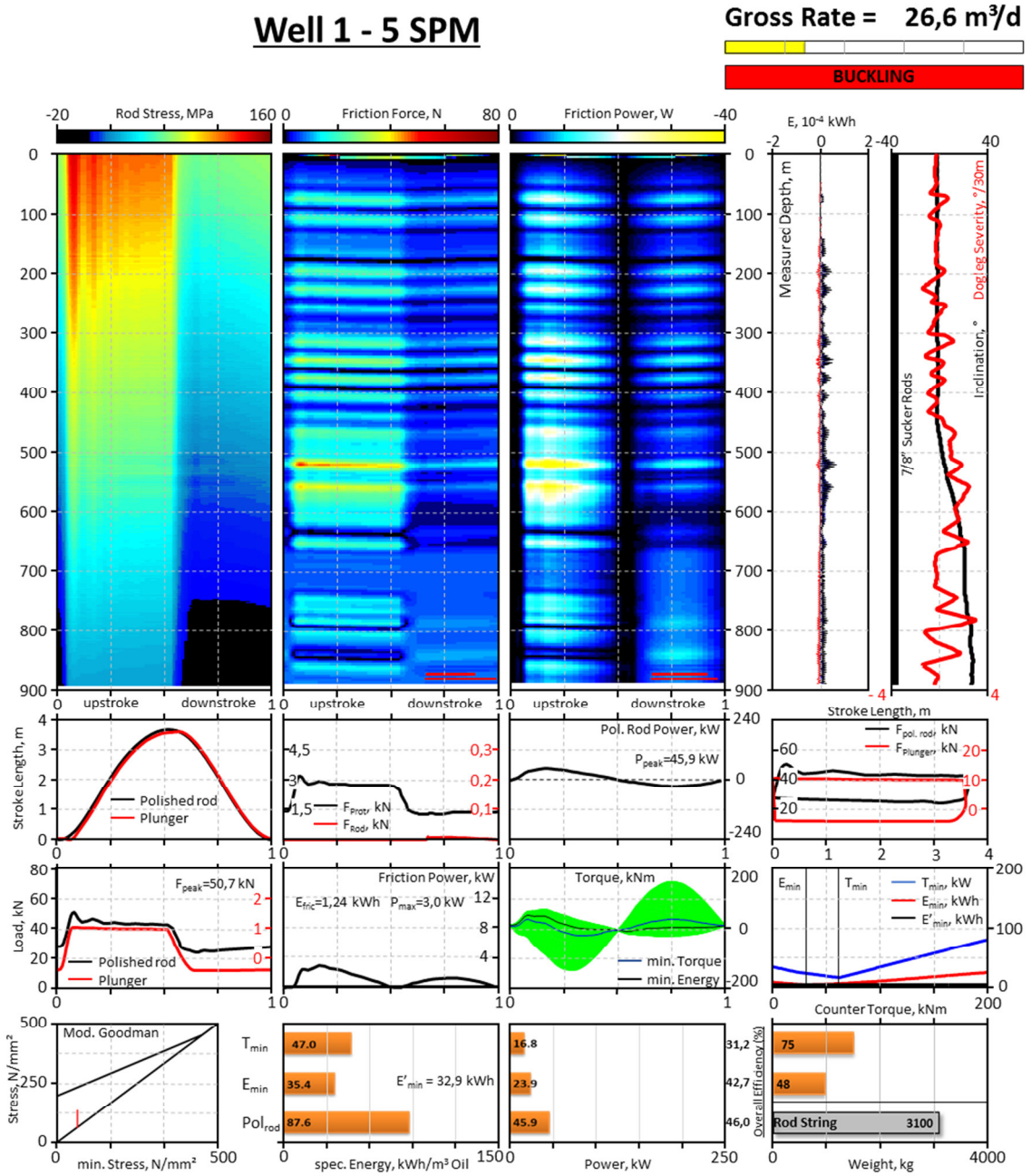


FIGURE 181: WELL OMV 1 - 5 SPM

Well 1 - 10 SPM

Gross Rate = 53,3 m³/d

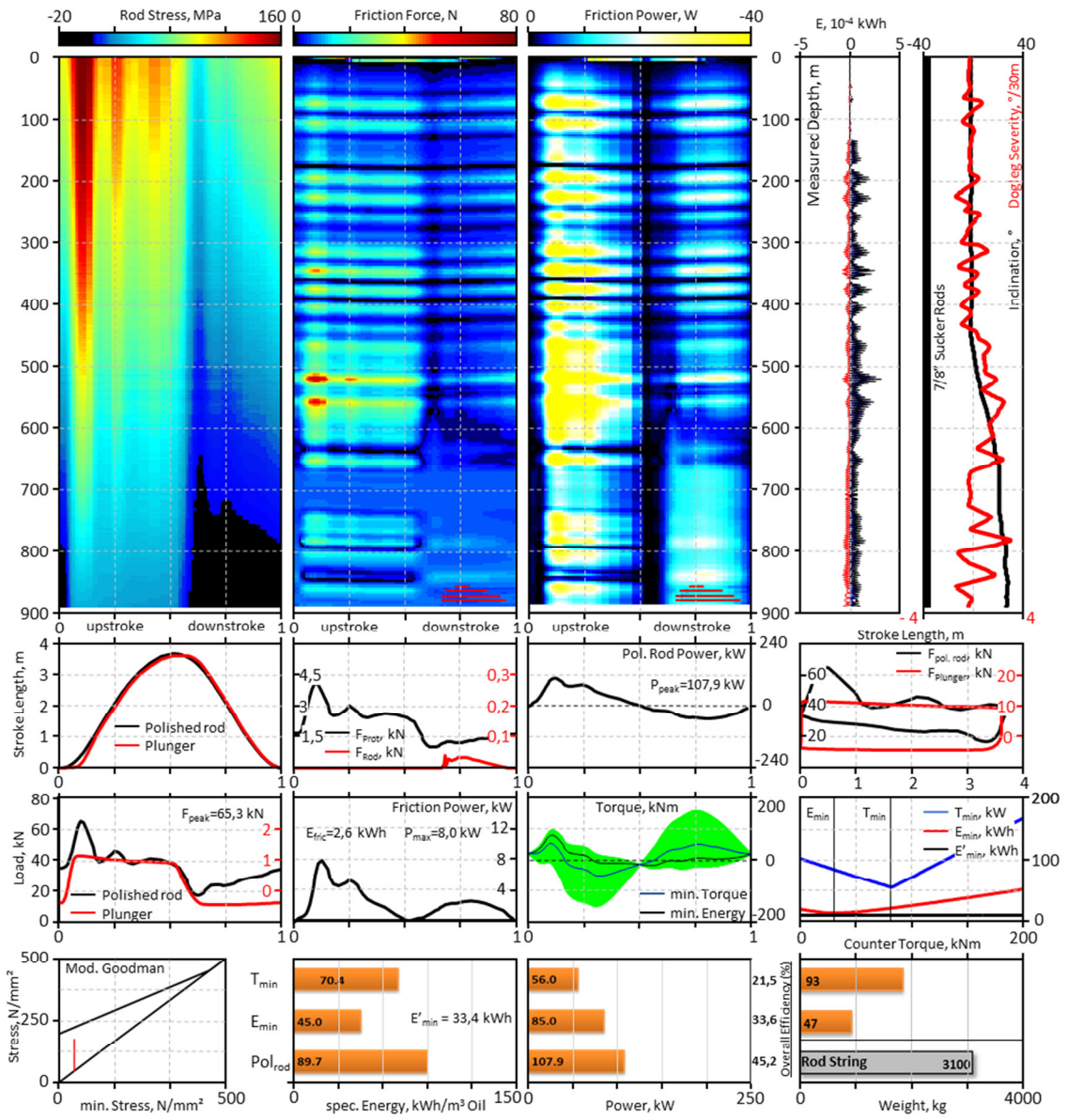


FIGURE 182: WELL OMV 1 - 10 SPM

Well 1 - 15 SPM

Gross Rate = 82,4 m³/d

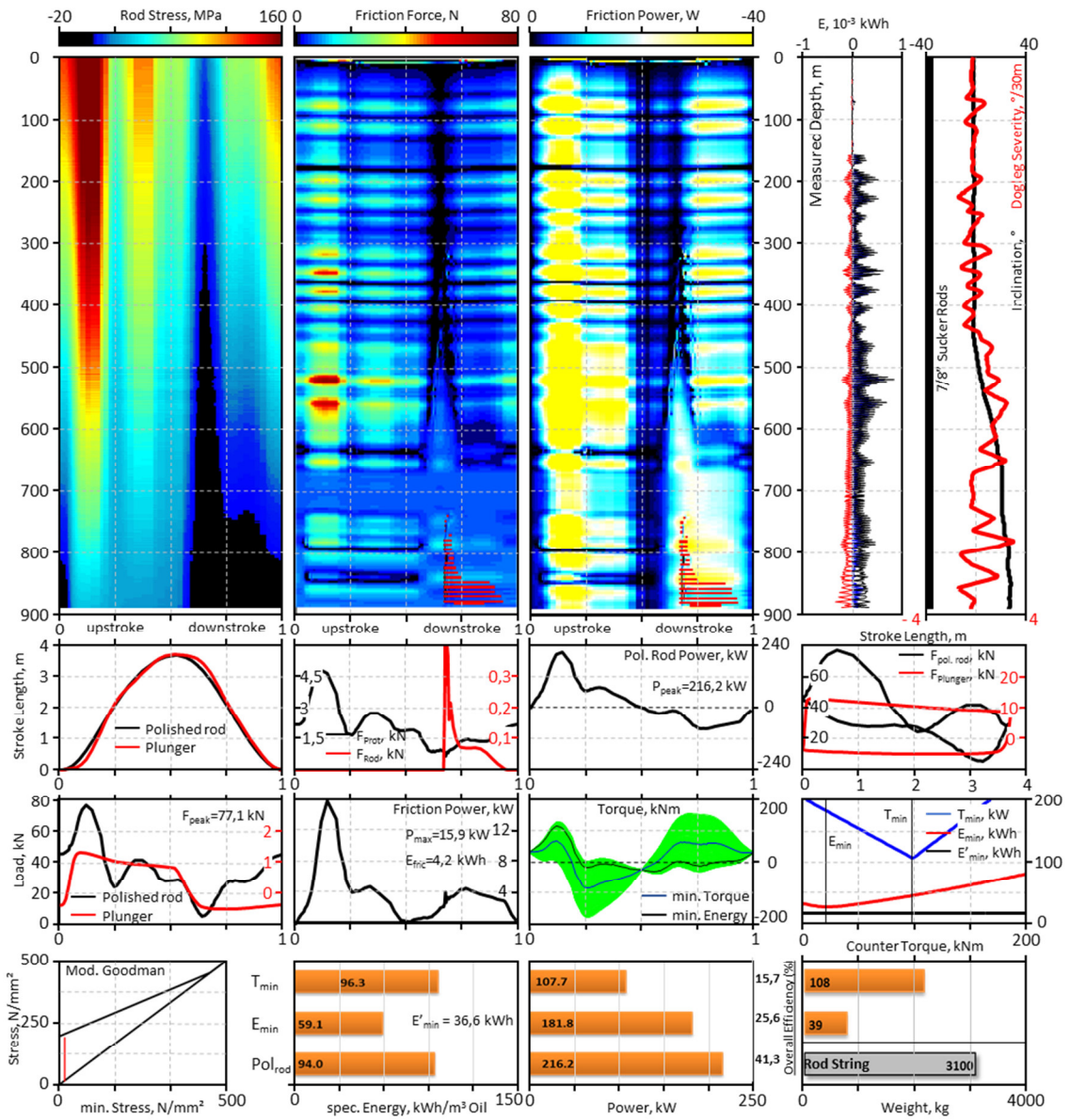


FIGURE 183: WELL OMV 1 - 15 SPM

Well 1 - 3,2 SPM – Sinker Bars

Gross Rate = 16,8 m³/d

NO BUCKLING

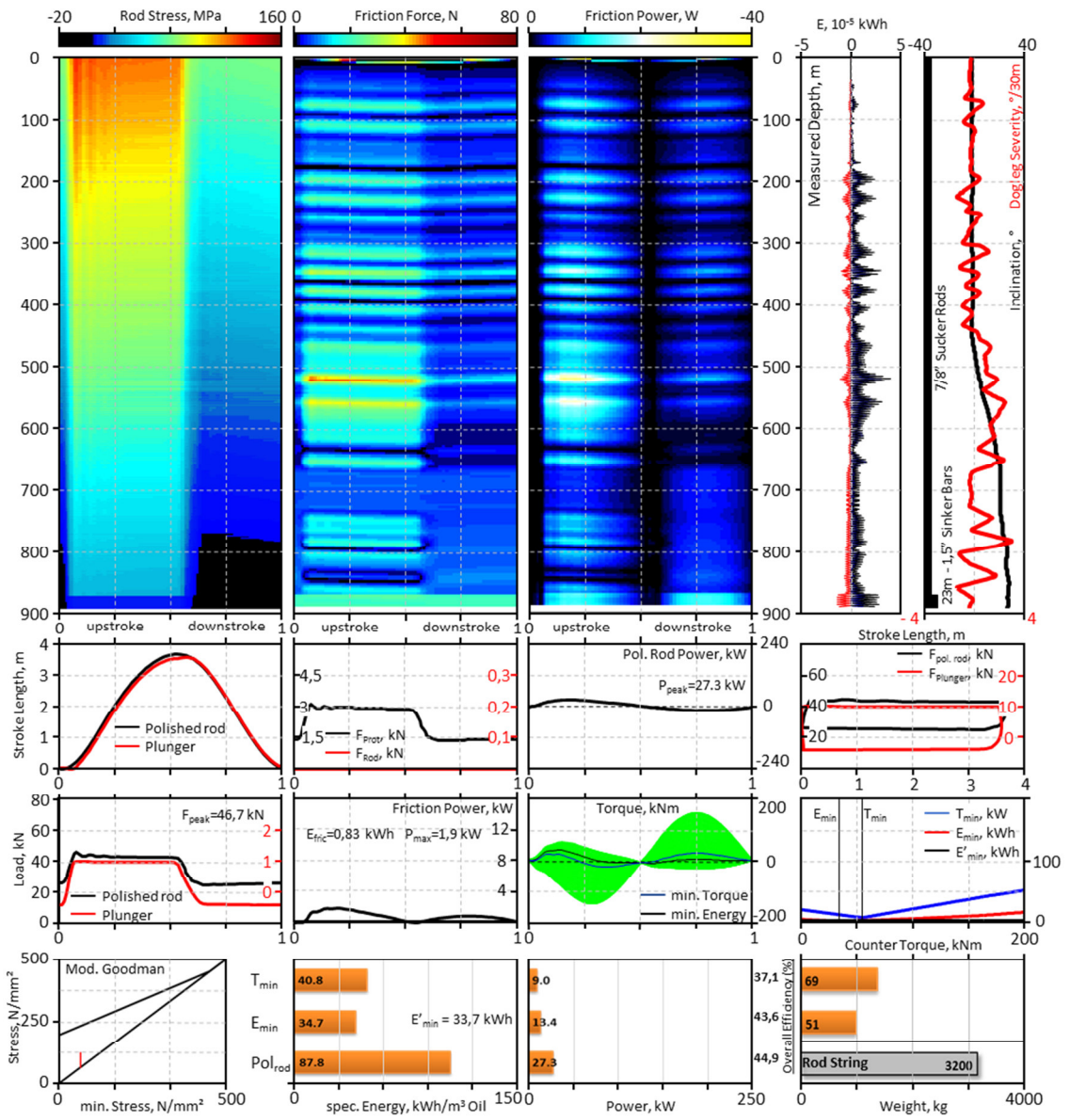


FIGURE 184: WELL OMV 1 – 3,2 SPM / SINKER BARS

Well 1 - 5 SPM – Sinker Bars

Gross Rate = 26,5 m³/d

NO BUCKLING

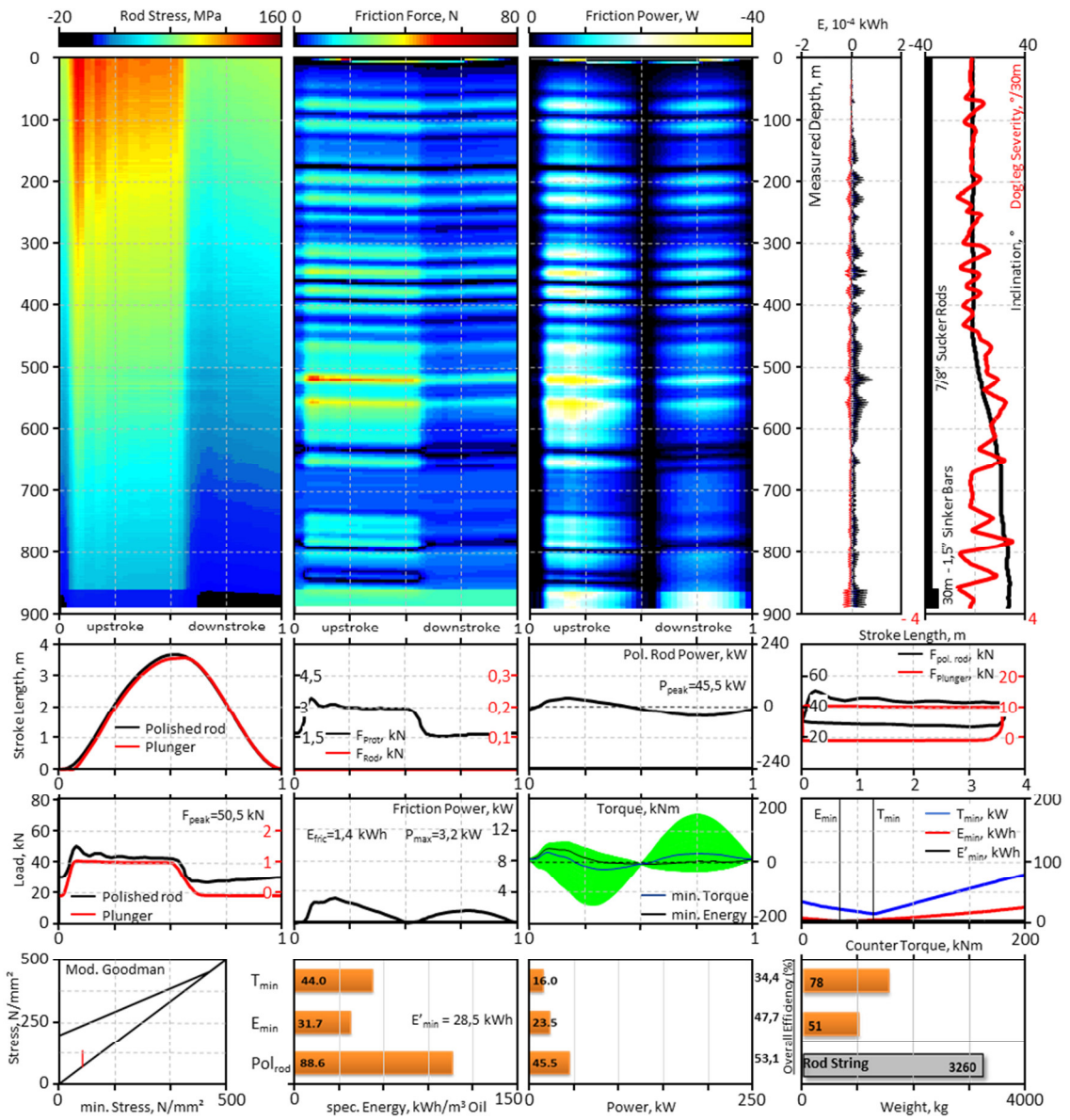


FIGURE 185: WELL OMV 1 – 5 SPM / SINKER BARS

Well 1 - 10 SPM – Sinker Bars

Gross Rate = 53,2 m³/d

NO BUCKLING

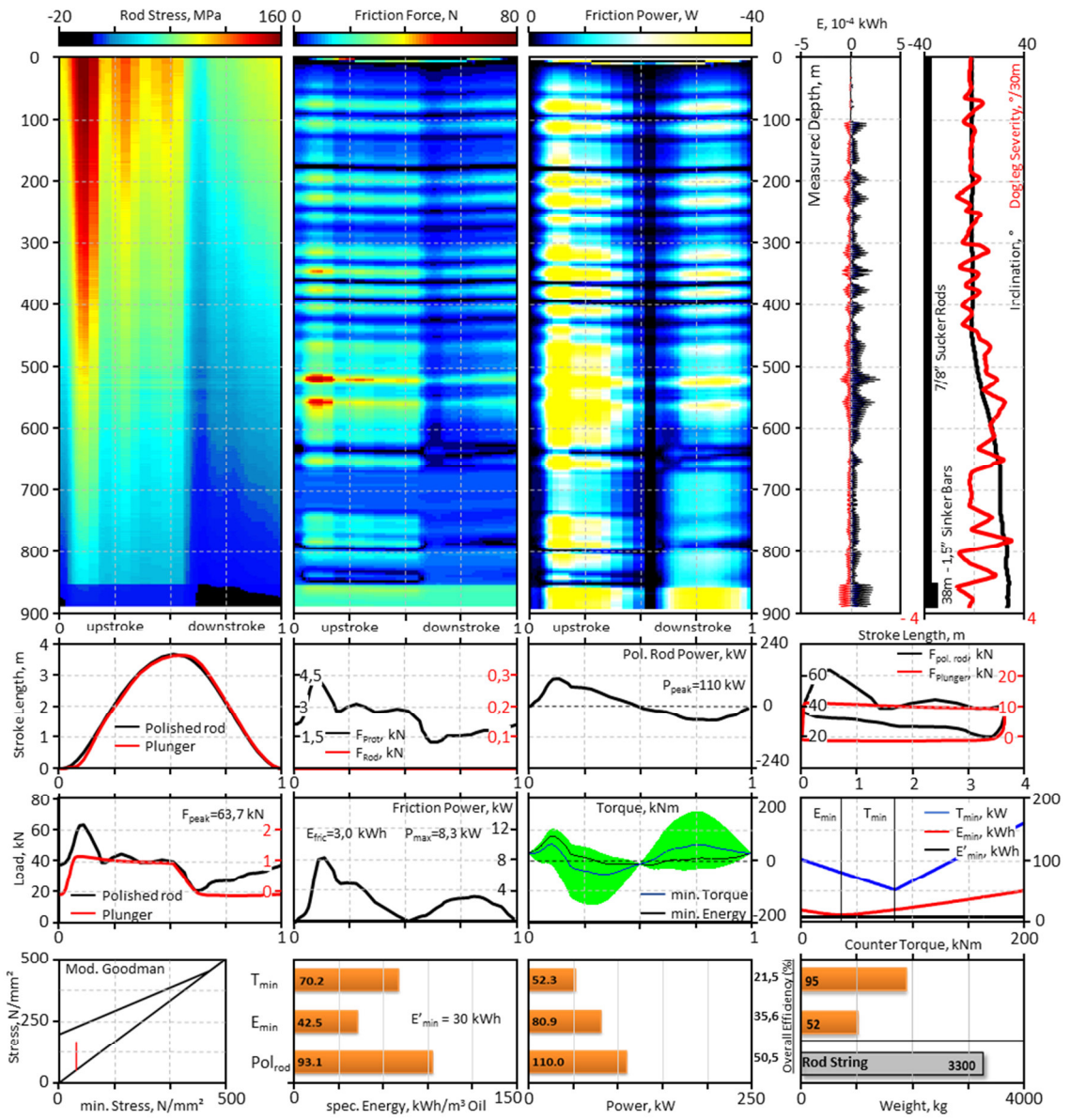


FIGURE 186: WELL OMV 1 – 10 SPM / SINKER BARS

Well 1 - 15 SPM – Sinker Bars

Gross Rate = 79,8 m³/d

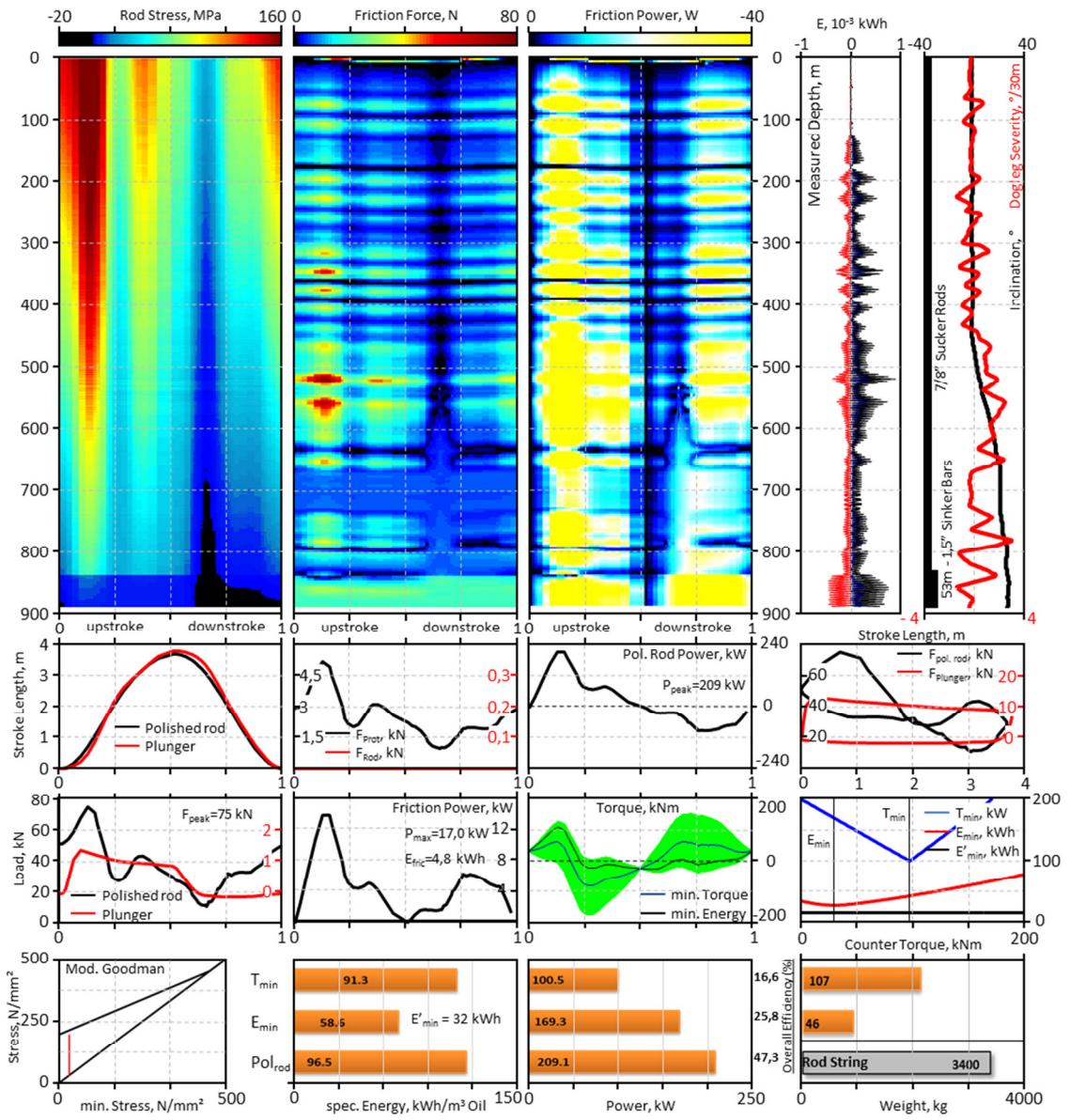
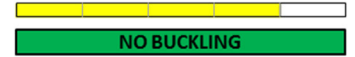


FIGURE 187: WELL OMV 1 – 15 SPM / SINKER BARS

Well 1 86 - 3,2 SPM

Gross Rate = 17,3 m³/d

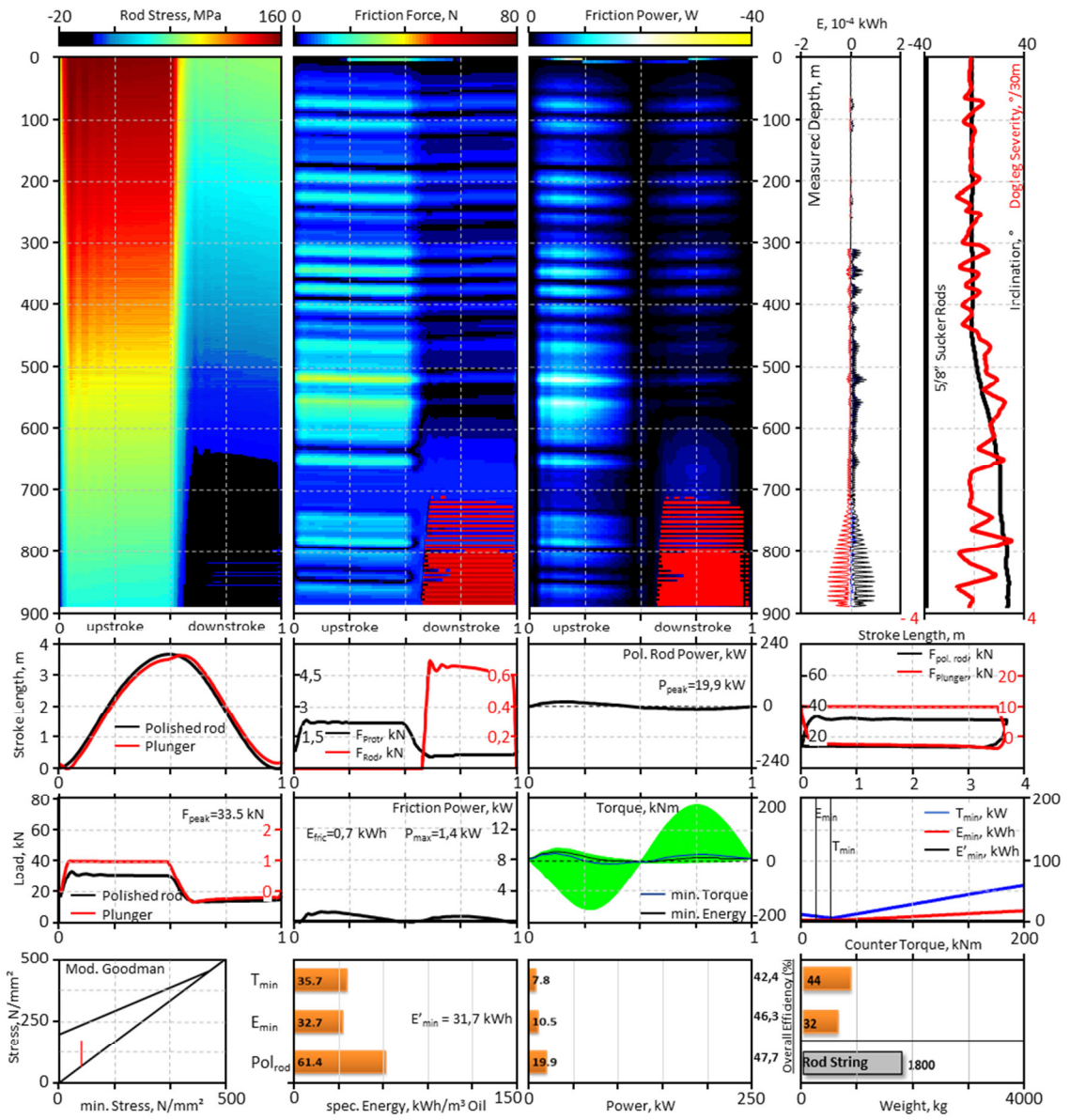
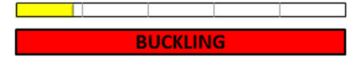


FIGURE 188: WELL OMV 1 - 3,2 SPM / 5/8" RODS

Well 1 – 5 SPM

Gross Rate = 27,2 m³/d

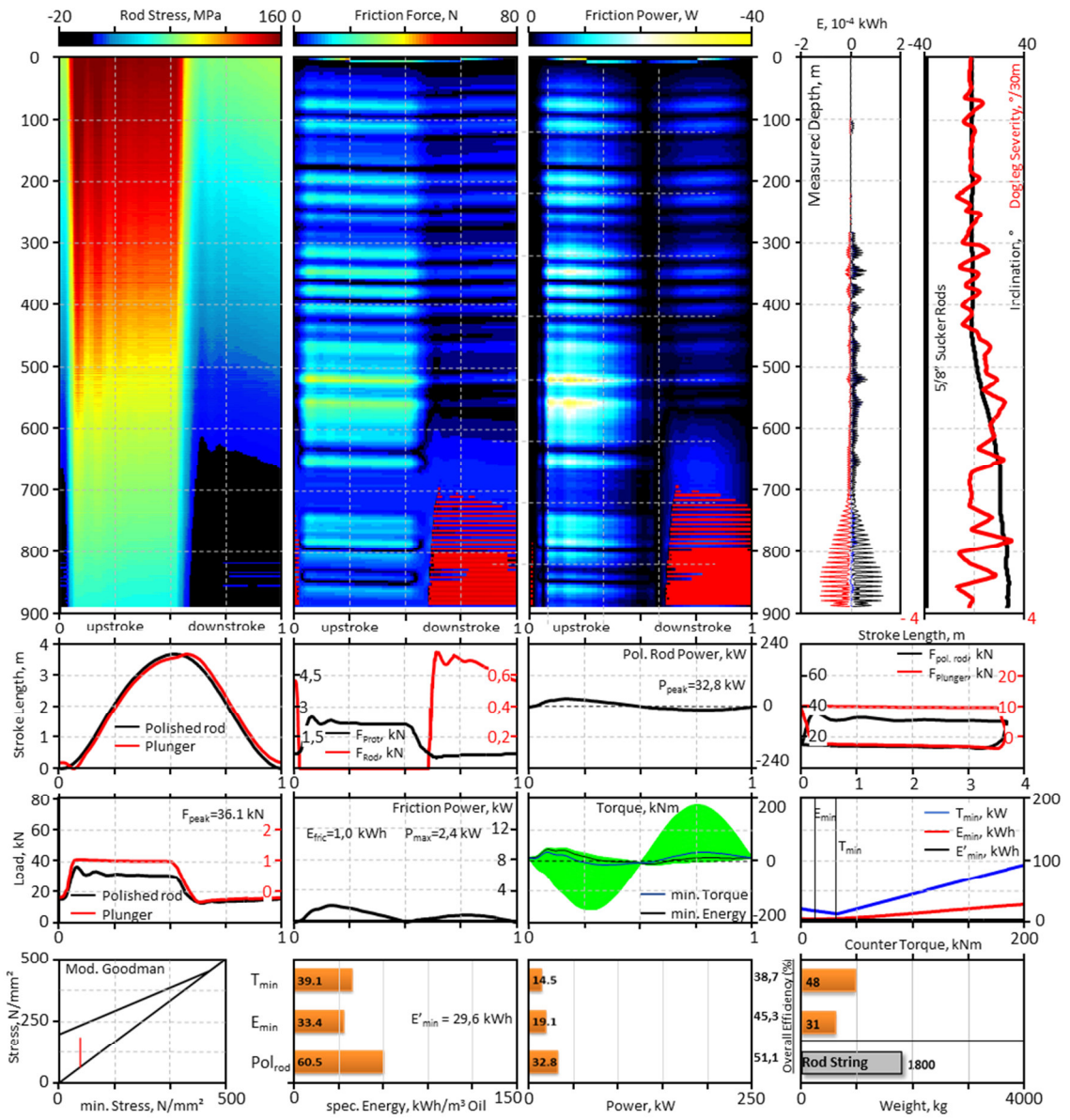
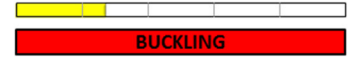


FIGURE 189: WELL OVM 1 – 5 SPM / 5/8" RODS

Well 1 – 10 SPM

Gross Rate = 53,8 m³/d

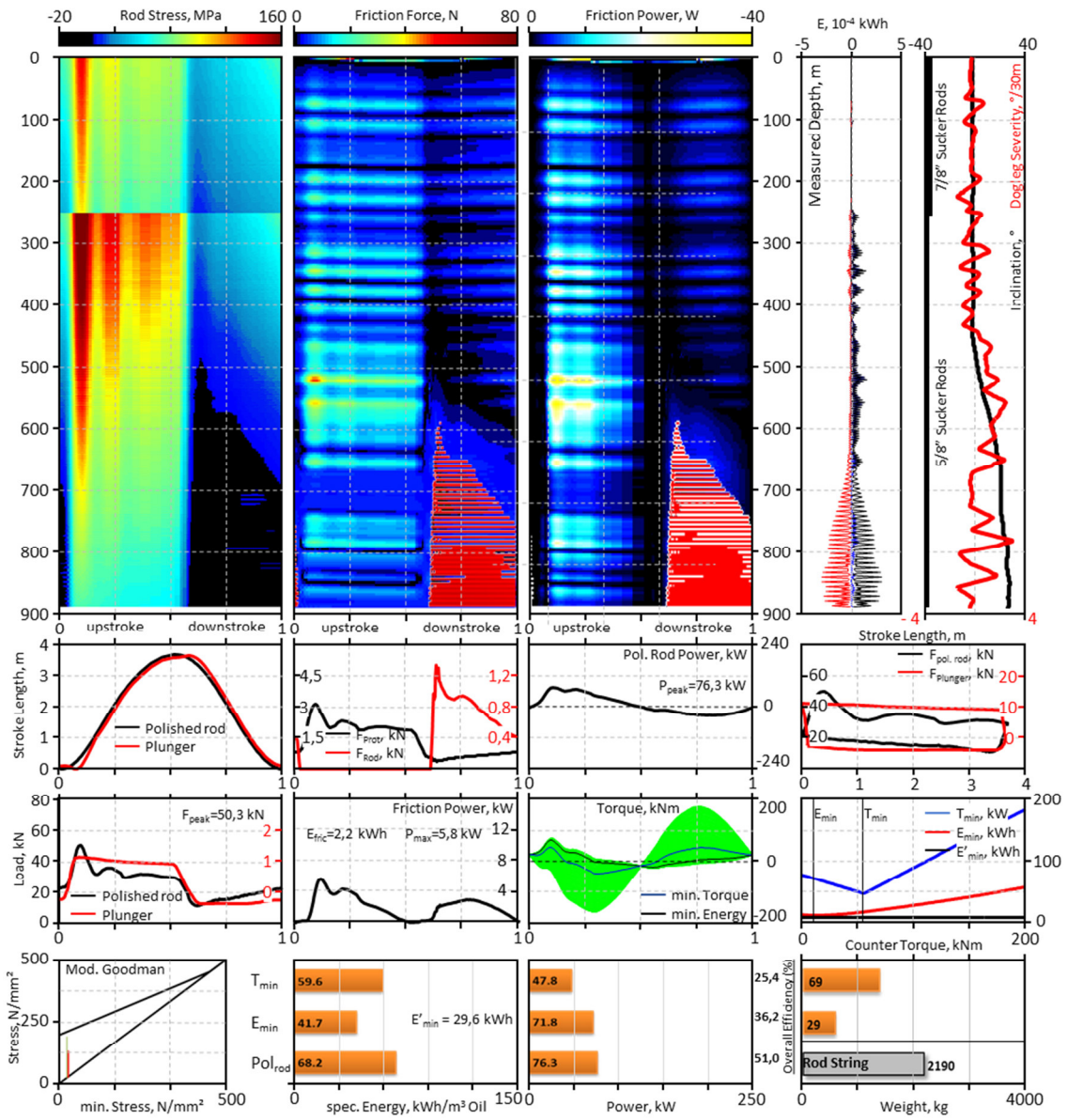
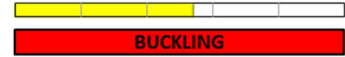


FIGURE 190: WELL OMV 1 – 10 SPM / 5/8" - 7/8" RODS

Well 1 – 15 SPM

Gross Rate = 80,9 m³/d

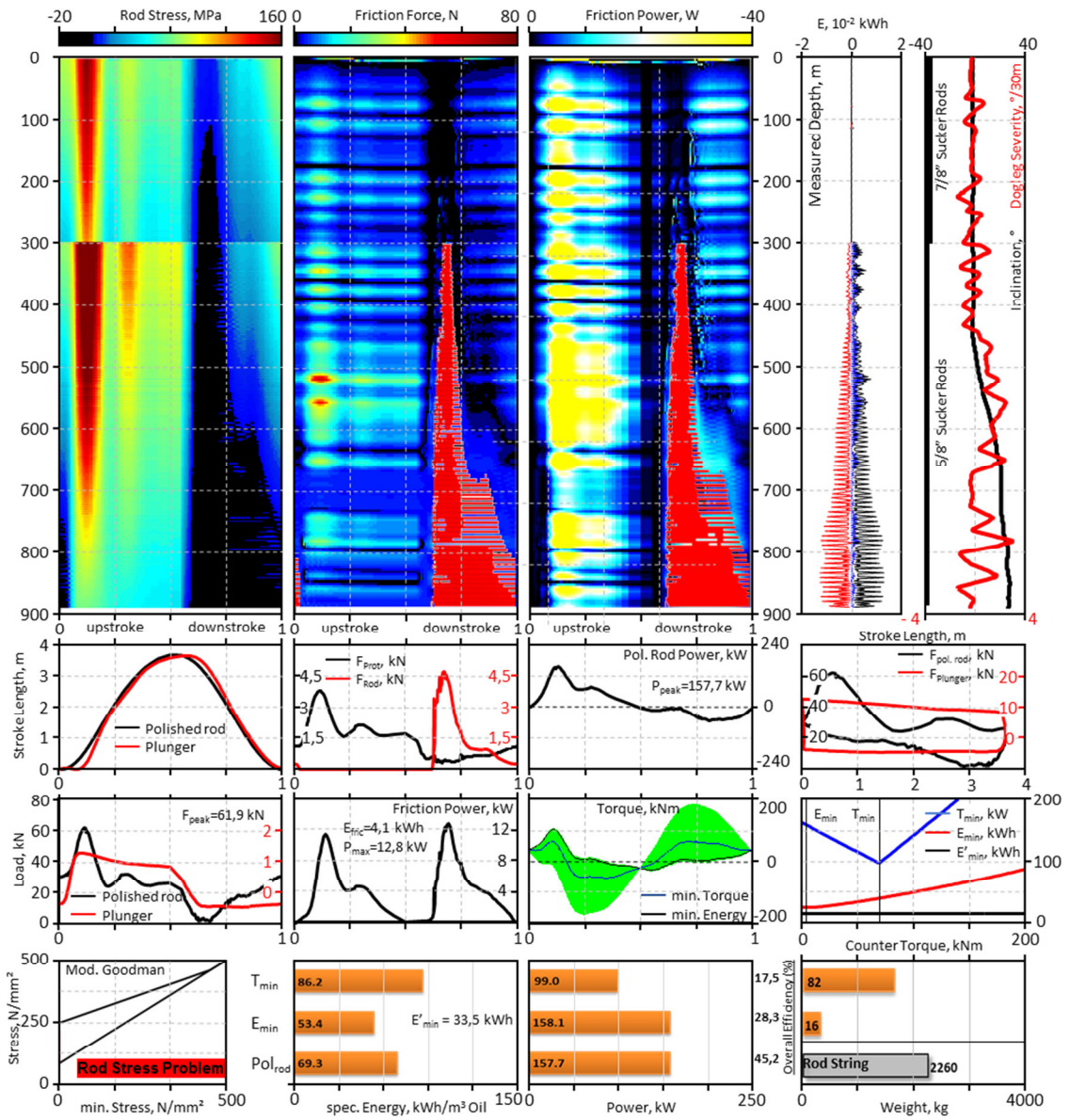


FIGURE 191: WELL OMV 1 – 15 SPM / 5/8" – 7/8" RODS

Well 1 – 4,85 SPM - SRABS

Gross Rate = 17,0 m³/d

NO BUCKLING

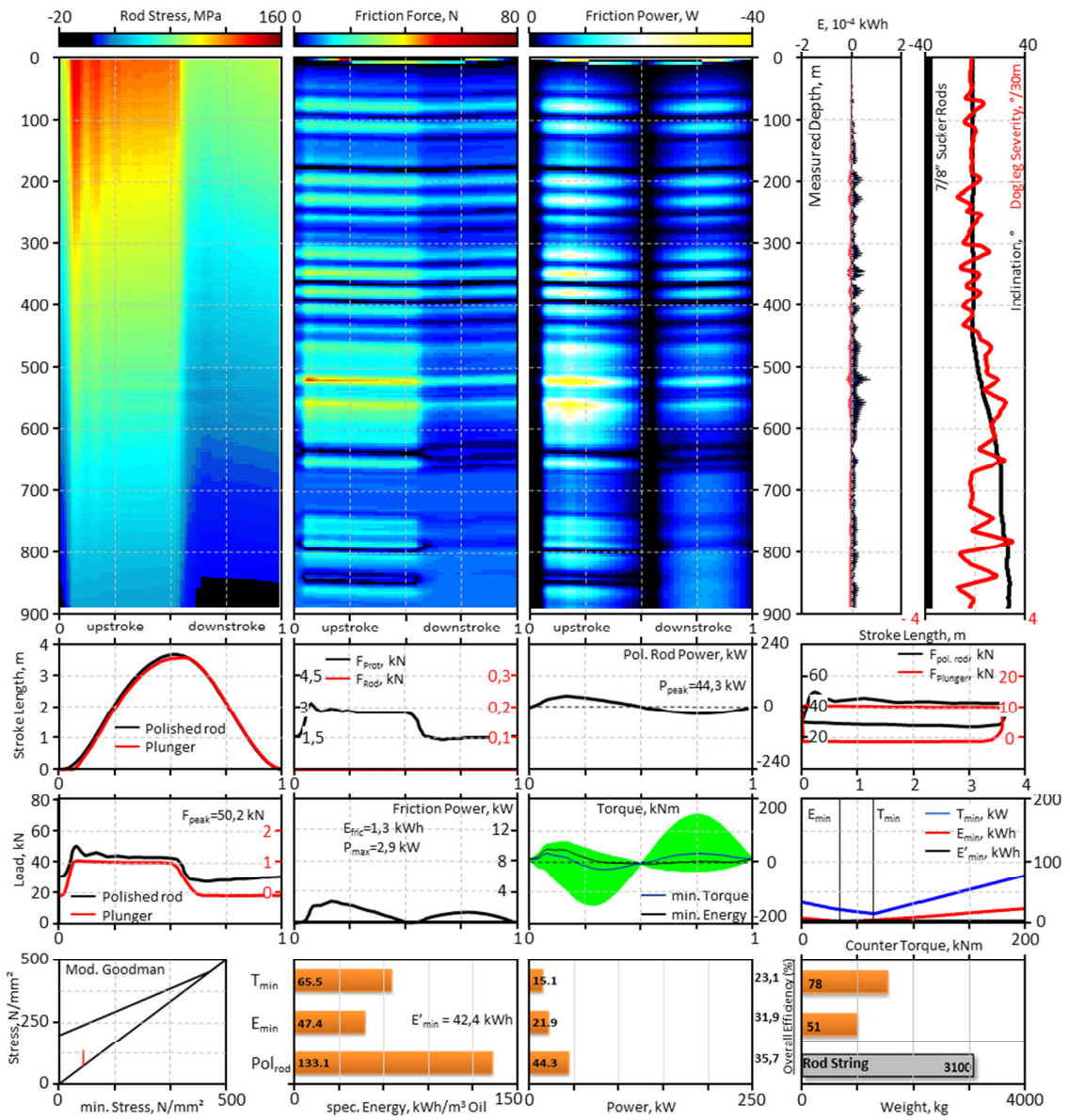


FIGURE 192: WELL OMV 1 – 4,85 SPM / SRABS – 7/8" RODS

Well 1 – 7,58 SPM - SRABS

Gross Rate = 26,6 m³/d

NO BUCKLING

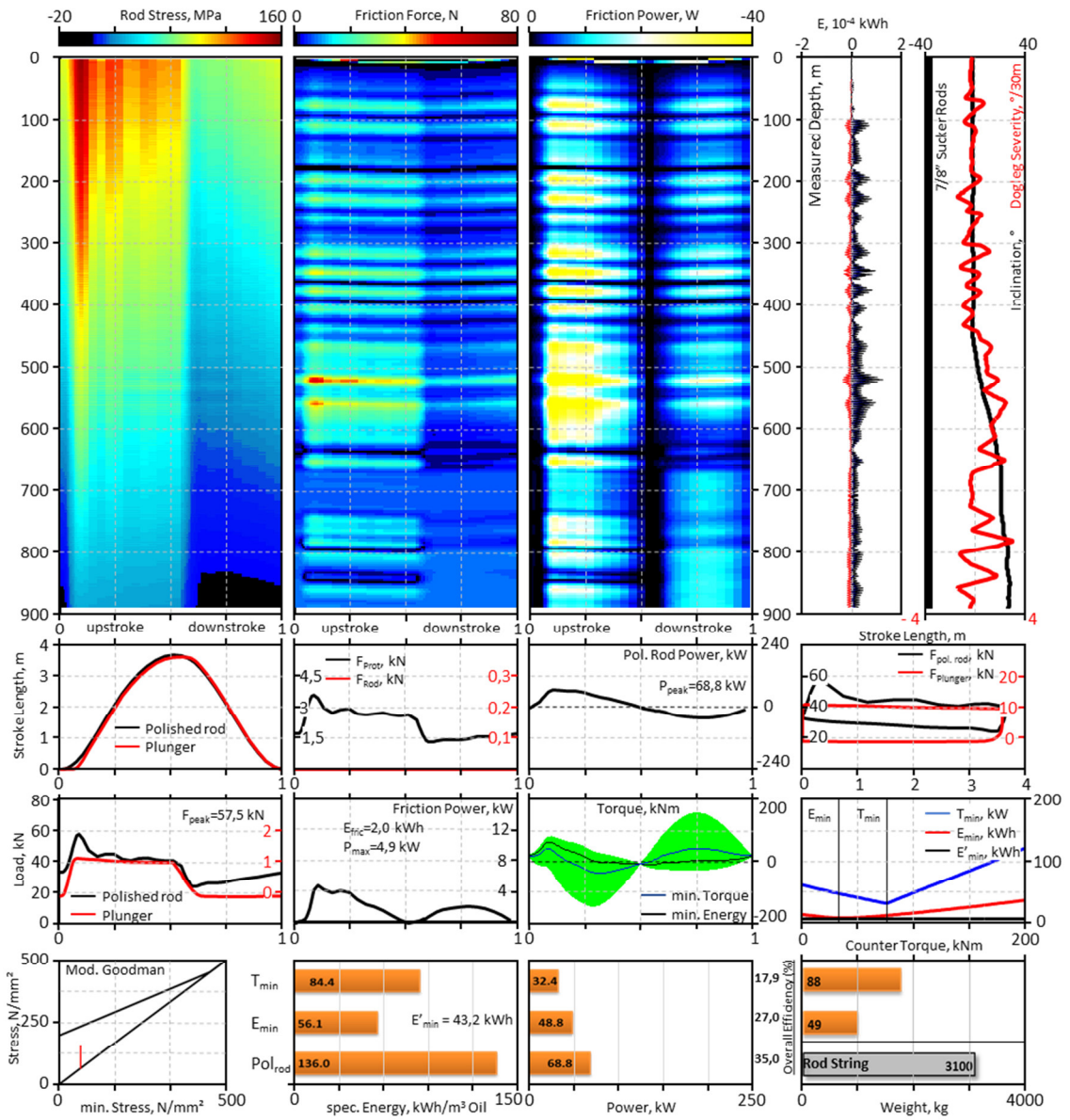


FIGURE 193: WELL OMV 1 – 7,58 SPM / SRABS – 7/8" RODS

Well 1 – 14,6 SPM - SRABS

Gross Rate = 53,1 m³/d

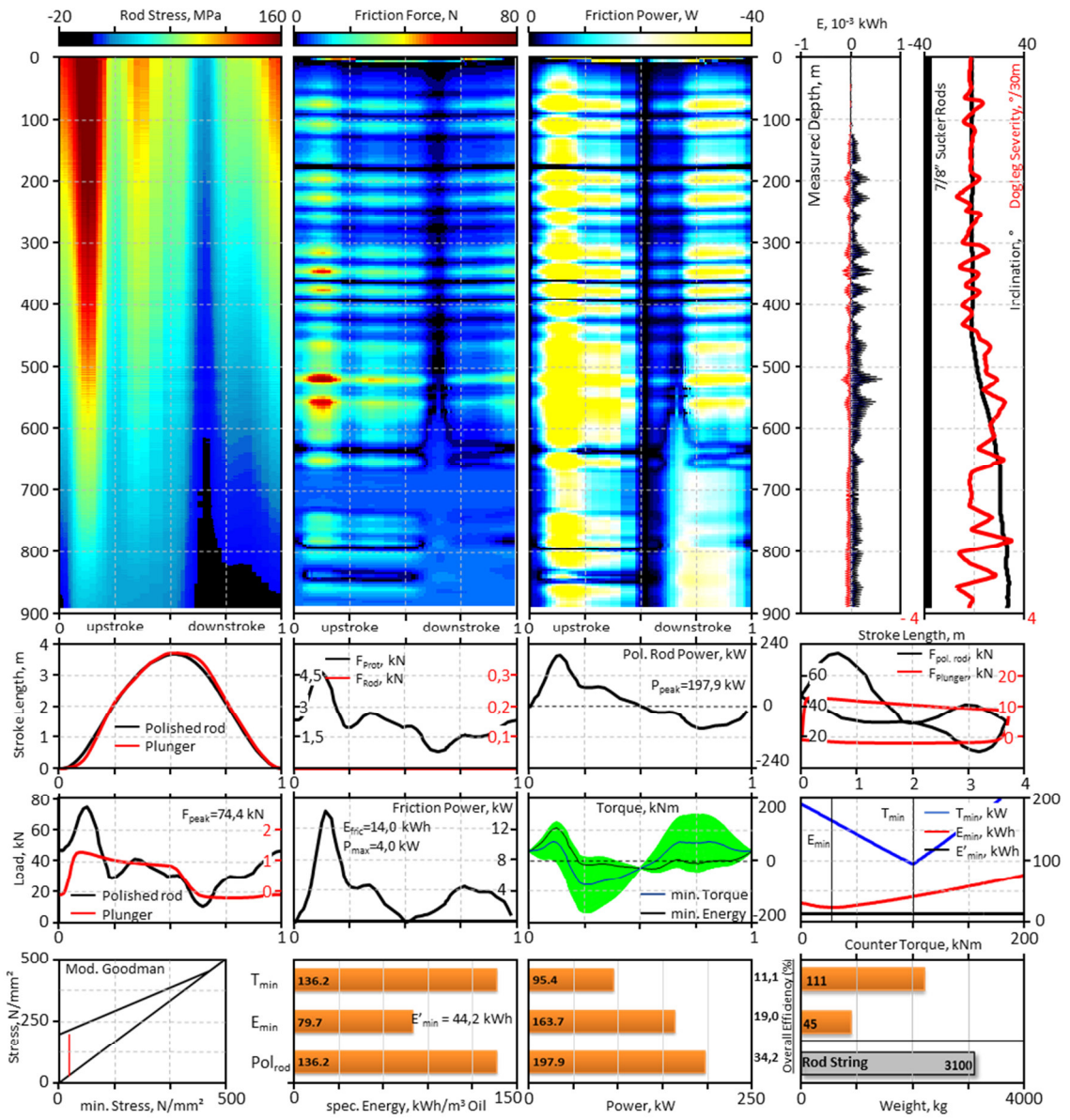
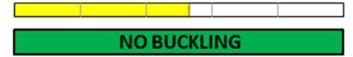


FIGURE 194: WELL OMV 1 – 14,6 SPM / SRABS – 7/8" RODS

Well 1 – 22 SPM - SRABS

Gross Rate = 84,1 m³/d

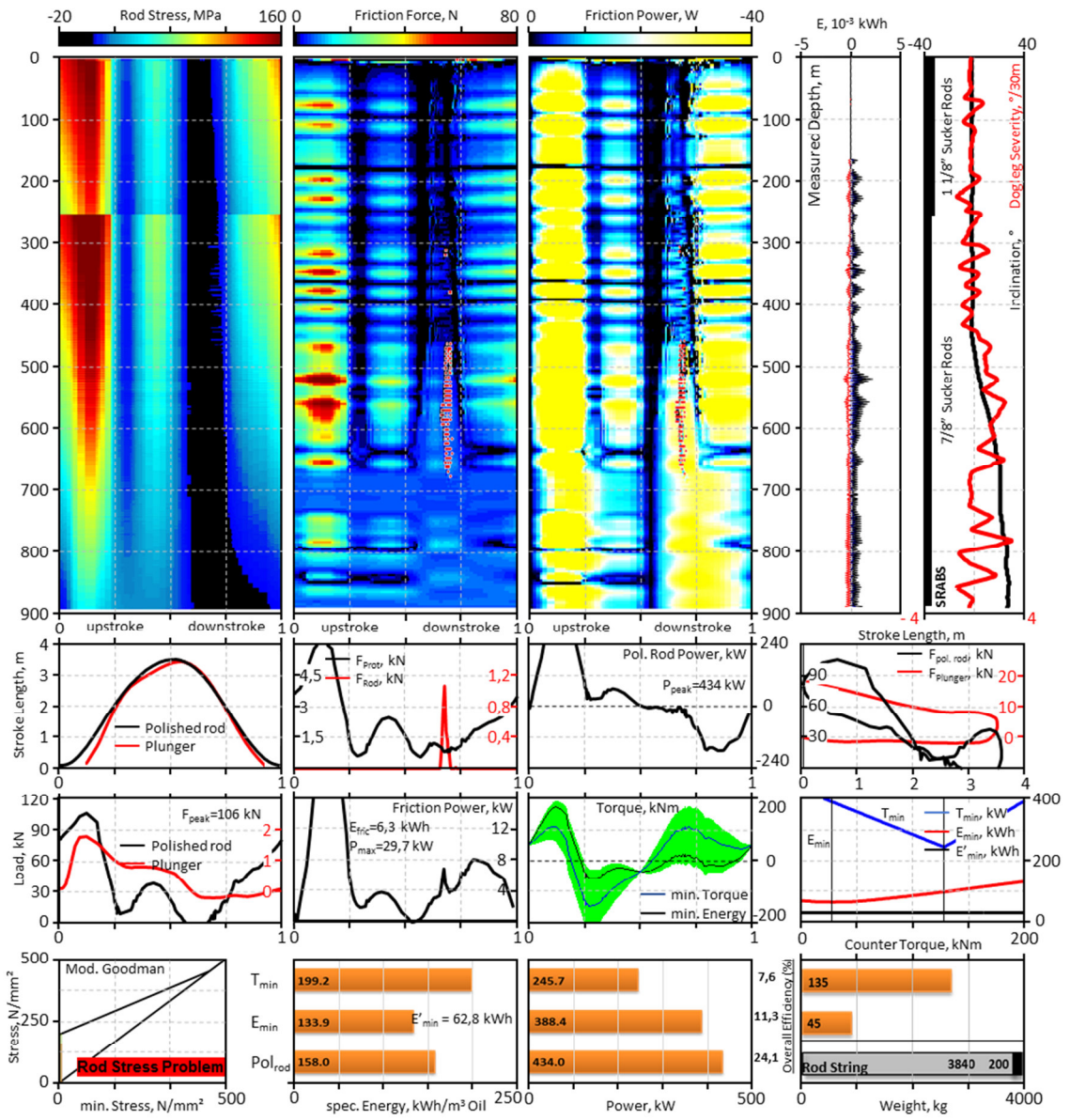
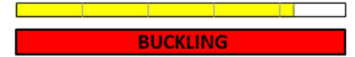


FIGURE 195: WELL OMV 1 – 22 SPM / SRABS – 7/8" & 1 1/8" RODS

Well 1 – 3,87 SPM - SRABS

Gross Rate = 17,1 m³/d

NO BUCKLING

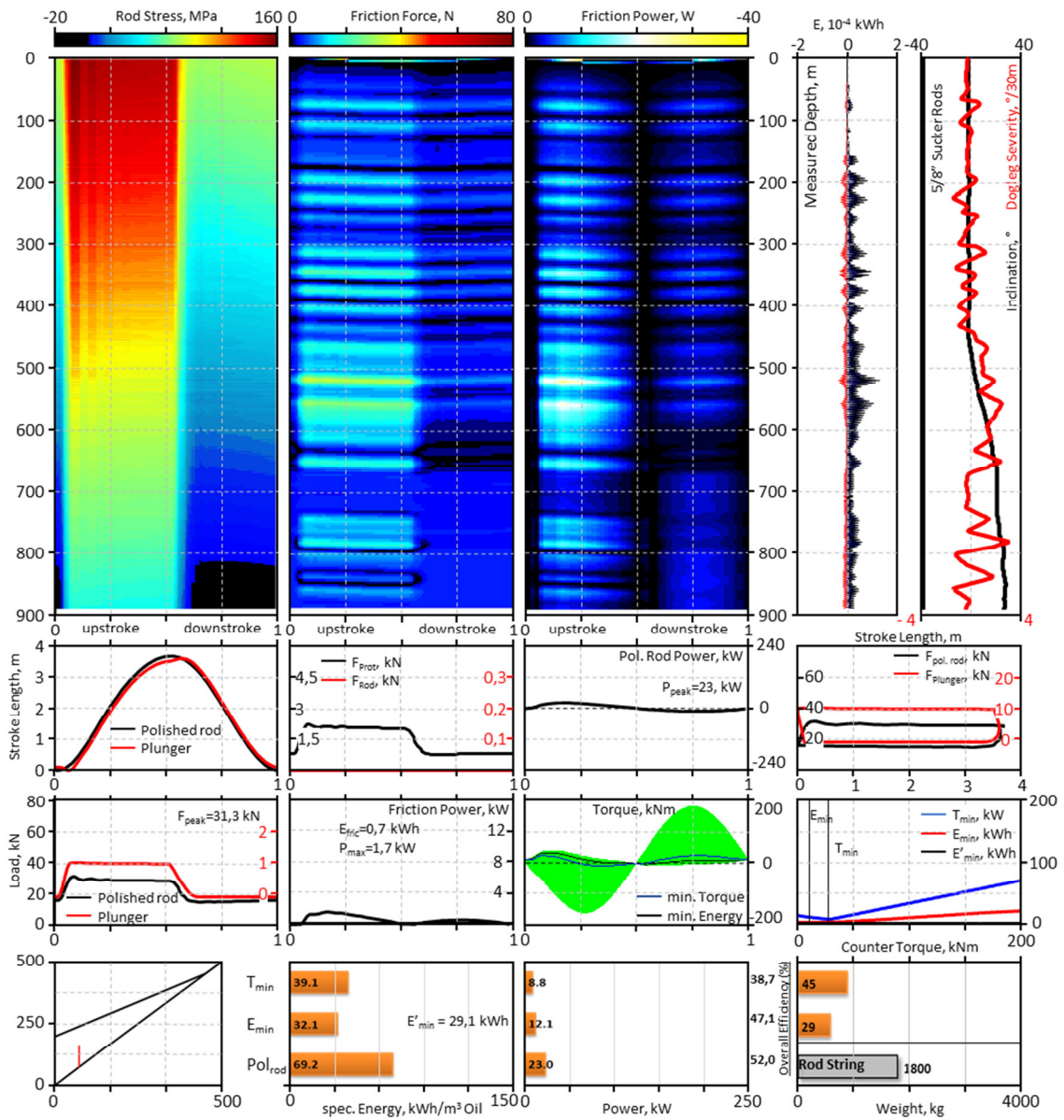


FIGURE 196: WELL OMV 1 – 3,87 SPM / SRABS – 5/8" RODS

Well 1 – 5,95 SPM - SRABS

Gross Rate = 26,4 m³/d

NO BUCKLING

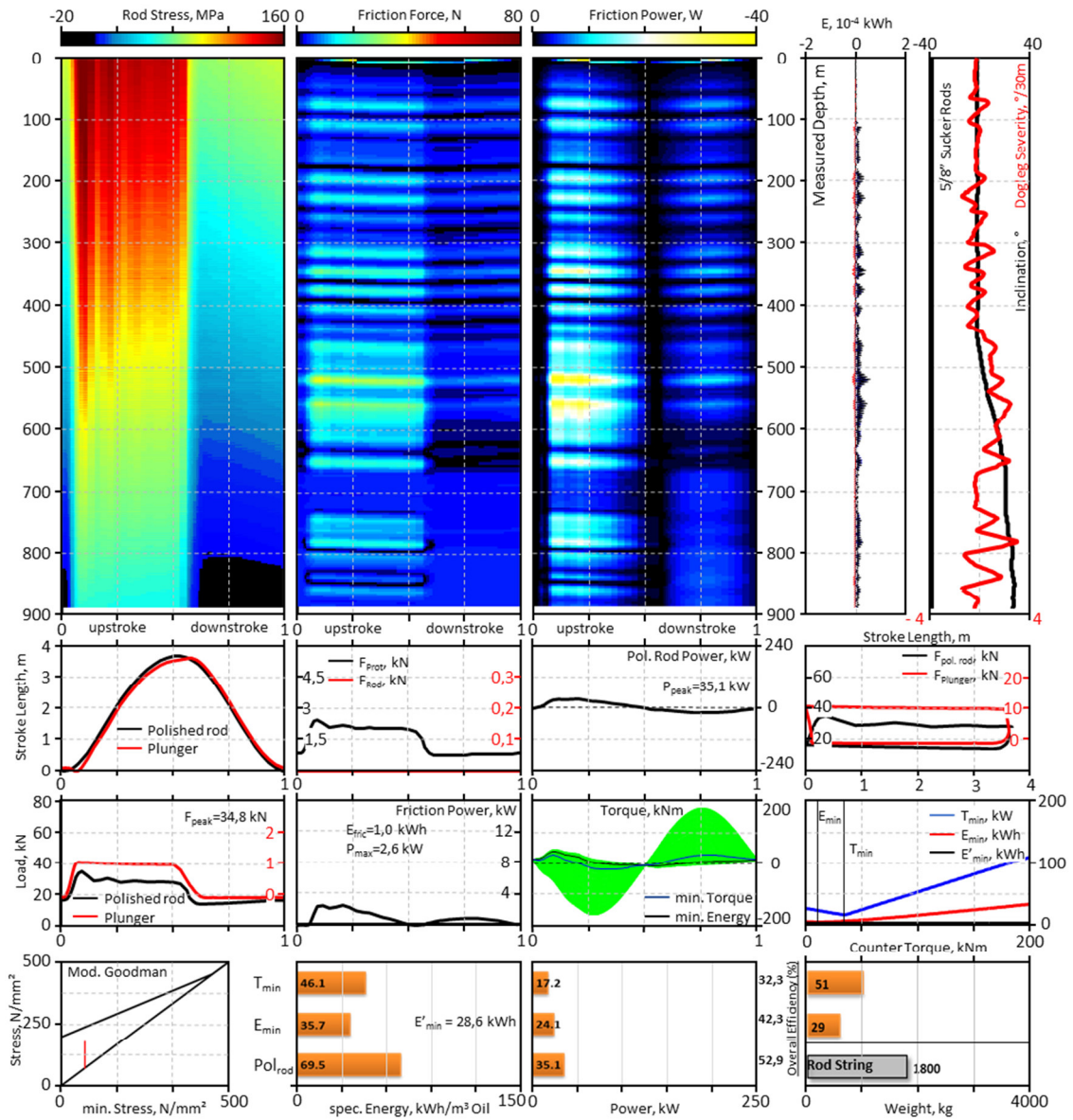


FIGURE 197: WELL OMV 1 – 5,95 SPM / SRABS – 5/8" RODS

Well 1 – 8 SPM - SRABS

Gross Rate = 35,4 m³/d

NO BUCKLING

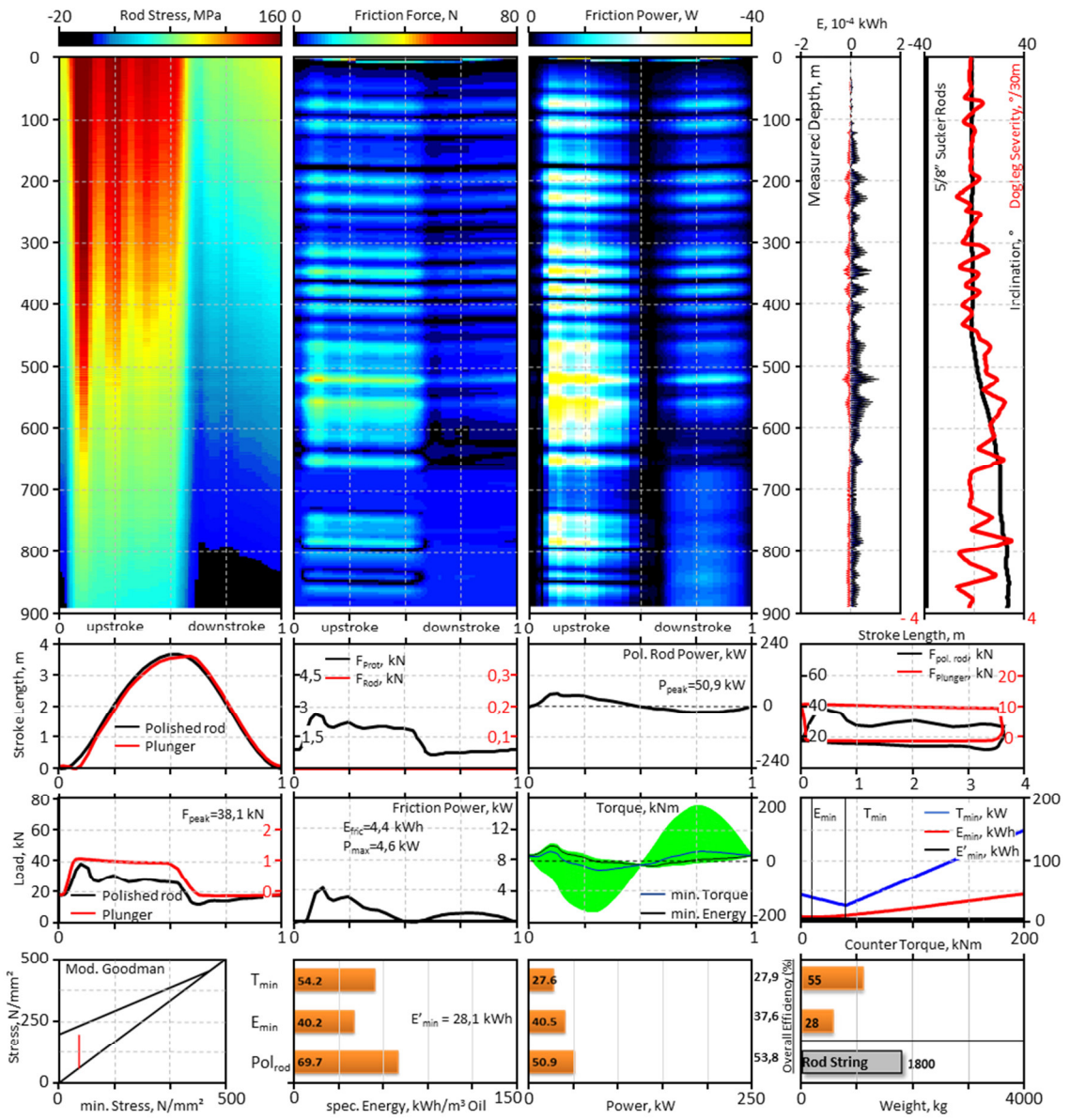


FIGURE 198: WELL OMV 1 – 8 SPM / SRABS – 5/8" RODS

Well 1 – 11,85 SPM - SRABS

Gross Rate = 52,1 m³/d

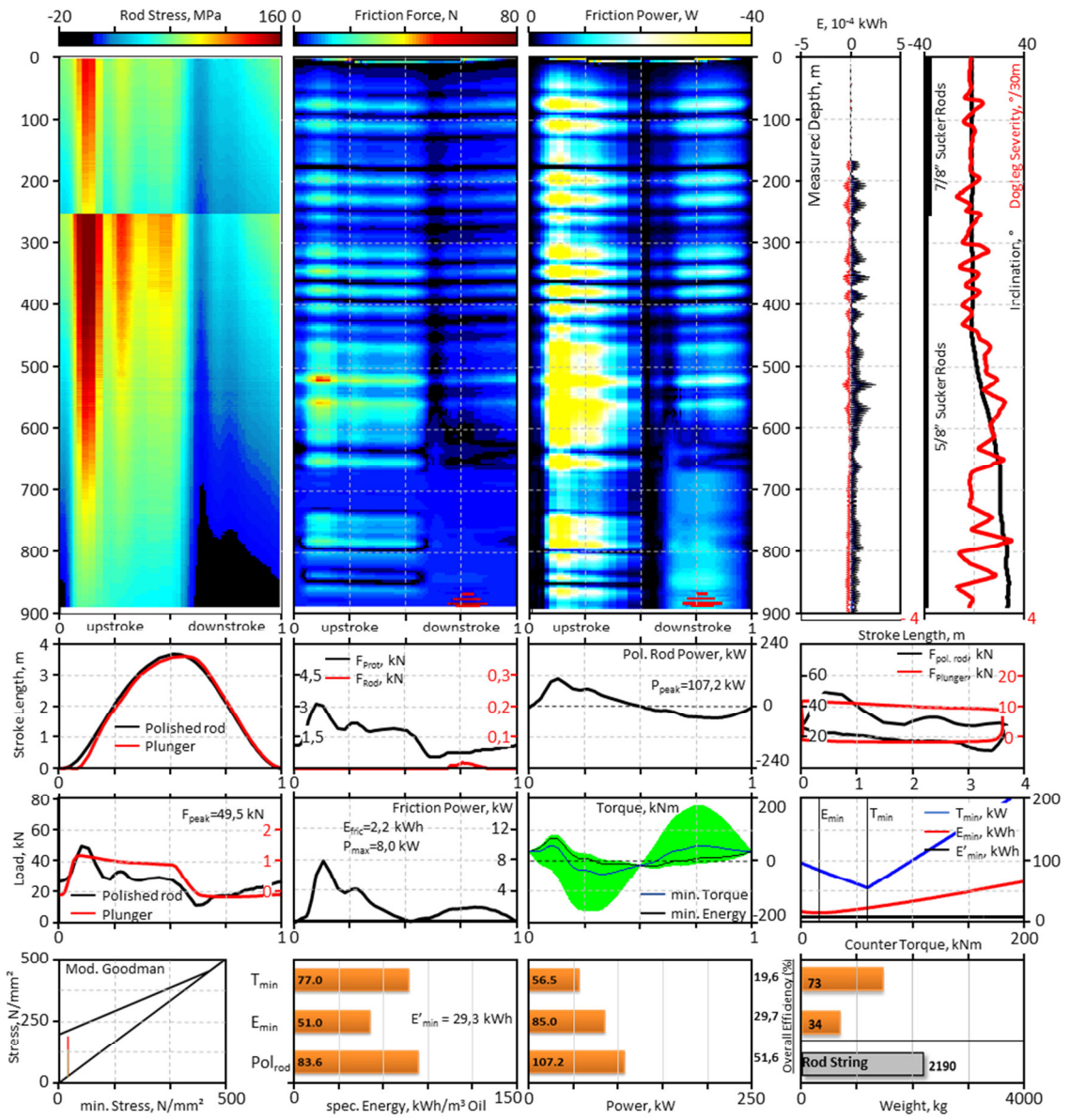
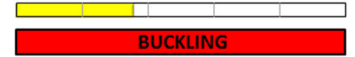


FIGURE 199: WELL OMV 1 – 11,85 SPM / SRABS – 5/8" & 7/8" RODS

Well 1 – 11,85 SPM - SRABS

Gross Rate = 52,1 m³/d

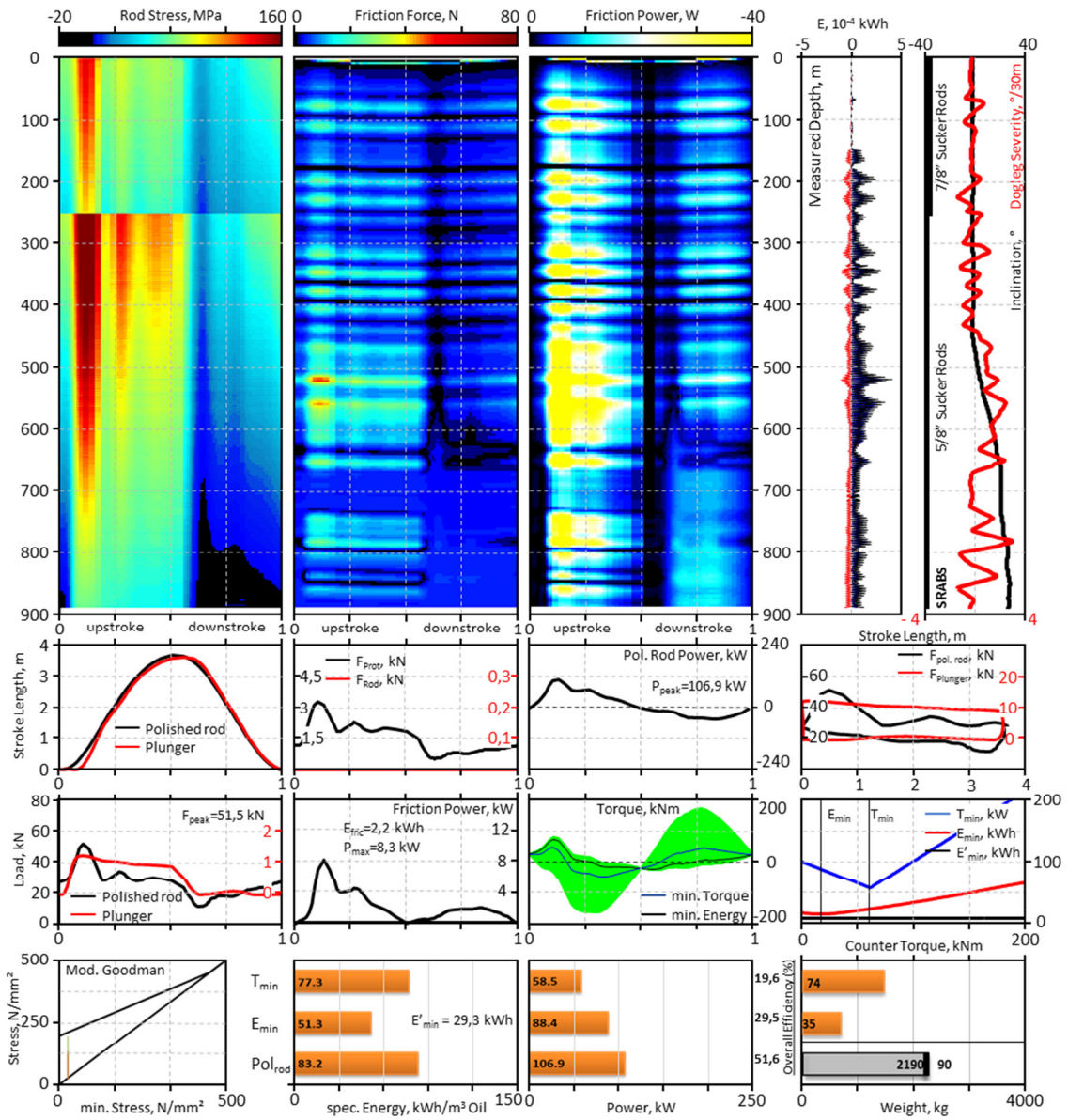
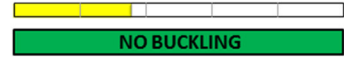


FIGURE 200: WELL OMV 1 – 11,85 SPM / SRABS – 5/8" & 7/8" RODS - MASS

Well 1 – 18,3 SPM - SRABS

Gross Rate = 86 m³/d

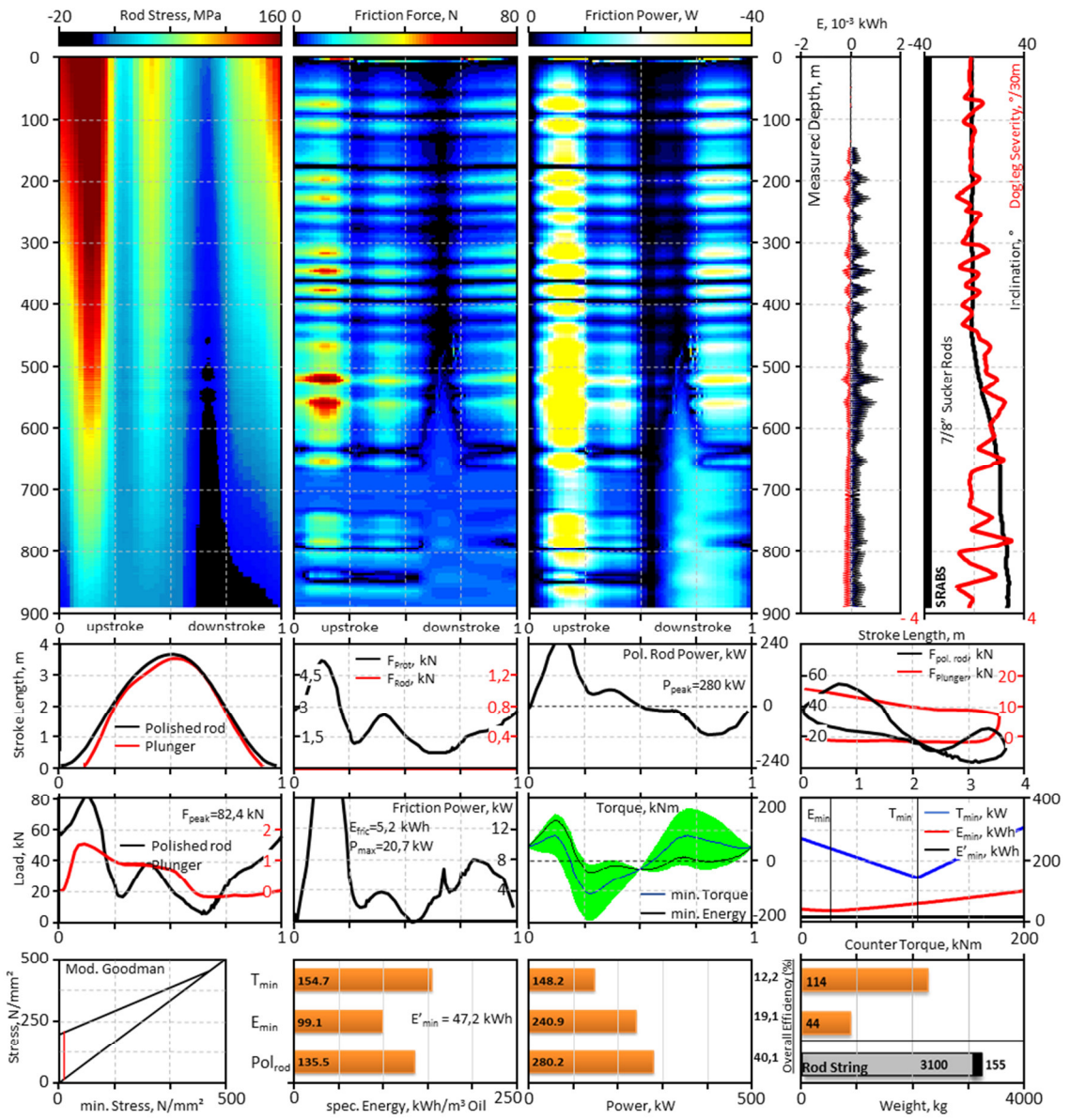
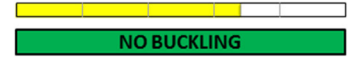


FIGURE 201: WELL OMV 1 – 18,3 SPM / SRABS – 7/8” RODS - MASS

Well 1 - 3,2 SPM – Sinker Bars

Gross Rate = 16,8 m³/d

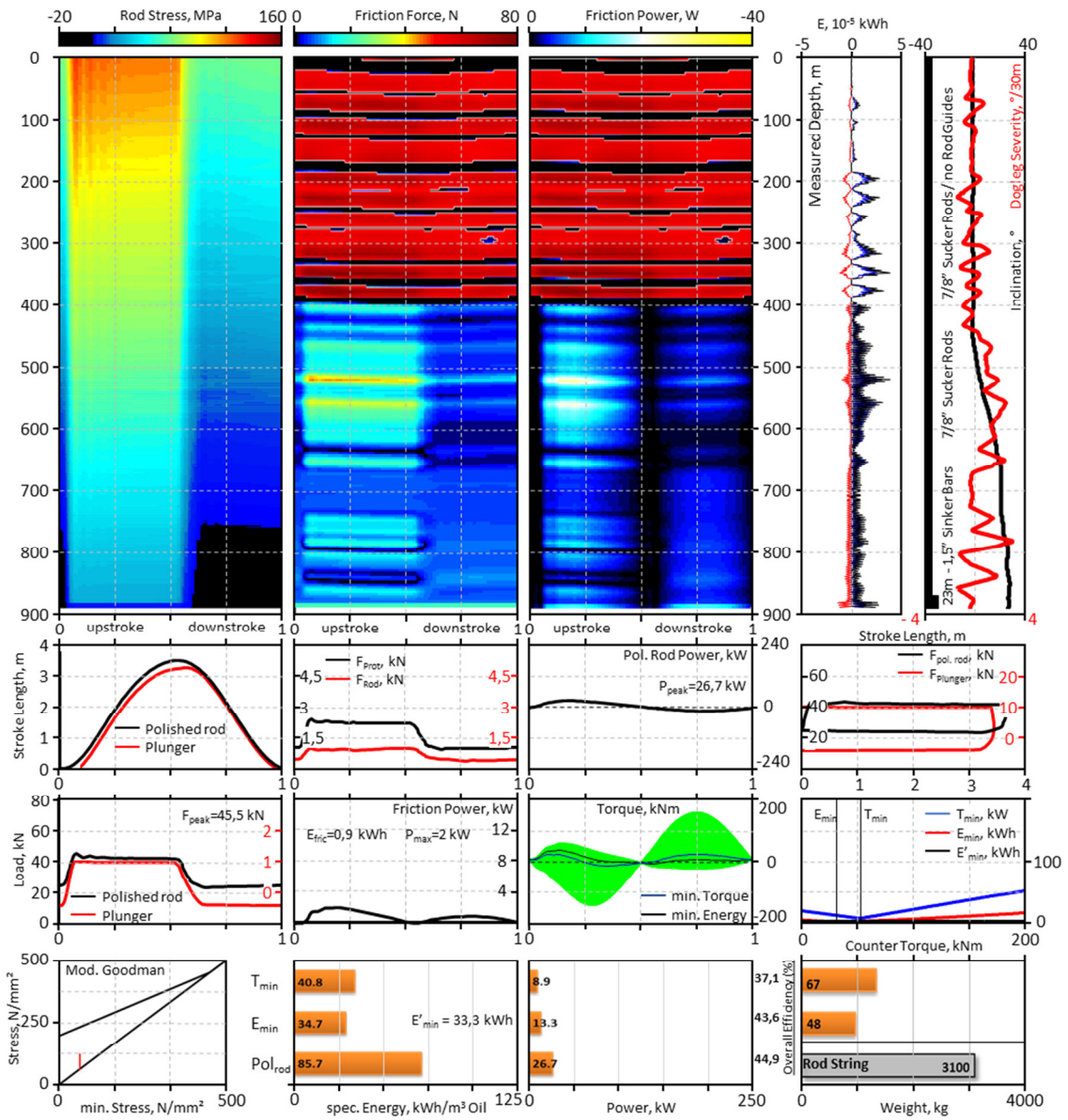
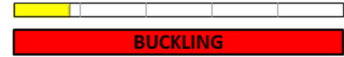


FIGURE 202: WELL OMV 1 – 3,2 SPM / SINKER BARS – NO ROD GUIDES

Well 1 - 3,87 SPM - SRABS

Gross Rate = 16,6 m³/d

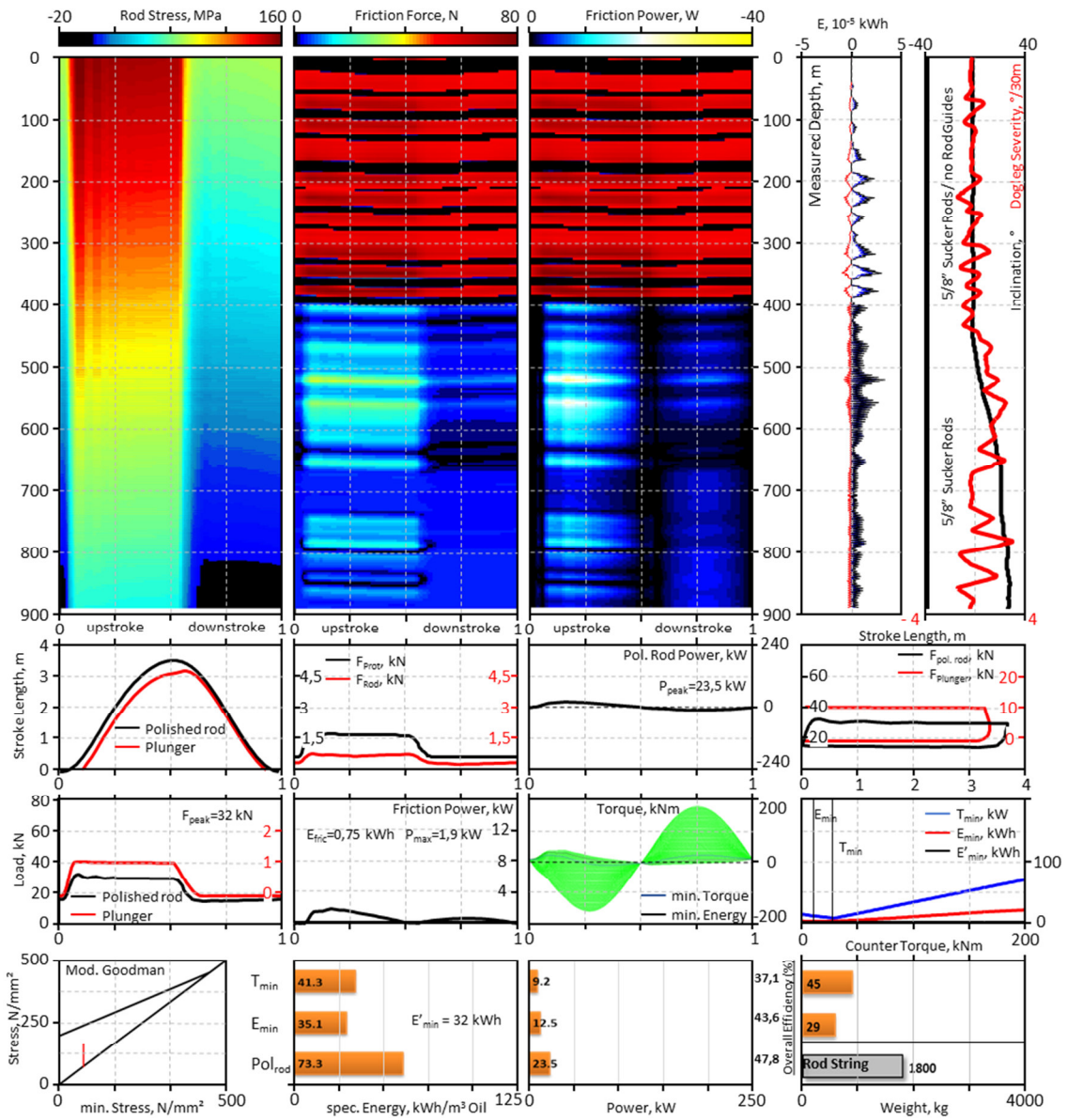
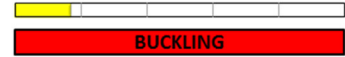


FIGURE 203: WELL OMV 1 - 3,87 SPM / SRABS - NO ROD GUIDES